

Characterization and modeling of zircaloy-4 recrystallization during hot forming

Victor Grand

▶ **To cite this version:**

Victor Grand. Characterization and modeling of zircaloy-4 recrystallization during hot forming. Mechanics of materials [physics.class-ph]. Université Paris sciences et lettres, 2022. English. NNT : 2022UPSLM090 . tel-04234774

HAL Id: tel-04234774
https://pastel.hal.science/tel-04234774

Submitted on 10 Oct 2023

HAL is a multi-disciplinary open access archive for the deposit and dissemination of scientific research documents, whether they are published or not. The documents may come from teaching and research institutions in France or abroad, or from public or private research centers.

L'archive ouverte pluridisciplinaire **HAL**, est destinée au dépôt et à la diffusion de documents scientifiques de niveau recherche, publiés ou non, émanant des établissements d'enseignement et de recherche français ou étrangers, des laboratoires publics ou privés.

PSL UNIVERSITÉ PARIS

THÈSE DE DOCTORAT

DE L'UNIVERSITÉ PSL

Préparée à MINES Paris-PSL

Characterization and modeling of zircaloy-4 recrystallization during hot forming

Caractérisation et modélisation de la recristallisation du zircaloy-4 lors de la mise en forme à chaud

Soutenu par

Victor GRAND

Le 05 Décembre, 2022

École doctorale n°264

ED SFA

Spécialité

Mécanique Numérique et Matériaux

Composition du jury :

Frank MONTHEILLET Directeur de recherche émérite, École Nationale Supérieure des Mines de Saint-Étienne	*Président du jury*
Lukasz MADEJ Professeur, AGH University of Science and Technology	*Rapporteur*
Javier SIGNORELLI Professeur, Instituto de Fisica Rosario	*Rapporteur*
Pierre BARBERIS Dr. Ingénieur R&D, HDR, Framatome	*Examinateur*
Nathalie BOZZOLO Professeur, Mines Paris, Université PSL	*Examinateur*
Baptiste FLIPON Dr. Ingénieur de recherche, Mines Paris, Université PSL	*Examinateur*
Alexis GAILLAC Dr. Ingénieur R&D, Framatome	*Examinateur*
Marc BERNACKI Professeur, Mines Paris, Université PSL	*Directeur de thèse*

MINES PARIS | PSL

Acknowledgements

First, I would like to thank my two supervisors, Marc Bernacki and Alexis Gaillac. Alexis, I really appreciated the way you supervised my work, from the first day we have started working together. I continue being impressed by your reliability and your benevolence. Marc, thank you for sharing your passion about simulation with me. I would like to express a special thank for the effort you made trying to convince me about the quality and interest of the work I produced. I am very pleased to still collaborate with both of you regularly.

I thank all the members of the jury. By reading your reports and answering your questions, I had the chance to benefit from your knowledge and expertise and to get a critical review of my work. I really appreciated it. I would like to thank Nathalie Bozzolo and Pierre Barberis for the very interesting discussions we had.

Baptiste, thank you very much for the time you spent with me, discussing about recrystallization and bicycles. These discussions helped me staying motivated in tough moments. I kept many new ideas, in both domains, from these discussions. I will forever remember the noise of a triple butted bike tubing, and I think you can be proud of it. For these reasons and a ton of others, I am very pleased to have worked with you these last three years.

I thank all the people I have worked with at CEMEF. I deeply thank Gilbert Fiorucci for the help and guidance he gave me for the many thermomechanical tests. I hope you will enjoy your retirement soon. Cyrille Colin, I thank you for all the hours we spent together polishing zirconium samples and trying to solve SEM problems. It has been a great pleasure to work with you.

Florence, I did not work with you directly but I express all my gratitude for your help and your happiness. You greatly participate to make the whole CEMEF a better work place.

I will miss all the coffee breaks shared with Diego, Brayan, Aakash, Alexis, Franco and Baptiste. They have greatly contributed to my happiness but also to my productivity. I have learned so many things about South American and Indian cultures. I hope I will have the opportunity to meet all of you again soon.

I finish by expressing my deepest gratitude to you, Justine. I immensely value all the moments we shared together during this period. Thanks to you, I had very good reasons for putting work aside. We shared priceless experiences, during hikes, bike rides or just by doing nothing but enjoying the present moment. There are so many reasons to thank you but I will keep it simple. Thank you Justine

for having decided two years ago that it would be nice to cross France to visit me in Mouans-Sartoux. I love you.

Introduction

For almost two centuries, thanks to the scientific and technical advances, the standards of living have improved on average in the world [1, 2]. These progresses are substantial and cannot be denied, especially in rich countries that have benefited the most from them. Nevertheless, the humankind is now facing one of the greatest challenge ever. With industrialization and the generalization of fossil fuel usage, the production of greenhouse gases have skyrocketed and the annual average of CO_2 concentration has reached 410 *ppm* (against 280 *ppm* before 18^{th} century) [3]. It is now proven by scientific evidences that this is responsible for the general temperature increase observed since 1970 (see figure 1). More widely, these advances are responsible for climate change and challenge the use and sharing of natural resources.

To ensure Earth remains a habitable place, we must act at all levels and change drastically our way of thinking, trading and consuming. Thus, a paradigm change is unavoidable and implies that inhabitants of rich countries must accept to change their way of living. This conclusion has already been formulated 20 years ago and the changes are very feeble [3]. Therefore, if scientific and technological progresses are not a panacea, it would be foolish to not use them at our advantage to provide some answers to specific challenges related to climate change. Nowadays, some solutions already exist to reduce the greenhouse gas emissions in the main economic sectors. For instance, in 2020, the electricity production of the United States of America was still representing 27% of the total country emissions [4]. However, some alternatives are available now to produce electricity without the use of fossil fuels: hydroelectric dams, wind turbines, solar panels, or even nuclear power plants. In combination with a general energy consumption decrease, these different electricity production modes constitute a relevant, sustainable and resilient alternative to fossil fuels.

Nuclear energy has been suffering from a bad public opinion for almost 40 years, due to several accidents that caused important damages and that have been largely broadcasted. If the risk of a nuclear accident is extremely low, the recent events in Japan and in Ukraine are here to recall that some unexpected scenarios can lead to complex situations. Thus, due to the potential terrible consequences of a nuclear accident, the security requirements must be drastic.

To fulfill such high requirements, everything must be understood and controlled, from the global reactor's operation to the behavior of each component. Ensuring that each part has the exact geometry and the required properties is

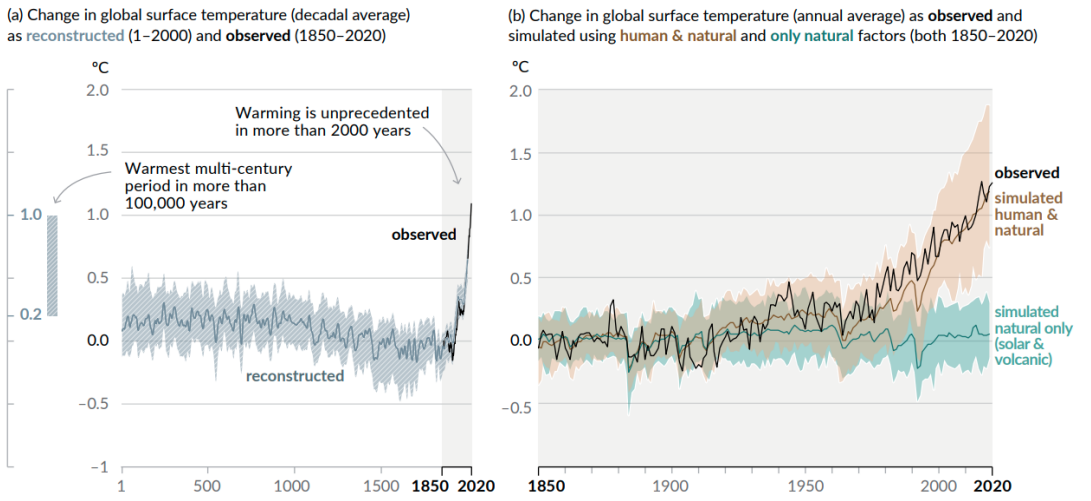


Figure 1: Changes in global surface temperature, from observations and simulations. From [3].

done by mastering every manufacturing stage. Indeed, during hot deformation, the material microstructure evolves and this affects the in-use properties, such as ductility, mechanical strength or corrosion resistance ... The parts constituting the nuclear fuel assembly follow that principle. Most of these parts (cladding and guide tubes, end plugs and grids) are made of zirconium alloys. This choice is motivated by the low neutron capture cross-section, the good mechanical strength and corrosion resistance of zirconium alloys, under boiling water or pressurized water reactor working conditions (respectively BWR or PWR). Until now, a large majority of the studies concerning zirconium alloys focuses on in-use properties: hydrogen embrittlement [5, 6, 7], corrosion [8, 9], creep [10, 11]. The studies addressing microstructure evolutions taking place during forming processes discuss to a large extent the texture evolution [12, 13, 14]. Nevertheless, the studies dedicated to mechanisms of microstructure evolution taking place during hot deformation and after a subsequent heat treatment remain limited [15, 16, 17].

Since recrystallization (i.e. formation and growth of new grains with a low defect density) is one of the main mechanism responsible for microstructure evolution and significantly affects the final microstructure [18], there is a need for additional data about the occurrence of this mechanism in zirconium alloys. Indeed, zirconium alloys present a complex microstructure, with some various and potentially complex grain topologies (such as Widmanstätten microstructures) and some second phase particles (SPP). Therefore, it would be highly valuable to obtain precise information relative to the impact of such microstructural characteristics over recrystallization.

To this end, this work proposes to use both experimental and numerical tools to investigate the microstructure evolution taking place during hot deformation and subsequent heat treatment of a given zirconium alloy: zircaloy-4 (Zy-4). This twofold approach presents multiple interests. First, having consistent experimen-

tal results remains the essential starting point for such study. It allows to identify the physical mechanisms, to constitute databases for identification of model parameters and evaluation of the results. Then, developing simulation tools adapted to the physical mechanisms of interest and applying them makes possible to limit the number of experiments required for upcoming studies. This is of first interest since experimental campaigns, especially at industrial scale, can be very costly. If the simulation framework is flexible and able to consider various features, then it allows to complement the experimental observations by discriminating the impact of such features over the evolutions observed.

Modeling and more generally improving the understanding of recrystallization and annealing phenomena are the objectives of the DIGIMU software [19] developed in the context of the DIGIMU consortium [20]. To do so, a level-set (LS) model embedded into a finite element (FE) framework is developed at CEMEF, in collaboration with the industrial partners taking part in DIGIMU consortium: Safran, Aubert & Duval, Framatome, CEA, Timet, ArcelorMittal, Constellium, Aperam and Ascometal. Using a LS formulation allows to describe efficiently typical microstructures of metallic materials at mesoscopic scale. It enables to retrieve the main interface characteristics, such as curvature, which contributes to the motion of grain boundaries. Embedding the LS model into a FE framework is essential for modeling microstructure evolutions in the context of large deformation, which is mandatory to apply such tools to industrial forming processes.

Various phenomena can be modeled in the existing LS-FE model developed in MSR team for more than 15 years: grain growth (GG), dynamic recrystallization (DRX), post-dynamic recrystallization [21, 22, 23, 24, 25, 26]. These mechanisms can be simulated taking into account the effect of various microstructural features: initial microstructure topology, SPP [27, 28], anisotropy of GB properties [29, 30, 31], ... in 2D and in 3D. Therefore, it constitutes a framework of choice for modeling Zy-4 microstructure evolutions.

To propose answers to the questions detailed earlier, the following methodology is used: samples with different initial microstructures are manufactured, then submitted to hot deformation and/or heat treatment testings, and finally characterized. The microstructure characterization campaigns provide a valuable amount of data for identifying the mechanisms, the impact of thermomechanical conditions and initial microstructure. Then, some implementations are performed to adapt the model to the mechanisms observed. Finally, the model is applied to simulate all the mechanisms: GG, DRX and PDRX. The numerical results are evaluated by comparing them to experimental results. Extensive analyses of both experimental and simulation results provide some new insights about the impact of several microstructure features, such as intragranular dislocation density gradients.

To present this work, the current manuscript follows the layout described below.

Chapter 1 details the state of the art regarding recrystallization of zircaloy-4,

from both experimental and simulation perspectives. First, the Zy-4 microstructural features that are likely to impact recrystallization are described. Then, recrystallization and related mechanisms are presented extensively, and a special attention is given to detail the specific features related to continuous recrystallization mechanisms. Finally, the numerical models that are commonly used in literature for recrystallization simulation are presented and the advantages and drawbacks of each method are listed.

Chapter 2 describes in details the experimental strategy chosen. The initial microstructures and the heat treatment and thermomechanical testing campaigns are presented. The characterization techniques employed are defined. A detailed analysis is described to estimate the uncertainty associated with the different measurements.

Chapter 3 presents the numerical framework. It describes the implementation made to model recrystallization of Zy-4. Finally, this implementation is assessed by analyzing the evolution of microstructures presenting a subgrain structure, in different conditions and with different assumptions.

Chapter 4 summarizes all the results related to GG, with and without SPP, from both experimental and simulation point of views. Reduced mobility, which constitutes one model parameter, is identified in absence of SPP. Finally, this parameter is applied to the modeling of GG in presence of SPP, with various microstructures and temperatures.

Chapter 5 details experimental and simulation results related to PDRX. The impact of the thermomechanical conditions of the previous hot deformation stage is discussed. The influence of initial microstructure is highlighted thanks to experimental data. Then, full-field simulations of PDRX are performed. The initial simulation results are compared to experimental data and the discrepancies are analyzed. Several hypotheses are formulated. Additional simulation cases point out the role of intragranular GND density gradients in the heterogeneous growth rate of recrystallized grains.

Chapter 6 applies a similar approach than chapter 5 to study CDRX. The differences of stored energy due to deformation are analyzed, for different thermomechanical conditions and initial microstructures. A discussion over the formation of substructure during CDRX is proposed. The consequences of these two features over PDRX are highlighted. Finally, the numerical implementations described in chapter 3 are applied to simulate CDRX and PDRX.

Lastly, a summary of the present work is proposed. The main outcomes are highlighted and some prospects are given.

Oral and written communications

These works have lead or contributed to the following written and oral communications.

Articles

- Baptiste Flipon, Victor Grand, Brayan Murgas, Alexis Gaillac, Alexis Nicolaÿ, Nathalie Bozzolo, and Marc Bernacki. Grain size characterization in metallic alloys using different microscopy and post-processing techniques. Materials Characterization, 174:110977, 2021.

- Alexis Gaillac, Victor Grand, Alan Arsen, Quentin Gaillard, and Marc Bernacki. Towards Multi-Scale Modeling of Zirconium Alloys Recrystallization and Application to Thermo-Mechanical Processes Optimization. Key Engineering Materials, 926:443-451, 2022.

- Victor Grand, Baptiste Flipon, Alexis Gaillac, and Marc Bernacki. Characterization and simulation of initial microstructure influence upon recrystallization of Zy-4. 20th International Symposium on Zirconium in the Nuclear Industry, ASTM STP, 2022, Accepted: ArXiv: https://arxiv.org/abs/2203.08447.

- Victor Grand, Baptiste Flipon, Alexis Gaillac, and Marc Bernacki. Simulation of continuous dynamic recrystallization using a level-set method. Materials, 15(23):8547, 2022.

Presentations

- Victor Grand, Baptiste Flipon, Alexis Gaillac, and Marc Bernacki. Modeling of CDRX of Zr alloys. Transvalor European Microstructure Simulation Days, March 2022, Frankfurt, Germany.

- Alexis Gaillac, Victor Grand, Alan Arsen, Quentin Gaillard, and Marc Bernacki. Towards Multi-Scale Modeling of Zirconium Alloys Recrystallization and Application to Thermo-Mechanical Processes Optimization. ESAFORM - 25th International Conference on Material Forming, 27-29 April 2022, Braga, Portugal.

- Victor Grand, Baptiste Flipon, Alexis Gaillac, and Marc Bernacki. Characterization and simulation of initial microstructure influence upon recrystallization of Zy-4. 20th International Symposium on Zirconium in the Nuclear Industry, June 2022, Ottawa, Canada.

Contents

Introduction **3**

1 Literature review **13**
1.1 Properties and manufacturing of zircaloy-4 14
1.1.1 Zircaloy-4 metallurgy 14
1.1.2 Hot deformation mechanisms 18
1.1.3 Deformation at mesoscopic scale 21
1.1.4 Texture of Zy-4 22
1.1.5 Industrial forming of Zy-4 parts 22
1.2 Recrystallization and related mechanisms 24
1.2.1 General terminology of recrystallization and grain growth . 24
1.2.2 Grain boundary description 25
1.2.3 Description of the microstructural mechanisms of recrystallized grain formation 31
1.2.4 Application to recrystallization of Zy-4 37
1.3 Numerical models of recrystallization 41
1.3.1 Analytical models 41
1.3.2 Mean-field models 44
1.3.3 Full-field frameworks 48
1.4 Conclusion 56

2 Materials and experimental methods **59**
2.1 Materials 60
2.1.1 Elaboration of initial microstructures 60
2.1.2 Characterization of initial microstructures 62
2.2 Heat treatments 67
2.3 Thermomechanical testing 67
2.3.1 Description of the experimental set-up 67
2.3.2 Thermomechanical simulation of hot compression 68
2.3.3 Definition of sample geometries 68
2.3.4 Definition of thermomechanical conditions 71
2.3.5 Post-processing of thermomechanical data 71
2.4 Microstructure characterization 78
2.4.1 Sample preparation 78

2.4.2 Measurement of grain size distribution using OM-PL and image analysis . . . 79
2.4.3 Characterization of microstructures using EBSD . . . 83
2.4.4 SPP characterization by TEM . . . 90
2.5 Conclusion . . . 91

3 Numerical methods 93
3.1 Level-set framework for simulation of microstructure evolutions . 94
3.1.1 Hardening and recovery . . . 94
3.1.2 Interface velocity formulation . . . 95
3.1.3 Grain boundary migration . . . 96
3.1.4 Definition of initial microstructure . . . 97
3.1.5 Generation and evolution of substructures . . . 97
3.2 Validation of the implementations related to substructures . . . 101
3.2.1 Modeling of GG of a fully substructured microstructure . . 101
3.2.2 Modeling of CDRX and PDRX . . . 110
3.3 Conclusion . . . 116

4 Characterization and modeling of grain growth 119
4.1 Characterization of grain growth . . . 120
4.1.1 In the absence of SPP . . . 120
4.1.2 In the presence of SPP . . . 121
4.2 Modeling of grain growth . . . 125
4.2.1 Identification of reduced mobility . . . 125
4.2.2 Application to GG modeling in presence of SPP . . . 130
4.3 Conclusion . . . 135

5 Characterization and modeling of post-dynamic recrystallization 137
5.1 Characterization of PDRX . . . 138
5.1.1 Mechanisms of PDRX . . . 138
5.1.2 Influence of thermomechanical conditions . . . 143
5.1.3 Influence of initial microstructure . . . 146
5.2 Simulation of PDRX . . . 151
5.2.1 Principle of PDRX simulations . . . 151
5.2.2 Influence of thermomechanical conditions . . . 152
5.2.3 Influence of initial microstructure . . . 153
5.2.4 Effect of intragranular dislocation density heterogeneities . 161
5.2.5 Impact of SPP . . . 166
5.3 Conclusion . . . 173

6 Characterization and modeling of continuous dynamic recrystallization 175
6.1 Characterization of CDRX . . . 176
6.1.1 Mechanisms of CDRX . . . 176
6.1.2 Influence of initial microstructure . . . 183

6.1.3 Application to hot extrusion . . . 188
6.2 Parameters identification for modeling of CDRX . . . 191
6.2.1 Definition of parameters related to mechanical behavior . . 191
6.2.2 Hardening and recovery parameters identification . . . 191
6.2.3 Definition of Gourdet-Montheillet model parameters . . . 194
6.3 Modeling of CDRX and PDRX . . . 195
6.3.1 Influence of thermomechanical conditions . . . 195
6.3.2 Initial microstructure impact . . . 196
6.3.3 Application to hot extrusion . . . 204
6.4 Conclusion . . . 208

7 Conclusion and perspectives 211

A Materials and experimentals methods 217
A.1 Sampling plan . . . 217
A.2 Hot compression set-up . . . 218

B Numerical methods 219
B.1 Description of the algorithm underlying the numerical framework 219
B.2 Evolution of the GB network in the whole simulated RVE . . . 220

C Characterization and modeling of post-dynamic recrystallization 223
C.1 Identification of deformation twin boundaries . . . 223
C.2 Evolution of microstructures during PDRX simulations . . . 225
C.3 Evolution of microstructures during PDRX simulations considering intragranular GND density gradients . . . 227

D Characterization and modeling of continuous dynamic recrystallization 229
D.1 Identification of hardening parameters . . . 229
D.2 Additional scatter plots relative to recrystallization modeling during hot compression . . . 230

Chapter 1

Literature review

This chapter has two objectives. First, to review in details the present knowledge concerning recrystallization of zircaloy-4. Second, to give an overview of the main numerical tools one could use to simulate microstructure evolutions of zircaloy-4 or other alloys presenting similar behaviors. To do so, the main information about zircaloy-4 metallurgy and common industrial processes are described. Later, a detailed description of recrystallization mechanisms is given. Finally, a complete summary of the main numerical methods available to model dynamic and post-dynamic recrystallization mechanisms is proposed.

1.1 Properties and manufacturing of zircaloy-4

Zirconium was discovered in 1789 by Klaproth. Almost 150 years later, in 1925, Van Arkel and de Boer developed a process to produce ductile zirconium [32]. The process that is still used now was developed few years later, in 1945 by Kroll [33]. These successive developments enabled to produce ductile metallic zirconium parts. However, the great interest of zirconium for nuclear applications appeared to scientists and manufacturers only when it has been found that the zirconium parts that have been manufactured until that time were containing 2 to 3% of hafnium [34]. Indeed, if pure zirconium has a very low neutron capture cross-section, hafnium presents the opposite property. Therefore, some separation processes were developed to obtain pure metallic zirconium that was then used to produce the first zirconium alloys, the zircaloy-1 and zircaloy-2. They have been first used in the United States for nuclear applications.

Zircaloy-4, a derivative of zircaloy-2 that contains no nickel, is one of the main material used for all parts composing nuclear fuel assemblies (cladding and guide tubes, end plugs and grids) since 1970. It constitutes an alloy of choice due to its low neutron capture cross-section, its good mechanical strength and its corrosion resistance under boiling water or pressurized water reactor working conditions (respectively BWR or PWR).

1.1.1 Zircaloy-4 metallurgy

Crystallographic structure

Zircaloy-4 exhibits two crystallographic structures. One is hexagonal close packed (hP), stable at room temperature and atmospheric pressure and noted α-phase. A scheme is presented in figure 1.1 to present the main crystallographic directions and planes. The other is body-centered cubic (cI) and is stable at high temperature (noted β-phase).

The $\beta \rightarrow \alpha$ transformation of pure zirconium is diffusionless and leads to a martensitic structure presenting fine needles. However, the $\beta \rightarrow \alpha$ transformation of Zy-4 can be described as bainitic. Indeed, during the phase transformation, Fe and Cr atoms are able to diffuse at low range [35, 36]. They then form intermetallics of type $Zr\,(Fe_{1-x},\ Cr_x)_2$. This leads to a Widmanstätten microstructure, with laths that typically measure few microns in width. Those laths are delimited by second phase particles (SPP). Lath orientation stems from parent grain orientation according to variant selection rules. All laths originating from the same β-grain and having the same variant form colonies. Due to the variant selection rule, they have really close orientations (typically with a disorientation lower than few degrees).

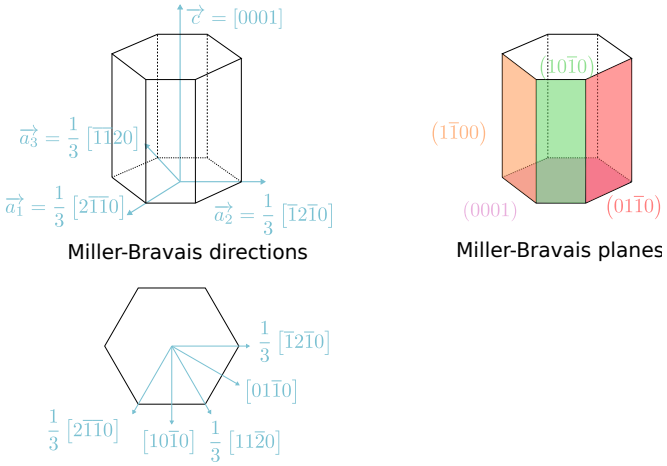


Figure 1.1: hP conventional unit cell showing the main directions and planes described with Miller-Bravais indices.

Composition

The alloying elements in Zy-4 lead to the presence of a domain where α and β phases are both stable. This domain is bounded by following limits: $810°C \leq T \leq 980°C$. Alloying elements are generally classified as α- or β-stabilizers. The first ones increase allotropic transformation temperature whereas the second decrease it. The role of the main alloying elements is described as follow:

- Sn: improve creep resistance.
- O: improve creep resistance and mechanical strength by changing solid solution composition.
- Fe and Cr: improve corrosion resistance by forming intermetallic compounds of composition $Zr\,(Fe_{1-x},\ Cr_x)_2$. These particles start to dissolve around $730°C$ [37].

Table 1.1 details the category of some additional alloying elements.

	Elements
α-stabilizers	Sn, O, Al, N, Hf, Ti
β-stabilizers	Fe, Cr, Ni, Nb, Cu, V

Table 1.1: Influence of the main alloying elements upon phase stability.

Fe and Cr form fine SPP populations. SPP can be considered as spherical. Their diameter ranges from tens of nanometers to 800 nanometers, depending on the thermomechanical route employed. To evaluate the impact of final annealing treatments over the evolution of the average SPP diameter, several models

have been developed [38, 39, 40]. Their volume fraction is equal to 0.0052 for temperatures below $810°C$ [37, 41].

The main info regarding stability domains of the phases are displayed in figure 1.2

Microstructure morphologies

The microstructure of Zy-4 is rather complex and can vary significantly depending on the previous thermomechanical processes employed. For the sake of clarity, microstructures are classified under two distinct categories: lamellar and equiaxed.

Lamellar microstructures Lamellar microstructures are obtained by quenching parts from β-domain. As discussed earlier, the transformation is partly diffusional. This is responsible for the formation of aligned SPP that delimit lamellae, as illustrated in figure 1.3. The lath morphology is directly influenced by the presence of alloying elements and by the thermomechanical conditions of the transformation [42, 43]. Indeed, it has been shown that impurities such as solute atoms (typically Si, P and N) or SPP stable in the lower β-domain can act as nucleation sites [42, 44, 45]. Consequently, the higher the number of nucleation sites, the more tangled lamellae are. On the other hand, if there are few nucleation sites, α-grains will start to grow from β-grain boundaries and form colonies of parallel plates. Regarding thermomechanical conditions, previous studies have shown that the proportion of tangled laths increases with cooling rate [43].

Typical quenched microstructures are depicted in figure 1.4. One should keep in mind that in practice, industrial parts are generally composed of zones with both organizations.

Equiaxed microstructures Those microstructures are typically observed after a heat treatment in the upper range of the α-domain, when recrystallization is complete. Precipitates are localized homogeneously throughout the microstruc-

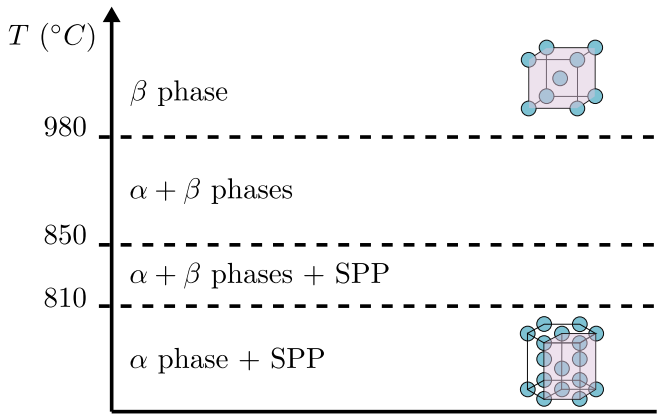


Figure 1.2: Phase diagram of zircaloy-4.

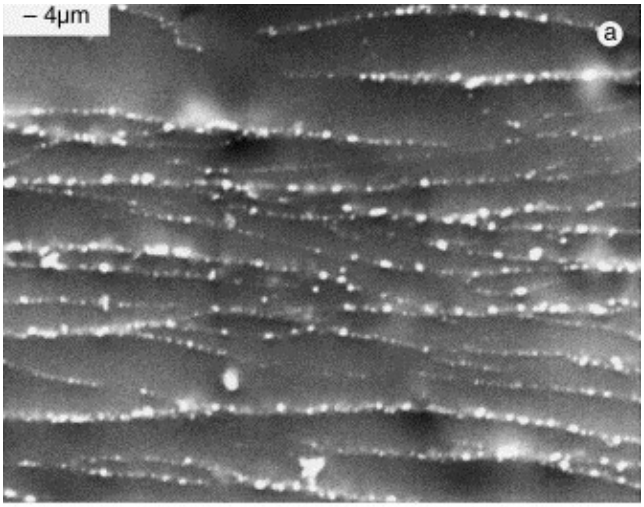
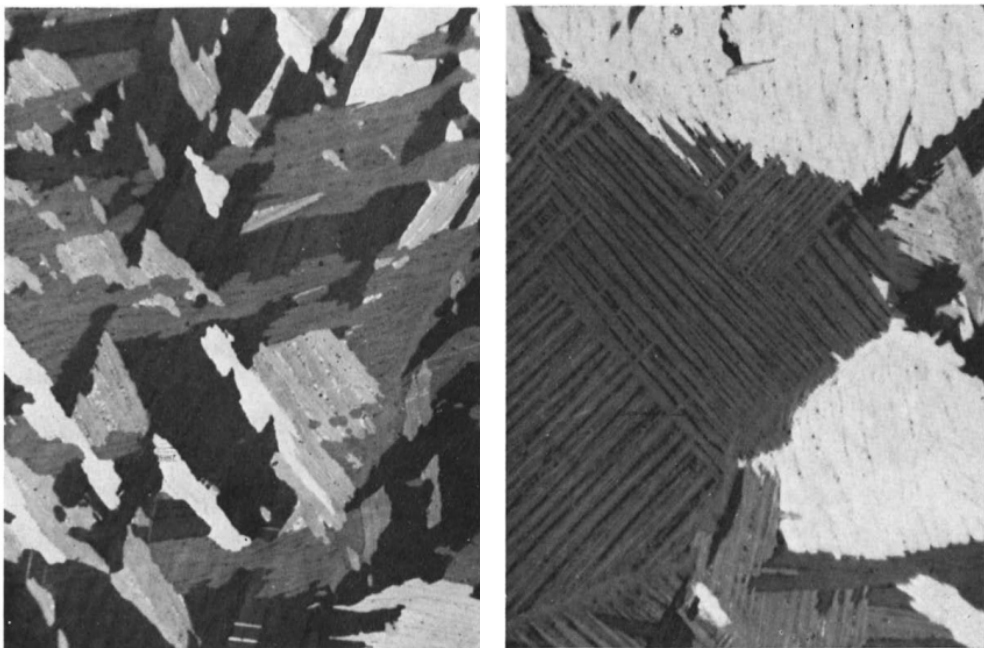


Figure 1.3: SEM observation of SPP after β-quenching Zircaloy-2 specimen, from [46].



(a) Basket-weave. (b) Parallel plate.

Figure 1.4: Typical microstructures after quench showing two typical Widmanstätten morphologies observed by optical microscopy at x250 magnification, from [42].

ture. Due to the presence of this population of fine precipitates, the average grain size is typically lower than 10 μm, as limited in their growth by the SPP pinning effect [47, 48]. An example of a typical equiaxed microstructure is provided in figure 1.5.

1.1.2 Hot deformation mechanisms

Two deformation mechanisms can take place in zirconium and titanium alloys: slip and twinning. The preferential activation of one or the other of these mechanisms is influenced by thermomechanical conditions and microstructure characteristics.

Slip systems

In metals adopting a hP crystal structure, five slip systems are commonly reported: basal <a>, prismatic <a>, pyramidal <a>, first order pyramidal <c+a> and second order pyramidal <c+a>. The slip systems are presented in figure 1.6 and summarized in table 1.2.

Name	Slip plane	Slip direction	Number of systems
Basal	$\{0001\}$	$<a> < 11\bar{2}0 >$	3
Prismatic	$\{10\bar{1}0\}$	$<a> < 11\bar{2}0 >$	3
Pyramidal	$\{10\bar{1}1\}$	$<a> < 11\bar{2}0 >$	6
1^{st} order pyramidal	$\{10\bar{1}1\}$	$<c+a> < 11\bar{2}3 >$	12
2^{nd} order pyramidal	$\{11\bar{2}2\}$	$<c+a> < 11\bar{2}3 >$	6

Table 1.2: Slip systems of hP metals.

Depending on the temperature, the chemical composition and the crystal orientation relative to the main stress directions, one or several slip systems can be activated. Slip can occur on a given system if the projection of the applied stress (called resolved shear stress, RSS) exceeds the critical resolved shear stress (CRSS) of this system. This is referred as Schmid's law [49]. For an ideal cylindrical crystal, the RSS (τ_r) is given by equation 1.1.

$$\tau_r = \frac{F}{A} \cos\phi \cos\lambda. \tag{1.1}$$

A designates the cross-section area of the cylinder and F the applied force. ϕ and λ are the angle between the force and the slip plane normal and the force and the slip direction, respectively. The CRSS magnitude is given by the dislocation interactions with themselves and other defects, such as vacancies, interstitials and impurities. Therefore, it depends on the solid solution and the strain hardening of the material [50].

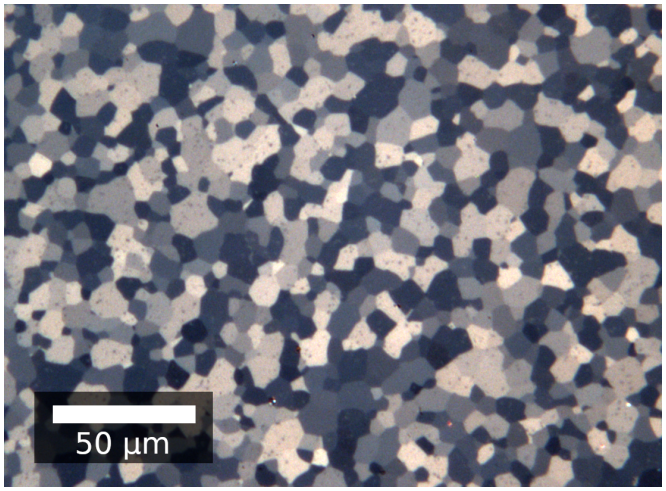


Figure 1.5: Typical equiaxed microstructure observed under optical microscope, with polarized light.

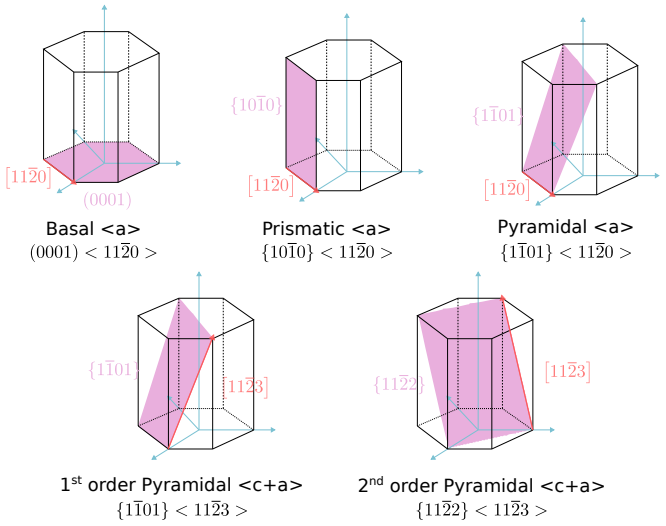


Figure 1.6: Slip planes and directions in hP metals.

In zirconium alloys, the main slip system is considered to be the prismatic one since it presents the lowest CRSS value [51]. Nevertheless, at temperatures exceeding 800 K, the CRSS ratio for basal/pyramidal versus prismatic systems is getting closer to one [52, 53]. Therefore, depending on the relative crystal orientation to the applied stress, several slip systems can be activated. In such conditions, the influence of crystal orientation is therefore of the first order. In the context of hot compression testings, the relative orientation of the <c> axis from the compression direction (CD) is especially important. Akhtar studied the deformation mechanisms by doing hot compression tests on α-Zr- monocrystals, with $CD \parallel < c >$. He confirmed that in such configuration, <a> slip systems are suppressed and that first order pyramidal slip is responsible for crystal plastic deformation. He noted that the CRSS of pyramidal slip was $10-20$ times higher than for prismatic slip [53]. This explains why grains having their <c> axis aligned with the applied stress are generally considered harder in zirconium and titanium alloys [54]. Some other evidences are reported by Ben Ammar [55] using numerical tools to model crystal deformation.

Twinning

During twinning, atoms are translated by shearing and the cell defined by $\overrightarrow{\eta_1}$, $\overrightarrow{\eta_2}$ and $\overrightarrow{S}$ is transformed into a cell defined by $\overrightarrow{\eta_1}$, $\overrightarrow{\eta_2}'$ and $\overrightarrow{S}$ of the same volume. This is described in figure 1.7. The most common twinning system for zirconium and titanium are described in table 1.3.

Solicitation	P_1 plane	η_1 direction	Rotation axis $\overrightarrow{S}$	Rotation angle (°)
Traction	$(10\bar{1}2)$	$< \bar{1}011 >$	$< 2\bar{1}\bar{1}0 >$	84.79
Traction	$(11\bar{2}1)$	$< \bar{1}\bar{1}26 >$	$< 10\bar{1}0 >$	34.85
Compression	$(11\bar{2}2)$	$< \bar{1}\bar{1}23 >$	$< 10\bar{1}0 >$	64.23

Table 1.3: Twinning systems of zirconium, from [56].

Deformations twins play an important role in ductility of hP materials at low temperatures [58]. With temperature, the occurrence of deformation twins

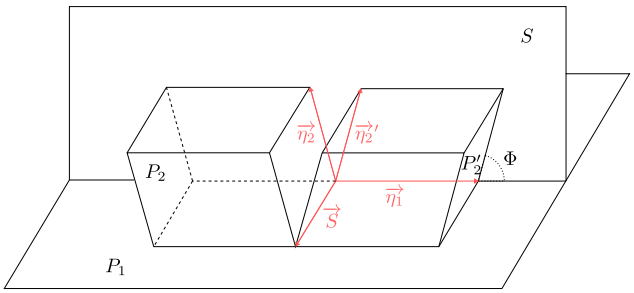


Figure 1.7: Schematic representation of twinning, from [57].

decreases notably. However, some deformation twins up to $750°C$ have been observed by [56] in some colonies of parallel plates with unfavorable orientations. Akhtar observed $\{11\bar{2}2\}$ and $\{10\bar{1}1\}$ twins for hot deformation in the $700-900\ K$ range and along <c> axis. The formation of twins in these two cases can be explained by the large grain size and the unfavorable crystal orientation.

1.1.3 Deformation at mesoscopic scale

In the two previous sections, the deformation mechanisms are supposed to occur in a single crystal submitted to a given macroscopic stress. However, in polycrystals, the situation is much more complex since every grain is surrounded by other grains that present a different crystallographic orientation and react differently to a given mechanical loading. Thus, each grain is actually submitted to a given local stress state and interacts with its neighbors.

Initially, two simplifying hypotheses have been proposed: the Taylor assumption, which supposes that all grains deform homogeneously [59] and the static assumption, which supposes that all grains experience the same stress state. In reality, upon a given applied stress, neighboring grains with different orientations will generate some deformation incompatibilities. To accommodate these incompatibilities, some geometrically necessary dislocations (GND) are generated. GND are line defects (see section 1.2.3) that accommodate the lattice rotation [60]. Since these incompatibilities are found at grain boundaries, GND start to form in grain boundary neighborhood.

Some specific features relative to lamellar microstructures affect their deformation. Basket-weaved microstructures present very complex topologies that could be compared to a 3D entanglement of lamellar grains. Since lamellae are thin, deformation incompatibilities could affect the whole volume. Quenched microstructures presenting parallel plates display different features. Since lamellae forming a colony are grouped and have almost the same orientation, one could suspect a colony to deform as a single grain. However, some results showed that prismatic slip takes place preferentially at lamellae interfaces [61, 56]. This is due to the lower tin concentration induced by the partial diffusion of alloying elements during the quench. This localization of deformation induces specific features [56, 55]:

- slip can happen at lamellae interfaces,
- shear bands crossing several lamellae are frequently observed,
- lamellae can kink and reorient progressively.

Consequently, not only the crystallographic orientation matters in lamellar microstructures, but also the lamellae topology and spatial orientation.

Some additional details about the deformation mechanisms of lamellar microstructures are provided in the PhD manuscripts of Vanderesse and Ben Ammar [56, 55].

1.1.4 Texture of Zy-4

The texture determines to a great extent the mechanical properties of zircaloy-4 parts, as all hexagonal metals [62]. For that reason, a large number of studies have described the texture evolutions during deformation processes and annealing [12, 13, 63]. The typical textures obtained after industrial processes vary significantly depending on many parameters:

- the stress state,
- the initial texture,
- the temperature,
- the chemical composition.

In the context of the present study, the investigations related texture changes are limited to their impact over deformation and recrystallization. Since the mechanical behavior of zircaloy-4 is conditioned to a great extent by the orientation of the <c>-axis relative to the applied stress, it is simply recalled that hot deformed microstructures generally see the basal poles being aligned with the compression direction [62]. This constitutes of course a strong simplification [64, 65].

1.1.5 Industrial forming of Zy-4 parts

The manufacturing processes of interest for this thesis are part of the forming route of cladding tubes. It starts by three vacuum arc remelting (VAR) steps. Then, the ingots are open-die forged in $\alpha + \beta$-domain and quenched. The subsequent steps are all executed within the α-domain. The forged bars are machined and hot extruded. Finally, they are successively cold pilgered and heat treated. All these steps are described in figure 1.8.

Hot extrusion is particularly suited to transpose the takeaways obtained by lab testing and to apply the simulation tools. Indeed, it is constituted by a hot deformation stage followed by a slow cooling stage in a confined environment. Moreover, the maximum temperature reached during is slightly lower than $700°C$, limiting the occurrence of other phenomena that are susceptible to happen at higher temperatures (phase transformation and dissolution of SPP). Therefore, some simulations of this process are presented in chapter 6 and some details about it are provided in the current section. A scheme of the process is provided in figure 1.9. It can be used to produce rods and tubes. For the production of tubes, a mandrel is placed inside the billet to ensure the final internal tube diameter is fulfilling the geometry specifications. The thermomechanical conditions experienced by a hot extrusion billet vary, across the radial and the extrusion directions. The front end of the tube, up to several hundreds of millimeters, experiences various thermomechanical conditions. Then, a rather steady-state is achieved and the thermomechanical conditions remain approximately constant along the remaining tube length.

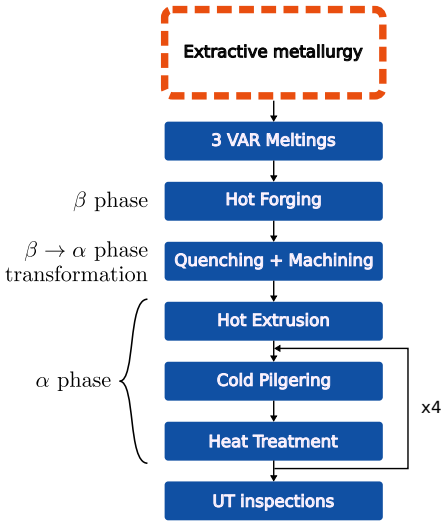


Figure 1.8: Manufacturing route for Zy-4 cladding tubes.

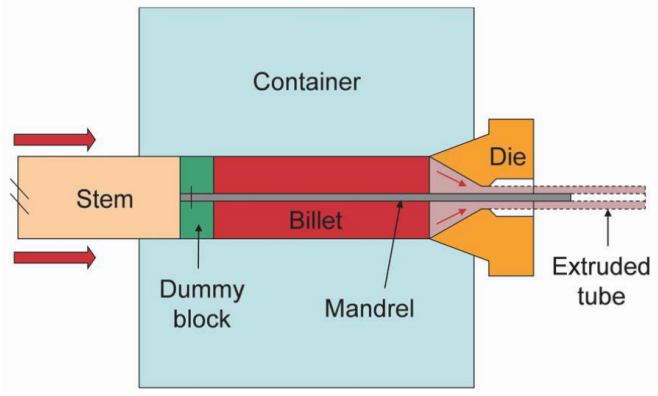


Figure 1.9: Schematic diagram of the extrusion process. From [66]

1.2 Recrystallization and related mechanisms

First of all, to be able to describe clearly recrystallization, a few basic concepts related to microstructure of metallic materials must be recalled. Most metals are polycrystalline materials, meaning that they are constituted by an aggregate of crystals, each of these crystals having a different crystallographic orientation [50]. The properties of any metallic material are conditioned to a great extent by the presence of microstructural defects. They can be of several types: point (vacancy, interstitial atom, ...), line (dislocation), surface (grain boundary) or volume defects (cavity, inclusion). Among these defects, a particular attention should be paid to dislocations. Indeed, along the dislocation line, the lattice is distorted and atoms are not surrounded by the regular number of neighbors. Therefore, an elastic energy and a stress field is associated to these distortions [67]. This energy can be released upon heat treatments, in particular by recrystallization [18].

Recrystallization is defined as the formation of new grains, having a very low defect density, and their growth at the expense of the deformed microstructure. It is motivated by the reduction of stored energy accumulated during plastic deformation through the increase of dislocation density. It is a complex phenomenon "where a variety of possible phenomena and their interactions have to be taken into consideration" [68]. Indeed, deformation and recovery play a huge role since they condition both the formation of new recrystallized grains and the driving pressures for the migration of the recrystallization front. As highlighted earlier, plastic deformation is responsible for the dislocation density increase. At the same time, dislocation organization leads to the formation of substructures which can turn into new recrystallized grains. Dislocations can also annihilate themselves which leads to a decrease of driving pressures for recrystallization. Therefore, recovery, which gathers those two mechanisms, can be both considered as favorable and detrimental to recrystallization, depending on its magnitude [18].

1.2.1 General terminology of recrystallization and grain growth

Recrystallization mechanisms are often classified under five main categories:

- Static recrystallization (SRX). Static recrystallization happens during annealing after cold or hot working. During static recrystallization, new crystallites with low dislocation content appear and grow to progressively replace the deformed matrix. Mesoscopic observations generally report discontinuous appearance of ReX grains, both in space and time. However, some continuous ones have also been reported, for instance in aluminum alloys where SPP play an important role in recrystallization [69].

- Discontinuous dynamic recrystallization (DDRX). DDRX occurs when a material is deformed at hot temperature and designates the microstruc-

tural transformation acting thanks to nucleation and growth of recrystallized grains. Under increasing deformation, recrystallized grains can progressively see their dislocation content increase. If their dislocation density reaches a critical value, some new recrystallized grains could form leading to a new recrystallization cycle [18].

- Continuous dynamic recrystallization (CDRX) characterizes recrystallization phenomena acting homogeneously through the whole microstructure with progressive changes, during hot deformation. In this case, one cannot distinguish nucleation and growth of recrystallized grains. CDRX does not imply large recrystallization front movement, by opposition to DDRX.

- Geometric dynamic recrystallization (GDRX) is employed to describe the formation of "small equiaxed grains of a size comparable with the subgrain size" due to pinching of serrated boundaries observed at high level of strains [18].

- Metadynamic recrystallization (MDRX) designates the growth, during heat treatment, of recrystallized grains that have been formed during an anterior hot deformation stage.

The term post-dynamic recrystallization (PDRX) is also used to a large extent in literature. It designates all recrystallization mechanisms that take place after hot deformation and includes mechanisms that could be either classified under SRX or MDRX.

Finally, if a fully recrystallized material is held at hot temperature, GB could migrate and induce an increase of the average grain size. In that case, the motion of GB is driven only by capillarity effects. This phenomenon is referred to as grain growth (GG).

Based on the definitions resumed in previous paragraphs, it appears that recrystallization could be decomposed into formation of new recrystallized grains and recrystallization front migration. Depending on material parameters, thermomechanical conditions and observation conditions, these two phenomena could display highly different features that justify the classification described above.

1.2.2 Grain boundary description

To understand recrystallization front movement, it is crucial to describe what is a grain boundary (GB) and how it migrates.

Grain boundary characteristics

GB are interfaces between zones of different crystallographic orientations, i.e. grains. They are surface defects that typically measure few angströms in thickness [70]. Figure 1.10 presents a GB observed by high resolution transmission electron microscopy (HRTEM).

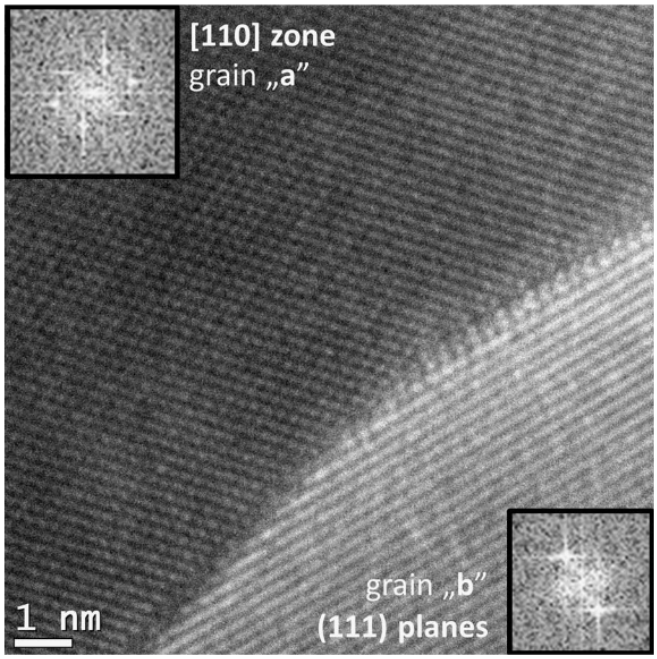


Figure 1.10: HRTEM image of a GB observed in an Al thin film. Reprinted from [70].

A given GB (Γ_{AB}) is characterized by its topology and by the misorientation relationship linking the two neighboring grains (G_A, G_B). At the mesoscopic scale, these features are generally defined by five macroscopic degrees of freedom (DOF). Three describe the misorientation between the two grains. The other two DOF define the GB unitary normal ($\overrightarrow{n}$) and are generally depicted as GB inclination. Misorientation can be described by several mathematical tools. The most common are the misorientation tensor (M_{AB}) and the couple rotation angle and rotation axis $\left(\theta_m,\ \overrightarrow{R}_m\right)$. Due to the symmetries of a crystal lattice, multiple M_{AB} tensors can be applied to go from G_A to G_B orientation. This is addressed by considering the rotation tensor that corresponds to the lower rotation angle. In that case, this angle is named disorientation (θ). These different notations are recalled on a scheme presented in figure 1.11. The five DOF condition GB properties, such as mobility (M) and energy (γ). These two properties impact greatly GB behavior in the context of recrystallization and grain growth.

The dependence of GB properties to (M_{AB}, $\overrightarrow{n}$) is a complex question that remains highly debated from both experimental and numerical point of views [71, 72]. Recently, several attempts to relate the product of GB energy and mobility (i.e. reduced mobility) to the five GB DOF have been reported. They have given rise to additional interrogations and question the impact of GB curvature over its kinetics or the five-parameter description of reduced mobility [71, 72, 73]. For decades now, these questions have generally been simplified by considering only the influence of misorientation or even of disorientation over GB properties. Following that idea of reducing complexity, GB are classically sorted into two

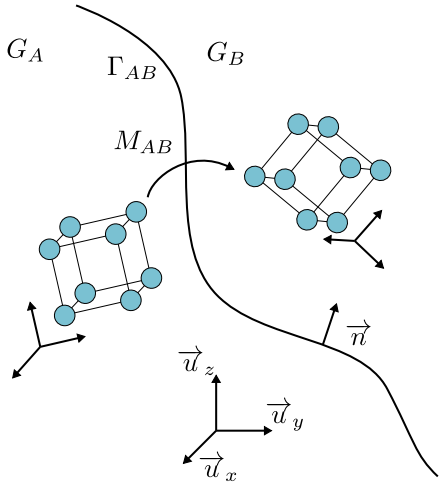


Figure 1.11: Scheme presenting a GB and its parameters.

categories based on a threshold condition upon disorientation (θ_{max}): low angle GB (LAGB) and high angle GB (HAGB). This classification has arisen from the observation that a clear distinction between LAGB and HAGB properties was observable [74] (see figure 1.12). Based on the evolution of γ activation enthalpy for GB motion, θ_{max} is generally considered equal to 15° [74].

If no exact analytical equation has been proposed to compute γ and M as functions of the five DOF (M_{AB}, $\overrightarrow{n}$), some attempts to predict their evolution with disorientation angle show satisfactory results at mesoscopic scale. Regarding GB energy, the most widely used is the Read-Schockley model [76]:

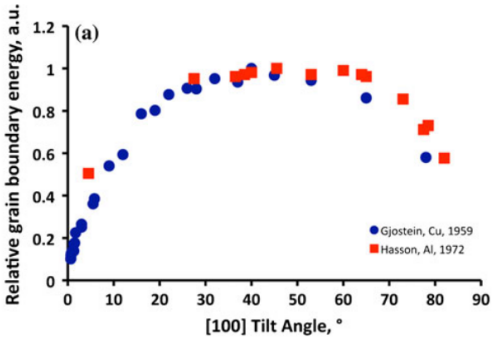
$$\gamma(\theta) = \begin{cases} \gamma_{max} \left(\dfrac{\theta}{\theta_{max}} \right) \left(1 - \ln \dfrac{\theta}{\theta_{max}} \right), \ \theta < \theta_{max}, \\ \gamma_{max}, \ \theta \geq \theta_{max}. \end{cases} \tag{1.2}$$

GB mobility is generally described as a sigmoidal function [77]:

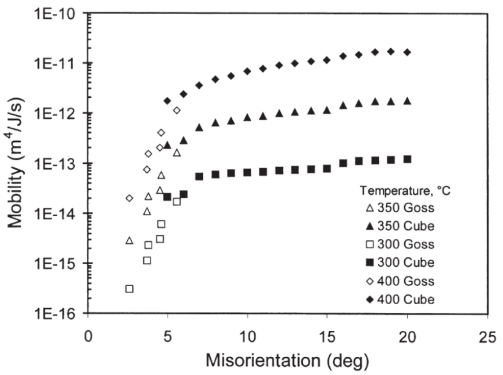
$$M(\theta) = \begin{cases} M_{max} \left(1 - \exp \left[-5 \left(\dfrac{\theta}{\theta_{max}} \right)^4 \right] \right), \\ M_{max}, \ \theta \geq \theta_{max}. \end{cases} \tag{1.3}$$

In previous equations, γ_{max} and M_{max} designates the HAGB energy and mobility, respectively. The following functions are plotted in figure 1.13.

More complex approaches, generally relying upon molecular dynamics simulations [78], propose refined formulations for GB energy and mobility. However, they will not be used in the context of this thesis for several reasons. First, the material of interest is not characterized by a significant presence of special GB. Second, the recrystallization mechanisms of interest are characterized by the presence of a high number of LAGB and their properties are generally well predicted

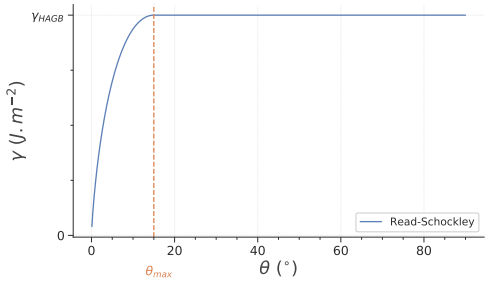


(a) $Al - 0.05\%Si$ GB energy at different temperatures. Combined results of subgrain growth in Goss and Cube orientations. From [18].

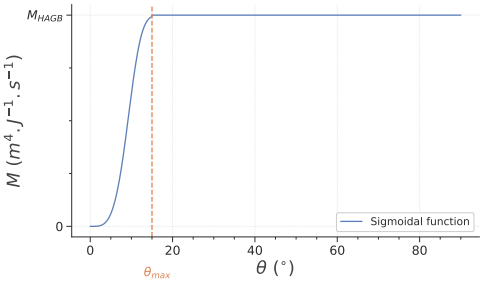


(b) Al and Cu normalized mobility of symmetric [100] tilt GB in Al. From [75].

Figure 1.12: Experimental data describing evolution of GB properties with disorientation.



(a) GB energy, computed using Read-Schockley equation.



(b) GB mobility, computed using sigmoidal function.

Figure 1.13: Evolution of GB properties with disorientation.

by equations 1.2 and 1.3. Third, there are very few data related to zirconium alloys.

Grain boundary motion

In the absence of solid state diffusion phenomena, such as phase transformation, driving pressures for GB migration are caused by:

- differences of stored energy due to plastic deformation (P_e).
- Capillarity effects (P_c). GB being defects, they contribute to increase the total energy of the system. Thus, the material has a tendency to reduce the total GB length to lower its energy.

When studying recrystallization at mesoscopic scale, GB velocity is generally described according to equations 1.4 and 1.5 [18, 23].

$$\overrightarrow{v} = \overrightarrow{v}_e + \overrightarrow{v}_c = M(P_e + P_c)\overrightarrow{n}, \tag{1.4}$$

$$\overrightarrow{v} = M(\tau[\![\rho]\!] - \gamma\kappa)\overrightarrow{n}. \tag{1.5}$$

In this equation, $\overrightarrow{v}$ is the grain boundary velocity and $\overrightarrow{n}$ the outward unit normal to the grain boundary. τ is the dislocation line energy, $[\![\rho]\!]$ the gap in dislocation density across the boundary and κ denotes the trace of the curvature tensor (curvature in 2D and sum of the main curvatures in 3D) of the grain boundary. τ is computed thanks to following equation: $\tau = \mu b^2/2$ with μ the shear modulus and b the Burgers vector [50]. In the first instant of recrystallization, GB migration is primarily motivated by local differences in stored energy of deformation. Then, once recrystallization has contributed to decrease sufficiently stored energy of deformation, both driving pressures start to be comparable and capillarity impacts significantly microstructure evolutions. When all the stored energy has been consumed, GB migration is only motivated by the reduction of interfacial energy (i.e. capillarity effects). This is the GG stage described earlier.

Equation 1.5 is often used for discussing the influence of the two main driving pressures for GB migration. However, it should be pointed out that other microstructural features affect the motion of these interfaces. For instance, the presence of alloying elements in solid solution can impact greatly the mobility. This effect is referred to as solute drag [79]. One other example lies in the impact of SPP. It has been observed that SPP could pin GB temporarily or even definitely through the well known Smith-Zener pinning pressure [47, 48]. In this formalism, the local pinning induced by SPP located close to a GB by the configuration presented in figure 1.14 can be described thanks to equation 1.6. This equation is obtained by multiplying the surface of the particle represented by the ellipse drawn in figure 1.14 ($2\pi r_{\text{SPP}}\gamma\cos\theta$) by the horizontal component of the surface tension ($\gamma\sin(\lambda+\alpha)$).

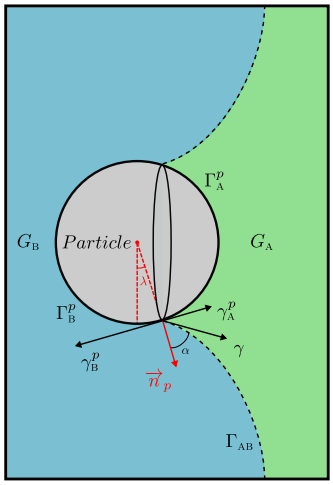


Figure 1.14: Scheme presenting interaction between a GB and a SPP.

$$F_Z = 2\pi r_{SPP}\gamma \cos\theta \sin(\lambda + \alpha). \tag{1.6}$$

When particles are incoherent, $\gamma_A^p \approx \gamma_B^p$ which implies that $\alpha \approx 0°$. Thus, equation 1.6 becomes simpler and the maximum dragging force can be directly computed:

$$F_Z^{max} = \pi r_{SPP}\gamma. \tag{1.7}$$

By multiplying the maximum pinning force per the number of SPP per unit surface of GB (i.e. the number of SPP effectively having an effect over GB), one can compute the average dragging pressure of SPP over GB. The volume number of SPP can be computed thanks to following equation:

$$n_{SPP} = \frac{3f_{SPP}}{4\pi\overline{r}_{SPP}^3}, \tag{1.8}$$

where $\overline{r}_{SPP}$ designates the average SPP radius and f_{SPP} the SPP volume fraction.

Then, since all the particles within a distance $\pm\overline{r}_{SPP}$ are in contact with the GB, the number of SPP per unit surface of GB is given by:

$$n_{SPP}^{GB} = n_{SPP} \times 2\overline{r}_{SPP} = \frac{3f_{SPP}}{2\pi\overline{r}_{SPP}^2}. \tag{1.9}$$

Finally, from equations 1.7 and 1.9, one can compute the average dragging pressure of SPP over GB:

$$P_{\text{Z}} = \frac{3 f_{\text{SPP}} \gamma}{2 \overline{r}_{\text{SPP}}}. \tag{1.10}$$

Introducing the pinning pressure term from equation 1.10 into equation 1.5, one can estimate the limit grain size obtained after long heat treatments when capillarity and pinning pressures are balanced [80]. The limit grain radius is given in equation 1.11.

$$\overline{R}_{lim} = K \frac{\overline{r}_{\text{SPP}}}{f_{\text{SPP}}}^{m} \tag{1.11}$$

In previous equation, K and m are constant that depend on the hypotheses made [80].

It should be mentioned that all the previous equations rely upon several hypotheses:

- particles are spherical and their position is random,
- they all exert the maximum dragging force,
- $r_{\text{SPP}} \ll R$,
- the GB thickness is negligible in comparison to SPP size. This supposes that SPP diameter exceeds at least tens of nanometers.

1.2.3 Description of the microstructural mechanisms of recrystallized grain formation

The formation of a new recrystallized grain consists in the organization of a given volume, at least partly bounded by HAGB, with a very low defect content (i.e. low dislocation density). In literature, many authors refer to this mechanism as nucleation [81, 82, 83] since it often takes place discontinuously in time and space throughout the microstructure, similarly to other typical mechanisms that involve a nucleation stage. Phase transformation is an example of choice of a common metallurgical phenomenon that implies nucleation and growth. However, in the case of recrystallization, the use of the term "nucleation" is abusive in regards of thermodynamic considerations. It has been proven that new grains cannot form by thermal fluctuations [68, 84]. Recrystallized grains can only develop from pre-existing zones that offer the required conditions. Therefore, their orientation is derived from the one held locally [85, 84]. If these particular zones are located close to specific microstructural features, the development of new recrystallized grains is heterogeneous. Additionally, if it is fast and can be dissociated from GB migration, it gathers both spatial and temporal discontinuity features. It is therefore described as discontinuous.

In following sections, the traditional discontinuous/continuous distinction has been adopted with the aim of clarifying the reasons of such different observed features. However, the readers should keep in mind that this classification is arbitrary and depends on the spatial and temporal scale considered. Indeed, it should be pointed out that the underlying physical phenomena are similar.

General description of underlying mechanisms

Submitted to strain, the microstructure evolves by different mechanisms. To accumulate plastic deformation, grains see their orientation change. Some defects, mainly line defects such as dislocations are created. If the material is subsequently annealed or if the deformation process is realized at hot temperature, dislocations can move, annihilate and rearrange themselves. If these mechanisms are sufficiently active, they can counterbalance the influence of strain hardening by reducing the number of free dislocations. The dislocation structures formed by these mechanisms are generally classified by growing organization degree:

- dislocation pile-ups,
- dislocation entanglements,
- cell walls, which can be defined as accumulation of dislocation tangles in thin strips forming a network and delimiting cells which exhibit a lower internal dislocation density,
- subgrain boundaries, also called LAGB, that differ from cell walls by the higher organization degree of dislocations,
- HAGB.

Both thermomechanical conditions and material properties impact how these structures evolve by influencing local dislocation density and/or dislocation mobility. Main process parameters affecting it are temperature and strain rate. To account for these two parameters simultaneously, one can use the Zener-Hollomon parameter [86], defined by:

$$Z = \dot{\varepsilon} exp\left(\frac{Q}{RT}\right), \tag{1.12}$$

with $\dot{\varepsilon}$ the strain rate, Q the apparent activation energy for hot deformation, R the gas constant and T the temperature.

In general, low Z values seem to promote recovery mechanisms whereas high Z values tend to favor strain hardening ones [87]. Major microstructural features that influence dislocations organization are the presence of defects such as precipitates or grain boundaries, the stacking fault energy (γ_{SFE}) and the availability of gliding systems. The presence of defects and the activation degree of gliding systems condition the ability for dislocations to move. The stacking fault

energy influences how dislocations organize themselves. It determines the likeliness of dissociation of a dislocation into partial ones. In materials presenting a low γ_{SFE} value, dissociations are frequent and hinder climb and cross-slip of dislocations which are responsible for recovery [18]. It should be noted that many other factors could influence development of dislocation structures, such as the type of mechanical solicitation and its principal direction in comparison to the orientation of the crystallographic structure.

Under adequate conditions, evolution of subgrain structure can result in the formation of recrystallized grains. This is achieved by the development of subgrains that fulfill both kinematic and energetic criteria. To get a better understanding of it, one can analyze the equation 1.5, described earlier. By doing so, one could assess the ability of a given subgrain to fulfill the energetic criterion [88]. The subgrain would require to have a size advantage or to present a lower stored energy to grow at the expense of its neighbors. Then, as GB velocity increases with mobility, the fulfillment of the kinematic criterion requires that the subgrain boundary has a sufficient mobility. Therefore, this criterion is generally considered as satisfied when a significant fraction of the LAGB surrounding the nucleus have been transformed to HAGB. The transformation of LAGB to HAGB can be produced by several means:

- subgrains can progressively rotate, generally to accommodate deformation. This can bring neighboring subgrains to share the same orientation and to coalesce [89]. Subgrain rotation and coalescence is kept as a viable mechanism for subgrains measuring tens of nanometers. Indeed, the energy required for rotation of larger crystals is too large to allow this phenomenon [84].
- LAGB could migrate in a zone presenting orientation gradient.
- Free dislocations generated by the deformation could stack into pre-existing LAGB.

Continuous mechanisms

The mechanisms described previously in section 1.2.3 can take place during hot deformation. If GB migration is sufficiently slow in comparison to formation of subgrains and their subsequent transformation into recrystallized grains, then DRX could be classified as CDRX. A typical microstructure would then be characterized by a high number of subgrains and small recrystallized grains distributed rather homogeneously throughout the whole microstructure. Such observations have been frequently reported for aluminum or titanium alloys [90, 91]. More widely, the ability to recrystallize by continuous mechanism is generally attributed to materials with a high stacking fault energy (γ_{SFE}) [18]. Indeed, the stacking fault energy conditions the dissociation, the climb and the cross slip of dislocations. In metals of high stacking fault energy, the two last phenomena are easier and lead to significant recovery.

Detailed studies about the physical mechanisms at a lower scale are still missing and the understanding of LAGB formation is still incomplete. This is of first importance in continuous mechanisms since LAGB formation is observed and plays a major role in global microstructure evolutions. Recently, an in-depth analysis of local misorientations enabled Qiang *et al.* to propose a detailed recrystallized grain formation process in a Ti alloy [92]. The corresponding mechanism sequence is composed by:

- grain boundary bulging, driven by the difference in stored energy across the corresponding interface.
- Formation of symmetrical-tilt boundaries.
- Evolution of these boundaries leading to subgrain formation.
- Separation of these subgrains to their parent grains by GB sliding.

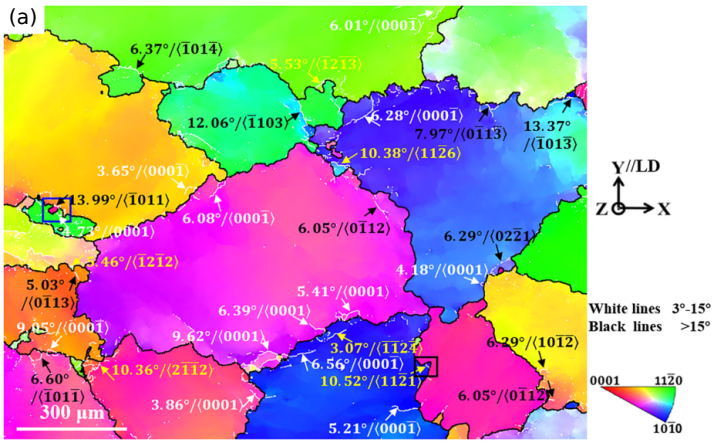
The whole sequence is illustrated in the following figure 1.15. It should be pointed out that the last step resulting in spatial separation of the newly formed grains has not been characterized directly. Therefore, the proposed explanation relying on GB sliding remains an hypothesis and further examinations would be needed to confirm it.

Discontinuous mechanisms

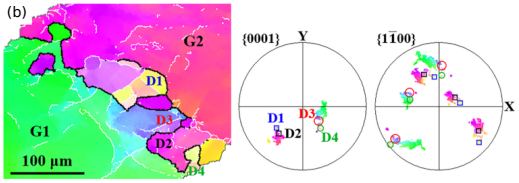
Discontinuous mechanisms rely on the same underlying physical phenomena. However, due to some specific material features or to the observation scale, they are quasi-instantaneous and localized at preferential sites within microstructure. These sites can be very different by nature but share common features: they are local zones of high deformation and present therefore high orientation and dislocation density heterogeneities. In literature, the formation of new recrystallized grains at those particular locations are presented as different mechanisms. They are named strain induced grain boundary migration (SIBM), particle stimulated nucleation (PSN) and nucleation at deformation bands.

Strain induced grain boundary migration (SIBM) At low strain levels, the main discontinuous mechanism that is considered to be responsible for the formation of nuclei is the strain induced grain boundary migration (SIBM) [93]. It consists in the bulging of a zone partially bounded by HAGB. This bulging is driven by a difference in stored energy on both sides of the HAGB [88, 94]. It is observed frequently at low strain [95] since zones located close to GB accumulate dislocations earlier to accommodate deformation incompatibilities. Due to this dislocation concentration, these zones frequently present subgrains. Figure 1.16 presents how a given subgrain partially bounded by a HAGB can bulge to the detriment of the neighboring subgrains.

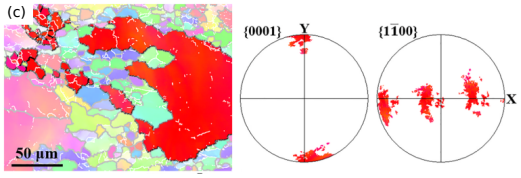
In materials containing SPP, SIBM is susceptible to adopt different morphologies. Multiple neighboring subgrains bulging at the same time to form a single



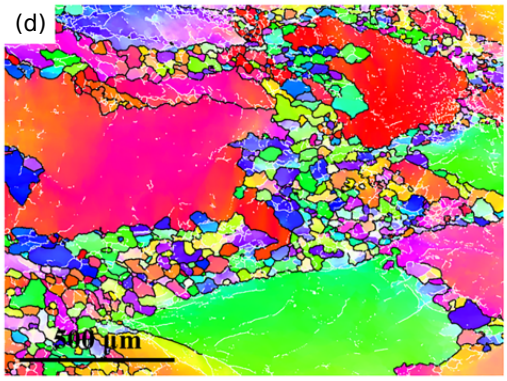
(a) Formation of subgrains at pre-existing GB. Map corresponding to a specimen deformed to a true strain of 0.07.



(b) Beginning of grain detachment.



(c) Intermediate phase of grain detachment.



(d) Microstructure presenting large zones of small grains formed by grain fragmentation. Map corresponding to a specimen deformed to a true strain of 0.29.

Figure 1.15: EBSD orientation maps with IPF Y color code and corresponding 0001 and $10\bar{1}0$ pole figures of the grains in two necklace regions. The alloy studied is: $Ti - 44.81Al - 3.96Nb - 0.98Mo - 0.15B$. From [92].

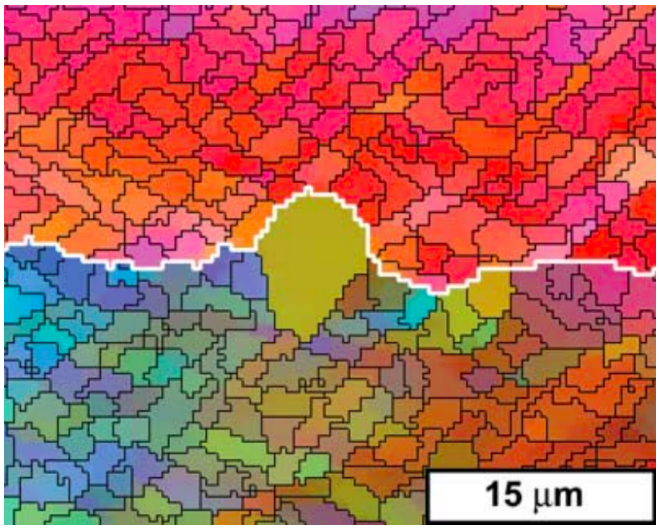
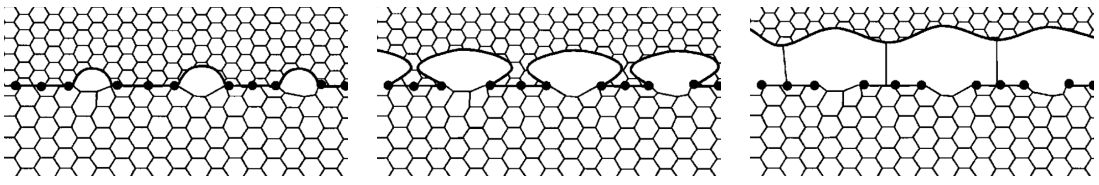


Figure 1.16: EBSD map pointing out SIBM of a single subgrain in a aluminum sample rolled out to a true strain of 0.7. From [95].

broad bulge have been observed. To explain that feature, it has been proposed that several subgrains could bulge simultaneously, spread laterally due to SPP pinning and finally coalesce to form a single front [96, 97]. This phenomenon in represented by a draw in figure 1.17.

Particle Stimulated Nucleation (PSN) Particle stimulated nucleation (PSN), described for the first time by Humphreys [98], designates the formation of recrystallized grains at the vicinity of large hard SPP (typically larger than 0.1 μm). It has been frequently observed in aluminum alloys and steels [99, 100, 101]. At SPP vicinity, zones of high orientation gradients are formed because of the strain incompatibility between the matrix and the SPP. Formation and migration of LAGB is favored due to the presence of important dislocation density heterogeneites. Finally, it leads to the formation of recrystallized grains clustered around SPP [18, 102] as shown in figure 1.18.



(a) Initiation of SIBM at regions with little precipitation.

(b) Spread of the bulging subgrains within the higher stored energy area.

(c) Large recrystallized front spreading over multiple subgrains.

Figure 1.17: Schematic diagrams illustrating the mechanism of broad front SIBM in presence of SPP (from [96]).

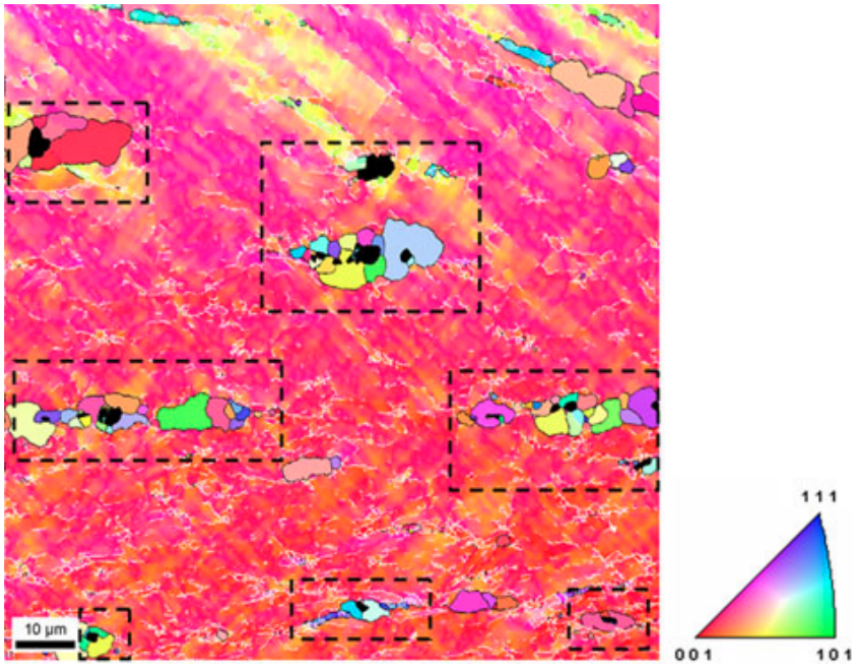


Figure 1.18: EBSD IPF map showing PSN in multiple areas bounded by dashed squares, in a coarse grained ferritic stainless steel. From [100].

Nucleation at deformation bands Deformation bands are regions that delimit two areas of a same grain that rotate to different orientations under strain. They are of finite size and adopt a slab-like structure of several volumes with alternating orientations [103]. Some other band-like structures, named kink bands and transition bands, are frequently observed in deformed materials. Kink bands are characterized by a 45° angle to the compression axis. Transition bands typically present progressive orientation gradients.

The different deformation structures presented constitute preferential nucleation zones. Because of the presence of deformation and dislocation density gradients, LAGB and subgrains formed in those areas have the adequate conditions for growing. LAGB migration is highly susceptible to induce HAGB formation due to the presence of orientation gradients. Finally, they form viable nuclei for recrystallized grains. This has been exhibited by Dillamore *et al.* [104]. They proposed some criteria upon local curvature and topological sub-boundary network for the transformation of subgrains to viable recrystallized grain nuclei [104].

1.2.4 Application to recrystallization of Zy-4

Few studies have been conducted regarding Zy-4 recrystallization behavior. The first one, conducted by Chauvy *et al.*, was considering Zy-4 samples with an initial lamellar microstructure [15]. Samples were containing zones with both basket-weaved structures and parallel plates. They were subjected to hot compression tests at temperatures between 500°C and 750°C. The EBSD characterizations

done after hot compression bring interesting information about evolution of the GB network during hot deformation. Evolution of HAGB and LAGB (GB with a disorientation lower than 15°) specific length are plotted in figure 1.19. These plots illustrate how LAGB start to form quickly as strain increases to reach a steady-state. Interestingly, HAGB evolution with strain shows two stages. Until a strain of 0.3, the increase is rather limited and slows down as deformation proceed. Then, it increases rather quickly. The authors attribute the first increase to the GB serration and the second to the transformation of LAGB to HAGB. These observations are consistent with previous observations of CDRX mechanisms.

These observations have been completed by subsequent studies focused on hot deformation of Zy-4 [56, 16, 55]. Each of these studies describe results with different initial microstructures and deformation routes:

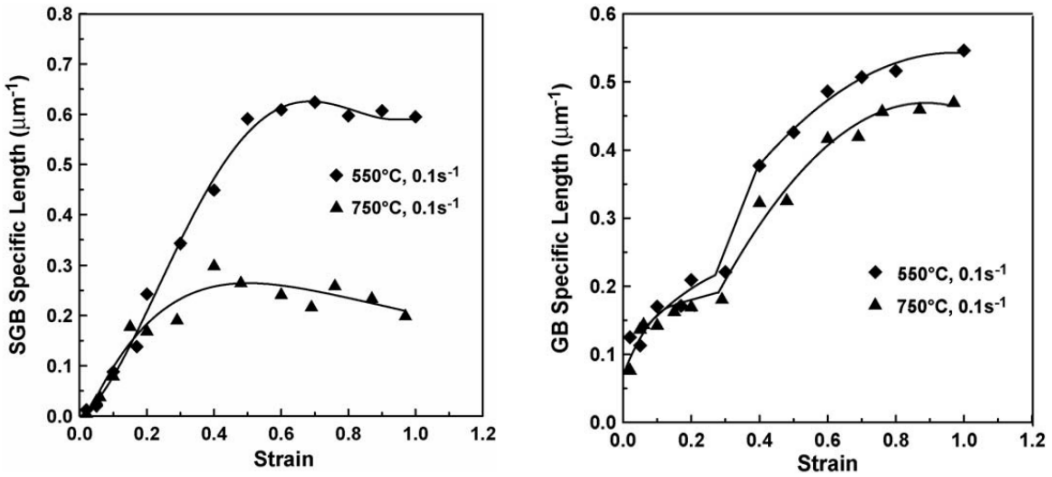
- uniaxial and channel-die hot compression on lamellar microstructures [56],
- uniaxal hot compression and hot extrusion on both lamellar and equiaxed microstructures [16],
- multiaxial hot compression on lamellar microstructures [55].

The characterization results from all the previous studies lead to the same conclusion. Hot deformed Zy-4 lamellar microstructures show zones with fine grains and large colonies that are slightly deformed. The fine grains seem to result from fragmentation of the large lamellae colonies. Then, under subsequent heat treatment, a number of recrystallized grains grow and consume the deformed microstructure.

Vanderesse discussed in details the structures that are formed from deformation of lamellar microstructures [56]. He noticed that kink bands, shear bands, and other typical deformation structures were present. They are potentially within a single colony or could spread across several. His observations allowed him to conclude that the recrystallization heterogeneities were caused by deformation heterogeneities [56]. The figure 1.20 illustrates these observations by showing preferential zones were small recrystallized grain form.

Ben Ammar characterized by EBSD microstructures after multiaxial hot compression tests ($T = 750°C$, $\varepsilon_{cumul} = 3 \times 0.4$) and deduced from these observations that for strain rate lower than 1.0 s^{-1}, the recrystallized fraction obtained by DRX remains lower than 10% [55]. He observed significantly higher recrystallized fraction (typically around 80%) at higher strain rates ($\dot{\varepsilon} = 2.0 - 3.0\ s^{-1}$). Since increasing strain rate causes the PDRX kinetics to increase significantly, it appears reasonable to conclude that this increase in recrystallized fraction is caused by the fast PDRX taking place within the short time interval before quench [55, 105]. Finally, Ben Ammar noticed that recrystallized fraction was increasing notably when microstructures were held at hot temperature after deformation.

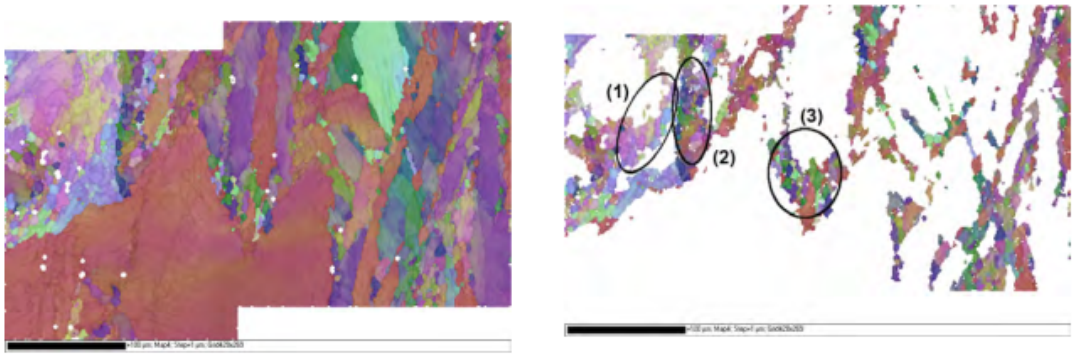
Gaudout observed that for similar thermomechanical conditions, measured recrystallized fraction were higher for initially equiaxed microstructures compared to quenched microstructures [16]. He attributed those differences in kinetics to



(a) LAGB specific length.

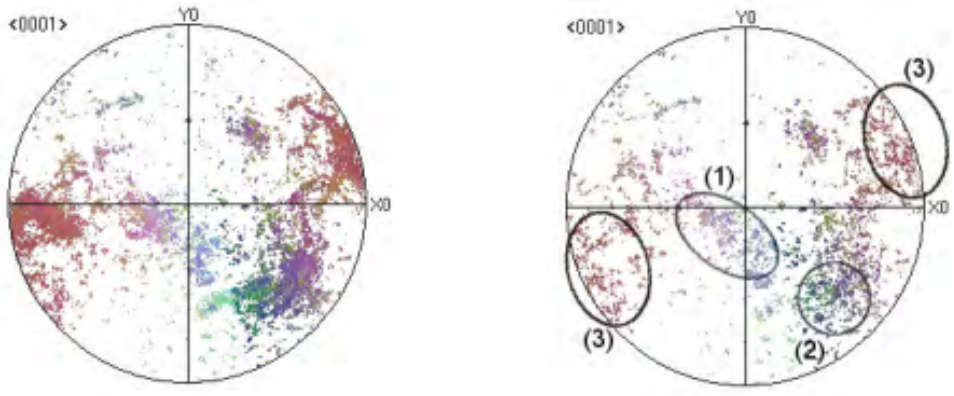
(b) HAGB specific length.

Figure 1.19: Evolution of GB network with strain. From [15].



(a) EBSD orientation map.

(b) EBSD orientation map showing only small grains.



(c) $< 0001 >$ pole figure corresponding to map 1.20a.

(d) $< 0001 >$ pole figure corresponding to map 1.20b.

Figure 1.20: EBSD orientation maps and corresponding $< 0001 >$ pole figures. From [56].

the higher number of recrystallized grains generated by CDRX for equiaxed microstructure. He proposed several hypotheses that could explain these differences [16]:

- the highest solute concentration in quenched microstructures,
- the differences of textures which leads to a different deformation distribution.

Additional studies have been conducted on other zirconium alloys, focusing particularly on texture evolutions during deformation and recrystallization. For instance, the importance of SIBM in formation of new recrystallized grains has been confirmed by Jedrychowski et al. [106]. They have illustrated that a Zr alloy (Zr702), after low level of cold deformation, can experience formation of recrystallized grains by SIBM during a following heat treatment. To do so, they rely upon the analysis of EBSD data [107] and upon the prediction of the right texture evolutions by Monte-Carlo modeling [106].

1.3 Numerical models of recrystallization

Numerical methods to model GG and ReX at mesoscopic scale are often classified under 3 categories, by growing degree of precision, complexity and computational cost:

- analytical models generally propose semi-empirical laws to predict mainly the evolution of the recrystallized fraction or the mean grain size during hot deformation or a consecutive heat treatment. The most famous one is certainly the Johnson-Mehl-Avrami-Kolmogorov (JMAK) model, originally developed for forecasting kinetics of phase change [108, 109, 110, 111, 112] and which has been used extensively by the past to predict the evolution of the recrystallized fraction with time during SRX. Another model that has been used at multiple occasions is the one proposed by Burke and Turnbull to predict the mean grain size evolution during GG [113].

- Mean-field model, which describe the microstructure thanks to a simplified representation that employs average values or distributions of the main microstructure characteristics such as dislocation density and grain radius. These models do not consider the precise microstructure topology. Hillert and Abbruzzese [114, 115, 116, 117] have initiated a new trend in the development of mean-field models that consider different grain populations. These models have been extended several times since and this strategy applied to other mechanisms. Indeed, it offers the opportunity to capture the dispersion of microstructure characteristics with limited increase of the computational cost.

- Full-field models propose the most thorough approach to predict microstructure evolutions at mesoscopic scale. They rest upon a description of the microstructure topology which allows to take into consideration the influence of specific phenomena or microstructure characteristics with physically based assumptions.

The next three sections (1.3.1, 1.3.2 and 1.3.3) describe the models that are the most frequently applied to simulate microstructure evolutions due to ReX. A specific attention will be paid to the models that have been applied to simulate CDRX and more generally ReX mechanisms similar to the ones observed for Zy-4, generally observed with Ti and Al alloys.

1.3.1 Analytical models

No analytical model has been proposed to assess CDRX taking into account its specific features. However, some common recrystallization models have been applied to materials presenting discontinuous mechanisms. For instance, SRX of $Zr - Nb$ alloys has been predicted using Johnson-Mehl-Avrami-Kolmogorov (JMAK) model [118, 119].

JMAK model [110, 108, 109] is based on the simple assumption that recrystallization happens by the growth of spherical nuclei. These nuclei form at a given rate ($\dot{N}$) in the deformed volume. This gives the following equation describing the evolution of recrystallized fraction with time:

$$F_{rx} = 1 - \exp\left(-Bt^n\right). \tag{1.13}$$

B and n are constant that depend on the hypotheses considered regarding nucleation and growth characteristics.

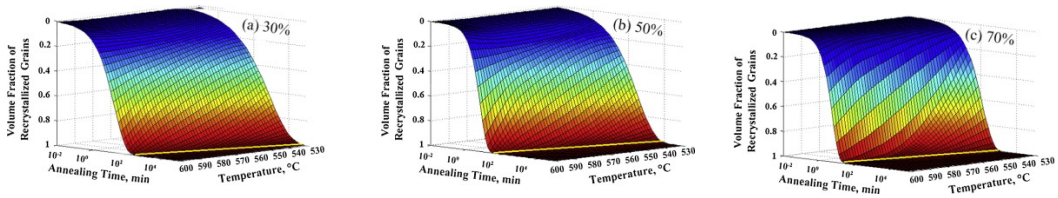
This type of model is frequently used for studying SRX, particularly in industry. It presents the advantage of relying upon simple assumptions that allow to estimate if the evolution of the coefficient B and n are consistent with the nucleation and growth mechanisms studied. Figure 1.21 illustrates how these models can be fitted based on simple characterization techniques to predict the evolution of recrystallized fraction, depending on annealing time, temperature and prior deformation level [118, 119].

50 years later, some new analytical models have been developed in order to consider the role of subgrains in formation of recrystallized grains. It has been mainly driven by the work of Humphreys *et al.* [120, 121, 122] and extended by Zurob *et al.* [123]. Humphreys *et al.* propose to represent microstructure as an array of grains and subgrains. Then, they estimate the boundary velocity by assuming that recovery is efficient enough to ensure that all the dislocations generated during deformation rearrange to form subgrains. Therefore, the only remaining pressure is the one related to capillarity and this leads to the following equation describing the growth of a subgrain in 3D:

$$\frac{dR}{dt} = M \times P = M\left(\frac{3\beta\overline{\gamma}}{2\overline{R}} - \frac{2\alpha\gamma}{R}\right). \tag{1.14}$$

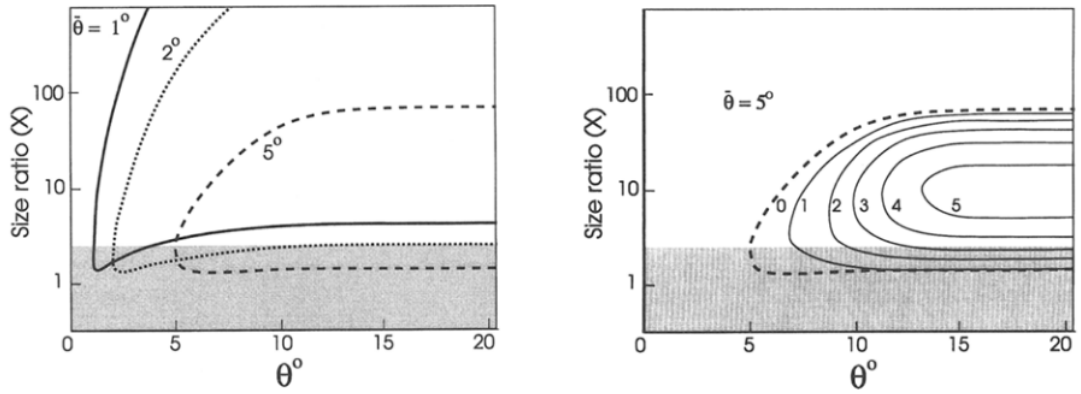
α and β are constants close to unity to correct the simplifications about subgrain geometry.

Thanks to equation 1.14, they can describe domains in which heterogeneous sugrain growth could happen (see figure 1.22).



(a) 30% rolling reduction. (b) 50% rolling reduction. (c) 70% rolling reduction.

Figure 1.21: Plots of recrystallized fraction as a function of annealing time and temperature, for $Zr - 1Nb$ cold-rolled sheets. From [119].



(a) Considering various average disorientation of subgrains.

(b) Considering various individual subgrain disorientation.

Figure 1.22: Plots presenting the size and disorientation domains in which a given subgrain is supposed to grow much faster, at the expense of other subgrains. From [120].

The model introduced by Zurob *et al.* relies upon the same basic principle: describing upon simple physically based assumptions the conditions for growth of subgrains. It differs from previous contributions by a refined microstructure description. It considers distributions of subgrain size and disorientation and allows the dislocation density to evolve by recovery. It assumes that nucleation is achieved by SIBM and relies upon Bailey–Hirsch criterion [88] (see equation 1.15) to predict: incubation time, critical strain and nucleation rate.

$$r_c \geq \frac{2\gamma}{\tau\rho}. \tag{1.15}$$

Dunlop *et al.* extended this model to simulate recrystallization of Zy-4 [124]. The proposed model relies upon the same assumptions regarding formation of recrystallized grains and introduces another equation for recovery. The authors provide an equation for the extended volume fraction (equation 1.16) and the actual volume fraction. Since they do not assume constant nucleation rate as for standard JMAK model, they are forced to reformulate the extended volume fraction as Minkowski functional. Finally, they are able to identify model parameters and to compute critical strain as a function of temperature and recrystallized fraction under non-isothermal conditions. Comparisons with experimental results from various studies show good agreement (see figure 1.23).

$$\psi(t) = \frac{4\pi}{3}\int_0^t \dot{N}(t')\left(\frac{2\gamma}{\tau\rho(t')} + \int_{t'}^t M\tau\rho(t'')dt''\right)^3 dt'. \tag{1.16}$$

$$F_{rx}(t) = 1 - \exp\left(-\psi(t)\right) \tag{1.17}$$

In previous equations, $\dot{N}$ is the nucleation rate and ψ the extended recrystallized volume fraction.

1.3.2 Mean-field models

As discussed in section 1.2, CDRX differs from DDRX mainly by the formation of subgrains and their progressive transformation to grains.

Gourdet-Montheillet model The first and probably most famous mean-field model of CDRX is the one proposed by Gourdet and Montheillet [125]. It proposes to represent the microstructure by an aggregate of crystallites (i.e. a mix of grains and subgrains). Three internal state variables are used to describe microstructure:

- ρ, the average dislocation density,
- $\overline{D}$, the average crystallite diameter,
- $\varphi(\theta)$, the misorientation distribution function of GB.

At each deformation step, the variation of dislocation density is computed thanks to a modified Yoshie-Laasraoui-Jonas equation:

$$d\rho = (K_1 - K_2\rho)\, d\varepsilon - \rho dV, \tag{1.18}$$

K_1 and K_2 are respectively strain hardening and dynamic recovery (DRV) parameters, $d\varepsilon$ is the strain increment and dV the volume swept by boundaries that are migrating. This equation considers the following phenomena:

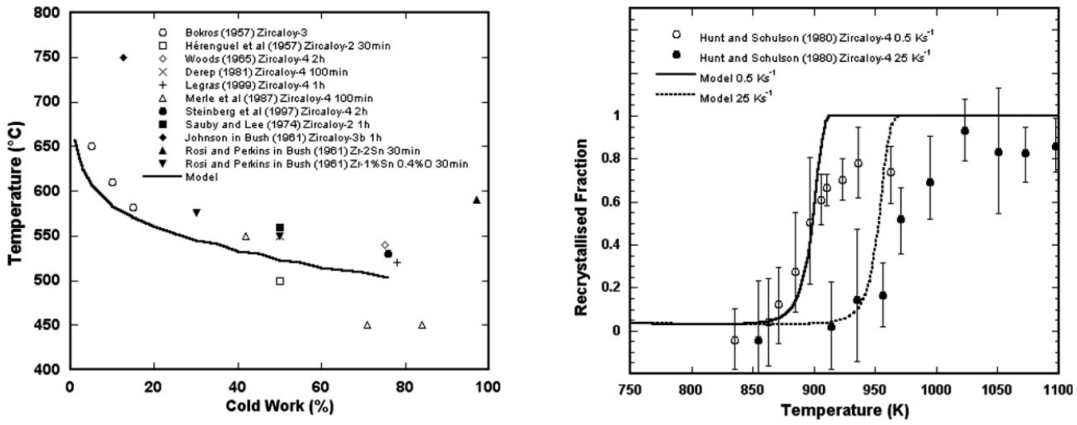
- dislocation increase due to strain hardening: $K_1 d\varepsilon$,
- dynamic recovery: $K_2 \rho d\varepsilon$,
- sweeping of dislocation by the migration of GB: ρdV.

DRV leads to increase disorientation of all LAGB. At the same time, it contributes to the formation of new LAGB. These two phenomena are described by equations 1.19 and 1.20, respectively.

$$d\theta = \frac{b}{2\eta}(1-\alpha)\overline{D}K_2\rho d\varepsilon, \tag{1.19}$$

$$dS^+ = \frac{\alpha b K_2 \rho \dot{\varepsilon} dt}{\eta\theta_0}. \tag{1.20}$$

b is the Burgers vector, η the number of sets of dislocation in LAGB, α is a coefficient describing the fraction of dislocations recovered that form new subgrains and is given by: $\alpha = 1 - \exp\left[-\left(\frac{\overline{D}}{D_0}\right)^m\right]$, with D_0 a grain reference diameter and m a fixed coefficient. Following that equation, in subgrains that have



(a) Evolution of critical strain with temperature.

(b) Evolution of recrystallized fraction with temperature for non-isothermal heat treatments.

Figure 1.23: Evolution of recrystallization parameters with various parameters. From [124].

a diameter $D \ll D_0$, most of recovered dislocations are stacked in pre-existing LAGB and lead to increase its disorientation. On the opposite, in subgrains that have a diameter $D \gg D_0$, most of recovered dislocations reorganize to form new subgrains.

Finally, dV is computed using equation 1.21:

$$dV = \frac{2 f_{\text{HAGB}} v_{\text{HAGB}}}{\overline{D}\dot{\varepsilon}} d\varepsilon, \tag{1.21}$$

with v_{HAGB} and f_{HAGB} the HAGB velocity and length fraction, respectively.

In practice, the misorientation distribution function is discretized in classes of width $\delta\theta$. At each deformation increment, a class $\varphi(\theta_{min})$ describing LAGB with a disorientation in $[\theta_{min};\ \theta_{min} + d\theta]$ range is added. Its value is initialized using next equation:

$$\varphi(\theta_{min}) = \frac{\alpha}{(1-\alpha)} \theta_{min}. \tag{1.22}$$

All pre-existing classes are shifted by a value $d\theta$ and their value are updated using next relation:

$$\varphi(\theta + d\theta) = \left(1 + \frac{1}{\overline{D}} \frac{d\overline{D}}{d\varepsilon} + dV\right) \varphi(\theta). \tag{1.23}$$

It should be pointed out here that several assumptions have been required to establish those equations. According to equation 1.19, one can see that disorientation increments are strictly positive and equal for all LAGB. First assumption

implies specific restrictions for dislocation motion whereas second is verified if the strain is distributed homogeneously.

Gourdet *et al.* applied this model to different aluminum alloys and noted that it was able to predict qualitatively the formation of LAGB and their evolution due to CDRX [126]. However, it was emphasized that the model was showing some limitations since it was not designed to take explicitly into account grain topology, intragranular property gradients or texture evolution [126]. Readers should know that this model has been criticized. In a series of articles, Mc Queen pointed out that the GM model was relying upon oversimplifying assumptions. Especially, he discussed the assumptions regarding dislocation motion that enable Gourdet *et al.* to consider a strictly positive disorientation increment for all LAGB. Besides, he considered that the continual disorientation increase was not reproducing accurately the complexity of the mechanisms in charge of formation of recrystallized grains (see section 1.2.3) [127, 128].

Recent extensions of Gourdet-Montheillet model Despite the critics supported by McQueen, the Gourdet-Montheillet model has been extended several times recently. Buzolin *et al.* proposed to simulate recrystallization of Ti-17 hot compressed samples [129]. To do so, they associate the Gourdet-Montheillet model to another one that is in charge of predicting PDRX. This PDRX model considers in fact three mechanisms responsible of microstructure evolutions:

- static recovery, which leads to a decrease of dislocation density.
- Evolution of the subgrain structure thanks to formation of new substructures by dislocation rearrangement and growth of existing subgrains.
- Transformation of subgrains to recrystallized grains by SIBM and growth of these recrystallized grains.

The proposed approach appears promising since it relies upon a precise description of the physical phenomena responsible for formation of subgrains during hot deformation and their transformation into recrystallized grains during the subsequent heat treatment. However, the proposed equations were including a larger number of parameters and the comparisons with experimental data show limited agreement.

A second series of recent studies present attempts to extend the Gourdet-Montheillet model [130, 131, 132]. Sun *et al.* proposed to modify the model (equation 1.19) by computing the progressive disorientation increase according to following equation:

$$d\theta = \frac{c_1}{2} b \rho^{1/2} K_2 \times P_{\mathrm{D}}^{c_2} d\varepsilon, \tag{1.24}$$

where c_1 and c_2 are two fitting constants and P_{D} is the element of subgrain stored energy and is computed by summing interfacial and deformation stored energy.

Then, Li *et al.* and Gan *et al.* proposed similar modifications of the subgrain disorientation rate. Li *et al.* added a multiplicative term $(1-\frac{\theta_c}{\theta_{sat}}\overline{\theta}_{sub})$ to equation 1.24 with θ_{sat} the steady-state average subgrain disorientation angle and $\overline{\theta}_{sub}$ the average subgrain disorientation angle. This implementation is supposed to tackle the remark made by McQueen [128]. However, this modification is purely phenomenological. Gan *et al.* intended to simulate the progressive change in disorientation by following simple equation: $\dot{\theta} = M_T T$ with M_T the rotational mobility and T a torque term. This formulation allows to compute the evolution of the average GB misorientation with strain and depending on GB energy.

In all of the three approaches presented above, they consider that the progressive increase in disorientation is induced by subgrain rotation. As discussed previously in section 1.2.3, previous studies have concluded that this phenomenon was limited to subgrains measuring less than hundred nanometers in width.

Finally, the Gourdet-Montheillet model was derived and coupled to a crystal plasticity (CP) framework to simulate CDRX of 7075 Al alloy [133]. CP models constitute advanced deformation models and rely upon evolutions rules to predict the stress and the hardening rate based on the strain rate. They present the advantage of predicting the strain distribution between grains and within a single grain, depending on macroscopic conditions, on material properties and on grain interactions [134, 135]. In the precise case described in ref. [133], a viscoplastic self-consistent (VPSC) model is used and enables to predict the average polycrystal mechanical behavior and the local dislocation density. Then, based on the Gourdet-Montheillet model, they can compute the nucleation rate thanks to equation 1.25.

$$\dot{N} = c_1 \left(1 - F_{rx}\right) \frac{\overline{D}_m^3}{3\overline{D}_{\text{SG}}^2} \times \left[f_{\text{LAGB,N}} S_{\text{LAGB}} \dot{\theta}_{\text{N}} \right]. \tag{1.25}$$

$\overline{D}_m$ is the initial average subgrain diameter, $\overline{D}_{\text{SG}}$ is the average subgrain diameter, and S_{LAGB} is the LAGB total surface. $f_{\text{LAGB,N}}$ and $\dot{\theta}_{\text{N}}$ are the LAGB surface fraction and disorientation rate for subgrains belonging to the highest disorientation class, respectively.

With this attempt, Chen *et al.* illustrate the possibility to couple the Gourdet-Montheillet with other more complex, such as the CP ones. However, one could regret that this model remains limited since the interest of such high level frameworks is to provide refined simulations with prediction of local heterogeneities. Many other examples of coupled deformation-recrystallization models have been proposed in literature. This constitutes an interesting approach since it has been described several times in previous sections that deformation could be highly heterogeneous and impacts significantly recrystallization.

To summarize, it appears that the approach proposed by Gourdet and Montheillet is interesting since it has been applied successfully at multiple occasions and is based on simple and straightforward description of physical phenomena.

However, it relies upon given assumptions that may limit its range of applications and its precision. Consequently, several researchers have tried to extend it recently [130, 131, 132, 133]. These attempts illustrate that the model could be used to model CDRX, notably for several Al alloys. They also highlight the importance of parameters identification. Nevertheless, extensive comparisons with experimental results are still missing.

1.3.3 Full-field frameworks

Five types of full-field models of recrystallization are commonly found in literature: Monte-Carlo Potts (MC), cellular automaton (CA), vertex, phase field (PF) and level-set (LS). MC and some CA approaches are based upon probabilistic rules and are therefore described as stochastic strategies. The others are deterministic methods and can be differentiated by the technique used to describe interfaces into the numerical framework. If interfaces are discretized, as done in vertex approaches, they are called front-tracking. In the other case, interfaces are implicitly described and the methods are defined as front-capturing. This is the case for PF and LS models.

Monte-Carlo Potts

MC simulations imply a division of the representative volume element (RVE) into a given number of discrete cells arranged on a regular grid, as represented in figure 1.24. Each cell stores a grain index as well as some properties that describe local physical state such as orientation. The total system energy is computed by summing GB energy and stored energy due to deformation.

At each MC step, a cell is selected randomly and its properties are changed to the ones of another site. The variation in total system energy (ΔE) induced by this change is computed. Then, the change is validated based on a probability function of this energy variation. If GB properties are considered isotropic, this function is generally defined as follows (with k a constant):

$$P = \begin{cases} \exp \dfrac{-\Delta E}{kT}, \ \Delta E \geq 0 \\ 1, \ \Delta E < 0. \end{cases} \tag{1.26}$$

When GB properties vary with disorientation, the probability function is adapted:

$$P = \begin{cases} \dfrac{M(\theta)\gamma(\theta)}{M_{max}\gamma_{max}} \exp \dfrac{-\Delta E}{kT}, \ \Delta E \geq 0 \\ \dfrac{M(\theta)\gamma(\theta)}{M_{max}\gamma_{max}}, \ \Delta E < 0. \end{cases} \tag{1.27}$$

The number of reorientation tries performed at each increment is generally defined as the number of pixels. However, a same pixel can be chosen several times.

Consequently, the link between time and MC steps for a simulation performed within a MC framework should be scaled carefully.

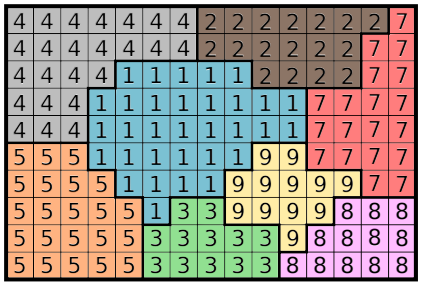


Figure 1.24: Microstructure representation using a regular grid, as used in MC and CA methods. Numbers correspond to grain indexes and GB are represented by bold lines.

This method has been first applied by Anderson *et al* [136]. In the last decades, it has been used at multiple occurrences due to its simplicity and low numerical cost [137]. It has been used to assess the influence of specific assumptions upon dynamic recrystallization [138, 139]

Applications of MC models to CDRX To the author knowledge, this type of model has never been extended to simulate CDRX. Nonetheless, it has been applied to simulate SRX by immersing EBSD data and studying different hypotheses regarding nucleation. A first example is provided by Chun *et al.*. They proposed to simulate SRX of a commercial purity (CP) cold rolled Ti alloy by immersing EBSD data [140]. Orientations are taken from EBSD data. GB energy and mobility are described by Read-Shockley and Huang-Humphreys equations, respectively (equations 1.2 and 1.3). The stored energy of deformation is estimated based on the index quality (IQ) value, that is correlated to the crystal lattice distortions. Nuclei are introduced at the beginning of the simulation. Nuclei locations are selected according to two different hypotheses:

- randomly throughout the microstructure,
- by selecting randomly 1000 sites among those belonging to the upper 1% having the highest stored energy.

The simulation results show that the spatial stored energy distribution plays an important role in microstructure evolutions. Moreover, they also point out that positioning nuclei in zones of higher stored energy leads to a faster recrystallization kinetics in the early stage and to a quicker impingement of recrystallized grains. An illustration of this work is showed in figure 1.25.

Jedrychowski *et al.* [141] recently described an attempt to model SRX of channel-die compressed Zr702. Initial microstructure is generated by immersing

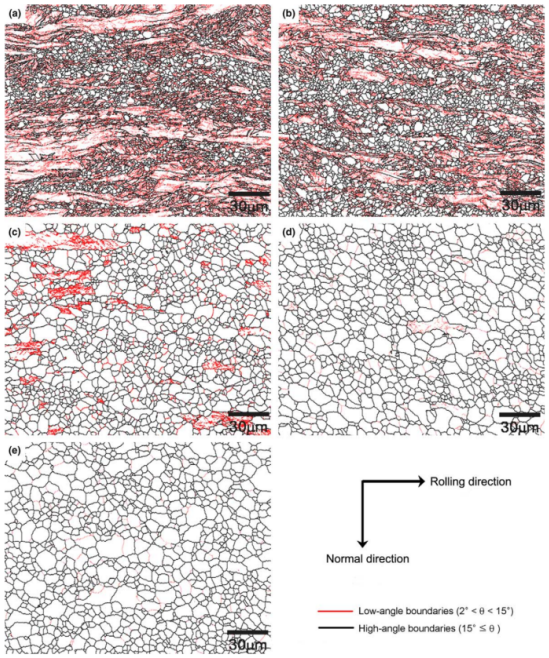


Figure 1.25: Microstructure evolution in 60% cold rolled CP Ti during annealing at 600°C. Annealing times are respectively: (a) 5 min, (b) 8 min, (c) 15 min, (d) 60 min, (e) 100 min [140].

EBSD. GB energy and mobility are computed using Read-Shockley and Huang-Humphreys functions, respectively. The stored energy of deformation is estimated by rescaling kernal average misorientation (KAM) values over a given range (here $[0,\ 4.5]$). Two configurations for formation of new recrystallized grain are considered:

- "classical nucleation". In that case, nuclei are placed at sites with highest stored energy. Their orientation is taken randomly, either from deformed sites located close to the nuclei, either from deformed sites throughout whole microstructure.
- SIBM. In the latter, some subgrains are placed in HAGB regions presenting the highest stored energy gradients.

The simulation results exhibit better agreement with experimental data, in terms of texture evolution and of recrystallized grain spatial distribution when SIBM is considered. This enables the authors to conclude that, for low strain values, this Zr alloy exhibits SIBM.

Cellular automata

Cellular automata (CA) were applied for the first time to model recrystallization in 1991 by Hesselbarth and Göbel [142]. As for MC models, they rely on discretization of the simulation space into lattice sites. Variables are attributed

to each lattice sites to describe various properties. Different cell geometries and neighborhoods can be considered. At each time step, properties of all cells are updated simultaneously based on transition rules. These rules dictate the cell state based on its previous state and on neighboring cell state.

CA have been used to model SRX [143, 144]. They also provide interesting results that enable to discuss the influence of specific nucleation mechanisms [145] or stored energy gradients [146].

Applications of CA models to CDRX In a recent article, Liu *et al.* described extensively a simulation strategy to model CDRX, based on a CA technique [147]. To do so, they generate a substructured microstructure by doing a two-step generation procedure. A fraction of the grains present in the microstructure are subdivided into subgrains. Then, at each simulation step, different phenomena are considered:

- new subgrains can form. This is achieved by updating substructure parameters and the grain subdivision.
- Every subgrain has a given activation probability. LAGB migration is performed for each activated subgrain, if the driving forces for its growth are higher than the ones of its neighbors.

This approach is interesting but its validation against experimental data remains limited. In addition, one could regret the repeated use of probabilistic laws which are not physically supported.

Azarbarmas *et al.* proposed to directly use a DDRX framework to model CDRX of a a TiNiFe alloy [148]. To do so, he supposes that new DRX grains form at a given rate computed using following equation:

$$\dot{n} = C\dot{\varepsilon} \exp \frac{-Q}{RT}. \tag{1.28}$$

In previous equation, C is a fitting constant. Based on experimental data, he fits a phenomenological law that provides the grain size as a function of the Zener-Hollomon parameter. This attempt to use a phenomenological model presents the advantage to be really simple and efficient. However, the comparison with experimental data is very limited and there are great chances that this approach could not be extended to large thermomechanical condition ranges.

Vertex

First applications of vertex models to simulate microstructure evolutions have been proposed by Kawasaki *et al.* [149] and extended by Weygand *et al.* [150]. In these models, interfaces are discretized using vertices. Two types of vertices are considered: actual vertices that are located at multiple junctions and virtual vertices that are located along interfaces to improve boundary description.

Kawasaki *et al.* were the first to propose an implicit equation to compute vertex' velocity:

$$\frac{\partial R}{\partial \overrightarrow{v}} = -\frac{\partial \nu}{\partial \overrightarrow{r}}, \tag{1.29}$$

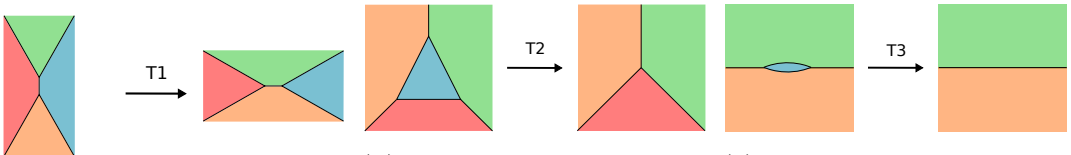
with R describing the dissipation and $\partial\nu$ the reduction of surface energy related to GB motion. $\overrightarrow{v}$ and $\overrightarrow{r}$ denote respectively vertex velocity and position. The dissipation term originates from the viscous drag opposing to GB migration and is inversely proportional to mobility.

Since this method requires that nodes are located at interfaces or at least at multiple junctions, topological events should be managed carefully. For instance, if a grain shrinks, the nodes located at grain triple points will collapse. Therefore, numerical operations should be implemented in order to manage all topological events (see figure 1.26).

Since most vertex models only discretize interfaces, they present a great computational efficiency. However, they present two significant limitations. First, if the number and the complexity of topological events is limited in 2D, extending it to 3D remains a huge challenge. Second, most vertex models are not able to store heterogeneous grain properties, such as orientation or dislocation density. Recently, a new methodology has been proposed inspired by vertex models [151]. It relies upon a complete discretization of the simulation domain with an evolving triangular mesh. As standard vertex models, interfaces are explicitly discretized by fitting nodes and managing topological events. This allows to use coarse elements without lowering the accuracy. In addition, it enables to store information about grains since grain interiors are meshed. An illustration of the proposed discretization strategy is provided in figure 1.27.

This method has been extended several times for being able to model DDRX [152] and to take into account GB anisotropy [72].

Applications to model CDRX To the author's knowledge, no vertex model has been applied to CDRX. However, several attempts to investigate recrystallized grains formation have been described [153, 154]. In both articles, Humphreys relies upon a vertex model and is not considering virtual nodes. The described framework is able to keep track of grain and subgrain orientation. Consequently,



(a) Recombination. (b) Annihilation of small three-sided grain. (c) Elimination of a grain with two triple points.

Figure 1.26: Topological operations of vertex models. Adapted from [150].

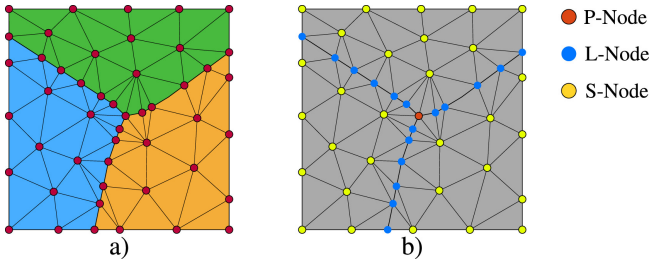


Figure 1.27: Example of the nodal geometric tagging performed on a body fitted mesh. (a) considered topology, (b) resulting nodal tagging. From [151].

he is able to compute GB misorientation. GB energy is computed by Read-Shockley equation. GB mobility is described by following function:

$$M(\theta) = \begin{cases} \theta^l, \\ M_{max}, \ \theta \geq \theta_{max}. \end{cases} \tag{1.30}$$

l being an exponent taken equal to 0.2.

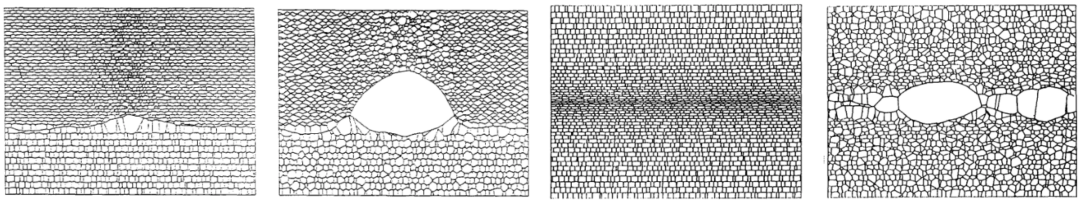
Humphreys used this simulation framework to examine the evolution of different substructure configurations. He successfully reproduced various mechanisms discussed previously (see section 1.2.3): SIBM, PSN and formation of recrystallized grains at transition band. It should be noted that it relies upon the strong assumption that no stored energy of deformation remains within subgrains. An illustration of this work is given in figure 1.28.

Phase field

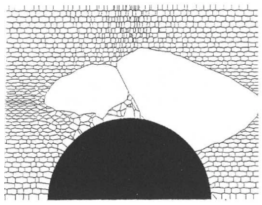
Phase field (PF) models describe microstructure using a set of field variables. Field variables are continuous over the whole domain. Thus, interfaces are diffuse (see figure 1.29a). Two types of variables are considered: conserved and non-conserved (noted $c_1, c_2, ...$ and $\eta_1, \eta_2, ...$, respectively). The former satisfy conservation laws. Solute concentration constitutes an example of choice to illustrate the need of such variables in the context of microstructure evolution modeling. The total free energy of the system is often summarized as:

$$F = \int \left[f(c_1, ...c_n, \eta_1, ..., \eta_p) + \sum_{i=1}^{n} \alpha_i \left(\nabla c_i\right)^2 + \sum_{i=1}^{3}\sum_{j=1}^{3}\sum_{k=1}^{p} \beta_{ij} \nabla_i \eta_k \nabla_j \eta_k \right] d^3r + \int\int G\left(r - r'\right) d^3r d^3r'. \tag{1.31}$$

In previous equation, f is the local free energy density and α_i and β_{ij} are gradient energy coefficients. The second integral describes the contribution to the total free energy of long range interactions [155].

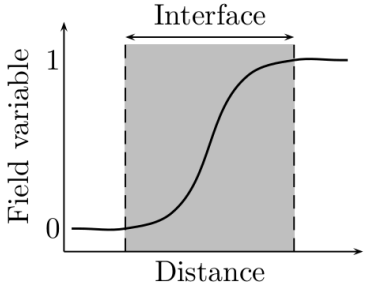


(a) SIBM initiation. (b) Advanced SIBM state. (c) Transition band initial state. (d) Transition band final state.

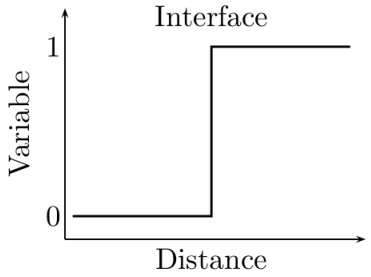


(e) PSN.

Figure 1.28: Simulation of various mechanisms leading to formation of recrystallized grains. From [153].



(a) Diffuse interface description.



(b) Sharp interface description.

Figure 1.29: Mathematical representations of interfaces. From [156].

Evolution of field variables is predicted by solving Cahn-Hilliard [157] and Allen-Cahn [158] equations:

$$\frac{\partial c_i\left(\overrightarrow{r},t\right)}{\partial t} = \nabla M_{ij} \nabla \frac{\delta F}{\delta c_j\left(\overrightarrow{r},t\right)}, \tag{1.32}$$

$$\frac{\partial \eta_p\left(\overrightarrow{r},t\right)}{\partial t} = -L_{pq} \frac{\delta F}{\delta \eta_q\left(\overrightarrow{r},t\right)}, \tag{1.33}$$

where M_{ij} and L_{pq} are related to energy dissipation. When modeling recrystallization, they are kinetic parameters related to GB mobility.

They have been developed originally to model solidification and phase transformation phenomena. It is noteworthy to mention that it has been applied to simulate the formation of Widmanstätten structure described earlier [159]. Later on, they have been extended to GG [160] and DDRX [161, 162]. No application of this kind of model to CDRX has been described in literature.

Level-set

As PF methods, LS approaches constitute generic strategies that are suited to study various phenomena. They rely upon LS functions ($\phi(x,t)$) that track the position of interfaces with time. For simulation of GG and MDRX mechanisms, where no deformation takes place, some formulations based on fast Fourier transform (FFT) have been proposed [163, 164]. In the context of large deformations, they are embedded into a FE framework (FE-LS) that enables to solve partial differential equations. They have been originally developed by Osher and Sethian [165] and improved to tackle multiphase problems [166, 167]. However, due to their implicit description of interfaces, they often require refined mesh in boundary regions. Thanks to the progresses of remeshing algorithms [168, 169], this methodology has finally been applied to modeling of microstructure evolutions [21, 22, 23]. In that context, LS track GB and their position can be retrieved by extracting the iso-zero values of LS functions. LS functions are initialized as signed Euclidean distance functions to GB:

$$\begin{cases} \phi(x,t) = \pm\, d\left(x, \Gamma(t)\right), \ x \in \Omega, \\ \Gamma(t) = \{x \in \Omega, \ \phi(x,t) = 0\}, \end{cases} \tag{1.34}$$

where d is the signed Euclidean distance function and Ω the simulation domain. By convention, $\phi(x,t)$ is generally taken positive inside the grain and negative outside.

The movement of GB is predicted by solving the following transport equation:

$$\frac{\partial \phi}{\partial t} + \overrightarrow{v} \cdot \overrightarrow{\nabla \phi} = 0, \tag{1.35}$$

with $\overrightarrow{v}$ being the velocity of interfaces. Velocity is classically described using equation 1.5. Originally, one distance function was defined per grain. Therefore, this equation was solved N_g times, N_g being the number of grains. Since this was costly, a graph coloring and recoloring technique has been developed [24]. The set of all distance functions required to describe all the grains is now: $\Phi = \{\varphi_i,\ i = 1,\ ...,\ N_d\}$, with N_d the number of distance functions, greatly smaller than N_g. After having solved transport equation, at least two operations should be performed. First, LS functions should be reinitialized to ensure they stay distance functions (i.e. that $\|\overrightarrow{\nabla\phi}\| = 1$). Indeed, the resolution generally induces LS functions to deviate from signed distance functions. In recent works using LS formulations, this is ensured thanks to a method developped by Shakoor *et al.* [170]. Second, since each LS function evolves separately, some overlaps or voids could appear at each time step. To ensure that every single point of the domain belongs to a unique LS function, LS functions are corrected according to equation 1.36 [166].

$$\varphi_i(x) = \frac{1}{2}\left(\varphi_i(x) - \max_{j\neq i}\varphi_j(x)\right),\ \forall i \in [1, N_d]\,. \tag{1.36}$$

Working with signed distance functions is highly convenient since it allows to compute GB unitary outside normal and curvature:

$$\overrightarrow{n} = -\overrightarrow{\nabla\phi}, \tag{1.37}$$

$$\kappa = \overrightarrow{\nabla} \cdot \overrightarrow{n} = -\Delta\phi. \tag{1.38}$$

LS models have been applied to simulate GG, to assess the influence of SPP [27], and applied to SRX [25] and DDRX [26]. Recently, some new implementations have been developed to capture the impact of anisotropy upon microstructure evolutions [29, 30, 31].

1.4 Conclusion

This chapter described briefly the main information about Zy-4 metallurgy and manufacturing. It presented the main features that characterize Zy-4 microstructures: the presence of a fine SPP population and the different grain morphologies. The formation of lamellar microstructures was detailed and the main parameters promoting the formation of microstructures containing mainly basket-weaved structures or parallel plate were discussed.

Then, the following section was dedicated to present recrystallization mechanisms. Since recrystallization involves consequent evolutions of GB network, this section described their properties, motion and formation. A specific attention was given to provide an extensive description of recrystallized grain formation.

Indeed, it influences significantly microstructure evolutions and is often oversimplified since these mechanisms happen at subgrain or even dislocation scale and are highly difficult to observe [84]. This allowed to discuss the common recrystallization terminology and to present the main features of CDRX.

Finally, a detailed review of the different numerical models for recrystallization was proposed. The main analytical, mean-field and full-field models were presented. For each category, discussions were centered around conceptualization and implementation of nucleation. This offered the opportunity to assess the model's ability to simulate CDRX. Indeed, it has been shown previously that CDRX differs mainly from the spatial and temporal characteristics of nucleation. Finally, this section allowed to identify the most promising strategies presented in the state of the art to simulate precisely CDRX. All these approaches describe substructures and involve:

- consideration of a pre-existing substructure,
- immersion of a deformed microstructure from EBSD data,
- modeling subgrain formation and evolution thanks to mean-field equations,
- coupling with CP models.

Résumé en français

Ce chapitre décrit brièvement les informations relatives à la métallurgie du zircaloy-4. Les principales caractéristiques microstructurales de cet alliage sont rappelées. En effet, le Zy-4 présente une population de particules de seconde phase et des grains de topologies variées. En particulier, la formation des microstructures lamellaires issues de la trempe est discutée. Les principaux paramètres conditionnant la formation de microstructure de type vannerie ou à platelets parallèles sont détaillés. Les mécanismes de recristallisation sont décrits. Dans un premier temps, les propriétés des joints de grains, leur formation et leur migration sont étudiées. La formation de nouveaux joints de grain, de grains et de sous-grains est détaillée avec une attention spécifique. En effet, ces mécanismes conditionnent la recristallisation dans son ensemble et sont souvent simplifiés à l'excès, pour diverses raison [84]. A partir de cette synthèse, une discussion sur la terminologie des mécanismes de recristallisation est proposée. Finalement, une revue détaillée des différents modèles de la recristallisation est proposée. Les principaux modèles analytiques, à champ moyen et à champ complet sont succinctement présentés. La description de chacun de ces modèles est centrée sur les stratégies de modélisation concernant la formation de nouveaux grains. Cela permet d'évaluer la capacité des différents outils numériques de modéliser la recristallisation dynamique continue. L'ensemble des approches décrites proposent généralement de représenter la sous-structure et de :

- considérer une microstructure initale comportant des sous-grains,

- immerger une microstructure déformée à partir de données EBSD,
- modéliser la formation et l'évolution de sous-grains à partir d'équations issues de modèles à champ moyen,
- coupler le modèle de recristallisation à un modèle de plasticité cristalline pour modéliser finement les mécanismes de déformation.

Chapter 2

Materials and experimental methods

The present chapter describes in details the manufacturing routes and microstructural states of the different materials tested in the context of this PhD thesis. The main microstructural features representative of each initial state are detailed. Then, the thermomechanical tests used and the thermomechanical conditions investigated are presented. Macroscale simulations of the hot compression tests are discussed to provide an estimation of the thermomechanical conditions at the center of the samples which corresponds to the characterized zones.

Microstructure characterization techniques and the different associated post-processing routines are described. A particular attention is given to assess the impact of the post-processing parameters and to evaluate the uncertainty over the experimental measurements.

2.1 Materials

2.1.1 Elaboration of initial microstructures

Samples tested and characterized during this work are classified in four different categories: without SPP (**Wo SPP**), equiaxed (**Eq**), basket-weaved (**BW**) and parallel plates (**PP**). The **Eq** category is then subdivided into **Eq** with small grains (**Eq SG**) and **Eq** with large grains (**Eq LG**). The first category corresponds to the initial state of the GG campaign and the second to the DRX-PDRX campaign. Selecting **Eq SG** samples is needed since **Eq LG** samples have a grain size close to $\overline{R}_{lim}$ (see equation 1.11 and section 1.2.2). Samples without SPP present a different chemical composition than the three other ones since the content of chromium and iron is kept as low as possible. This is done to ensure minimal SPP volume fraction since chromium and iron are the main alloying elements responsible for the formation of SPP in Zy-4, as discussed in section 1.1.1 [37, 41]. The chemical compositions representative of the four different initial states are described in table 2.1.

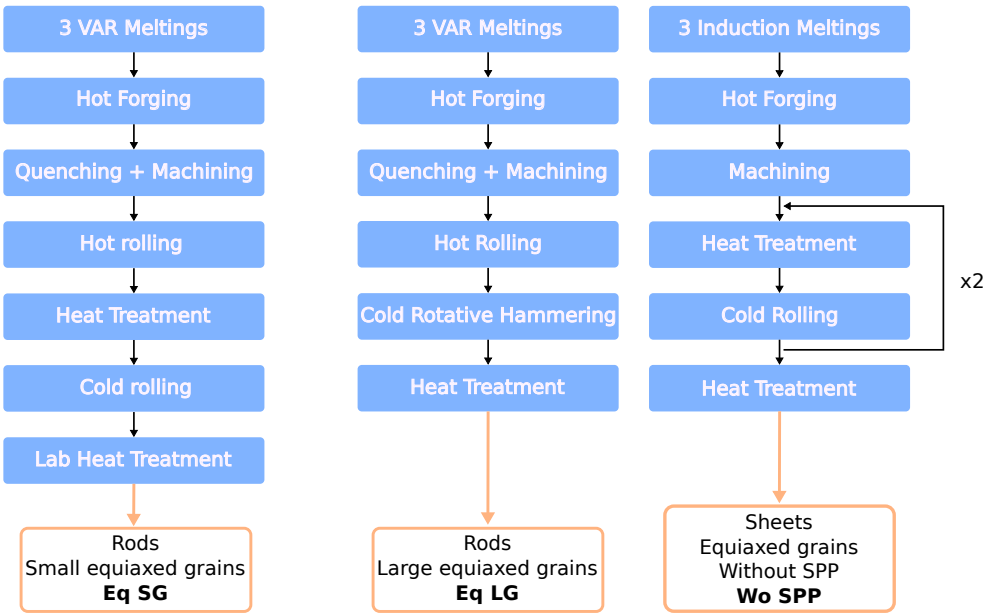
	Sn	Fe	Cr	O	Zr
Eq ; PP ; BW	1.34	0.21	0.11	0.12	Balance
Wo SPP	1.35	0.015	0.0020	0.126	Balance

Table 2.1: Chemical composition of the different materials used ($wt.\%$).

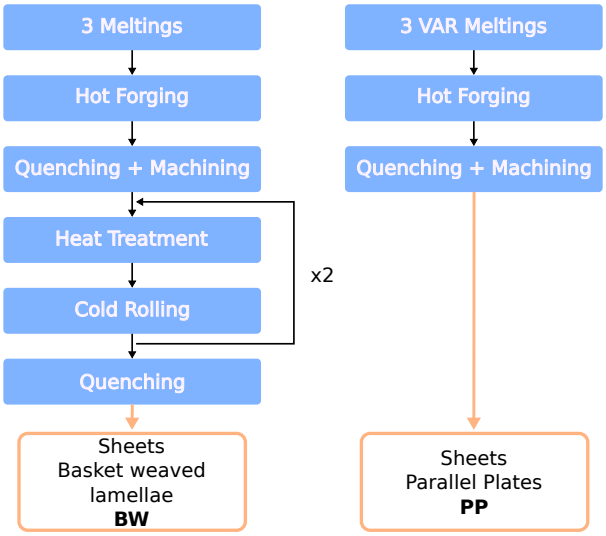
Eq SG, **Eq LG** and **PP** samples are sampled from intermediate products of industrial manufacturing routes. **Eq SG** are sampled right before the final industrial recrystallization heat treatment. A custom recrystallization heat treatment ($T = 600°C;\ \Delta t = 1\ hour$) is applied to ensure that microstructure could still exhibit significant GG during subsequent heat treatments. **BW** and **Wo SPP** materials are manufactured at Framatome research center. Complete thermo-mechanical paths are presented in figure 2.1. After the final elaboration stage, samples are obtained by:

- cutting the rods to obtain small cylinders for **Eq** samples,
- electrical discharge machining cylindrical samples into **BW** and **PP** sheets,
- cutting the plate into rectangular bars along transverse direction (see figure A.1b) and cutting them again to form small parallelepipeds for **Wo SPP** samples.

All samples are cylindrical, expect the ones from **Wo SPP** sheet. These samples being only required for heat treatment experiments, the machining procedure is kept as simple as possible. Figure A.1 available in appendices presents the sampling plans. Sample geometries are described in details in figure 2.6 and table 2.5.



(a) Samples with equiaxed microstructures.



(b) Samples with lamellar microstructures.

Figure 2.1: Presentation of the manufacturing routes of each material.

2.1.2 Characterization of initial microstructures

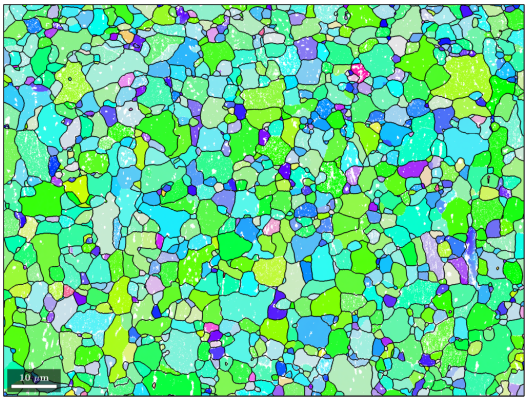
For each microstructure, at least one sample has been characterized both by EBSD and optical microscopy under polarized light (PL-OM). The details about all the characterization techniques used are available in section 2.4. Figures 2.2 and 2.3 display EBSD maps and PL-OM images for each initial state. For direct comparison of the three microstructures presenting equiaxed grains, figure 2.3 is preferred over figure 2.2 since the latter contains EBSD data obtained at different magnifications.

The main characteristics of initial microstructures can be measured based on the characterizations presented previously. They are measured from EBSD data for all the microstructures and gathered in table 2.2. For lamellar microstructures, the average lamella width ($\overline{w}_l$) and the average ex-β grain equivalent circle diameter ($\overline{ECD}$) are provided. It should be pointed out that the ex-β grain $\overline{ECD}$ are rather estimations than measurements. Indeed, very few ex-β grains are present in both EBSD and OM observation zones.

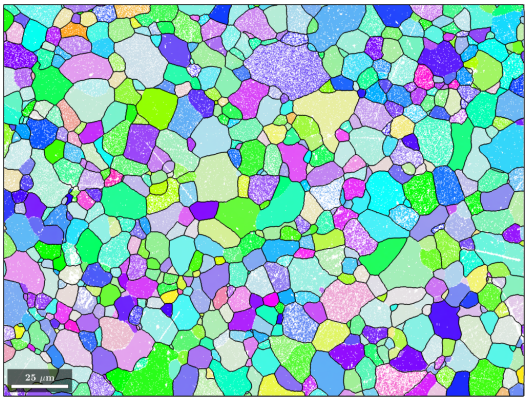
	$\overline{ECD}$ (μm)		σ_{ECD} (μm)
Eq SG	2.7		1.9
Eq LG	5.3		3.1
Wo SPP	7.8		4.7
	$\overline{w}_l$ (μm)	σ_w (μm)	Ex-β grain $\overline{ECD}$ (μm)
PP	4.1	0.4	≈1000
BW	6.5	1.3	≈1000

Table 2.2: Initial grain sizes measured by EBSD.

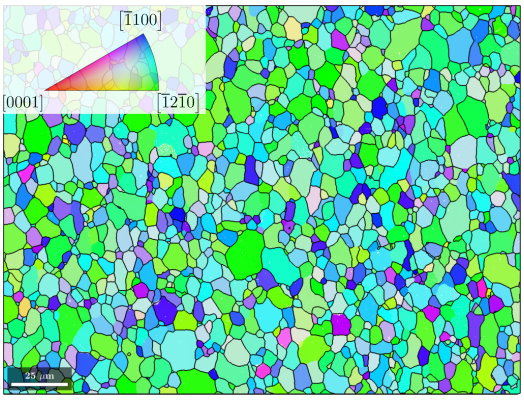
Finally, the $\{0002\}$ and $\{10\bar{1}0\}$ pole figures are displayed in figure 2.4. From these figures, it is clear that all equiaxed microstructures present a strong texture. **BW** and **PP** microstructures, on the other hand, have few orientations that are spread over the orientation space.



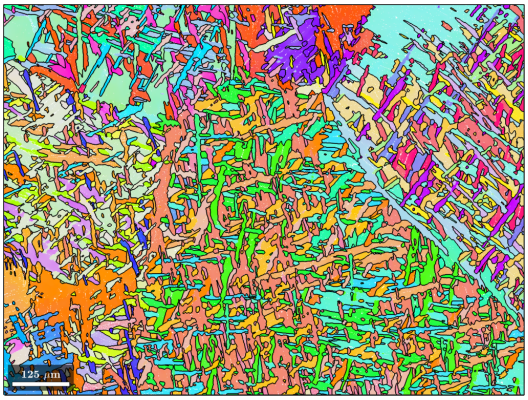
(a) Initial state representative of **Eq** microstructure with small grains (**Eq SG**).



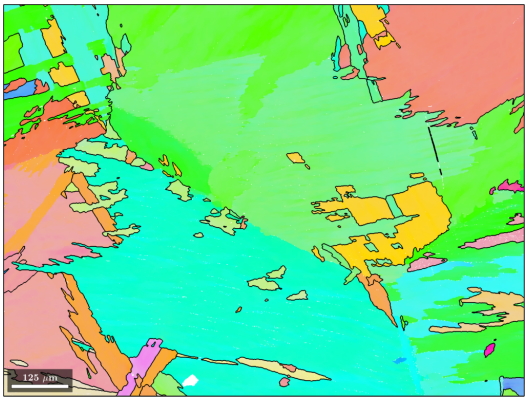
(b) Initial state representative of No SPP. microstructure (**Wo SPP**).



(c) Initial state representative of **Eq** microstructure with large grains (**Eq LG**).

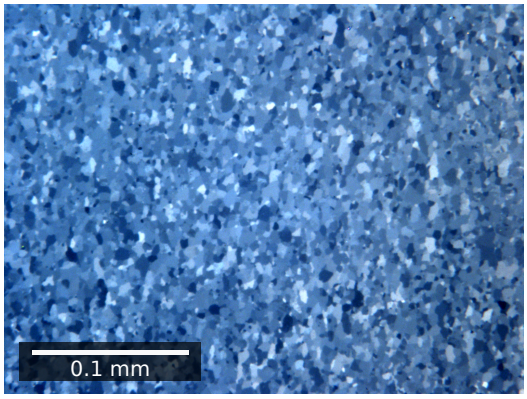


(d) Initial state representative of **BW** microstructure.

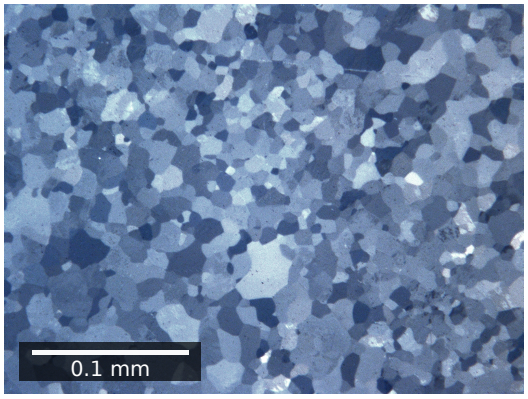


(e) Initial state representative of **PP** microstructure.

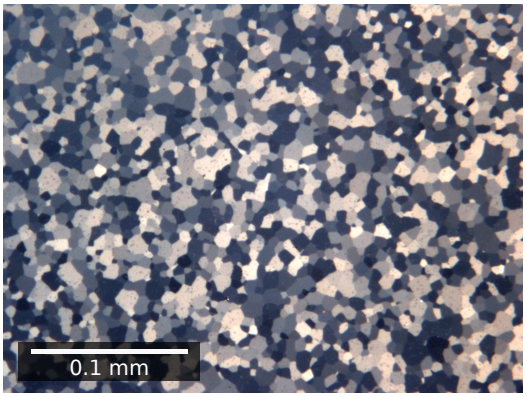
Figure 2.2: EBSD orientation maps representative of the five initial microstructures. Colors are attributed thanks to an IPF Y color code, as illustrated in subfigure 2.2c.



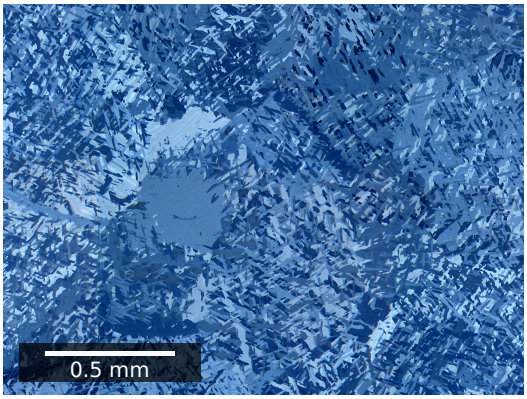
(a) Initial state representative of **Eq** microstructure with small grains (**Eq SG**).



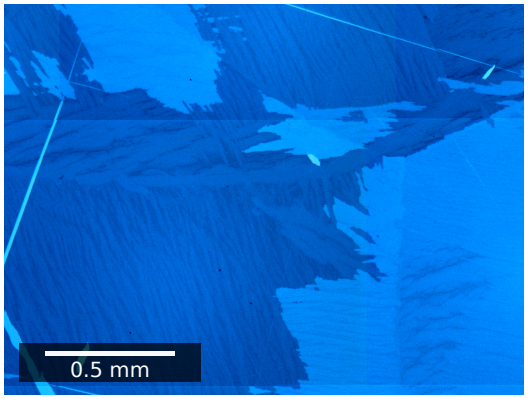
(b) Initial state representative of No SPP. microstructure (**Wo SPP**).



(c) Initial state representative of **Eq** microstructure with large grains (**Eq LG**).

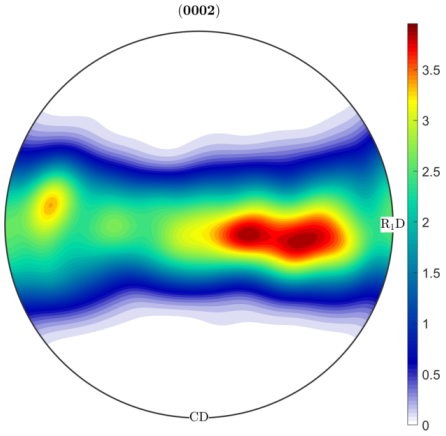


(d) Initial state representative of **BW** microstructure.

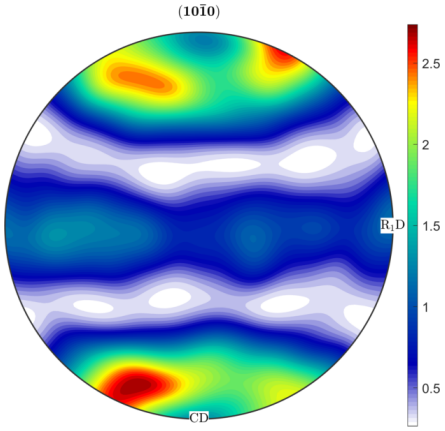


(e) Initial state representative of **PP** microstructure.

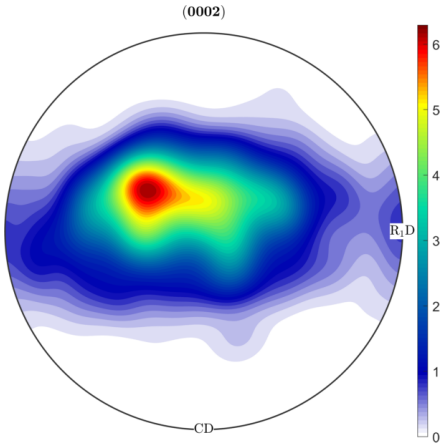
Figure 2.3: OM-PL images representative of the five initial microstructures.



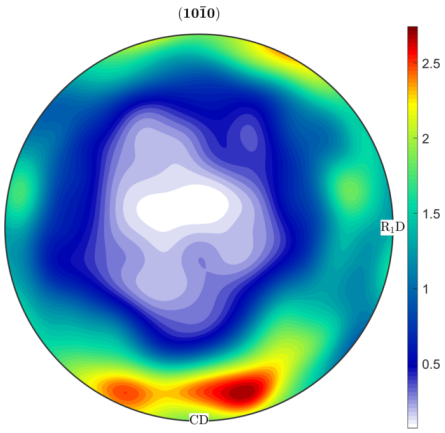
(a) {0002} pole figure. **Eq SG**.



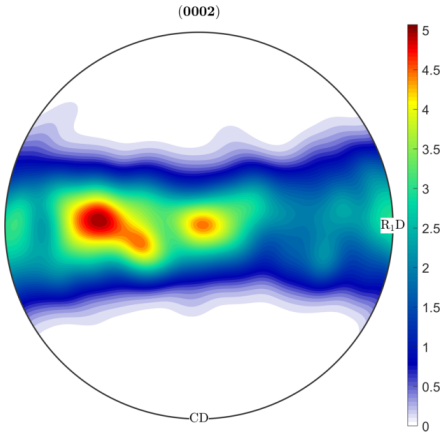
(b) {10$\bar{1}$0} pole figure. **Eq SG**.



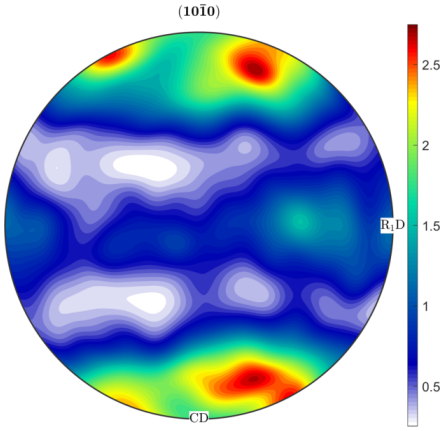
(c) {0002} pole figure. **Wo SPP**.



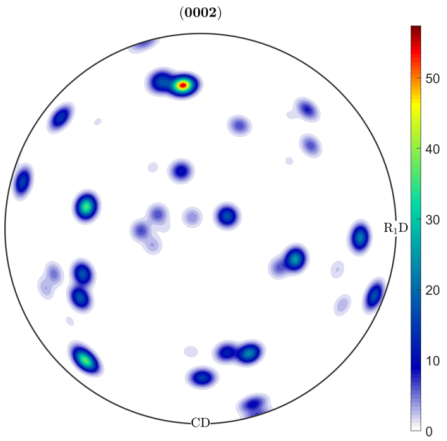
(d) {10$\bar{1}$0} pole figure. **Wo SPP**.



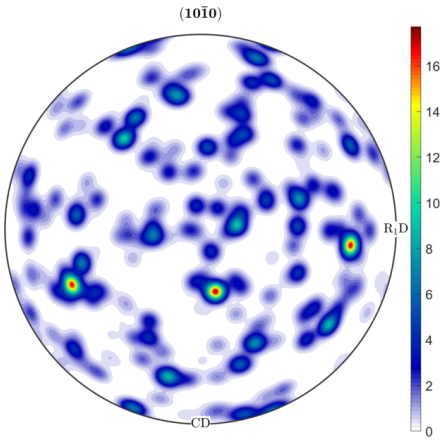
(e) {0002} pole figure. **Eq LG**.



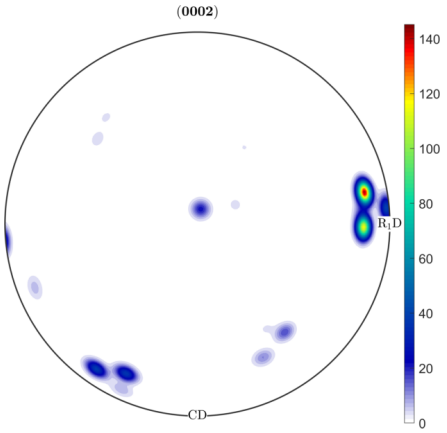
(f) {10$\bar{1}$0} pole figure. **Eq LG**.



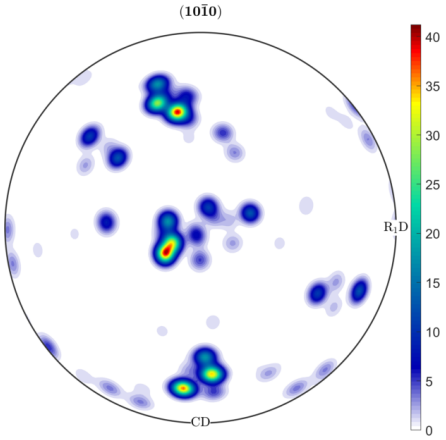
(g) {0002} pole figure. **BW**.



(h) {10$\bar{1}$0} pole figure. **BW** .



(i) {0002} pole figure. **PP**.



(j) {10$\bar{1}$0} pole figure. **PP**.

Figure 2.4: {0002} and {10$\bar{1}$0} pole figures from EBSD data. Representativity is ensured only for the following microstructures: **Eq SG**, **Wo SPP** and **Eq LG**.

2.2 Heat treatments

To characterize GG in Zy-4 and calibrate reduced GB mobility, performing some heat treatment campaigns on both **Eq** and **No SPP** samples is required. The ranges of duration and temperature investigated are described in tables 2.3 and 2.4. Since Zy-4 oxidizes quickly at high temperatures, the heat treatments are performed either under vacuum or under a protective atmosphere mainly composed of argon. Heating and cooling phases are kept shorter than 5 minutes. Therefore, their influence upon microstructure evolutions is considered negligible.

2.3 Thermomechanical testing

2.3.1 Description of the experimental set-up

Hot compression experiments are made using a hydraulic mechanical testing machine (*MTS Landmark 370-25*). A radiant furnace is used to heat samples and dies at the temperature setpoint. The set-up allows the furnace to move along compression direction in order to put sample in place before experiment and to remove it quickly at the end. Temperature regulation is achieved using two thermocouples positioned on top and bottom tools. The movement of the dies is controlled by a software and a control unit to respect the constant macroscopic strain rate set by the user. Silicon nitride dies are coated using a spray of boron nitride. This operation is executed at the beginning of each batch since it requires that the dies are cold. Once the temperature of interest is set, the tools are maintained at that temperature for at least one hour to be sure that the temperature is stable and homogeneous. Before beginning each series of experiments, all samples are coated using the same lubricant. For each test, the following procedure is executed:

- the furnace is opened and the sample is positioned on the lower tool.
- The furnace is closed and a waiting time is respected. The waiting time is set equal to 10 minutes to ensure that tool temperature has returned to its initial value and that sample temperature is homogeneous and equal to the prescribed one.

Temperature ($°C$)	Duration ($hours$)		
600	1	3	8
650	1	3	8
700	1	3	8

Table 2.3: Conditions of the heat treatments performed on the model material (**No SPP**).

Temperature ($°C$)	Duration ($hours$)			
600	1	2	4	6
650	1	2	4	6
700	1	2	4	6

Table 2.4: Conditions of the heat treatments performed on equiaxed zircaloy-4 (**EQ SG**).

- Sample is deformed at prescribed stain rate. Once the aimed final strain is reached, the dies go back to initial position.
- If required, a holding time is respected.
- Furnace opens and operators push the sample into a water bucket right after to quench it.

A scheme presenting the set-up is presented in figure 2.5 and some photos are available in appendix (figure A.2). The whole test is filmed to estimate the delay between the end of deformation and the quench. Typical delay ranges from 1 to 1.5 s.

2.3.2 Thermomechanical simulation of hot compression

Defining and running appropriate simulations of the thermomechanical tests is essential to correctly set experimental conditions and to analyze results. To do so, the software Forge NxT® is used. Rheological behavior of Zy-4 is set following a point-to-point data file that has been built at Framatome CRC based on a consequent experimental database. Initial temperature of tools, sample and atmosphere are supposed homogeneous and equal to the instruction temperature. Temperature exchanges between sample and tools follow an adiabatic law. A standard heat exchange law with air is assumed for the ambient medium. Friction between sample and tools is described by a Tresca law. Friction coefficient is adjusted by inverse analysis according to a procedure that is described later on.

2.3.3 Definition of sample geometries

First, sample geometry should be defined. This is done considering several constraints. Geometry should be as close as possible to the standards prescribed by ASTM requirements [171, 172]. Number of machining operations should be limited. Finally, thermomechanical conditions at the zone of interest, in our case the center of the sample, should vary as little as possible during the experiment. This constitutes a requirement since each hot compression test is used to identify material parameters for a given set of thermomechanical conditions (T, $\dot{\varepsilon}$, ε).

To be consistent with the standard sample geometry used at CEMEF, to respect the ASTM requirements and to limit the machining operations, sample

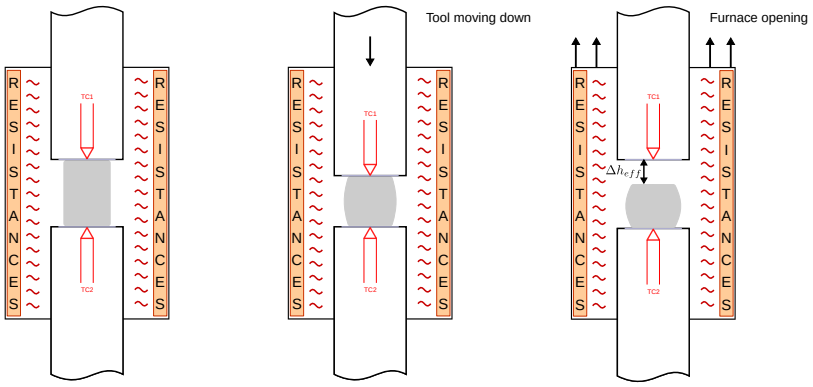


Figure 2.5: Scheme of the hot compression set-up.

height is kept within [9.0 ; 14.0] mm range. The height over diameter ratio is set to 1.4 (see table 2.5).

To assess how thermomechanical conditions (T and $\dot{\varepsilon}$) vary during a test, simulations described in previous section are used (section 2.3.2). They are run for the three sample geometries and the following thermomechanical conditions: $T = 650°C$; $\dot{\varepsilon} = 1.0\ s^{-1}$. These conditions are selected since the highest strain rate induces the highest heating and because the lower phase transformation temperature for Zy-4 is around $730°C$ (see section 1.1.1). Results corresponding to the largest geometry ($d_i = 9.95\ mm$; $h_i = 14.0\ mm$) are plotted in figure 2.7. Some statistics about these variations are presented in table 2.6. The values are comparable for all the geometries.

The results presented in figure 2.7 and table 2.6 illustrate several features that should be considered. First, the increase in temperature during deformation is significant ($\Delta T_{def} \approx 50°C$). Nevertheless, the maximum temperature remains approximately $30°C$ lower than the SPP dissolution temperature (lowest phase transformation temperature). Second, the average local strain rate is approximately 1.5 times higher than the macroscopic strain rate. Local strain rate also varies significantly during deformation with a standard deviation being equal to 0.18. These results confirm that the geometries are suited in regards of thermomechanical conditions since the temperature increase does not lead to any

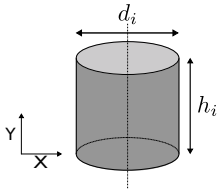


Figure 2.6: Sample geometry.

	d_i (mm)	h_i (mm)
Eq	9.95	14.0
BW	7.0	10.0
PP	6.3	9.0

Table 2.5: Description of compression sample geometries.

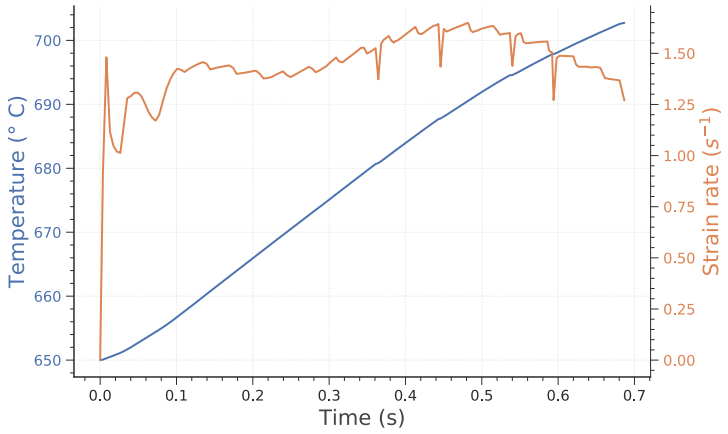


Figure 2.7: Evolution of thermomechanical conditions at sample center, for the geometry: $d_i = 9.95\ mm$; $h_i = 14.0\ mm$.

Property	Range	Average value	Standard deviation
Temperature ($°C$)	[650 ; 703]	680	16
Strain rate (s^{-1})	[1.01 ; 1.65]	1.46	0.18

Table 2.6: Statistical descriptors of local thermomechanical conditions at sample center for the three sample geometries, obtained thanks to Forge NxT® simulations.

phase transformation and the strain rate variation during deformation is limited ($Err \leq 15\%$). They also highlight the differences of local and macroscopic thermomechanical conditions. This will be discussed later on in section 6.2.

2.3.4 Definition of thermomechanical conditions

After having defined sample geometry, one should define the thermomechanical conditions to investigate. To do so, two criteria are used. First, microstructure evolutions should be significant. Second, thermomechanical conditions should be representative of industrial processes. Based on previous studies [15, 16] and on industrial data, the following test matrices (table 2.7) are defined. This represents a total of 95 hot compression tests.

Temperature and strain rate described in table 2.7 are the macroscopic ones. The strain values correspond to the local state at the center of the sample. Since we must provide the final sample height to the software controlling the tests, we use again the simulations presented earlier to estimate these values. They are given in table 2.8.

2.3.5 Post-processing of thermomechanical data

The acquisition system related to the testing machine tracks axial force and displacement during the experiment. These parameters are used for computing true macroscopic strain and stress using following equations.

$$\varepsilon = \ln \frac{h}{h_i}, \tag{2.1}$$

$$\sigma = \frac{F}{S},\ with\ S = \pi \frac{{d_i}^2}{4} \times \frac{h_i}{h}, \tag{2.2}$$

where h and h_i are the current and initial sample height, respectively. F is the axial force, S the actual sample surface and d_i the initial diameter.

Correction of set-up stiffness Macroscopic true strain computed using equation 2.1 is corrected to take into account the set-up stiffness. If we estimate that the displacement due to set-up deformation (u) is linear with the applied force, we can derive the following equations:

$$K = \frac{F_{max}}{u}, \tag{2.3}$$

$$u = \Delta h_{eff} - \Delta h_{instr}, \tag{2.4}$$

$$\Delta h_{eff} = h_i - \left(h_{f,meas} + \delta h_{th}\right), \tag{2.5}$$

$$\Rightarrow K = \frac{F_{max}}{h_i - \left(h_{f,meas} + \delta h_{th} + \Delta h_{instr}\right)}. \tag{2.6}$$

ε_{local}	**0.01 s^{-1}**			**0.1 s^{-1}**			**1.0 s^{-1}**		
450°C	0.65	1.0	1.35	0.65	1.0	1.35	0.65	1.0	1.35
550°C	0.65	1.0	1.35	0.65	1.0	1.35	0.65	1.0	1.35
650°C	0.65	1.0	1.35	0.65	1.0	1.35	0.65	1.0	1.35

(a) Hot compression with equiaxed microstructures.

ε_{local}	**0.01 s^{-1}**			**0.1 s^{-1}**			**1.0 s^{-1}**		
450°C	0.65	1.0	1.35	-	-	1.35	-	-	-
550°C	-	-	1.35	0.65	1.0	1.35	-	-	1.35
650°C	-	-	-	-	-	1.35	0.65	1.0	1.35

(b) Hot compression with lamellar microstructures.

Holding time (s)		**0.1 s^{-1}**						**1.0 s^{-1}**					
650°C	**0.65**	-	-	-	-	-	-	7	12	25	50	100	200
	1.35	7	12	25	50	100	200	7	12	25	50	100	200

(c) Hot compression and holding at temperature with equiaxed microstructures.

Holding time (s)		**0.1 s^{-1}**				**1.0 s^{-1}**			
650°C	**0.65**	-	-	-	-	12	25	50	100
	1.35	12	25	50	100	12	25	50	100

(d) Hot compression and holding at temperature with lamellar microstructures.

Table 2.7: Description of the thermomechanical conditions of the hot compression campaigns.

	h_i (mm)	ε 0.65	1.00	1.35
	14.0	9.52	8.01	6.50
h_f (mm)	10.0	6.41	5.19	3.98
	9.0	5.74	4.61	3.48

Table 2.8: Final height targets for the three geometries and final strain levels.

In previous equations, Δh_{eff} is the effective height difference of the sample before and after compression. It is computed by subtracting to h_i the following terms: $h_{f,meas}$, the measured final height of the sample after quenching and δh_{th} the thermal expansion. Δh_{instr} is the displacement measured by the sensors and F_{max} is the maximal force applied, at the end of the testing. One must keep in mind that this method for estimating the set-up stiffness relies on the approximation that u is only caused by linear deformation of the set-up. Consequently, it remains less precise than running a compression test without any sample in order to record the deformation of the set-up. Nevertheless, because of the brittle behavior of the ceramic dies, our set-up does not allow that kind of procedure. At the end, K is estimated for each experiment. The average K value is equal to 80 $kN.m^{-1}$. This value is close from the technical specifications of the manufacturer. The values obtained for some experiment are far from the average value. This highlights the high sensitivity of this estimation method to various uncertainties. Using the value of K, the displacement and finally true strain can be corrected. An example of the influence of this correction is presented in figure 2.8. The impact of set-up deformation is limited when using these data for material parameters identification.

Identification of friction coefficient Several methods are available to evaluate friction during hot compression tests. In this study, two inverse analysis methods are applied [173, 174]. They both rely on measuring final sample width at different positions to compute a bulging parameter. The results obtained with the parameter proposed by Roebuck [174] show unrealistic values of friction coefficients. Consequently, the method described by Nicolaÿ [173] is preferred. The parameter used to quantify sample bulging is computed thanks to following equation:

$$B_{\mathrm{N}} = \frac{d_t + d_b}{2d_c}, \tag{2.7}$$

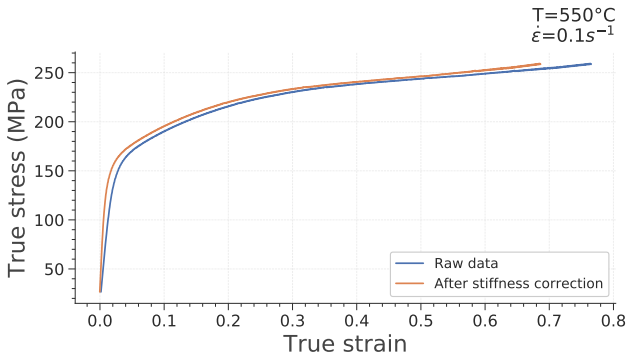


Figure 2.8: Effect of stiffness correction on flow curve.

where d_t, d_b and d_c designate the sample diameter at the top, bottom and at mid height, respectively. The first step of the procedure consists in establishing a relationship between the friction coefficient and the two bulging parameters. To do so, simulations using various friction coefficient (f_C) values are run and a correlation is established between f_C and B_N. Values of B_N obtained from simulations are plotted and fitted using 3^{rd} degree polynomials. This step is illustrated in figure 2.9.

Then, using these fitted functions, values of f_C^{exp} are estimated from the values of B_N^{exp}. Based on the 27 hot compression tests performed on samples with equiaxed microstructure, the average friction coefficient values and standard deviation are respectively estimated as: $\overline{f_C} = 0.24$ and $\sigma_{f_C} = 0.12$. The high standard deviation associated with this estimation highlights that uncertainty is significant. This is illustrated by figure 2.10. The uncertainty remains reasonable and reducing it is difficult. Indeed, even if diameter measurement is done using an optical comparator to limit the error, the precision is limited to 0.1 mm. Moreover, deformed samples are not fully axisymmetric due to the anisotropy of Zy-4 mechanical behavior.

Correction of the local final strain Because of some equipment limitations, of the error related to the initial upper die zero position and of some friction variations, the final effective sample height h_f is not perfectly equal to the prescribed one and varies from one test to the other. Thus, the hot compression simulations are used to get a better estimate of the local strain at the center of the sample. The simulations are run using the average friction coefficient value estimated previously ($\overline{f_C} = 0.24$). The results are gathered in table 2.9. The final height variations between two samples having the same initial height and being deformed at the same prescribed deformation level are small. Since the uncertainty on f_c plays a significant role on the predicted local strain, it is not significant to present precise values individually for each sample. The differences between samples with $h_i = 14.0$ mm and $h_i = 9.0$ mm or $h_i = 10.0$ mm are sig-

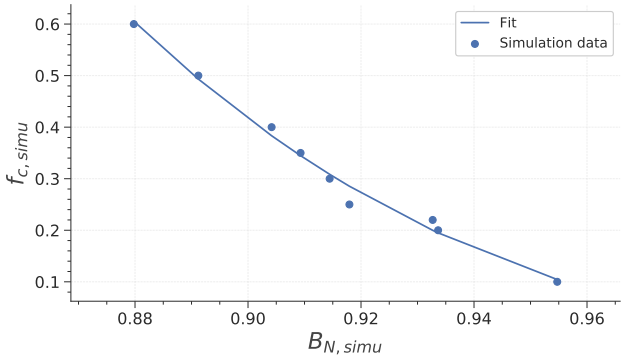


Figure 2.9: Evolution of friction coefficients as function of geometrical parameters.

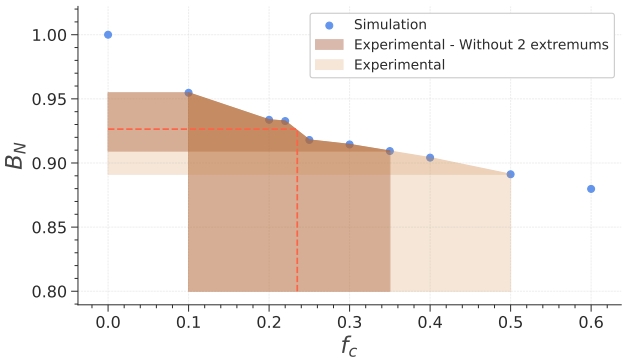


Figure 2.10: Evolution of B_N with f_C. The two zones in light brown present the ranges of measured experimental data and the corresponding identified friction coefficient values. The dashed orange line represents the average value.

nificant. These differences are addressed later on, in regards of the microstructure characterization results presented in section 6.1.

Sensitivity analysis The simulation results can be used to estimate the impact of experimental or observation parameters. In the following, the error made when preparing the sample and selecting the observation zone in EBSD is evaluated first. Then, the influence of friction over the thermomechanical conditions experienced by the observation zone is estimated.

To quantify the error over the thermomechanical history made when an observation zone is selected, several sensors are positioned at positions around the exact sample center. Their final position are presented in figure 2.11. The origin of the coordinate system is the center of the sample. Initial sample dimensions are the following: $d_i = 9.95\ mm$; $h_i = 14.0\ mm$.

Two plots are displayed in figure 2.12 and illustrate how an error made on the observation zone location can impact the thermomechanical history seen by that zone. Figure 2.12a describes the relative error that would be made if the observation zone is located at $X_f = 0.82\ mm$, $Y_f = 0.37\ mm$ from the sample center. That particular position is presented here since it is a realistic value of

h_i (mm)	$\varepsilon_{local}^{eff}$
14.0	0.45
10.0	0.55
9.0	0.55

(a) $\varepsilon_{local}^{target} = 0.65$

h_i (mm)	$\varepsilon_{local}^{eff}$
14.0	0.75
10.0	0.9
9.0	0.9

(b) $\varepsilon_{local}^{target} = 1.0$

h_i (mm)	$\varepsilon_{local}^{eff}$
14.0	1.0
10.0	1.2
9.0	1.2

(c) $\varepsilon_{local}^{target} = 1.35$

Table 2.9: Effective local final strain for the three geometries and target local final strains.

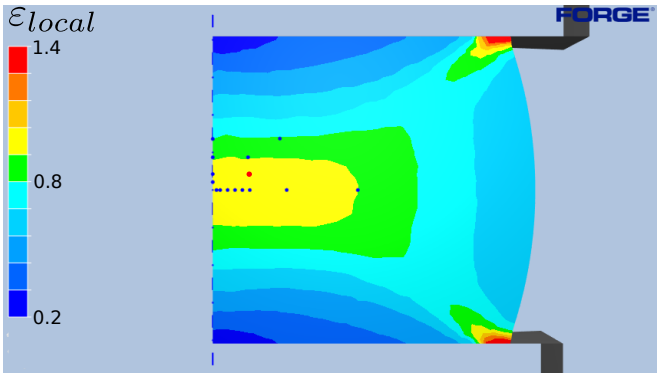
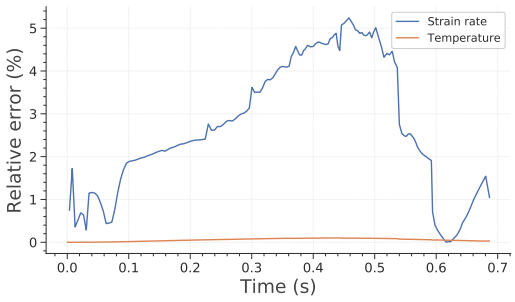


Figure 2.11: Sample state after hot compression ($T = 650°C$; $\dot{\varepsilon} = 1.0\ s^{-1}$; $\varepsilon = 0.6$). Blue points indicate the final position of the sensors. The red point indicates the final position of the sensor corresponding figure 2.12a. The color scale indicates the local final strain.

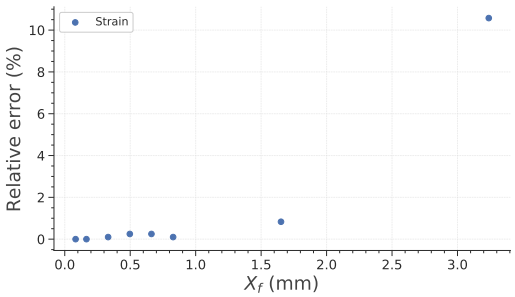
the maximal error made by the experimenter when the sample is cut and the observation zone is set in the microscope chamber. The distance along radial direction (X_f) is twice the one along the vertical direction (Y_f). This choice is motivated by the fact that the error over X_f is also affected by the cutting process. Figure 2.12a points out that the relative error over thermomechanical conditions is limited. Figure 2.12b shows that the error over the local final strain becomes significant only when the distance from the center along radial direction is greater than 2.0 mm. Based on these results, one could conclude that the error due to imprecision during cutting or positioning is limited.

Thermomechanical simulations are used to evaluate the impact of friction over the thermomechanical conditions at the center of the sample. Main results are plotted in figure 2.13. They highlight that friction has a high impact over local strain and strain rate. Consequently, a special attention to conserve the same lubrication conditions between experiments is paid.

From the results of the macroscale simulations of the hot compressions presented above, it is possible to conclude that the strategy of combining macroscopic results (such as stress strain curves) and local results (such as EBSD results) is relevant. Nevertheless, a preliminary study should be done properly to ensure that the range of conditions investigated, the sample geometry and the position of the observation zones are suited for such analysis. In the present case, the results confirmed that the temperature elevation and the strain rate variations should be taken into account to improve the precision of the analysis.

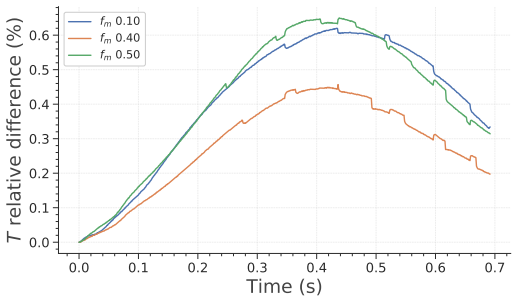


(a) Relative error over strain rate and temperature versus time for an observation zone with the following coordinates: $X_f = 0.82\ mm,\ Y_f = 0.37\ mm$.

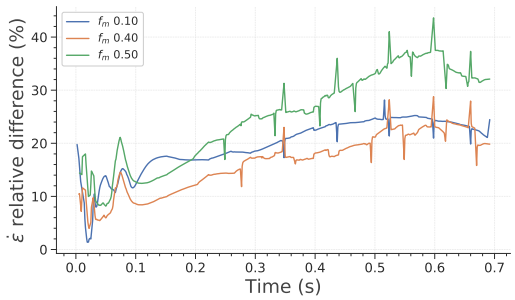


(b) Relative error over strain versus distance from sample center along radial direction (X).

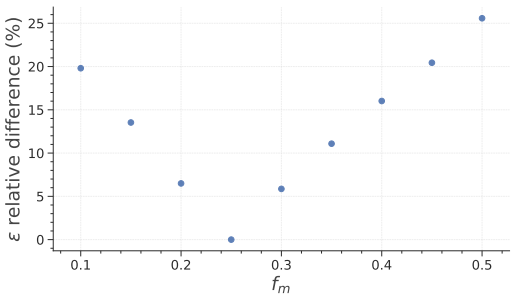
Figure 2.12: Influence of observation zone position over local thermomechanical conditions.



(a) Relative difference over temperature versus time. Differences are computed against conditions for $f_m = 0.25$.



(b) Relative difference over strain rate versus time. Differences are computed against conditions for $f_m = 0.25$.



(c) Relative difference over local strain versus f_m. Differences are computed against conditions for $f_m = 0.25$

Figure 2.13: Influence of friction over the local thermomechanical conditions experienced.

2.4 Microstructure characterization

Since there are a large number of samples, the number of characterization techniques are kept small. Three methods are used: optical microscopy under polarized light (OM-PL), electron backscattered diffraction (EBSD) in a scanning electron microscope (SEM) and transmission electron microscopy (TEM).

2.4.1 Sample preparation

Two sample preparation procedures have been established depending on the characterization technique. To observe samples using EBSD technique, one must be sure the preparation procedure is optimized to limit the formation of scratches, avoid any hardening and get a perfectly flat surface. For characterization of Zy-4 samples, the optimized procedure follows the subsequent steps:

- cutting of the samples following a plane that includes the revolution axis of the cylinder (see figure 2.14).
- Removal of the oxide layer around the sample by manual polishing with coarse grinding papers. This step is required to avoid any contamination within SEM chamber and to improve the electrical contact between the sample and the stage during the experiment.
- Sample surface polishing with first grinding papers and then a polishing solution that contains diamond particles with a size of 15 nm (noted DCS15 in following table). The parameters of all these steps are given in table 2.10.
- Electro-polishing using a solution of 90% methanol and 10% perchloric acid. Voltage is set equal to 25 V, polishing is performed during 27 s at a temperature between 5 and 10$°C$.

The thickness of one sample is measured before and after the surface preparation protocol. The removed thickness is estimated to be equal to 0.45 mm. This thickness is added to the sample radius before the cutting step. In doing so, the observation zone is effectively located at the sample center.

To observe samples with OM-PL technique, similar surface quality measurements are required. However, the observation techniques requires the presence of

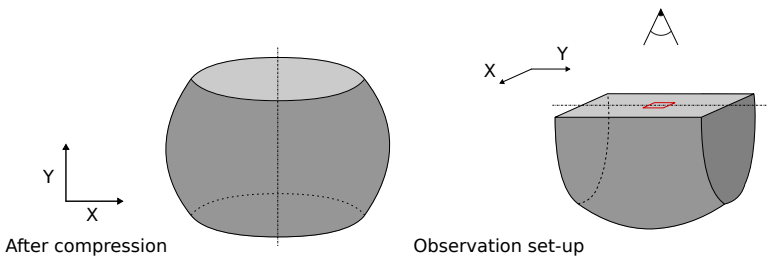


Figure 2.14: Representation of sample handling.

Step number	Abrasive type	Head rotation speed (RPM)	Stand rotation speed (RPM)	Applied force (N)	Duration (s)
1	Grinding paper P320	250	150	17	60
2	Grinding paper P600	250	150	17	60
3	Polishing cloth + DCS15	180	100	17	360
4 (OM-PL)	Polishing cloth + OPS-H_2O_2-HF	150	80	17	600
4 (EBSD)	Electro-polishing	90% methanol, 10% perchloric acid $U = 25\ V$, $dt = 27\ s$ and $5 < T < 10°C$			

Table 2.10: Parameters of the different polishing steps performed before observation. The two last steps, in grey, are used depending on the observation technique.

an oxide layer on top of the surface sample. Therefore, electro-polishing step is replaced by a last polishing step performed using a solution composed of 7 mL of OPS colloidal silica, 3 mL of H_2O_2 and 5 to 10 droplets of hydrofluoric acid (HF).

2.4.2 Measurement of grain size distribution using OM-PL and image analysis

Acquisition of OM-PL images

To perform optical imaging at CEMEF, an Olympus PMG 3 optical microscope with an Olympus DP 20 camera are used. This experimental equipment allows to perform optical imaging with a spatial resolution up to 0.2 μm. In our case, all images are acquired under polarized light since this allows to increase the contrast between grains. Indeed, because of its crystallographic structure, zirconium α-phase and the oxide layer present on top of the sample surface modify the polarization plane of light, depending on their relative orientation to the slicing plane. Since crystallographic orientation of the top oxide layer is influenced by the orientation of the underlying grain, grains with different crystallographic orientations appear with different colors and/or intensity levels.

By capturing images at various polarization angles, a set of images of the same zone exhibiting different intensity levels for each grain is obtained. This is illustrated in figure 2.15. The proposed method aims to take advantage of these

contrast variations to improve GB detection.

Post-processing of OM-PL images

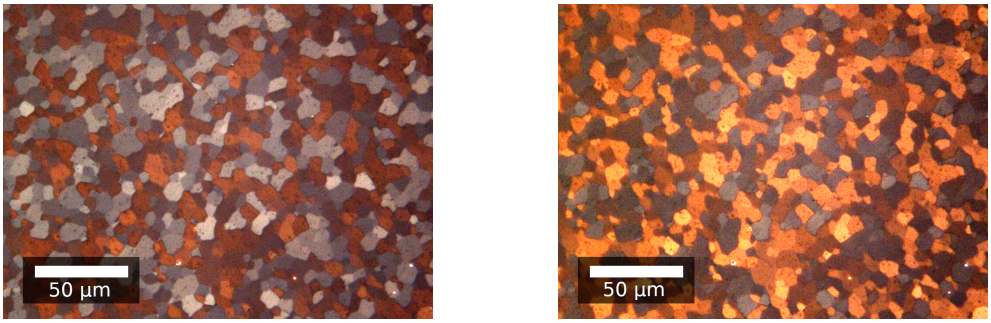
Principle of the technique An image analysis algorithm has been developed to automatically analyze sets of images and get the grain size distribution (GSD). All the tools used are available within the software bundle *Fiji* [175] as built-in functions or additional plugins. In the context of this manuscript, this method is only applied to OM-PL images of Zy-4 samples. However, it is worth mentioning that it has also been applied with success to BSE images of a 304L steel sample [176].

Post-processing method makes use of sharp intensity variations between adjacent grains to detect GB on each image of the original set. As it has been discussed previously, intensity of each grain varies between images (see figure 2.15). Hence, some neighboring grains could exhibit steep contrast variations or not. This method aims to take advantage of this by superposing GB detected for each image. This allows the use of a relatively high detection threshold for contrast variations to limit detection of other features frequently found on experimental images, such as scratches or dust and silica particles.

For each image of a given set, the following steps are completed:

- pre-processing. This step consists in an automatic brightness and contrast adjustment thanks to a user-defined saturation parameter. Then, a denoising operation is achieved using the non-local-means denoising algorithm [177]. Auto-estimation of denoising parameters has proven to give satisfactory results.

- Detection of grain boundaries. This operation is realized by applying a Sobel edge detector filter. This allows to detect abrupt intensity variations in the image, such as the ones at grain boundaries between two grains presenting different intensity levels. In this step, some additional image processing



(a) Polarization condition A. (b) Polarization condition B.

Figure 2.15: Example of typical images obtained using OM, under polarized light, close to extinction conditions.

is necessary in order to provide a suitable image for the next processing operation. This includes the use of a mean filter, which permits to avoid over-segmentation later on. A morphological segmentation of grains is then realized. Segmentation is performed thanks to the library MorpholibJ [178] and is based on watershed transform.

Because input images are RGB pictures, the channels are initially split and all the operations described above are applied to each color channel (red, green and blue). Hence, for each input image, three binary images are obtained with grain boundaries detected in black and all the remaining parts of the image in white. It is therefore necessary to superpose them. This is achieved simply by multiplying all images and performing some erosion and dilation operations to correct any small shift in the position of the GB detected on each image. One should note that this step could slightly affect the position and morphology of the detected grain boundaries on the final resulting image. The main steps described in the paragraphs above are detailed in figure 2.16. Once all these operations have been executed for each input image, GB detected on each image are superposed following the same method detailed for superposing the GB detected on each channel.

Finally, grains are identified and their morphological attributes are measured thanks to the automatic particle counting function available in Fiji [175]. Grains crossed by image boundaries are systematically ignored in this operation.

An overview of the main steps of the image analysis process is outlined in figure 2.17, as well as intermediate results obtained for an PL-OM images of a Zy-4 sample.

Post-processing parameters

To validate the algorithm, the exact same zone is analyzed both by EBSD and OM-PL and a sensitivity study is performed to assess the influence of post-processing parameters. For EBSD orientation data, the effect of the misorienta-

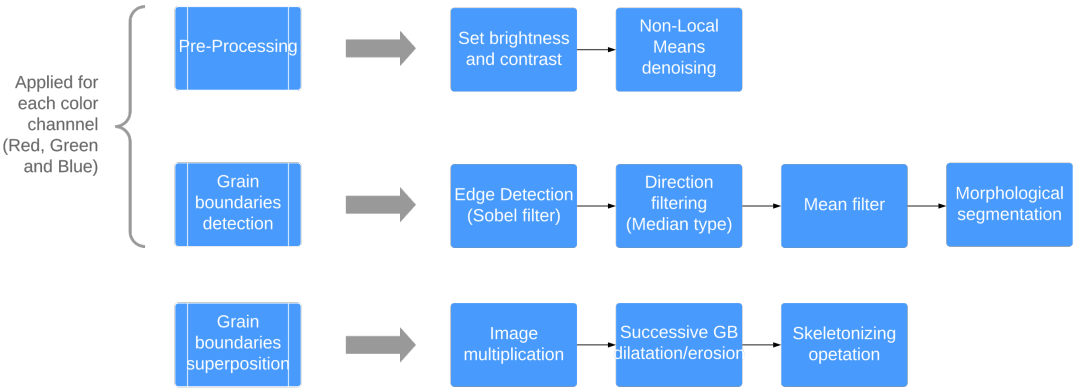


Figure 2.16: Flow-chart detailing main steps of the image analysis method.

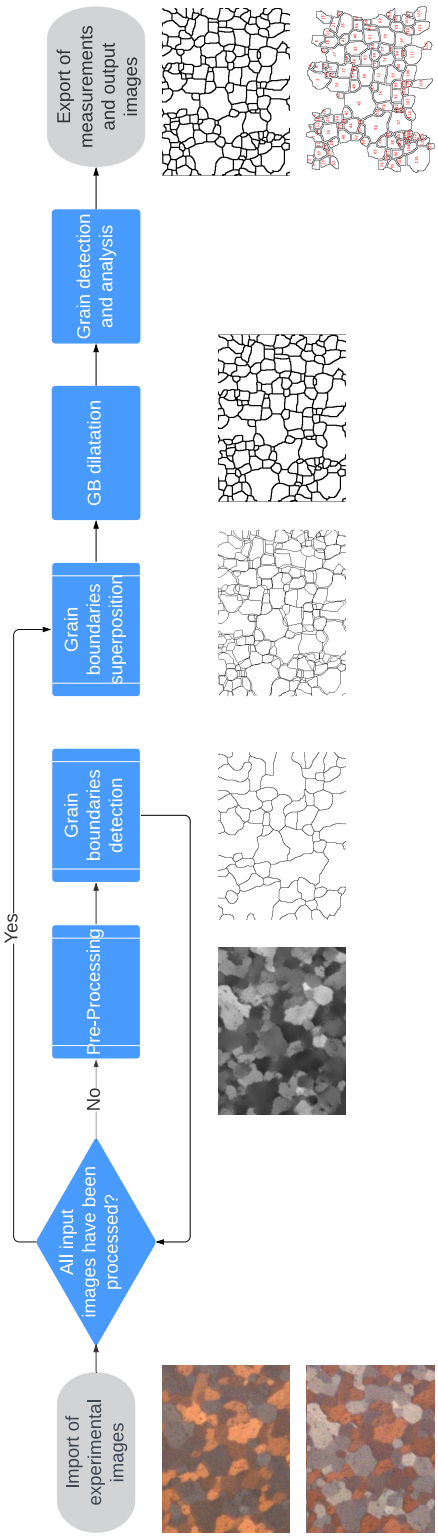


Figure 2.17: Flow-chart illustrating the main steps of the image analysis method. Example images are coming from PL-OM images of a Zy-4 sample.

tion angle threshold selected for GB detection is investigated. Regarding OM-PL data, two key parameters are under study: the number of PL images used and the radius of the mean filter applied before segmentation. These two parameters have been selected because they cannot be automatically optimized and because they depend on the quality of the input images.

The detailed results about the comparison and the sensitivity analysis are described in reference [176]. They confirm the developed method is adequate and enables to define the set of adequate parameters for processing OM-PL images to measure grain size distribution on fully recrystallized samples. The final set of parameters includes:

- the characterization of three zones per sample on **Eq** samples and ten zones per samples on **Wo SPP** samples. Multiples zones are characterized to improve results reliability and provide an estimation of the measurement uncertainty. A larger number of zones is selected for **Wo SPP** samples since initial images have shown a larger dispersion of the grain size distribution, especially at longer holding times.
- The use of two extreme polarization conditions per zone observed.
- Setting a mean filter radius R_m equal to 6 pixels.

Uncertainty is estimated by assuming that the mean grain size measured value on a given zone for a sample follows a normal distribution. Therefore, a 95% confidence interval can be computed thanks to following equation:

$$\left[\overline{ECD} - \frac{1.96\sigma_{\text{ECD}}}{\sqrt{N_{img}}};\ \overline{ECD} + \frac{1.96\sigma_{\text{ECD}}}{\sqrt{N_{img}}}\right]. \tag{2.8}$$

σ_{ECD} is the standard deviation of the $\overline{ECD}$ measured in each zone, $\overline{ECD}$ is the average ECD when all the zones are considered and N_{img} is the number of zones.

2.4.3 Characterization of microstructures using EBSD

Principle

All the SEM characterization techniques are based upon the same principle: scanning the sample surface with an electron beam and measuring one of the signals resulting from the interaction between electrons and the sample. EBSD analysis is based on the analysis of backscattered electrons (BSE) that are diffracted by the lattice. Electrons diffracted by a reticular family form two double cones that intersect a screen. These intersections are defined as Kikuchi bands. The intensity and the thickness of Kikuchi bands vary depending on the diffracting planes. The diffraction pattern formed by all the bands on the EBSD screen are analyzed

to determine the phase and the crystal orientation of the point considered. This step is called indexing and is generally achieved by applying Hough transform. Raw EBSD data describes the orientation and the phase of each pixel

EBSD results are a mine of information. They describe the microstructure topology (grain size distribution, grain shape, ...) and the local misorientation state which can be analyzed to quantify the effects of deformation. Finally, they also measure the local texture which constitutes an important microstructural feature since it conditions the material properties (see 1.1.4 for more details). It should be mentioned here that the texture measured by EBSD can be used to evaluate the evolution of the main texture components but should not be used for detailed analysis. Indeed, the number of grains in the maps is too low to ensure statistical representativity [179].

Angular resolution of EBSD measurement is generally considered to be equal to 0.5° [180]. However, it can be affected by several analysis parameters (pattern resolution, exposure time, number of frame averaged per pixel, ...) and material properties (presence of defects, ...) [181].

Convention and parameters

EBSD analysis are performed using a *Carl Zeiss SUPRA 40* field emission gun scanning electron microscope (FEG-SEM) equipped with a *Bruker Quantax* system (EBSD $e^{-}Flash^{HR}$). Acceleration voltage is set equal to 20 kV and step size to 0.10 μm. The step size is kept constant for all samples and is set sufficiently low to be able to capture local orientation variations such as subgrains that are in general few hundred nanometers wide. Step size is not set lower to keep reasonable acquisition times. Each observation zone dimensions are: 130 μm in width and 85 μm in height. This area contains between 500 and 3000 grains which is enough to ensure representativity [182]. Each map is represented according to the sample reference frame with Y being the compression direction and X the radial one. The standard color code used for attributing colors to orientations is obtained from inverse pole figure color code in which Y axis is projected in standard triangle. The standard triangle corresponds to the crystal axis system reduced thanks to symmetry operations. These two conventions are presented in figure 2.2.

Few EBSD analyses are performed with a higher step size to characterize larger zones. It will be explicitly detailed in the legend of the corresponding figures.

Finally, due to recurrent problems with the SEM, some EBSD maps display abrupt leaps (see figure 5.1 for instance). An analysis on few maps is performed. The maps are cropped to consider areas that do not contain any leap. The differences of recrystallized grain size and recrystallized fraction between original and cropped maps are limited to 5%. Thus, these maps are considered as usable in the following investigations.

Post-processing

EBSD data are processed using MTEX toolbox developped on MATLAB [183]. An automated routine is developed to do in-depth post-processing on a large number of EBSD data. Several post processing parameters must be defined to ensure that the post processing is relevant and the results are meaningful.

Grain identification parameters Since EBSD results can present a significant level of noise, isolated indexed points must be filtered out. This is done by setting a minimal number of 10 pixels per grain. It corresponds to areas that are 300 nm wide. Then, the threshold angle values should be defined for low and high angle grain boundaries (LAGB and HAGB). $\Delta\theta_{\text{LAGB}} = 3°$ and $\Delta\theta_{\text{HAGB}} = 15°$ are set as references. Once grains have been identified, their area are measured by counting the number of pixels. The non-indexed pixels belonging to the grain are considered for that measurement. This measured area is then used to compute the ECD, defined as the diameter of a circle with the exact same area.

Processing operations First, LAGB and substructures can be retrieved by:

- using the built-in method that allows for reconstruction of internal substructures,
- identifying both grains and subgrains at first, using $\Delta\theta_{\text{LAGB}}$ as a unique threshold value. Then, HAGB are identified by looking at misorientation angle of all boundaries and the ones exhibiting $\Delta\theta \geq \Delta\theta_{\text{HAGB}}$. Finally, subgrains and grains can be discriminated by defining a subgrain as an entity with at least half of its boundaries being LAGB.

These two methods being complementary, both are used. The second method considers only LAGB enclosing subgrains. Consequently, when it is used for measurement of LAGB length, the LAGB length is explicitly defined as closed LAGB length.

To investigate more in details local misorientations, several parameters can be computed:

- the grain orientation spread (GOS). It is computed by averaging over all the pixels of the considered grain, the disorientation to the average grain orientation.
- The kernel average misorientation (KAM) and its average per grain (grain average KAM, $GAKAM$). KAM is pixel dependent whereas $GAKAM$ is constant per grain. The KAM and GAKAM are defined thanks to following equations:

$$KAM_i = \frac{1}{N_i} \sum_{j \in V_i} \Delta\theta\left(i,j\right), \tag{2.9}$$

$$GAKAM_k = \frac{1}{n_k} \sum_{l \in G_k} KAM_l. \tag{2.10}$$

i is the index of the pixel of interest, N_i the number of its neighboring pixels and V_i the set of its neighboring pixels. k is the index of grain of interest, n_k the number of indexed pixels of the grain k and G_k all the indexed pixels belonging to the grain. The default KAM order is one, which means only the first order neighbors are used in the computation.

Grain properties, such as $GAKAM$ or GOS, are averaged by the number of indexed pixels belonging to the grain of interest.

Finally, some filtering operations can be applied to reduce noise but also to fill missing data [184]. In this study, a half quadratic filter is applied before any post-processing operation to reduce the noise. If data are used as input for simulations, a filling operation is applied. To do so, missing orientation data at non-indexed pixels are interpolated using the half quadratic filter.

Discrimination of recrystallized grains If we refer to the original definition, recrystallized grains are zones surrounded by HAGB that are dislocation-free [18]. EBSD data can be used to estimate geometrically necessary dislocation (GND) density. GND are dislocations that are required to accommodate lattice rotations linked with deformation [185, 186]. From that definition, it appears reasonable to deduce that the most appropriate way to identify recrystallized grains is to set a threshold based on the average GND density. However, the computation of GND density is significantly affected by the chosen step size and the measurement noise. Therefore, some other simpler grain properties related to intragranular misorientations can be used to discriminate recrystallized grains. The different criteria considered in the present study are the following ones:

1. $GOS \leq 3.0°$ [187],
2. $GAKAM \leq 0.4°$ and $GOS \leq 3.0°$,
3. $\tilde{\rho}_{\text{LAGB}} = \dfrac{L_{\text{LAGB}}}{A_{\text{G}}} \leq 0.4\ \mu m^{-1}$, with L_{LAGB} and A_{G} the LAGB length and grain area, respectively,
4. $\rho_{\text{GAGND}} \leq 1.0 \times 10^{14}\ m^{-2}$.

In the equations detailed above, ρ_{LAGB} is a grain property which is computed as the total length of LAGB inside the grain divided by the grain area. It allows to quantify the length of LAGB per grain. ρ_{GAGND} designates the GND density averaged per grain. To ensure the best consistency with the criterion applied to simulation data, ρ_{GAGND} is computed by omitting the subgrain boundaries. Indeed, in simulation, the dislocations that have recovered and formed subgrain boundaries are subtracted from the total dislocation density (see equation 3.1).

For each of these criteria, selection of a threshold value is performed by the user based on surface weighted histograms and on an incremental procedure. In materials experiencing DDRX, a clear distinction between nucleation and growth phases of DRX grains is observed. Therefore, one could expect to clearly observe

two grains populations, one composed of small recrystallized grains with really low dislocation density and another one of larger grains with high dislocation density inherited from deformation. However, since Zy-4 is prone to CDRX, the microstructure contains a wide variety of grains which makes the exercise of setting a threshold value much more complex.

To propose a thorough analysis, the criterion selection among those defined previously is motivated by two points. First, it should enable to set a unique threshold value to discriminate recrystallized grains as precisely as possible, on all EBSD maps. Second, the criterion must be insensitive to grain features that are not related to deformation. Following that second rule, one could already downgrade the criteria $n°1$ and $n°3$. GOS is directly affected by the grain size and setting a threshold on its value alone makes difficult the discrimination of small deformed grains. Criterion $n°3$ is also downgraded since the ability to form LAGB is not only affected by the grain deformation state but also by many parameters impacting recovery, such as the nature of dislocations created.

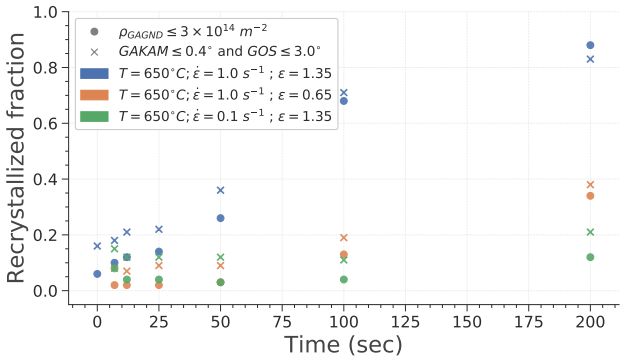
Finally, the two remaining criteria are the criteria $n°2$ and $n°4$. The results given by both on **Eq** samples after hot compression followed by a heat treatment are presented in figure 2.18a. The results show that both criteria present a good agreement in terms of trends and general kinetics. They point out that the coupled criterion based on $GAKAM$ and GOS tends to overestimate slightly the recrystallized fraction compared to the $GAGND$ criterion. It is also worth mentioning that at first instant, when recrystallized fraction is lower than 20%, the two criteria show significant discrepancies. This is due to several factors. Microstructure is more deformed and thus EBSD maps present lower indexed fraction. Recrystallized grains are more difficult to discriminate since they are often still partly bounded by LAGB and could present some remaining dislocations. Figures 2.18b and 2.18c illustrate these explanations. They also point out that both techniques certainly overestimate a little the recrystallized fraction by identifying as recrystallized a number of small grains that are very close to the threshold values.

Uncertainty over recrystallization measurements by EBSD

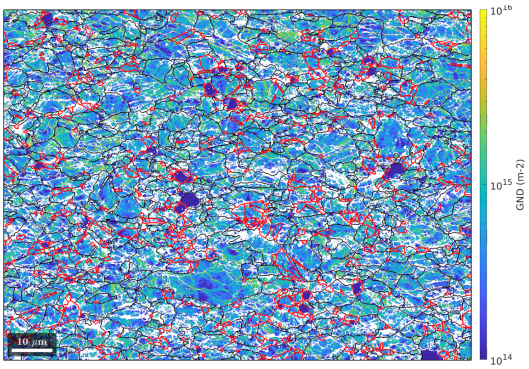
Providing an estimation of the uncertainty associated with EBSD measurements is complex since results are affected by features inherent to the material investigated, the acquisition parameters and the post-processing routines. Among the features related to the material of interest, the most significant are the deformation state, including the variability inherent to material heterogeneities and the surface state resulting from the sample preparation procedure.

The aim of this section is to provide a reasonable estimation of uncertainty over various microstructural features to help the discussions relying on experimental results. However, it does not pretend to provide a precise computation of uncertainty since this would require a dedicated thorough study.

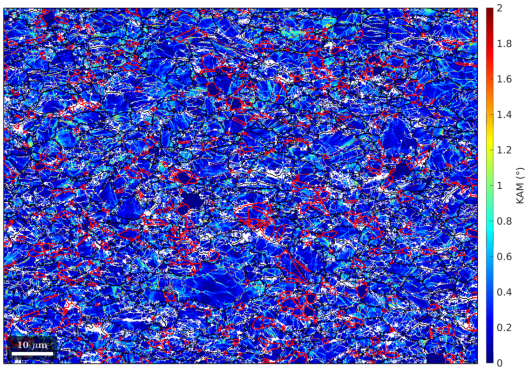
For the sake of clarity, uncertainty will not systematically be displayed when several datasets are plotted on the same graph.



(a) Recrystallized fraction versus holding time. The recrystallized fraction is computed from the two criteria selected earlier.



(b) GND map with grains identified as recrystallized surrounded by thick red boundaries. Based on the GAGND criterion.



(c) KAM map with grains identified as recrystallized surrounded by thick red boundaries. Based on the coupled GAKAM-GOS criterion.

Figure 2.18: Comparison of the two criteria for discrimination of recrystallized grains.

Uncertainty over recrystallized fraction Two contributions to uncertainty are considered here: the criterion set for identification of recrystallized grain and the one related to microstructure variability. Regarding the recrystallization criterion, ranges of acceptable threshold for the two criteria discussed in previous sections are defined. The range of recrystallized fraction obtained, when combining both criteria, displays an average uncertainty of recrystallized fraction of approximately ±10%.

Based on the large quantity of the results obtained during the different experimental campaigns, it is possible to conclude about the influence of thermomechanical conditions and initial microstructure upon uncertainty. First, it decreases with holding at temperature. Second, it is higher for microstructures presenting higher degrees of deformation heterogeneities. Consequently, uncertainty is higher for lower deformation levels and quenched microstructures. A more detailed discussion over microstructure heterogeneities is provided in section 6.1. These observations suggest that ±5% and ±15% constitutes a realistic estimation of the average uncertainty related to material variability, for **Eq/BW** and **PP** initial state, respectively.

To be conservative, the two uncertainties are summed and the absolute uncertainty is equal to ±15% or ±25%.

Uncertainty over GND density According to the equation presented in ref. [188], the uncertainty over GND density due to noise is equal to $3 \times 10^{14}\ m^{-2}$ with the parameters selected. To complete this estimation, an alternative strategy is used within this study. A subset of an EBSD map is taken by selecting randomly 75% of the indexed pixels and considering the others as not indexed. The average GND density measured over this subset is equal to $8.5 \times 10^{14}\ m^{-2}$ whereas it is equal to $10^{15}\ m^{-2}$ for the original dataset. This provides a relative uncertainty of 15%. This value is relatively consistent with the previous estimation.

Uncertainty over $\overline{ECD}$ The same statements apply to the measurement of $\overline{ECD}$ and $\overline{ECD}$ of recrystallized grains ($\overline{ECD}_{rx}$). The following uncertainty contributions are considered:

- HAGB disorientation threshold. Based on the study presented in [176], it is estimated to ±3%.
- Microstructure variability. Based on two EBSD maps realized on the same sample with a **PP** structure and having the maximum variability, a consistent estimate for $\overline{ECD}$ error caused by sample variability is: ±12%.

The global relative uncertainty over $\overline{ECD}$ is taken equal to ±15%.

One additional contribution should be taken into account for $\overline{ECD}_{rx}$: the error associated to discrimination of recrystallized grains. Following the same principle as for recrystallized fraction, $\overline{ECD}_{rx}$ with the different criteria and threshold values are compared. This leads to an estimation of ±5%. The total relative uncertainty is approximately ±20%.

Uncertainty over $f_{\mathbf{lagb}}$

- Disorientation threshold for detection of LAGB. By testing a disorientation threshold for LAGB detection from 2° to 3°, the average error is equal : ±5%.

- Microstructure variability. Based on two EBSD maps realized on the same sample for a PP having the maximum variability, we can provide an estimation of this uncertainty: ±2%

By summing these contributions, the confidence interval becomes: ±7%.

2.4.4 SPP characterization by TEM

SPP present in Zy-4 samples are small ($\overline{D}_{\text{SPP}} \approx 100\ nm$). Therefore, OM and SEM are not the most appropriate techniques since 100 nm is lower or equal to their spatial resolution. Some specific surface preparation protocols, generally involving an etching of the surface, enables SPP observation by SEM or OM by consuming preferentially the matrix or the SPP. Nevertheless, this is not suited to measure the size of SPP since the etching creates some surface roughness which impacts the image observed and then the measurement. Consequently, TEM constitutes a method of choice since it benefits from a higher spatial resolution [189]. As SEM, it relies upon an electron beam to characterize materials. However, in the conventional mode used here, the beam is focused over the whole observation zone and the signal collected is the transmitted one. Because electrons must be able to go through the sample, the sample section should be smaller than a few hundreds of nanometers. Since SPP do not have the same chemical composition and crystallographic structure as the matrix, they present different electron absorption properties and therefore exhibit different contrasts.

To characterize SPP by TEM, two thin foils are prepared per sample. They are obtained by the following sequence of operations:

- cutting of a thin sample,

- chemical etching with a diluted solution of HF/HNO_3,

- die-cutting of a zone at the center of the sample,

- electrolytic drilling.

Then, these thin films are observed using a *JEOL 2100F* at a ×80000 magnification. For each sample, images are captured while the number of SPP is lower than 500. Then, SPP size is manually measured using a raster graphics editor (*GIMP*). A TEM image showing precipitates is provided in figure 2.19.

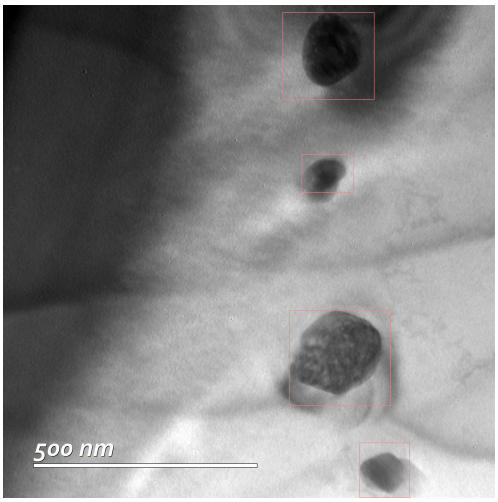


Figure 2.19: Typical TEM image showing the presence of precipitates. The SPP counted are surrounded by a thin pink box.

2.5 Conclusion

This chapter started by describing the five initial states used within this study. The thermomechanical routes used to obtain these samples were detailed. Their impact over initial microstructures was emphasized by displaying the texture and grain topology.

The conditions of the heat treatment and hot compression campaigns were then detailed. The results of hot compression test macroscopic simulations confirmed that it is possible to combine macroscopic results from the hot compression tests as well as local characterization results. Nevertheless, it was pointed out that such strategy requires to consider the impact of self-heating and to correct the strain and strain rates.

Finally, the characterization techniques used were presented. A specific attention was given to describe in details the post-processing of EBSD data. The choice of a threshold criterion for identification of recrystallized grains was discussed and it was established that the one relying upon GND density would be used, since it can be applied to both EBSD and simulation data.

Résumé en français

Ce chapitre est consacré à la description des matériaux et méthodes expérimentales utilisés dans l'ensemble de l'étude. Il décrit les cinq états métallurgiques initiaux et les chemins thermomécaniques utilisés pour les obtenir. Leur influence sur la microstructure initiale est explicitée.

Les protocoles et conditions de traitement thermique et de compression à chaud sont détaillés. Les résultats de simulation à l'échelle macroscopique de ces derniers permettent de faire le lien entre l'échelle locale, au centre de l'échantillon,

et l'échelle macroscopique. Cela confirme que des résultats provenant des deux échelles peuvent être utilisés, à condition de considérer l'impact de ce changement d'échelle sur les conditions thermomécaniques.

Enfin, les techniques de caractérisation sont présentées. Le post-traitement des données EBSD est détaillé. Différents critères pour l'identification des grains recristallisés sont comparés. L'analyse des résultats permet de retenir de préférence un critère basé sur la densité de dislocations géométriquement nécessaires, puisque ce critère est applicable de manière identique aux données expérimentales et de simulation.

Chapter 3

Numerical methods

Within this work, microstructure evolutions are modeled using LS formulations in a FE framework. The basic principles of these methods have been presented in section 1.3.3. The current chapter expands on that and details precisely all the components required to consider all the features impacting recrystallization of Zy-4, by simulation. It starts by presenting the methods used to predict hardening and recovery and the influence of stored energy of deformation over GB kinetics. Then, the strategies used to consider the anisotropy of GB properties and the pinning by SPP are described. Then, since recrystallization of Zy-4 is characterized by the presence of LAGB, two strategies for introducing them into simulations are described. In a second part, an extensive numerical study is carried out to ensure the framework is able to correctly take into account the effect of substructures. The results are discussed, starting with a comparison to results presented in literature and obtained using other numerical methods. Then, the scope is broadened and the influence of various parameters is discussed.

3.1 Level-set framework for simulation of microstructure evolutions

3.1.1 Hardening and recovery

Under hot deformation, dislocation density varies locally due to hardening, recovery and recrystallization. As discussed in sections 1.1.2 and 1.2.3, hardening and recovery are complex phenomena that are affected by various features. To model hardening at mesoscopic scale, crystal plasticity constitutes an interesting solution since it relies upon strong physical assumptions. It predicts the formation of intergranular and intragranular dislocation density gradients by relating the relative grain orientation to the macroscopic stress state. A CP-FEM method is already available within the current framework thanks to recent works by Ruiz Sarrazola *et al.* [190, 191]. However, CP methods are not suited to our study because they generally cannot achieve high deformation levels without complex FE remeshing procedures and imply strong approximations concerning the activated slip systems. In addition, using a CP model would increase significantly computation time and lead to a reduction of the simulation cases investigated. Consequently, for simulations including a hot deformation stage, an alternative simplified strategy is considered. During deformation, it is assumed that each grain has an average dislocation density ρ which evolves according to the Yoshie-Laasraoui-Jonas equation [192]:

$$d\rho = (K_1 - K_2\rho)\, d\varepsilon, \tag{3.1}$$

with K_1 and K_2 two material constants describing strain hardening and recovery, respectively. They are function of strain rate and temperature. To be able to reproduce to some extent heterogeneous grain deformation, K_1 varies from grain to grain according to a distribution defined using experimental data.

One can deduce from equation 3.1 that:

$$\rho_{sat} = \lim_{\varepsilon \to \infty} \rho = \frac{K_1}{K_2}. \tag{3.2}$$

Making the assumption that for local strain values greater than 1.0, all grains have reached their saturation GND density (ρ_{sat}) and using equation 3.2, it is possible to deduce from experimental grain average dislocation density distribution the K_1 distribution. This hypothesis is justified by the fact that the macroscopic stress reaches a plateau for strain values greater than 0.5.

Identification of $\overline{K}_1$ and K_2 is performed by fitting experimental true stress-true strain curves. To compute the flow stress from the average dislocation density, the Taylor equation is used:

$$\sigma = \sigma_y + M_{\text{T}}\alpha_{\text{T}}\mu b\sqrt{\overline{\rho}}, \tag{3.3}$$

where σ_y is the yield stress, M_{T} the Taylor factor, α_{T} a constant and μ the shear modulus.

A detailed description of the identification procedures, using experimental data, for hardening and recovery parameters as well as for GB properties are given in the following chapters (chapters 6 and 4, respectively).

3.1.2 Interface velocity formulation

As described earlier, GB velocity at mesoscopic scale can be defined as the sum of surface and volume energy effects (see equation 1.5). The term related to capillarity is computed naturally thanks to distance function properties (equations 1.37 and 1.38). The other, related to differences of stored energy across GB, requires a dedicated treatment. Initially, Bernacki et al. [21] proposed to weight the contribution of each grain stored energy by a function of the distance to the GB. This is done using equation 3.4.

$$\overrightarrow{v}_e(x,t) = \sum_{i=1}^{N_d}\sum_{j=1}^{N_d} M_{ij}\chi_i(x,t) f(\phi_i(x,t),l) \times \left[E_j(x,t) - E_i(x,t)\right] \overrightarrow{n}. \tag{3.4}$$

$\chi_i(x,t)$ is the characteristic function of the i^{th} LS function. $\chi_i(x,t) = 1$ inside a grain belonging to the i^{th} LS function and $\chi_i(x,t) = 0$ everywhere else. f is a decreasing function being equal to 1 for $\phi_i = 0$ and 0 for $\phi_i = l$. To limit the number of LS functions, new algorithms have been developed by Scholtes et al. [25]. They notably imply the use of N_d energy fields, that are initialized as: $E_i(x,0) = \chi_i(x,0) \times E(x,0)$. These fields are tracked and updated to ensure they are consistent with the LS functions and the exact location of interfaces. Finally, before computation of GB velocity, a reinitialization is performed and the multiple energy fields are extended in a small contiguous zone to make possible the computation of v_e at each node located in that zone. This strategy enables to consider either stored energy as a homogeneous or heterogeneous field within a grain. Since heterogeneous stored energy per grain could induce high velocity gradients, an intermediate strategy is to average this field at GB vicinity. This methodology has been implemented and discussed by Ilin et al. [193].

As mentioned in section 1.2.2, GB properties are functions of the five GB DOF. Thanks to recent developments [29, 30, 31], the present framework is able to handle fully anisotropic formulation with GB mobility and energy being functions of the five DOF. Such formulation requires detailed data about evolution of GB properties with GB misorientation and inclination. It also necessitates to run $3D$ simulations and to have the adequate experimental database. If these data are not available, some intermediate formulations developed earlier and considering only GB misorientation (i.e. 3 DOF) or disorientation (i.e. 1 DOF) can be used. The main objective of this work is to propose realistic description of LAGB properties. Therefore, based on the GB characteristics presented in section 1.2.2, a simple heterogeneous description of γ and potentially M is required. In that

case, γ is a function of disorientation, $\gamma = \gamma(\theta)$ and M is either considered homogeneous ($M(T)$) or heterogeneous ($M(\theta,\ T)$), depending on cases. This induces the introduction of an additional term for the velocity due to capillarity effect (see eq. 1.5) [29, 30, 31], such that:

$$\overrightarrow{v}_c = -M\left(\overrightarrow{\nabla\gamma}\cdot\overrightarrow{n} - \gamma\kappa\right)\overrightarrow{n}, \tag{3.5}$$

which, using equations 1.37 and 1.38 becomes:

$$\overrightarrow{v}_c = -M\left[\left(\overrightarrow{\nabla\gamma}\cdot\overrightarrow{\nabla\phi}\right)\overrightarrow{\nabla\phi} - \gamma\Delta\phi\overrightarrow{\nabla\phi}\right]. \tag{3.6}$$

Finally, transport equation becomes:

$$\frac{\partial\phi}{\partial t} + \overrightarrow{v}_e\cdot\overrightarrow{\nabla\phi} + M\left[\overrightarrow{\nabla\gamma}\cdot\overrightarrow{\nabla\phi} - \gamma\Delta\phi\right] = 0. \tag{3.7}$$

The weak formulation of previous equation, with $\varphi \in H_0^1(\Omega)$ is defined as:

$$\begin{aligned}\int_\Omega \frac{\partial\phi}{\partial t}\varphi d\Omega + \int_\Omega M\gamma\overrightarrow{\nabla\varphi}\cdot\overrightarrow{\nabla\phi}d\Omega - \int_\Omega \overrightarrow{v}_e\cdot\overrightarrow{\nabla\phi}\varphi d\Omega \\ +2\int_\Omega M\overrightarrow{\nabla\gamma}\cdot\overrightarrow{\nabla\phi}\varphi d\Omega + \int_\Omega \gamma\overrightarrow{\nabla M}\cdot\overrightarrow{\nabla\phi}\varphi d\Omega \\ -\int_{\partial\Omega} M\gamma\varphi\overrightarrow{\nabla\phi}\cdot\overrightarrow{n_{\partial\Omega}}d(\partial\Omega) = 0.\end{aligned} \tag{3.8}$$

M and γ are by definition highly discontinuous since they present positive values in elements crossed by GB and are null in all other elements. To avoid numerical issues during computation of $\overrightarrow{\nabla\gamma}$ and $\overrightarrow{\nabla M}$, a Laplace equation is solved to obtain first order differentiable fields with the correct values at GB [29].

As discussed earlier, this formulation is not the most complete available at that time since some others are able to consider anisotropic grain properties, i.e. that depend on misorientation and on inclination [72]. However, according to the conclusions of the study made by Murgas *et al.* [31], this heterogeneous formulation remains a good compromise between computation costs and prediction of GB kinetic and morphology.

3.1.3 Grain boundary migration

Once GB migration is performed, several operations must be performed. Specific operations are done to eliminate the voids or overlaps created by incompatible kinetics of GB [166]. All the fields that are treated as a grain property, such as the stored energy, are tracked [25]. Finally, the dislocation density of the surface swept by each interface is reset to a low value (ρ_0). If stored energy is considered homogeneous per grain, an averaging operation is performed. Therefore, the dislocation density decreases in grains/subgrains that grow whereas it stays constant for the ones shrinking.

3.1.4 Definition of initial microstructure

Polycrystal generation

Initial microstructures are generated using two methods: immersion of experimental data or generation based on statistics. The first methodology produces a digital twin of the characterized microstructure which presents the exact same grain topology. Various properties can be initialized, such as grain orientation or dislocation density.

When generating an initial microstructure based on statistics, the same properties can be initialized (orientation, dislocation density). To generate the grain topology, a Laguerre-Voronoï algorithm [194] with an optimized sphere packing strategy [195] is used. This enables the generation of a microstructure composed of polyhedral grains representing an equiaxed microstructure. Thanks to that method, the grain size distribution (GSD) of the digital microstructure provides a satisfactory agreement with the prescribed GSD. The grain sizes and the other properties are set to respect a discrete distribution of experimental data. If needed, they can also be set according to typical continuous distribution functions, such as log-normal distribution. In that case, the parameters of the distribution are fitted on experimental results beforehand.

Introduction of SPP

As for polycrystal generation, a population of SPP can be generated by immersing an image or prescribing a discrete or continuous size distribution. SPP generated using a size distribution can be positioned uniformly with the REV or only at GB. Immersion of an image, generally coming from experimental data, is particularly relevant if particle morphology and/or size distribution are highly heterogeneous.

Once the position and size of SPP are defined, remeshing operations are performed to remove finite elements located at SPP positions. By imposing a null Neumann boundary condition at mesh boundaries, the holes representing SPP are naturally exerting a tension on GB that are consistent with the Young-Herring equilibrium for incoherent particles [27, 196].

Recently, a new numerical strategy for SPP consideration has been developed by Alvarado *et al.*. This formulation allows to consider evolutive SPP populations while avoiding to remove finite elements located at SPP position [28].

3.1.5 Generation and evolution of substructures

Generation of a two-levels microstructure

A first method to obtain a microstructure containing substructures is to employ a two-levels generation strategy. The generation algorithm presented in section 3.1.4 is called twice. First, it is used to generate the grain structure in a standard way. Then, it is called again to generate the subgrain structure. The nuclei of

the Voronoï cells located too close to initial GB are removed. Then, LS functions are defined based on those cells.

The generation algorithm is in charge of respecting the prescribed grain and subgrain size distributions. Grain orientations are affected in order to respect a given distribution taken from experimental data obtained on an **Eq LG** sample. Subgrain orientation is computed by applying a specific misorientation to the parent grain orientation, similarly to what has been achieved in ref. [197]. This misorientation distribution is also taken from the subgrain misorientation distribution of an **Eq LG** sample deformed under following conditions: $T = 650°C$; $\dot{\varepsilon} = 1.0\ s^{-1}$; $\varepsilon = 1.35$. Finally, an illustration of such initial microstructure is shown in figure 3.1. The zone at the center that is enlarged is kept for figure 3.6 to improve the readability.

It is worth noting that this method allows to generate various initial configurations and to study in details the influence of topology. As illustrated in section 3.2.1, this enables to enrich the rare existing discussions about the full-field modeling of the evolution of subgrain structures during grain growth [197, 198, 199].

Progressive formation of subgrains

As described in section 1.2.4, under deformation, LAGB network does not evolve only by capillarity growth. Dislocations could rearrange themselves to form new LAGB or accumulate into preexisting LAGB. This last phenomenon is responsible for a progressive increase of LAGB misorientation [18, 87]. To be able to consider these mechanisms, equations from the Gourdet-Montheillet model are implemented [125]. Implementing these equations into the frameworks enables to consider several mechanisms of dislocation density evolution:

- rearrangement into LAGB that bound new subgrains. Subgrain formation is described through following equation [125]:

$$dS^{+} = \frac{\alpha b K_2 \rho d\varepsilon}{\eta \theta_0}, \tag{3.9}$$

  where dS^{+} is the surface of LAGB created. $\alpha = 1 - \exp\left(\frac{D}{D_0}\right)^m$ is a coefficient describing the fraction of dislocations recovered to form new subgrains. D is the grain diameter, D_0 is a grain reference diameter and m is a fixed coefficient. η is the number of sets of dislocations and θ_0 the disorientation of newly formed subgrains.

- Stacking into preexisting LAGB which is modeled according to the following equation [125]:

$$d\theta = \frac{b}{2\eta}(1-\alpha) D K_2 \rho d\varepsilon. \tag{3.10}$$

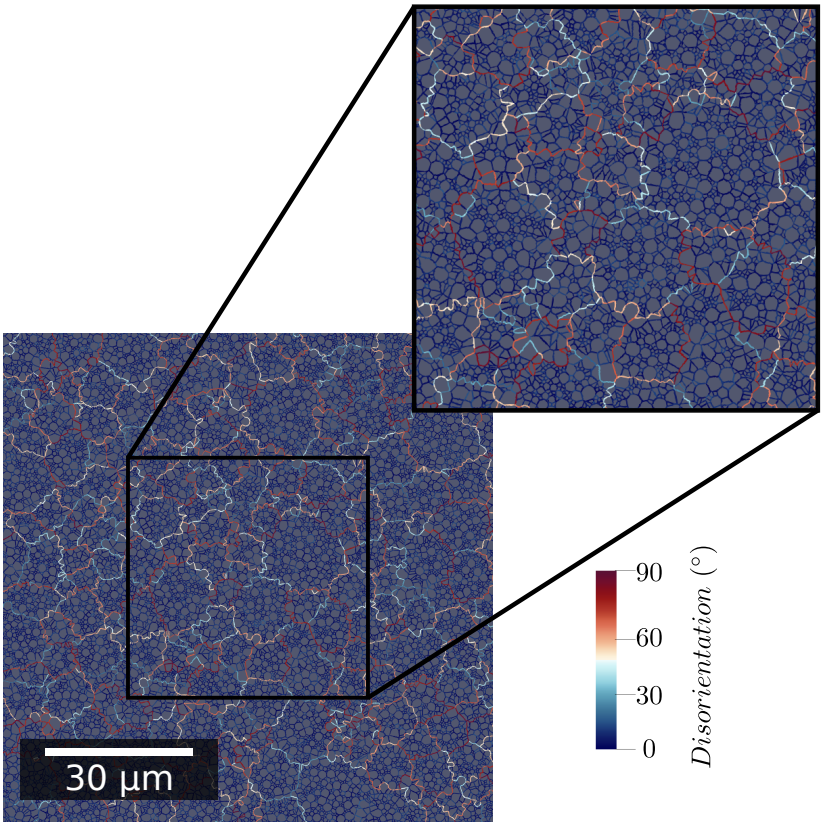


Figure 3.1: Initial microstructure example with color code corresponding to GB misorientation angle.

- Absorption during HAGB migration. This is naturally captured by affecting to the areas swept by moving boundaries a low dislocation density as described earlier.

At each time step, dislocation density of each grain is updated using equation 3.1 which impacts the computation of the velocity term related to stored energy differences. Then, the length of subgrain interfaces formed into each grain is computed using equation 3.9. Depending on the simulation case (see section 3.2.2), subgrains are added grain by grain based on the value of this grain property or globally, after having summed the length of subgrain interfaces for all grains. Subgrain orientation is initialized by applying a small misorientation to the parent grain orientation (similarly to what is described in section 3.1.5). The misorientation angle is selected to respect a distribution measured experimentally whereas the misorientation axis satisfies a uniform distribution. The misorientation axis attributed to a subgrain at its formation is kept constant. Then, during next increments, the misorientation increase described by equation 3.10 is realized by rotating of $d\theta$ around this axis. In addition, to evaluate the influence of subgrain formation localization, a distance from pre-existing boundaries criterion is tested. Therefore, for the cases where this option is enabled, subgrain centers cannot be set closer to pre-existing interfaces than d_{SG}^{f}. This will be discussed in more details in section 3.2.2.

Finally, at each time step, isotropic remeshing is performed to keep a fine mesh around GB and precise description of interfaces [22, 200]. This is illustrated in figure 3.2. All those operations are presented in an algorithmic diagram in appendix B.1.

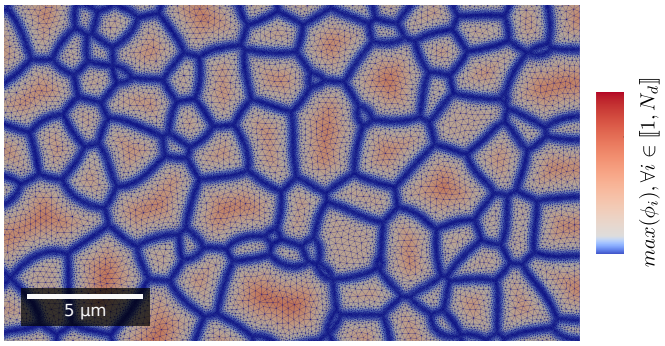


Figure 3.2: Example of a finite element mesh considered in the simulations performed within this study. The color code corresponds to the maximum of level-set functions. The finite element edges are displayed as fine blue lines.

3.2 Validation of the implementations related to substructures

3.2.1 Modeling of GG of a fully substructured microstructure

Influence of microstructure topology

To evaluate the influence of microstructure topology, two different initial microstructures are considered:

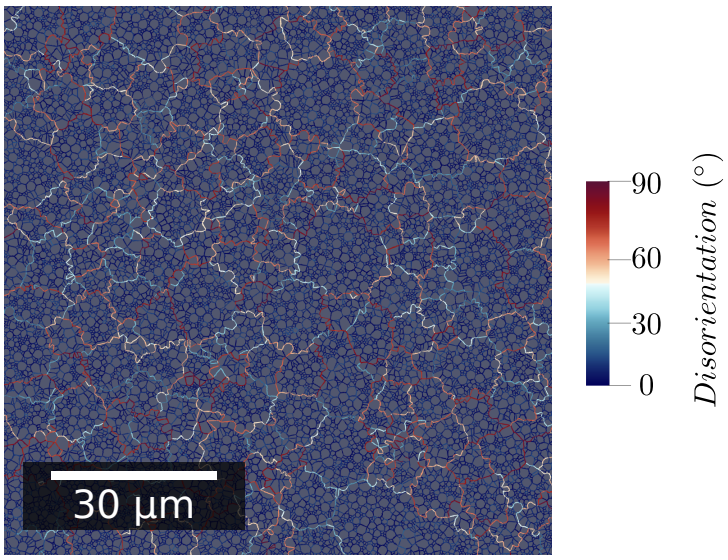
- with subgrains located inside grains using the generation method described in section 3.1.5 (figure 3.3a),
- with LAGB and HAGB evenly distributed throughout the whole RVE (see figure 3.3b).

The first microstructure topology is named in the following discussions as *Standard grain/subgrain topology*. The second is named *No grain/subgrain topology*. The two initial microstructures are presented in the following figure 3.3

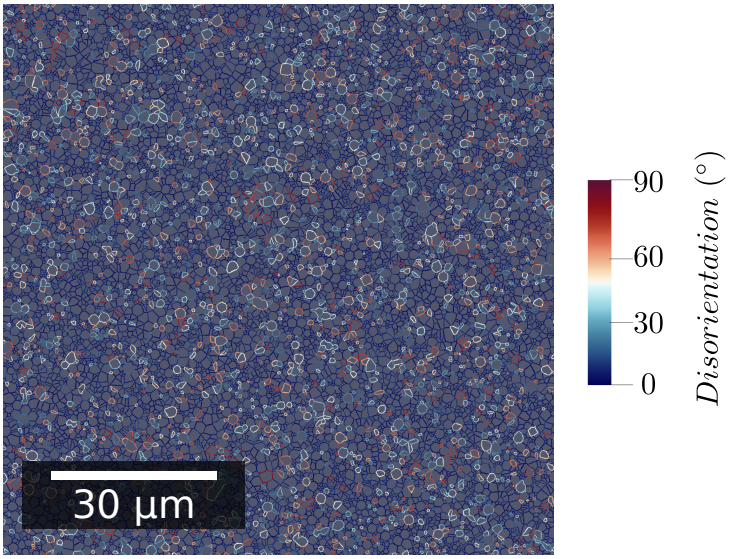
For all simulation cases presented in this section, GB energy is taken heterogeneous and GB mobility is considered isotropic, stored energy due to dislocations is considered negligible (i.e. $v_e = 0$). The RVE area is equal to 0.01 mm^2.

Figures 3.4 and 3.5 point out how spatial correlation of HAGB and LAGB impacts microstructure evolutions. First, it is interesting to note that the absence of spatial correlation decreases grain growth kinetic. This can be explained partly by the fact that grains (i.e. bounded by HAGB) disappear faster when no correlation is assumed (as illustrated in figure 3.5a). Therefore, this leads to lower the global grain growth kinetic since the global system energy is initially lowered much faster. It is interesting to note that this behavior is different from the one expected by Desprès *et al.* [197]. Two reasons can lead to these differences. First, Desprès *et al.* [197] consider subgrains partly bounded by HAGB. Second, initial subgrain distribution is different from our study case, which could also impact the microstructure evolution.

Finally, when considering the influence of spatial distribution of orientations and misorientations, one limitation of this work should be pointed out. Indeed, using the generation method presented earlier, it is not possible to generate subgrains inside a grain presenting gradient of misorientations, a feature which is commonly observed in experiments and which could also impacts the microstructure evolutions. This could for instance lead to speed up the formation of HAGB by the migration of LAGB that could end up in the contact between two subgrains with a disorientation greater than 15°. Nevertheless, this limitation could be overcome by directly immersing experimental data.



(a) Standard grain/subgrain topology.



(b) No grain/subgrain topology.

Figure 3.3: Initial GB network with color code corresponding to GB disorientation.

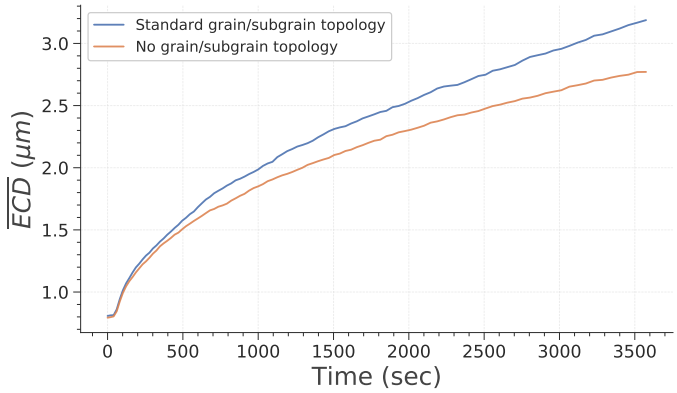
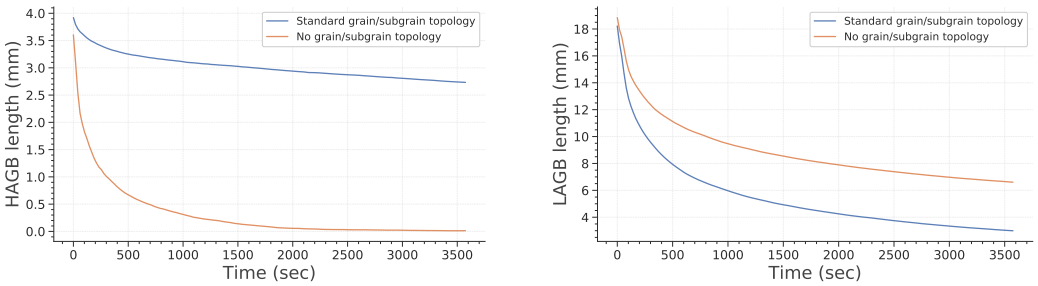
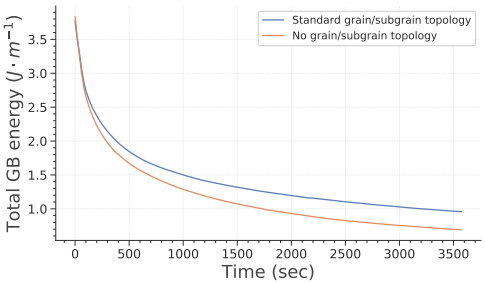


Figure 3.4: Evolution of subgrain $\overline{ECD}$ as a function of time.



(a) Total HAGB length.

(b) Total LAGB length.



(c) Total GB energy.

Figure 3.5: Evolution of GB length and energy with time.

Influence of subgrain parameters

To assess the influence of subgrain parameters, two different initial microstructures are considered:

- with grain and subgrain size distributions taken from experimental data,
- with grain distribution taken from experimental data and a unique subgrain size.

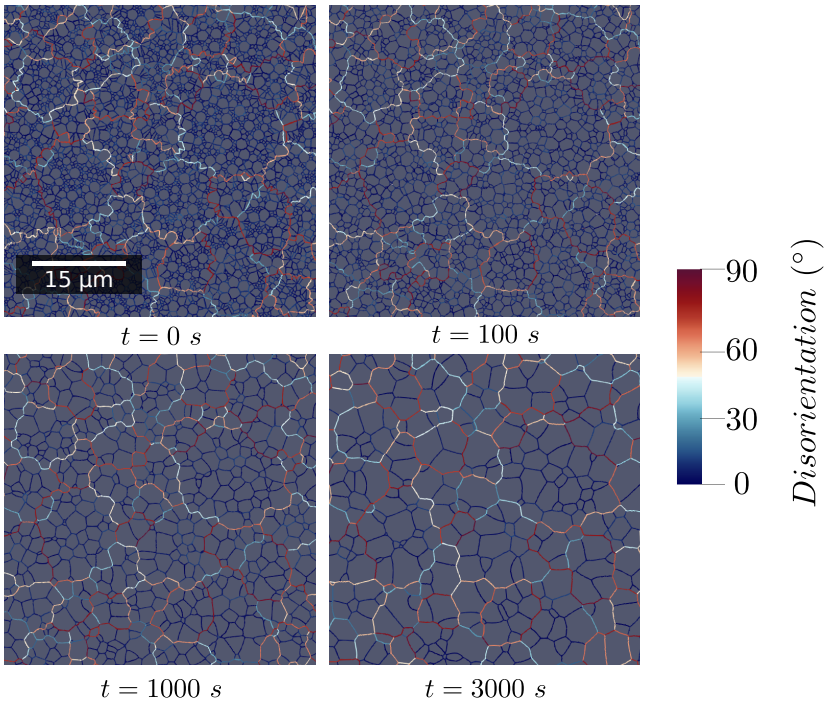
For each of these initial microstructures, two cases are considered in which some material parameters differ:

- GB energy is taken heterogeneous and GB mobility is considered constant,
- GB energy and mobility are both considered heterogeneous, following equations 1.2 and 1.3.

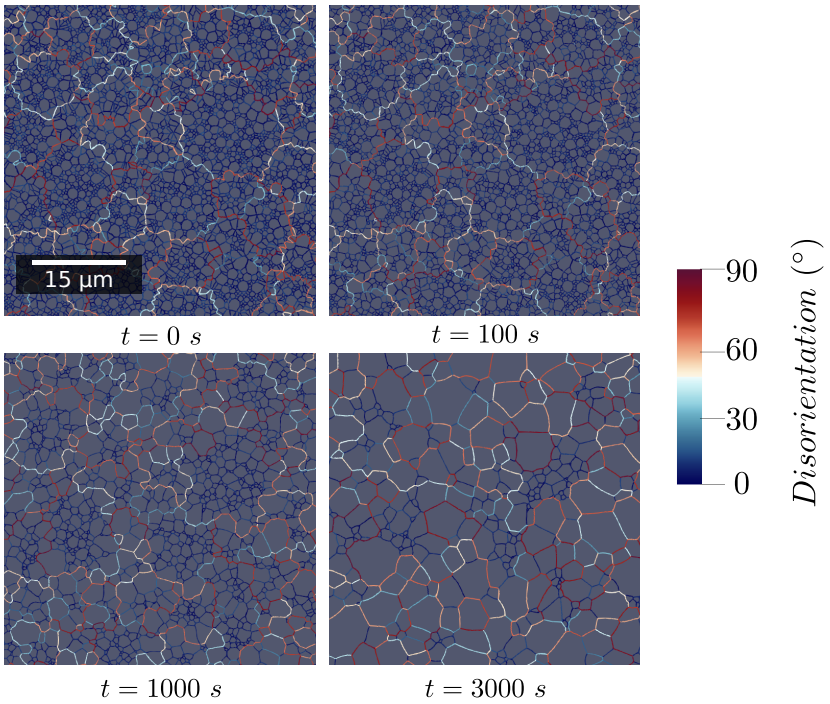
In these cases, the standard grain/subgrain topology is assumed and stored energy is neglected (i.e. $v_e = 0$).

Figure 3.6 presents for each simulation case the GB network in a part of the RVE. Evolution of the whole RVE are available in appendix B.2. This illustrates how microstructure evolves in a noticeable manner in case (d).

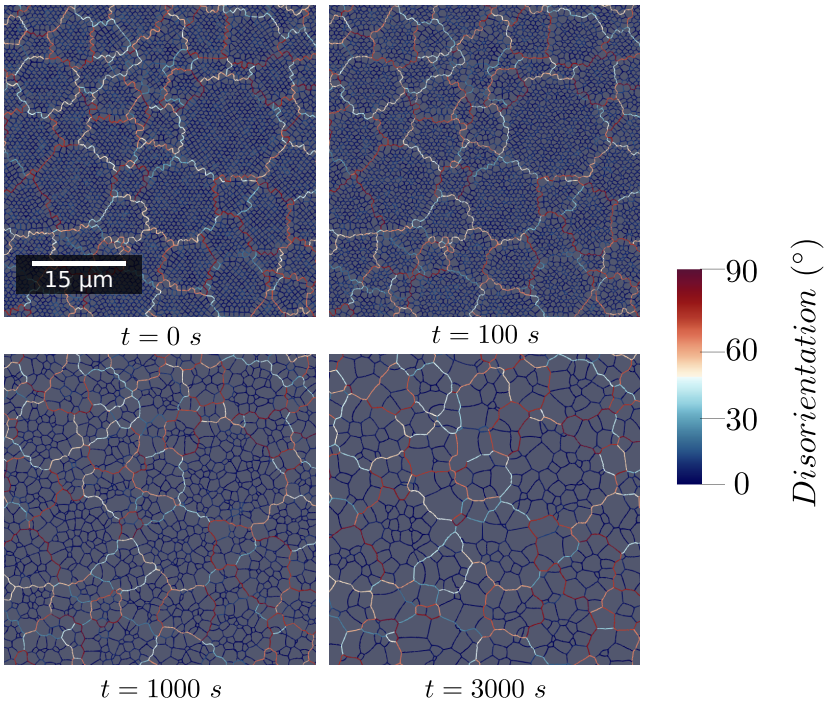
Figure 3.7 describes how the mean ECD evolves with time during simulation. First, it is interesting to note that considering heterogeneous mobility (according to eq. 1.3) affects significantly subgrain growth and that its impact depends on initial subgrain size distribution. To assess this in more details, the evolution of total HAGB and LAGB length and of HAGB length fraction are plotted in figure 3.8. HAGB length ratio (fig. 3.8a) exhibits how heterogeneous mobility favors the migration of HAGB and their formation by putting in contact subgrains originally located in different grains. At the end of the simulation, this leads to a higher HAGB length fraction. Moreover, as heterogeneous mobility favors HAGB migration, subgrains partially bounded by HAGB have a greater chance to grow. This is particularly true in the case presented in figure 3.6d, in which all subgrains initially have the same size. Consequently, the advantage given by the high mobility of those boundaries is increased and their growth dominates the whole microstructure evolution. Figures 3.8b and 3.8c confirm those remarks by showing a temporary increase of HAGB total length if mobility is heterogeneous. Finally, it is interesting to note that if subgrains initially have the same diameter, an incubation time is needed for the subgrains partially closed by HAGB to take a significant advantage and start to consume the whole microstructure. Finally, figure 3.9 confirms these observations. Both study cases assuming homogeneous mobility tend to keep a significant higher fraction of LAGB. This demonstrates that a higher heterogeneity of GB induces a change in the behavior adopted to lower the total energy of the system. It changes from global reduction of both LAGB and HAGB length to temporary increase of HAGB length in order to speed up the decrease of total GB length.



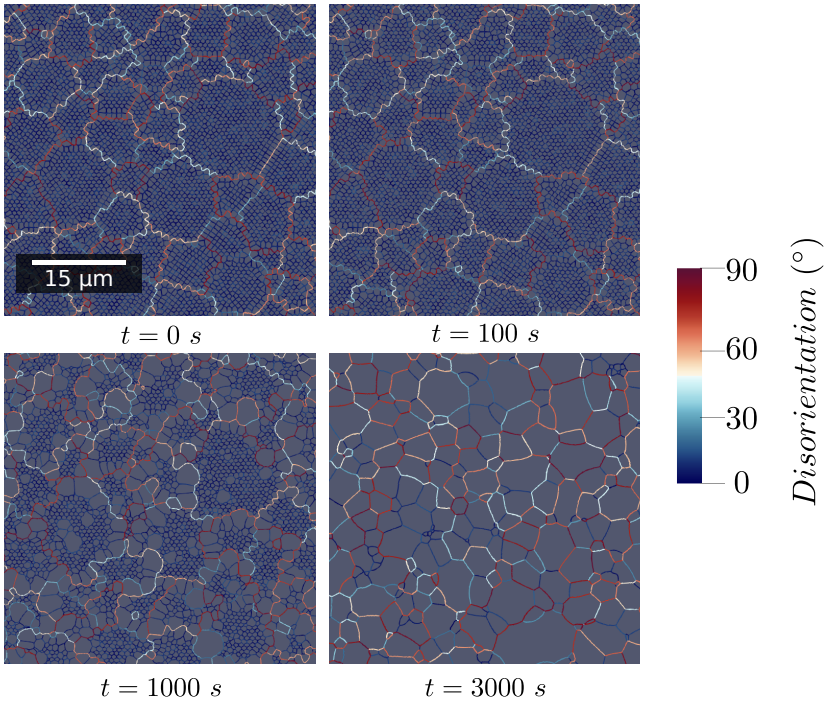
(a) Experimental subgrain size distribution - γ_h.



(b) Experimental subgrain size distribution - $\gamma_h,\ M_h$.



(c) Uniform subgrain size distribution - γ_h.



(d) Uniform subgrain size distribution - γ_h, M_h.

Figure 3.6: Evolution of the GB network with time for the four test cases, in a zone at the center of the RVE.

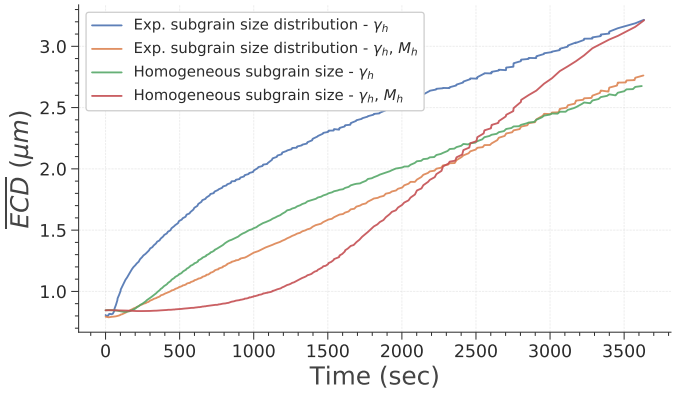
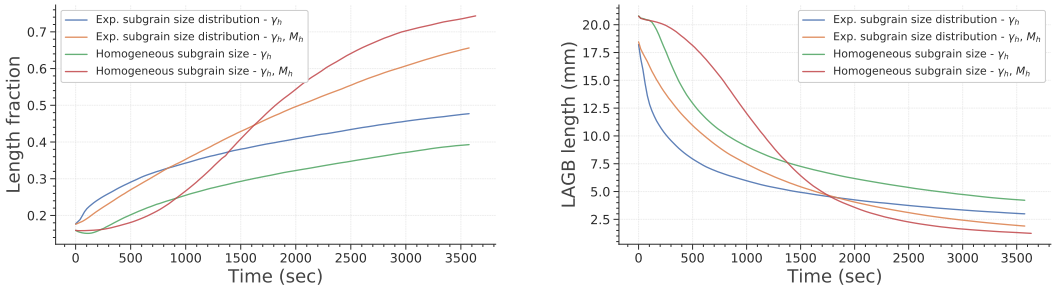
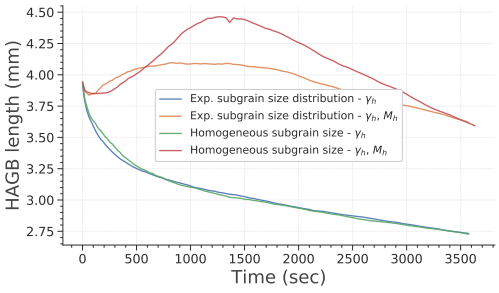


Figure 3.7: Evolution of subgrain average ECD as a function of time.



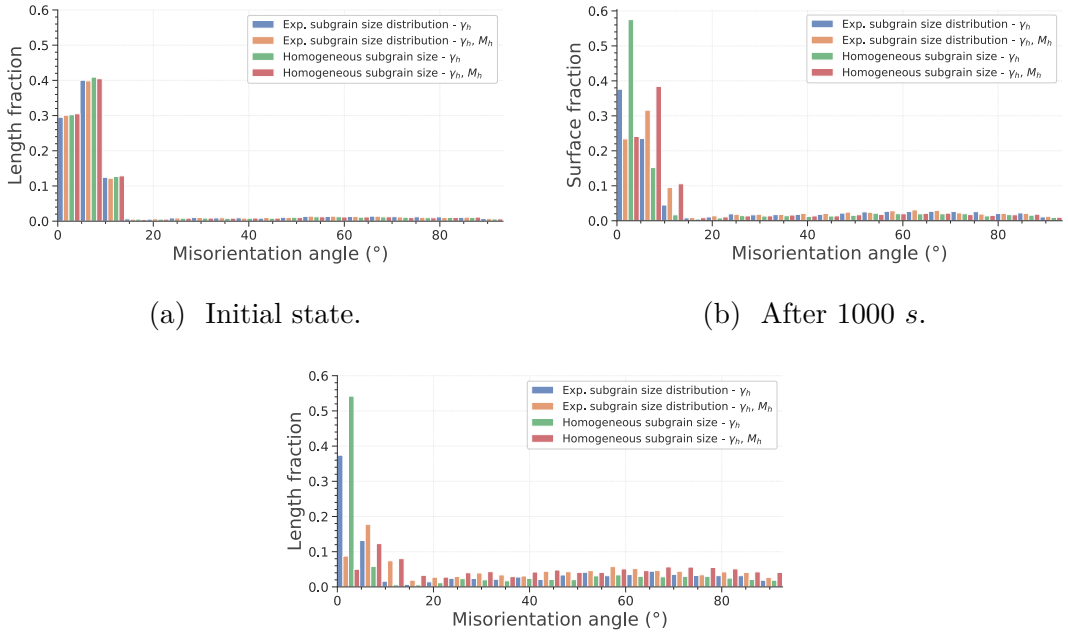
(a) HAGB length ratio.

(b) Total LAGB length.



(c) Total HAGB length.

Figure 3.8: Evolution of GB length with time.



(a) Initial state.

(b) After 1000 s.

(c) Final state.

Figure 3.9: Disorientation histograms at three instants of the simulation.

These detailed observations confirm that the faster growth of a small fraction of subgrains is only observable if mobility is considered heterogeneous, as described by Holm *et al.* [198]. They also broaden the remarks made by Suwa *et al.* [199] about the conditions allowing preferential subgrain growth. Indeed, this phenomenon is much less significant if initial subgrain size is not homogeneous and representative of experimental data.

Influence of stored energy

In previous papers describing similar full-field simulations, driving pressure due to dislocation density heterogeneity is generally neglected [197, 198, 199]. This rests upon the simplification that deformation energy is fully consumed thanks to recovery, by annihilation and/or organization into GB network. The available framework allows us to assess the influence of the assumptions by considering that each subgrain has its own dislocation density. Two simulation cases are defined:

- stored energy is initialized per subgrain by considering a dislocation density distribution taken from estimation of geometrically necessary dislocations (GND) by EBSD measurements.

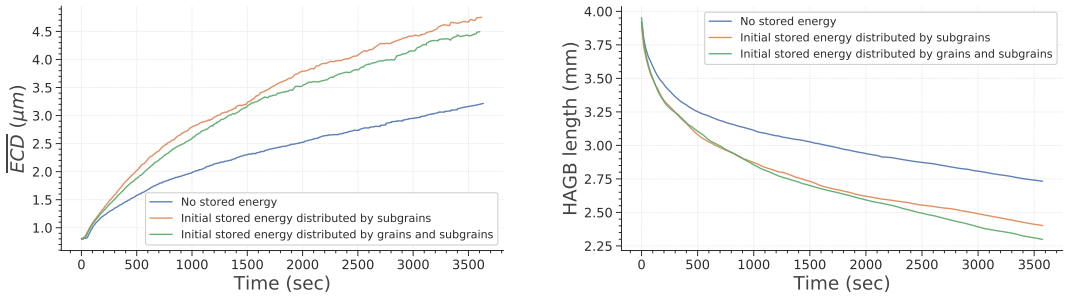
- Stored energy is initialized per grain using the same distribution. Then, subgrain energy is initialized weighting the parent grain using coefficients (named w_i) respecting normal distribution. Parameters of this normal dis-

tribution are defined as follow: $w \in [0.1; 2.0]$; $\overline{w} = 1.0$; $\sigma^2 = 0.2$. Distribution parameters have been set as thereby to ensure subgrains inside grains do not have the exact same energy and that it is still a driving pressure.

Figure 3.10 presents the main microstructure features that are influenced by the presence of stored energy. As expected, considering stored energy variations between grains leads to an increase of the driving pressures and consequently to a faster growth of subgrains presenting an initial lower stored energy and so a kinetic advantage. Since the total stored energy in the two last simulations is the same, differences in terms of kinetics are rather small. However, it is interesting to note that in the second case considering stored energy, subgrains and the complete microstructure evolve slightly slower whereas total HAGB length decreases faster. The faster disappearance of HAGB should be related to the stored energy distribution. Indeed, stored energy gaps between subgrains located at grain interfaces is higher than between subgrains belonging to the same parent grain. This contributes to speed up the movement of HAGB and to reduce the growth of subgrains located in inner grain regions.

Discussion of numerical criterion for identification of recrystallized grains

In all of the papers presenting full-field simulations of microstructure evolution including substructures, recrystallized grains are identified based on their size. Subgrains are generally considered as recrystallized grains as soon as they are 6 to 8 times bigger than the initial mean subgrain size [197, 198, 199]. This relies on the hypothesis that all subgrains are free of energy and could become recrystallized grains. However, in recent experimental studies, recrystallized grains are generally identified based on some parameters quantifying internal disorientation or directly upon GND density [18, 201]. To correctly evaluate recrystallized fraction and being able to compare experimental to numerical data, several criteria are here defined and compared. Subgrains are considered as recrystallized if:



(a) Evolution of $\overline{ECD}$ as a function of time.

(b) HAGB total length as a function of time.

Figure 3.10: Main microstructural feature evolutions impacted by initial stored energy.

C1: they are 8 times bigger than the initial mean subgrain size,

C2: their internal dislocation density is lower than a given threshold,

C3: their internal dislocation density is lower than a given threshold and at least half of the boundaries surrounding it are HAGB.

Obviously, the last two criteria are only tested against the simulations that consider stored energy (see section 3.2.1).

Figure 3.11 illustrates how recrystallized surface fraction evolves during simulation, for the first simulation case described in section 3.2.1. As one could have expected, the recrystallized fraction behaves differently depending on its definition. Consequently, ensuring that the criteria used to discriminate recrystallized grains from experimental and simulation data are consistent is critical.

3.2.2 Modeling of CDRX and PDRX

Let's have a look now at simulations of CDRX and PDRX. To present the abilities of the model and evaluate the influence of subgrain formation rules, the results obtained with four different test cases are described below. All of them consider initial microstructures respecting the same grain size and hardening coefficient distributions. They include approximately 300 grains. The initial number of grains is taken low since it will increase substantially during deformation. Material parameters correspond to the ones estimated in chapter 6 based on experimental data. Thermomechanical conditions corresponding to these simulations are the following: $T = 650°C$; $\dot{\varepsilon} = 1.0\ s^{-1}$; $\varepsilon_f = 1.35$. The four test cases differ by the GB properties and the restrictions set for formation of subgrains. In all of the cases, except the last one, subgrains cannot be placed too close to grain boundaries. They are defined as follows:

(a) The number of subgrains that are formed at each deformation increment is computed individually per grain/subgrain (equation 3.9). GB energy is

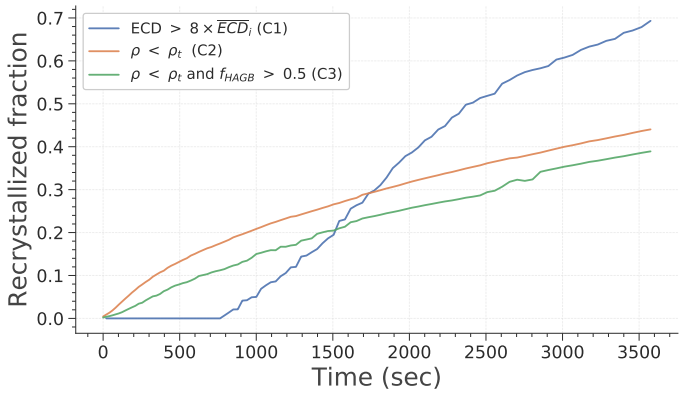


Figure 3.11: Evolution of recrystallized fractions with time.

described by RS equation (equation 1.2) and GB mobility is isotropic.

(b) The number of subgrains that are formed at each deformation increment is computed for the whole domain. Then, new subgrains are positioned randomly within the RVE. GB energy is described by RS equation (equation 1.2) and GB mobility is isotropic.

(c) The number of subgrains that are formed at each deformation increment is computed individually per grain/subgrain (equation 3.9). GB energy is described by RS equation (equation 1.2) and GB mobility is heterogeneous and computed using equation 1.3.

(d) This last case respects the same rules than the first one, except that new subgrains can be placed on pre-existing grain boundaries.

Based on the discussion presented previously (see section 3.2.1) and to be as close as possible to the criterion used commonly when working with experimental data, it has been decided to define as recrystallized the grains that fulfill the two following criteria:

- $\rho \leq \rho_{th} = 1.0 \times 10^{14}\ m^{-2}$,
- only grains, i.e. entities bounded by at least 50% of HAGB, are included into the measure of recrystallized grains.

Evolution of main microstructure descriptors during CDRX and PDRX

Figure 3.12 presents evolution of digital microstructures for the four test cases, after a deformation of 1.35 and a subsequent holding at temperature (hundreds of seconds at $650°C$). Figure 3.13 presents the evolution of the main microstructural descriptors with time. First, one could see that the recrystallized fraction is null during the deformation process and starts to increase significantly only after tens of seconds of holding at temperature. This can be explained easily by analyzing the criteria defined previously for discrimination of recrystallized grains in regards of the mechanisms introduced into the numerical framework. First, only subgrains are formed during deformation due to recovery of a certain fraction of dislocations. These objects do not fulfill the second criterion. Then, under subsequent deformation, their misorientation increases as prescribed by equation 3.10. However, at the same time, their internal dislocation density increases. Therefore, with the material parameters considered here, new subgrains see their dislocation density exceed the threshold value before they have time to transform into grains. Then, under holding at temperature, grains and subgrains that have an energetic advantage over the surrounding grains start to grow. Their dislocation density is progressively lowered. They are also likely to encounter new grains which generally leads to an increase of the bounding HAGB fraction. Consequently, more and more candidates are meeting both of the criteria and are flagged as recrystallized. The evolution of average recrystallized grain size

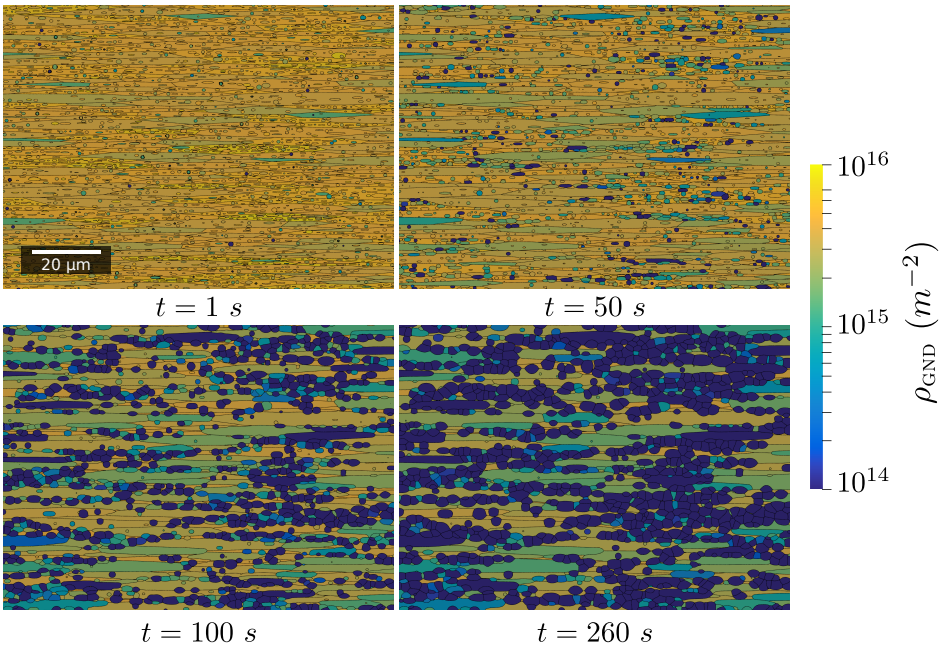
presents a sigmoidal shape, except for the first instants where there are abrupt and erratic variations. This is due to the small number of grains considered as recrystallized at those times.

It is interesting to discuss how HAGB length ratio evolves during the whole process (figure 3.13d). First, it decreases quickly with strain due to the fact that some new subgrains form. Then, once deformation is stopped, it increases by approximately 10% instantaneously. One reason for that observation is that the hardening parameter, K_1, attributed to each subgrain is taken from a distribution. Therefore, some subgrains have a higher hardening parameter than the parent grains and disappear as soon as their dislocation density is higher than the one of the parent grain. This is not visible during deformation since the formation of new subgrains is much more significant. Secondly, it is noteworthy to mention the rapid stagnation of HAGB length ratio. This would mean that grains and subgrains that have a lower dislocation density grow at similar rates. It makes sense since the driving pressure induced by interface energy is negligible in regards of the one linked to differences in deformation stored energy.

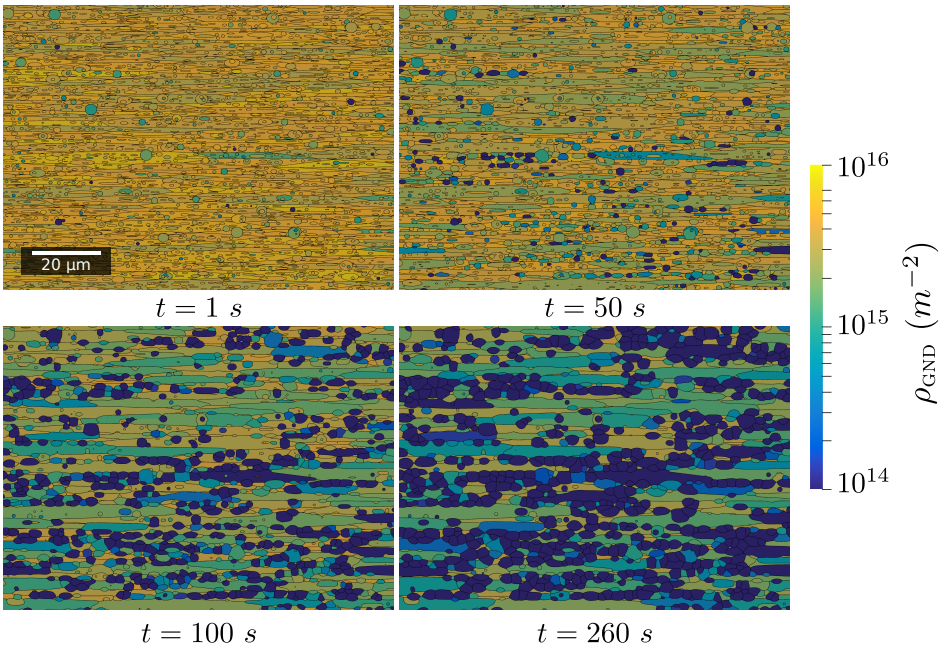
The differences between the results obtained with the four test cases tend to show that considering a heterogeneous GB mobility does not impact significantly the statistical descriptors discussed here. One could also notice that introducing subgrains over the whole domain globally affect recrystallized fraction at intermediate times and induces an increase of the average recrystallized grain size by approximately 15%. This difference in recrystallized fraction can be explained by the fact that the main driving pressure for the growth of recrystallized grains is the difference in stored energy between those grains and the surrounding ones. Therefore, if the quantity of interfaces created during deformation is individualized per grain, one can deduce from equation 3.9 that more subgrains will be placed in zones with high dislocation density. Thus, the kinetics of recrystallization will be higher for intermediate holding times. The difference in average recrystallized grain size is explained by the fact that, when global nucleation is used, viable subgrains can grow much significantly before encountering other recrystallized grains. Finally, regarding the last test case, allowing new subgrains to form at GB leads to 10% higher recrystallized fraction. The reason behind that difference is that subgrains that form over pre-existing GB have already a fraction of their boundary as HAGB.

Evolution of the subgrain network during deformation

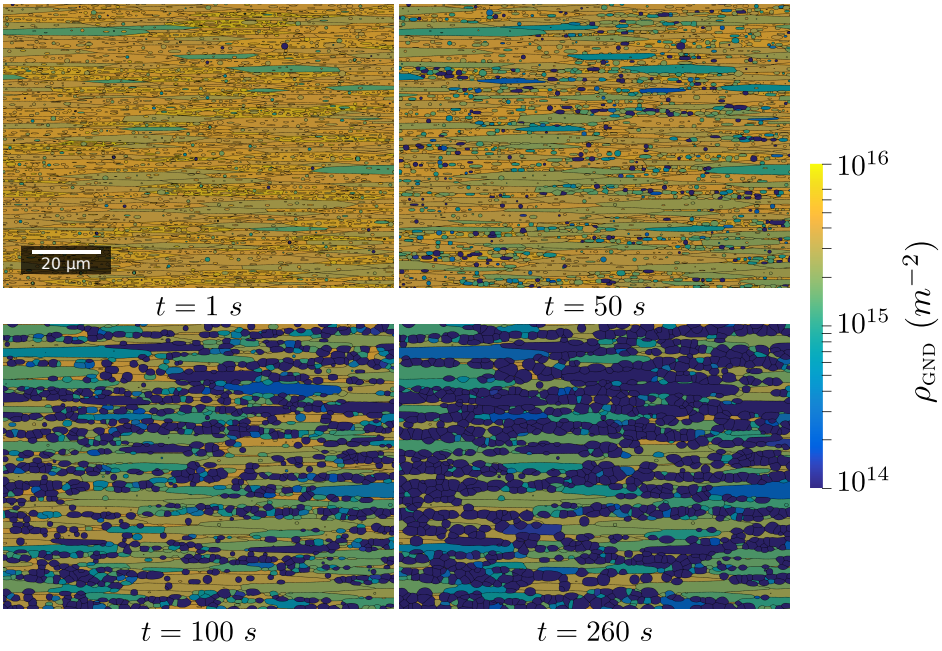
The evolution of the HAGB length ratio and of the mean LAGB disorientation with strain are presented in figure 3.14. Focusing on HAGB length ratio first, it is interesting to note that it reaches a steady state after a strain of 0.6. This is consistent with some experimental observations reported by Chauvy *et al.* [15]. As discussed in previous section, some subgrains disappear during deformation since they harden too much to stay viable. The average LAGB disorientation increases by approximately 1° during deformation. It is a rather low increase. However, it is important to note that new subgrains continue to form whereas



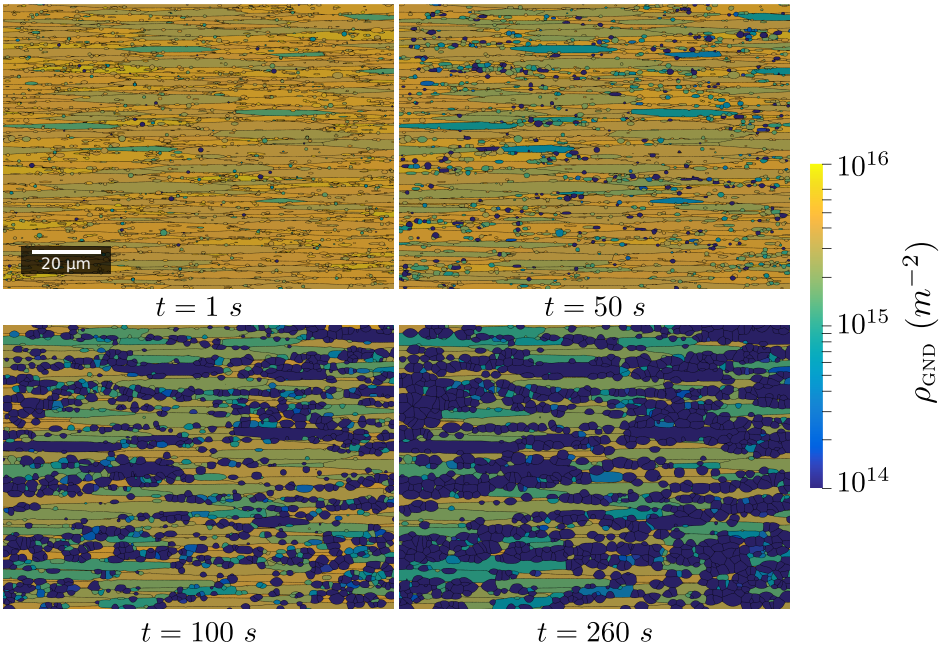
(a) Local nucleation - γ_h.



(b) Global nucleation - γ_h.

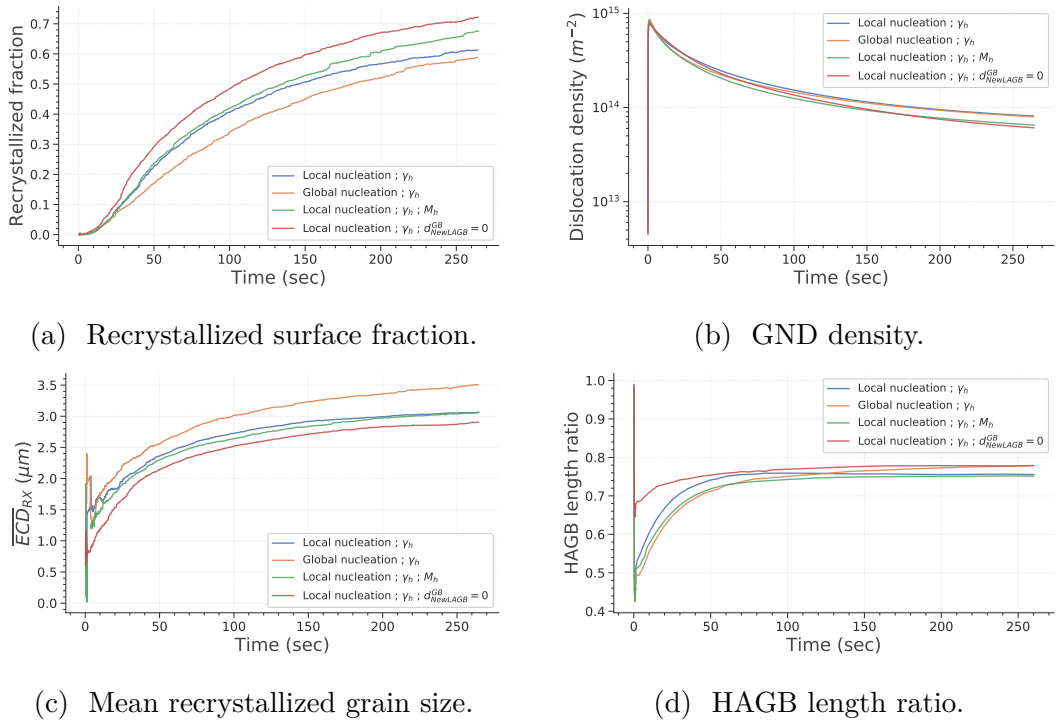


(c) Local nucleation - $\gamma_h,\ M_h$.



(d) Local nucleation - $\gamma_h,\ d^{GB}_{NewLAGB} = 0$.

Figure 3.12: Evolution of digital microstructures with time for the four different test cases.



(a) Recrystallized surface fraction.

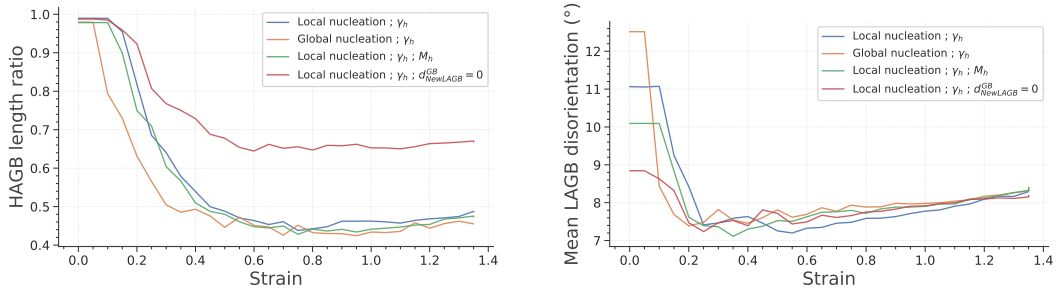
(b) GND density.

(c) Mean recrystallized grain size.

(d) HAGB length ratio.

Figure 3.13: Main microstructural feature evolution with time.

some other shrink. Therefore, this evolution is not only representative of the disorientation increase due to equation 3.10.



(a) HAGB length ratio.

(b) Mean LAGB disorientation.

Figure 3.14: Main microstructural feature evolution with strain, during deformation.

Finally, the last worth mentioning point is that the only case that exhibits different results regarding those two features is the last one, in which subgrains can form onto GB. To investigate the reason behind this difference in HAGB length ratio, the evolution of LAGB and HAGB length with strain is plotted in figure 3.15. This figure shows comparable HAGB length evolution in the two cases. However, it appears that in the reference case in which subgrains form at a given distance from GB, the increase of LAGB length is much higher. This is

consistent since the formation of subgrains over pre-existing GB gives rise to a lower quantity of LAGB and to the disappearing of HAGB. A scheme is provided in figure 3.16.

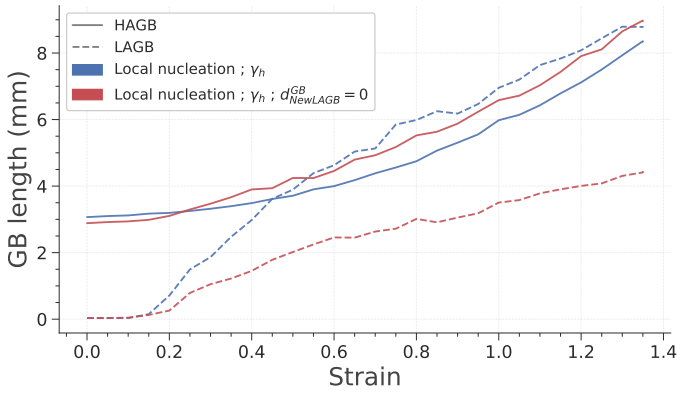


Figure 3.15: Evolution of LAGB and HAGB length with strain during deformation.

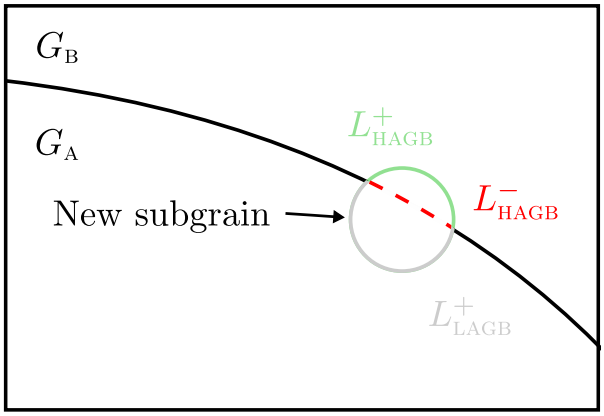


Figure 3.16: Scheme summarizing the different interfaces formed and removed when a subgrain is positioned at a pre-existing GB.

3.3 Conclusion

Firstly, the present chapter described in details the numerical framework used to simulate recrystallization and related annealing phenomena. The equations used to describe hardening an recovery were recalled first. A new strategy to reproduce the intergranular deformation heterogeneities was presented. This strategy proposes to define a hardening parameter for each grain, according to a distribution measured experimentally. Then, the GB velocity formulation is detailed.

Finally, the two different strategies developed to consider substructures are presented. The first one allows to consider an initial fully substructured microstructure whereas the other relies on the equations of the Gourdet-Montheillet [125] model to predict the subgrain formation and evolution upon hot deformation.

Secondly, the different developments described previously were tested and the impact of several assumptions and numerical parameters were assessed. The results were used to expand on the few numerical simulations described in literature that consider microstructure evolutions in presence of substructures. The results highlight that the equations considered for GB mobility affect to a great extent the microstructure evolutions for grain growth simulations. The results obtained with the new implementations related to CDRX highlight that the differences observed with the selected working assumptions are reasonable. These results allow to select the second numerical formulation, considering global nucleation over the whole domain with heterogeneous GB energy as suited for the upcoming simulations. Indeed, this formulation provides similar results than the three others while being simpler to implement and more efficient.

Résumé en français

Ce chapitre est dédié à la présentation des méthodes numériques employées afin d'étudier la recristallisation du zircaloy-4. Les équations utilisées pour décrire les mécanismes d'écrouissage et de restauration sont rappelés. Une nouvelle stratégie permettant de tenir compte des hétérogénéités intergranulaires est présentée. Elle consiste à définir un paramètre d'écrouissage par grain, sur la base d'une distribution estimée à partir de données expérimentales. Ensuite, la formulation mathématique permettant de modéliser la migration des interfaces est détaillée. Enfin, deux stratégies permettant d'introduire des sous-grains dans les microstructures numériques sont décrites. La première consiste à générer une microstructure totalement sous-structurée. La seconde repose sur les équations du modèle Gourdet-Montheillet [125] pour prédire la formation et l'évolution de sous-grains durant la déformation à chaud.

Dans un second temps, les différents développements numériques sont évalués. L'influence de différentes hypothèses et paramètres numériques est quantifiée. Les résultats sont utilisés pour discuter différents cas présentés dans l'état de l'art. Ils permettent de mettre en évidence le rôle de certaines hypothèses. L'influence de l'équation employée pour décrire la mobilité des joints de grains est mise en exergue, dans le cas de la simulation de la croissance de grains. Les résultats de simulation de CDRX montrent que les différentes hypothèses permettent d'obtenir des résultats proches et sensés. Ces résultats permettent de sélectionner la deuxième formulation numérique pour les simulations présentées dans les prochains chapitres, puisque les résultats obtenus avec cette méthode sont cohérents et que l'implémentation est plus simple et efficace.

Chapter 4

Characterization and modeling of grain growth

The present chapter takes advantage of the experimental techniques and numerical methods detailed in chapters 2 and 3 to study the grain growth phenomenon.

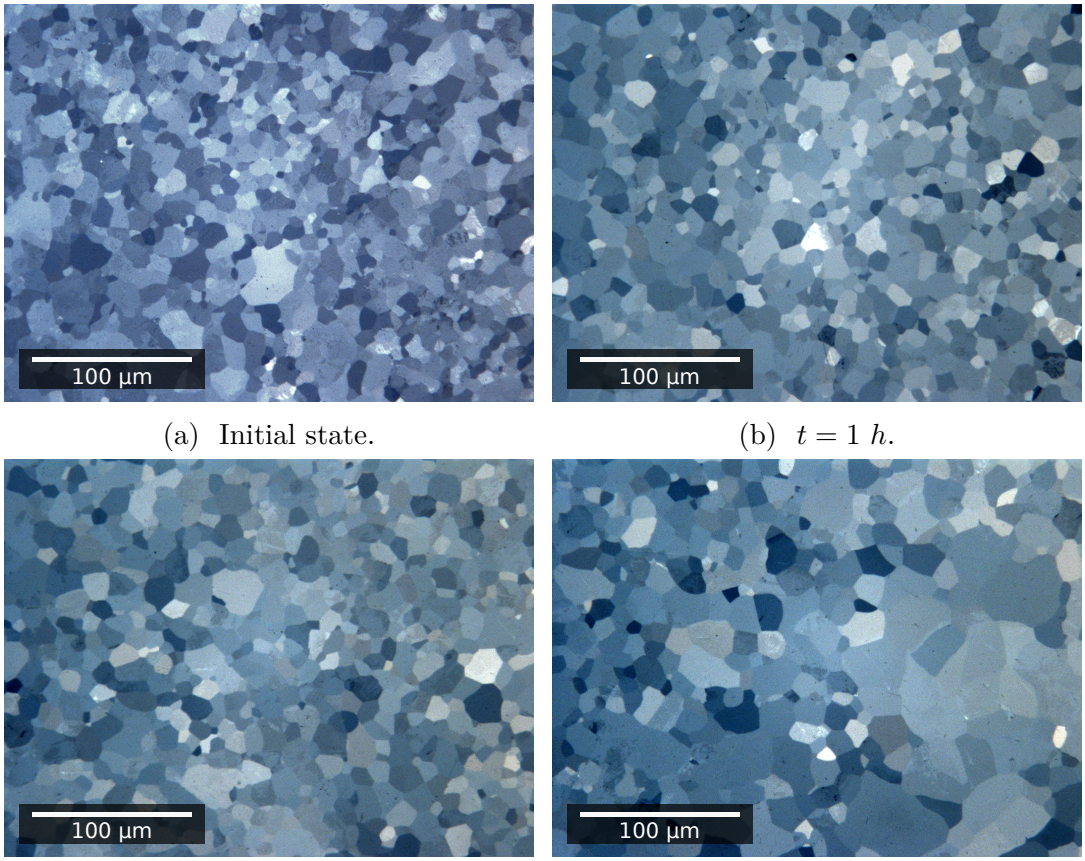
To our knowledge, there are no complete experimental dataset related to grain growth of zircaloy-4. Consequently, the chapter aims first to apply the image analysis tools to optical microscopy images to quantify the grain growth kinetics in samples with or without second phase particles. Complementary transmission electron microscopy analyses are performed to assess precisely the evolution of the precipitate population during the heat treatments. Then, this extensive dataset is exploited to identify the reduced mobility. These values are applied to run simulations representative of materials containing some or no second phase particles. Finally, the interest of such advanced numerical tools is highlighted by comparing simulation cases with or without second phase particles to evaluate their impact on both equiaxed and basket-weaved microstructures.

4.1 Characterization of grain growth

GG is characterized by quantifying the evolution of the grain size distribution with holding time, at different temperatures and for a fully recrystallized microstructure. To do so, samples free of stored energy of deformation are heat treated under the conditions presented in tables 2.3 and 2.4 and characterized by the PL-OM technique. All the parameters related to image acquisition and post-processing are described in section 2.4.2.

4.1.1 In the absence of SPP

First, heat treatments are performed on samples without SPP. PL-OM images corresponding to a group of heat treatments performed at $650°C$ are available in figure 4.1.



(a) Initial state. (b) $t = 1\ h$.

(c) $t = 3\ h$. (d) $t = 8\ h$.

Figure 4.1: PL-OM images displaying the general microstructure evolution during a heat treatment at $T = 650°C$, for **Wo SPP** samples.

The main results provided by the observations made after the different heat treatments are summarized in figure 4.2. The evolution of the average ECD

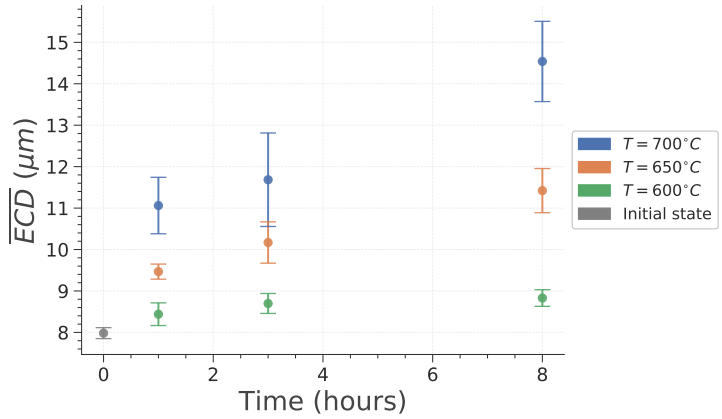
($\overline{ECD}$) with time is presented in figure 4.2a for the three temperatures investigated. Error bars are computed using equation 2.8. The automatic post-processing technique enables to compute the average ECD but also to quantify the evolution of the grain size distribution. Figure 4.2b illustrates that feature by describing the evolution of the grain size distribution with time for a heat treatment performed at $T = 650°C$. Figure 4.2b confirms the presence of large grains (with an ECD larger than 40 μm) observed in figure 4.1d but shows that on average, their surface fraction remains limited (around 5%). One can note that these large grains are present for samples at the three heat treatment durations and that a smaller fraction is already present at initial state. This tends to prove that they originate from the preceding manufacturing stages. The model material presenting no SPP has been manufactured at laboratory scale. Therefore, the manufacturing route differs from the common industrial manufacturing routes (see figure 2.1a). The deformation increments and the total deformation are lower for the manufacturing route used to produce samples without SPP. The lower deformation values could cause some deformation and recrystallization heterogeneities that could in turn be responsible for the presence of large grains that are stable upon subsequent heat treatments. This has been already reported in literature [202].

4.1.2 In the presence of SPP

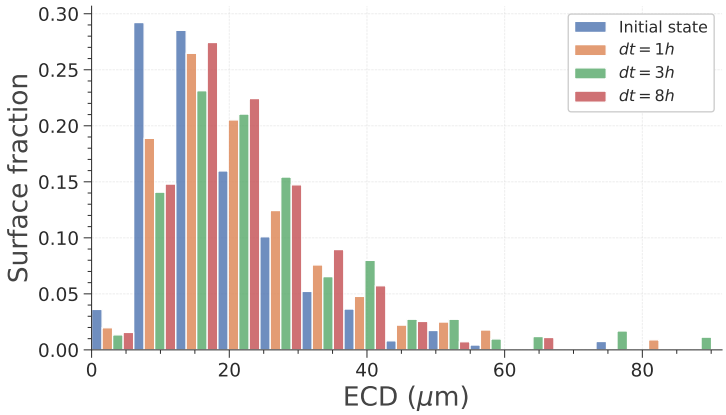
Heat treatments are now performed on commercial Zy-4. The OM-PL characterizations allow to plot figure 4.3 which describes the evolution of the average ECD with time.

One can see that the GG kinetics of commercial equiaxed Zy-4 seems to plateau after 2 hours of thermal treatment for all the considered temperatures. The limit grain size ($\overline{ECD}_{lim}$) is equal to: 4.2 μm, 4.7 μm and 5.4 μm for heat treatment temperatures of $600°C$, $650°C$ and $700°C$, respectively. This increase of limit grain size with temperature suggests that the SPP population evolves during holding at temperature. Using equation 1.11, one could deduce that the average SPP diameter is increasing and/or the SPP volume fraction is decreasing. To assess the potential SPP size increase during the heat treatments, a sample representative of the initial state and three samples heat treated at the temperatures of interest for 6 hours are characterized by TEM. A typical TEM image with SPP is displayed in figure 4.4. The distributions of SPP ECD are plotted in figure 4.5 and the main statistical descriptors of these measurements are summarized in table 4.1.

First, one can deduce from figure 4.5 and table 4.1 that SPP size remains coherent with the hypothesis of the Smith-Zener equations described in section 1.2.2. Indeed, the SPP size remains small comparatively to the grain size but sufficiently large comparatively to the grain interface thickness. Second, it appears that the increase of SPP size is limited. Using equation 1.11, one can do a cross-multiplication to estimate how this increase could affect the limit average



(a) $\overline{ECD}$ versus time.



(b) ECD distribution evolution during a heat treatment performed at $T = 650°C$.

Figure 4.2: Evolution of grain size descriptors with time, for heat treatments performed on **Wo SPP** samples.

grain diameter $\overline{ECD}_{lim}$. The results are presented in table 4.2. While of a good precision, these predictions underestimate the increase of limit grain size noticed from figure 4.3. Three hypotheses could explain these differences. The measurement of $\overline{ECD}_{lim}$ and/or $\overline{ECD}_{\text{SPP}}$ could be affected by some error. The equation 1.11 remains a rough approximation based on numerous approximations considered in the Smith-Zener analysis. Therefore, it could be inappropriate for such small variations. Finally, a small fraction of SPP could be dissolved during the heat treatment, this effect being not measurable by doing TEM characterizations at room temperature. Some of these hypotheses are discussed using full-field simulations and are presented in section 4.2.2.

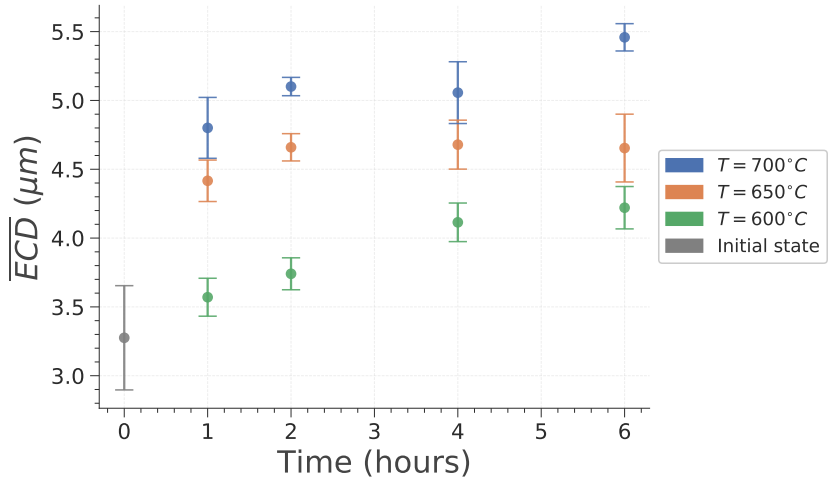


Figure 4.3: $\overline{ECD}$ versus time. Samples with equiaxed microstructure.

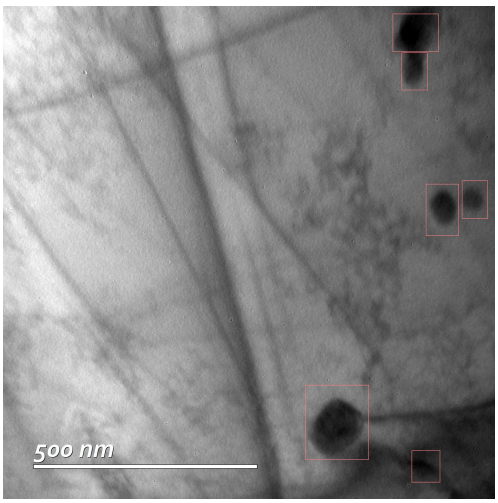


Figure 4.4: TEM image showing the presence of 6 precipitates. The SPP counted are surrounded by a thin pink box.

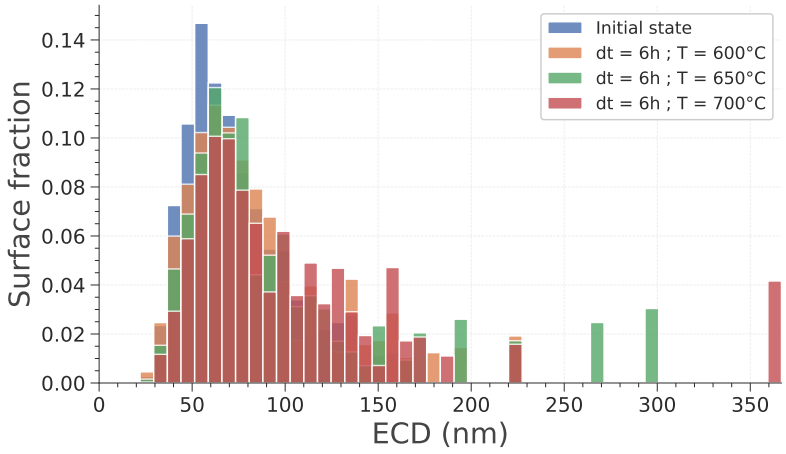


Figure 4.5: ECD distributions of SPP of the four samples of interest.

		Heat treatment temperature ($°C$)		
	Initial state	600	650	700
$\overline{ECD}_{\text{SPP}}$ (nm)	57.7	59.9	63.2	67.6
Standard deviation	20.6	25.2	28.0	30.4
$min\,(ECD_{\text{SPP}})$ (nm)	8.0	22.9	25.1	22.6
$max\,(ECD_{\text{SPP}})$ (nm)	154.6	223.4	294.2	366.8
SPP count	532	618	606	576
Number of images	90	98	111	87

Table 4.1: Main statistical descriptors of SPP population of the four specimens of interest: no heat treatment, 6 hours at $600°C$, 6 hours at $650°C$, 6 hours at $700°C$.

T ($°C$)	$\overline{ECD}^{exp}_{lim}$ (μm)	$\overline{ECD}^{pred}_{lim}$ (μm)
600	4.2	-
650	4.7	4.4
700	5.4	4.7

Table 4.2: Average limit $\overline{ECD}$ predicted using Smith-Zener equations.

4.2 Modeling of grain growth

4.2.1 Identification of reduced mobility

To identify the reduced mobility, a three step procedure that has been developed at CEMEF and successfully applied to other alloys is followed [28]. It relies upon an inverse analysis approach that leads to a satisfactory agreement between the predicted and measured average grain size. Some other inverse analysis methods are presented in literature [73]. Inverse analysis techniques present the advantage of simplifying experimental procedures and providing mobility values that are tailored to the numerical framework.

The present method allows to get an estimation of the reduced mobility, i.e. the product of the GB energy and mobility. An estimate of the GB energy is then taken from literature data to deduce GB mobility. In the present case, the value of γ is considered equal to 0.22 $J.m^{-2}$ [124]. It should be pointed out that Dunlop *et al.* do not have any experimental evidence to support that value. However, it is in the range of values generally considered [18] and the simulation results show a very good agreement with the experimental ones [124].

Estimation of reduced mobility by fitting a B&T law The first step of the identification procedure consists in obtaining initial values of reduced mobility by fitting a B&T law (equation 4.1) to the experimental data.

$$\overline{ECR}^2 - \overline{ECR}_i^2 = \frac{1}{2} M\gamma t \tag{4.1}$$

In equation 4.1, $\overline{ECR}_i$ designates the average equivalent circle radius of the initial state.

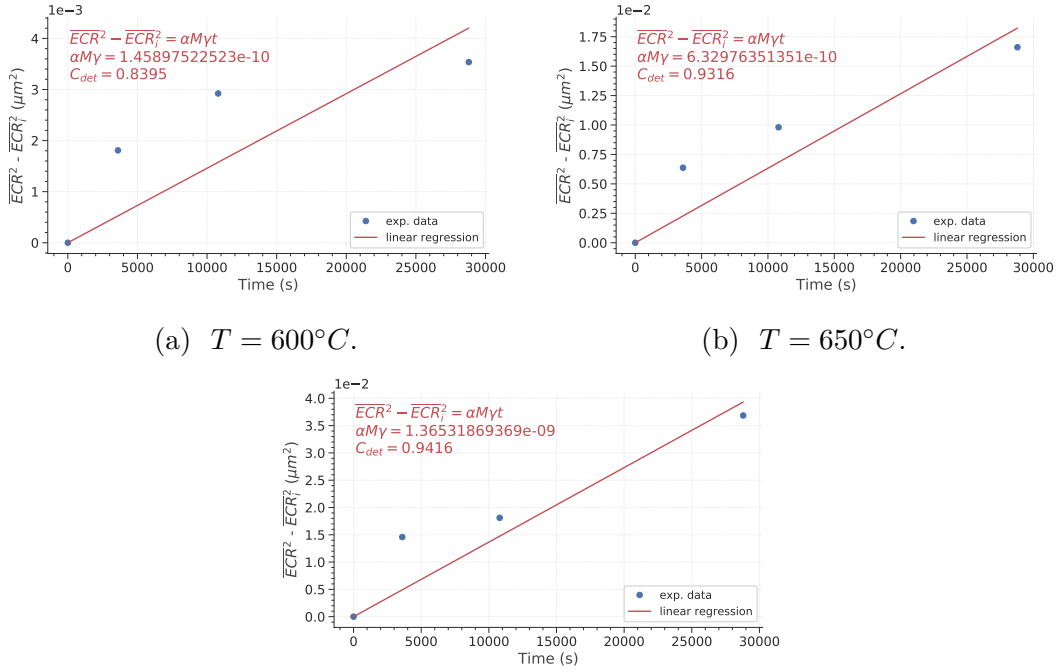
To do so, the slope of the curve plotted in figure 4.6 is multiplied by a factor 2 to obtain initial values of reduced mobility at the different temperatures tested. Figure 4.6 presents how B&T law fits the experimental data.

One can observe from figure 4.6 that the fitted B&T law does reproduce the trends but does not describe accurately the experimental data. The values of correlation coefficient belonging in the range [0.84; 0.94] agree with this qualitative observation.

This fitting operation provides us a rough initial approximation of the reduced mobility ($M\gamma$) at the three temperatures of interest.

Fine tuning of reduced mobility Once a set of reduced mobility parameters are available, first full-field GG simulations are run at the different test temperatures.

To do so, initial microstructure should be generated. In the present case, the two generation strategies presented in section 3.1.4 are tested. First, initial microstructure is generated based on the measured grain size distribution. This



(a) $T = 600°C$. (b) $T = 650°C$.

(c) $T = 700°C$.

Figure 4.6: $\overline{ECR}^2 - \overline{ECR}_i^2$ versus heat treatment duration. Three different heat treatment temperatures are considered. B&T law are fitted.

is done using a Laguerre-Voronoi algorithm [194, 195]. The digital microstructure generated presents the grain size distribution (GSD) displayed in figures 4.7a and 4.7b and referred to as *Generation from original GSD*. When comparing this GSD to the GSD obtained by immersing experimental data, which is exactly equal to the experimental one and is used as reference, it seems that the generation underestimates slightly the number of large grains (above 10 μm approximately). To correct that, a second microstructure is generated according to a GSD modified only for the large grains. The digital microstructure presents the GSD referred to as *Generation from alternative GSD* in figure 4.7. Figure 4.7b highlights that the microstructure generated according to that alternative GSD presents a peak around 20 μm. The surface fraction of this peak is equal to 0.18, which is very close to the cumulative surface fraction of the grains above 10 μm for the immersed microstructure (equal to 0.16).

One can observe that fine tuning the initial grain size distribution as well as immersing experimental data both lead to a better agreement between the measurements and the simulation results. To be precise, this allows to improve the prediction of the kinetics at the first instant of the simulation by reproducing the initial faster grain size increase. In the following study, the initial microstructure will be generated according to the optimized grain size distribution (GSD). Indeed, this reproduces the kinetics obtained when immersing experimental image and allows to have a microstructure with a very large initial number of grains,

comparatively to the immersion of experimental images.

Then, once initial microstructure is properly defined, GG simulations are run for the three considered temperatures. A multiplying factor is applied to the predicted $\overline{ECD}$ values in order to reduce the L_2 error. This multiplying factor allows to refine the values of reduced mobility used until now. This step is presented in figure 4.8.

Description of mobility evolution with temperature using an Arrhenius equation Finally, the last step of the identification procedure consists in fitting an Arrhenius relation to interpolate and extrapolate evolution of mobility with temperature. This is presented in figure 4.9.

This step enables us to express mobility using equation 4.3.

$$M = M_0 \exp\left(\frac{-Q_m}{RT}\right) \tag{4.2}$$

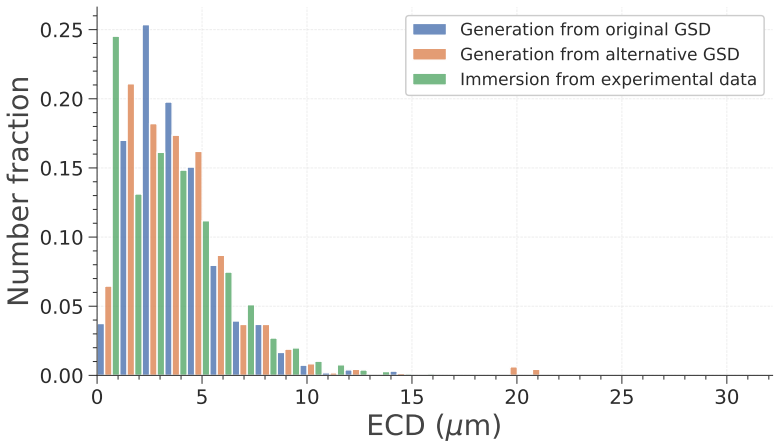
$$M = 1.35 \times 10^{-7} \exp\left(\frac{-134000}{RT}\right) m^4.J^{-1}.s^{-1} \tag{4.3}$$

The identified reduced mobility values from the three step process are described in table 4.3. This table illustrates how the identified values are progressively refined by each step. In average, the final values have a 40% relative difference from the values given by the B&T fit.

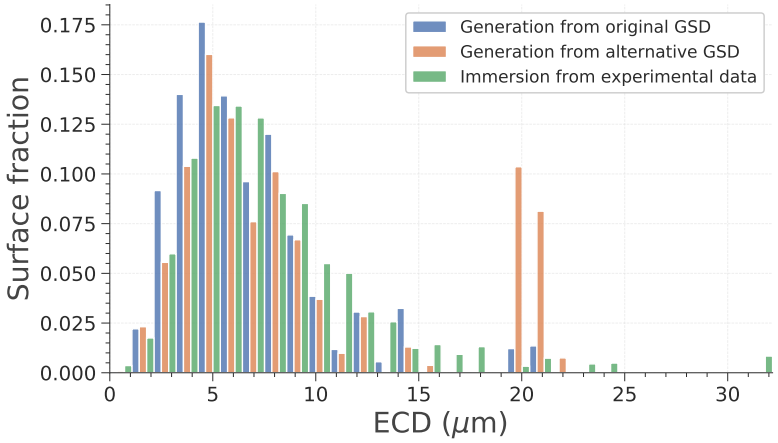
Simulations are run with the final reduced mobility values at the three temperatures of interest. The evolution of the average ECD with time is plotted in figure 4.10. The simulation results are in good agreement with the experimental ones, except for 8 hours at $600°C$. Looking at figure 4.8, it seems that at $600°C$, the maximum grain size stabilizes whereas it is not the case for the other temperatures. The most plausible hypothesis is that there is some variability in the experimental results. Indeed, the presence of some remaining SPP would result in the presence of a grain size plateau at higher temperatures as well. Putting aside this result, the general good agreement of experimental and simulation data confirms that the identified values are adequate and provide satisfactory results.

Temperature ($°C$)	Reduced mobility ($m^2.s^{-1}$) ($\times 10^{-16}$)		
	Step 1	Step 2	Step 3
600	3.05	2.66	2.80
650	13.2	8.47	7.61
700	25.5	17.7	18.7

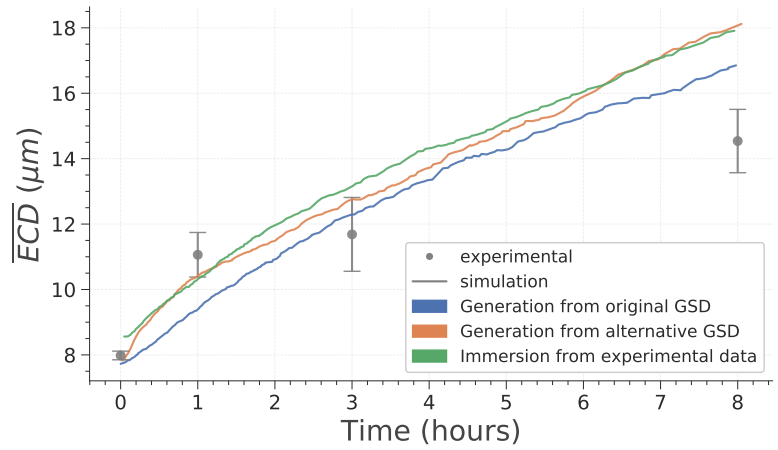
Table 4.3: Values of reduced mobility obtained at the three different temperatures.



(a) Initial ECD number distributions of the digital microstructures.

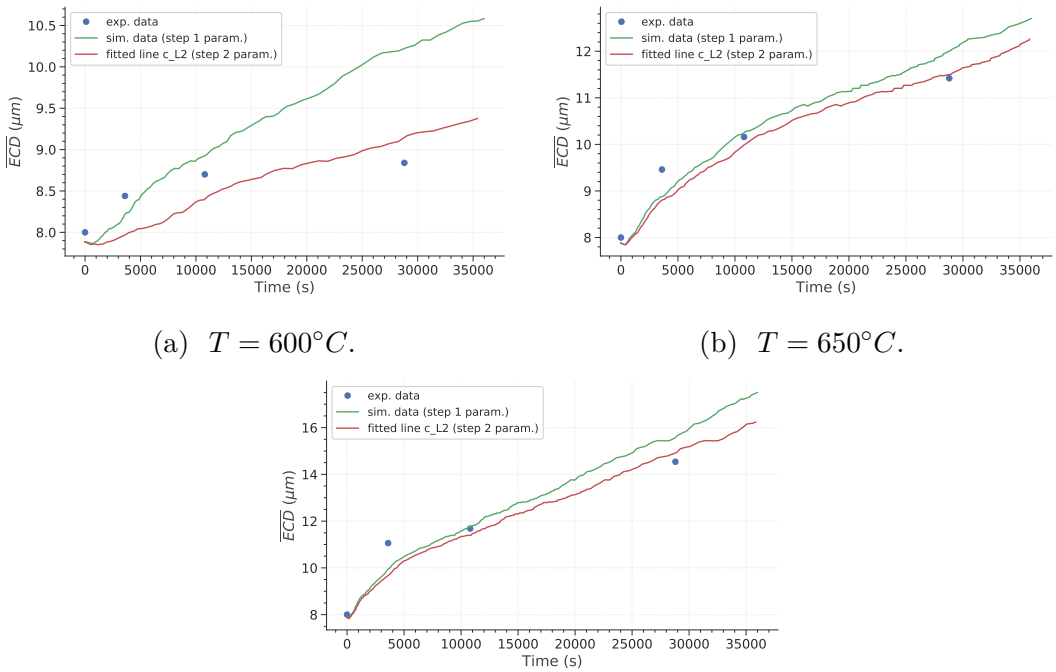


(b) Initial ECD surface distributions of the digital microstructures.



(c) $\overline{ECD}$ vs time.

Figure 4.7: Influence of initial microstructure generation upon GG kinetics.



(a) $T = 600°C$. (b) $T = 650°C$.

(c) $T = 700°C$.

Figure 4.8: Comparison of the measured and predicted evolutions of $\overline{ECD}$ with time. Green curves correspond to the values predicted by the full-field simulations with the values obtained at first identification step. Red curves are obtained by applying a correction factor to the green ones in order to reduce the L_2 error.

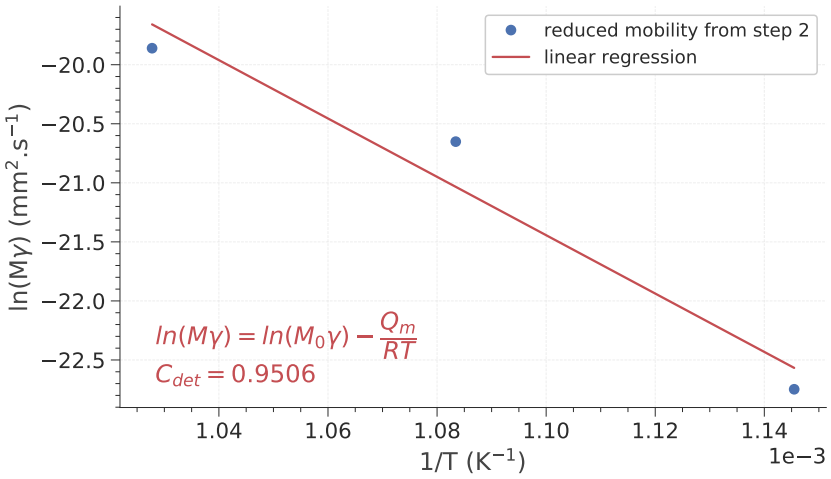


Figure 4.9: $\ln(M\gamma)$ versus $1/T$. $M\gamma$ values correspond to the three values identified in step 2.

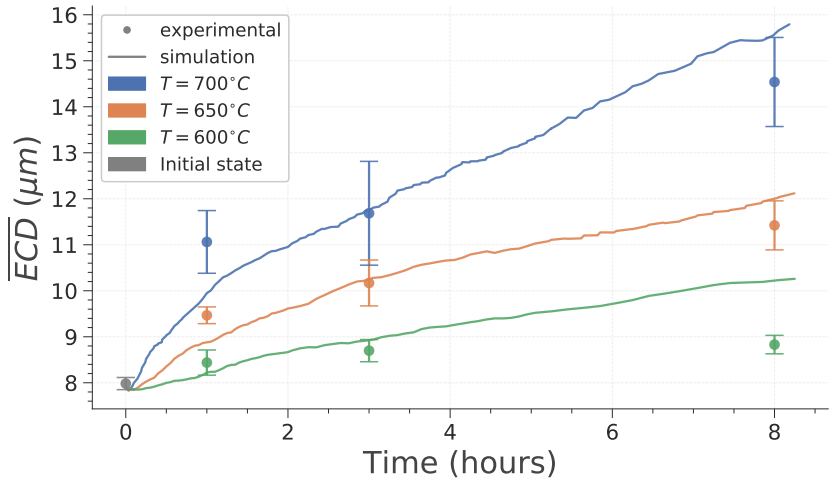


Figure 4.10: $\overline{ECD}$ versus time. **Wo SPP** samples.

4.2.2 Application to GG modeling in presence of SPP

Having identified mobility for the temperature range of interest, it is now time to model GG in presence of SPP. The first simulation cases that are presented in the following sections aim to predict how equiaxed microstructures evolve due to GG. This offers an opportunity to evaluate the results provided by the model using the mobility identified earlier. In a second time, GG simulations of equiaxed and basket-weaved microstructures are presented and confirm the role of SPP to control grain morphology and size.

GG of equiaxed microstructure

Validation of the set of parameters First, GG simulations representative of the heat treatments performed earlier (see section 4.1.2 and table 2.4) are run. To do so, initial microstructure of the simulation cases is defined according to the experimental distribution measured on a sample representative of the initial state (described in section 4.2.1). For each case, SPP are introduced according to the experimental size distribution measured by TEM. This distribution is different for each simulation since it is measured after 6 hours of heat treatment at the corresponding temperature (see section 4.1.2). The surface fraction of SPP is set to 0.52% [37, 41] for all three simulations. The evolution of $\overline{ECD}$ with time is plotted in figure 4.11. A comparison between experimental and digital microstructure after six hours of heat treatment at $600°C$ and $700°C$ is proposed in figure 4.12. It clearly exhibits a good visual agreement.

These results bring new elements to discuss the influence of SPP over GG during heat treatment performed on **Eq** samples. First, the simulation results are in very good agreement with the $\overline{ECD}_{lim}$ measured experimentally and show the limitations of estimations realized with a simple analytical law and presented

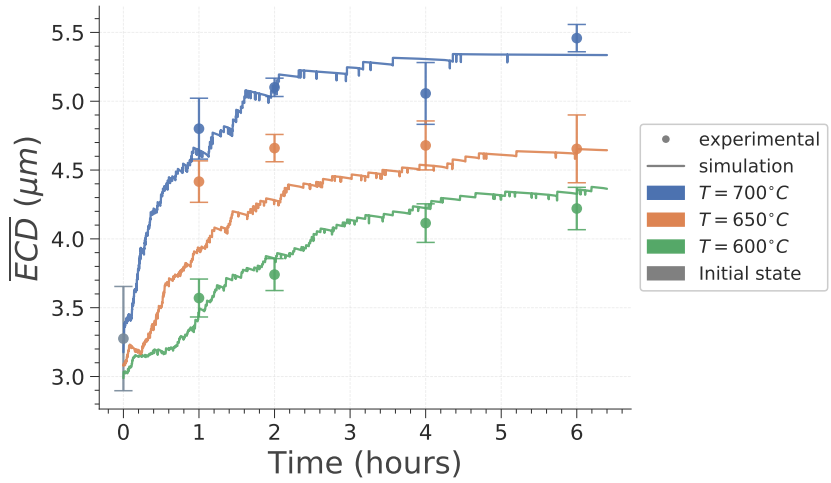
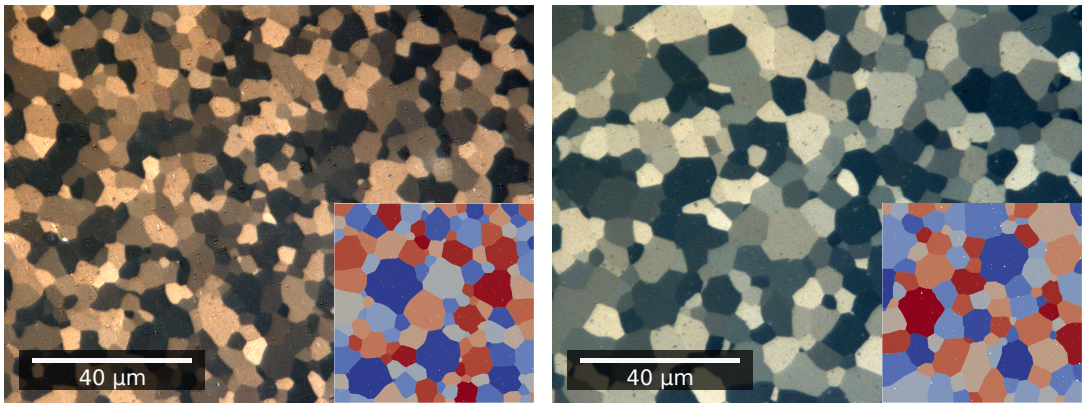


Figure 4.11: $\overline{ECD}$ versus time. Samples with equiaxed microstructure.



(a) $T = 600°C$. (b) $T = 700°C$.

Figure 4.12: Experimental and digital microstructures for six hours heat treatment performed at two temperatures. The color code for simulation results corresponds to grain identification number.

in table 4.2. Therefore, they highlight the relevance of using such high level simulation tools when a high degree of precision is required. Nevertheless, the importance of numerical parameters (time step and REV dimensions) should be recalled here. First, the time step has a significant impact when this level of details is required and defining it in this condition is always a trade-off. It is set small enough to ensure that GB cannot move across a SPP within a single time step but large enough to reduce the errors introduced at each increment due to the reinitialization procedure [170]. Secondly, the REV dimensions ($50 \times 50\ \mu m^2$) used in these simulations are probably too small to ensure statistical representativity. Indeed, due to the large number of SPP, the mesh and the time step are both kept small and consequently the REV contains only 100 to 150 grains at the end of the simulations. This explains why the graphs of $\overline{ECD} = f(t)$ in figure 4.11 present some roughness. Some supplementary simulations would be required to ensure a better representativity. This could be achieved, for instance, thanks to the recent advances made in the context of Sebastian Florez's PhD [151].

Finally, these results confirm that using a model material without SPP is an appropriate strategy. Indeed, by using the values of reduced mobility identified without SPP, it is possible to reproduce by simulation the grain growth kinetics of materials with or without SPP.

Influence of SPP on GG To evaluate the influence of SPP over GG kinetics by simulation, a simulation representative of the heat treatment performed at $700°C$, for eight hours, is performed with the same initial microstructure, with and without SPP. The initial microstructure is generated according to the same initial grain size distribution than in section 4.2.2. Figure 4.13 displays the $\overline{ECD}$ versus time for the two simulations: with and without SPP. As one could have expected, without SPP, the average ECD increases much faster and does not saturate. After six hours of heat treatment, the $\overline{ECD}$ is equal to 4.6 μm when SPP are considered whereas it reaches 11.6 μm when no SPP are introduced. These results allow to quantify the impact of GG inhibition by SPP.

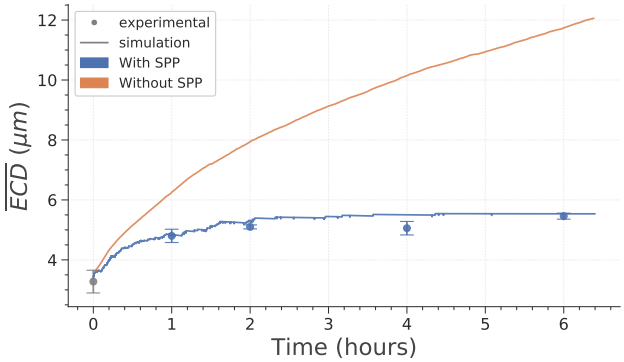


Figure 4.13: $\overline{ECD}$ versus time. Samples with equiaxed microstructure.

Simulation of GG of a basket-weaved microstructure

Now, it could be interesting to extend the previous observations to quenched microstructures. In the context of GG, colonies of parallel plates could be considered as large grains ($\overline{ECD} \approx 1\ mm$) with SPP distributed at parallel plate boundaries. Since the initial grain size is very large, the capillarity pressure is very low and no significant GB movement is expected. On the contrary, **BW** samples present thin grains that are adopting a lath shape. The curvature could be high at specific locations, such at lath ends. These grains are separated by SPP. From industrial experience, it is known that these microstructures are very stable upon heat treatments in the α-domain. Nevertheless, thanks to simulation, one could quantify the impact of SPP in such given case. To do so, two simulation cases are defined reproducing a heat treatment performed at $700°C$ and for eight hours. The initial microstructure is generated by immersing EBSD data to ensure the complex GB topology of **BW** microstructure is accurately described. In a first case, a REV of $500 \times 500\ \mu m^2$ is considered and no SPP are introduced. In a second case, a smaller REV at the center of the first case is extracted and SPP are introduced only at GB. To limit computational costs, the SPP population introduced is not the same as in previous section. An equivalent population is considered with bigger SPP, in order to use a coarser mesh and a larger time step. A unimodal SPP population is considered with diameter equal to 135 nm, which corresponds to twice the average diameter measured experimentally for the corresponding SPP population (see last column of table 4.1). To keep the ratio $\overline{r}_{\text{SPP}}/f_{\text{SPP}}$ and therefore the same global pinning pressure (see equation 1.10), the SPP volume fraction is set to $2 \times 0.52 = 1.04\%$. Initial and final microstructures are displayed in figure 4.14. This confirms the role of SPP spatial distribution over stability of **BW** microstructures.

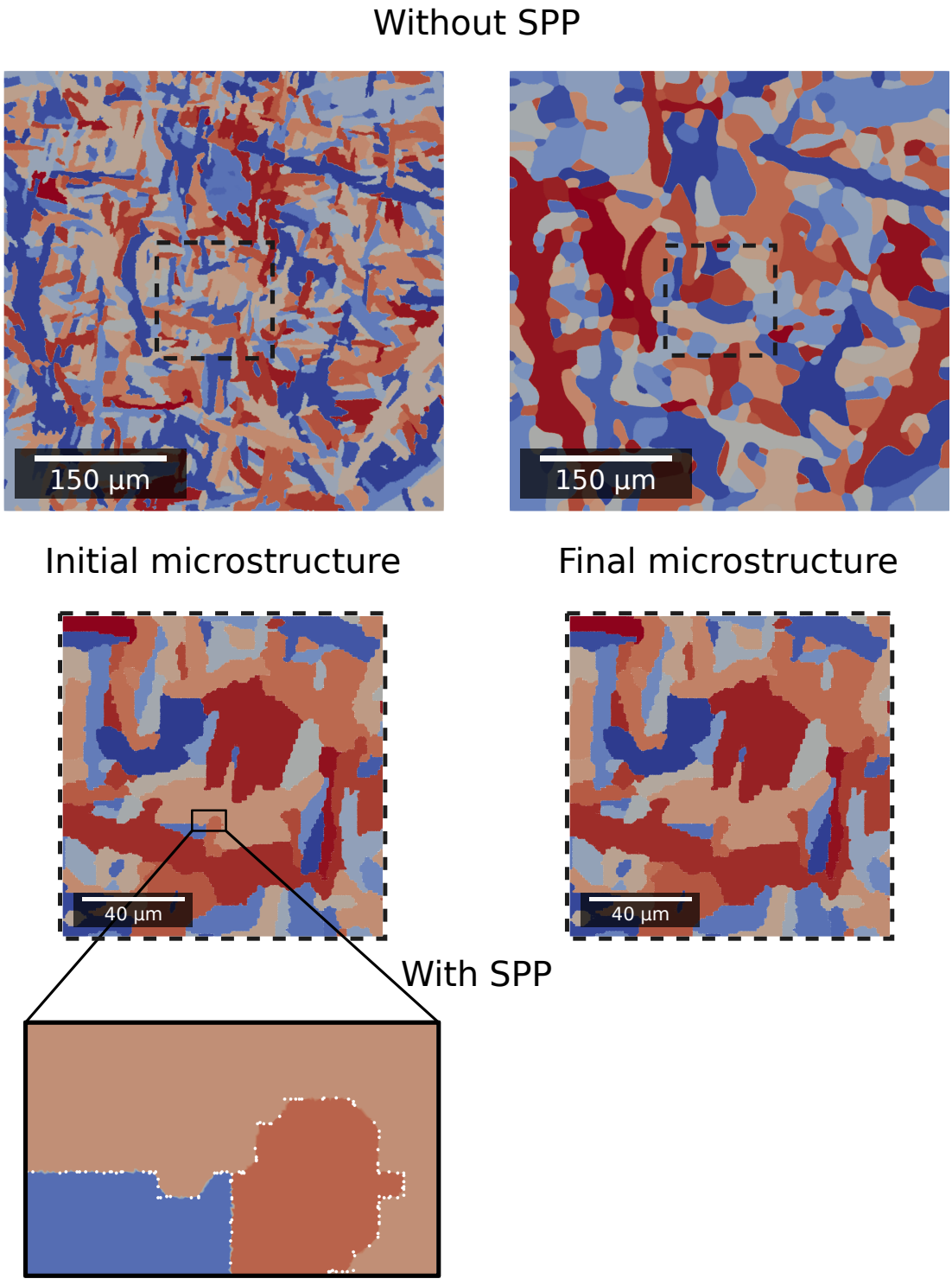


Figure 4.14: Microstructures during a five hour heat treatment at 700°C. Arbitrary color code corresponding to grain identification number. SPP are depicted as white dots, and are visible only at a greater magnification, due to their size.

4.3 Conclusion

Both experimental and numerical tools have been used successfully to quantify the role of SPP during GG of Zy-4. The experimental results confirm that the model material presenting a very low iron and chromium content (referred to as **Wo SPP**) exhibits a significantly higher GG kinetics and is able to reach $\overline{ECD}$ values approximately equal to twice the ones observed in commercial Zy-4. Finally, results obtained at three temperatures on **Eq** samples show that the limit grain size varies slightly with the heat treatment temperature, in the $600 - 700°C$ range. The TEM investigations confirm that the SPP sizes are coherent with the hypothesis of the Smith-Zener equations described in section 1.2.2. They also show that the changes in SPP size distribution are very small.

The experimental results on **Wo SPP** samples are used in a second time to identify reduced mobility for the models used in this study. The calibration procedure is detailed and a particular attention is paid to the initial grain size distribution. The parameters are then applied to simulations of GG in presence of SPP. A very good agreement with experimental data is obtained and the model ability to capture such small differences is highlighted. Finally, the influence of SPP in **Eq** and **BW** microstructures is quantified by simulations with the exact same initial microstructure, with and without SPP.

The results presented and discussed in this chapter confirm that using a model material presenting no SPP is a suitable strategy to identify reduced mobility. They also evaluate the SPP impact on final grain size in Zy-4 and confirm that they are responsible for the stability of basket-weaved microstructures under heat treatments. These takeaways are of major interest for industrial applications since they could allow to improve the control over final grain size, which is decisive to get adequate material properties.

Résumé en français

Ce chapitre concentre l'ensemble des résultats numériques et expérimentaux en lien avec la croissance de grain. Les résultats expérimentaux confirment que le matériau modèle disposant d'une proportion très faible de chrome et de fer présente une cinétique de croissance de grain bien plus rapide. Les tailles de grain limites atteintes par ce matériau sont approximativement égales au double de celles atteintes par le zircaloy-4 commercial. Les résultats sur ce dernier matériau montrent que la taille de grain maximale varie légèrement avec la température de traitement thermique. Les analyses en microscopie électronique à transmission mettent en évidence que les particules de seconde phase évoluent légèrement durant les traitements thermiques.

Les résultats expérimentaux issus du matériau ne présentant pas de précipités sont ensuite utilisés pour identifier la mobilité réduite. La procédure d'identification est décrite en détail. Ces paramètres sont ensuite appliqués afin de modéliser la croissance de grain en présence de précipités. L'accord entre ré-

sultats numériques et expérimentaux est excellent et confirme que l'utilisation d'un matériau modèle pour la calibration de la mobilité réduite constitue une solution de premier choix. Des simulations avec une microstructure initiale de type vannerie sont effectuées et confirment que les particules de seconde phase sont responsables de la stabilité de ces microstructures lors de traitements thermiques dans le domaine α.

Chapter 5

Characterization and modeling of post-dynamic recrystallization

The previous chapter has shown the abilities of the framework to predict grain boundary migration motivated by capillarity effects only. The simulation results presented in chapter 3 have shown that the implementations are able to predict formation and evolution of substructures, under various conditions. It is now time to apply these new functionalities to cases with deformation stored energy and to evaluate how complex microstructures containing both low and high angle grain boundaries evolve in this context.

This chapter gathers the experimental and simulation results related to microstructure evolution during holding at temperature in presence of stored energy due to deformation. EBSD results are analyzed extensively to obtain a broad overview of the specific features of Zy-4 PDRX. The influence of thermomechanical conditions and initial microstructure is quantified. Then, simulation and experimental results are compared in order to evaluate the model abilities and limitations. An extensive discussion is proposed to dissociate the impact of several microstructural features upon microstructure evolutions.

5.1 Characterization of PDRX

5.1.1 Mechanisms of PDRX

As discussed in section 1.2.1, the term PDRX covers different mechanisms of microstructure evolution occurring after hot deformation: recovery, formation of new recrystallized grains and migration of GB. To evaluate these mechanisms, several hot deformed microstructures are held at temperatures and characterized by EBSD (see table 2.7 for the details of the thermomechanical conditions investigated). Figures 5.1 and 5.2 illustrate the microstructural changes characterized by EBSD for **Eq** microstructure and the following thermomechanical conditions: $T = 650°C$; $\dot{\varepsilon} = 1.0\ s^{-1}$; $\varepsilon = 1.0$. The lower heat treatment duration corresponds to the delay before quenching, which is rather consistent and equal to 1 s.

In the first orientation map displayed in figure 5.1, which is representative of the initial state quenched after deformation without subsequent hold at temperature, most grains have an elongated shape. They present orientation gradients and well-defined substructures. A large number of small equiaxed grains are also noticeable. They are distributed rather homogeneously throughout the whole microstructure. The corresponding KAM map in figure 5.2 points out that some of the small grains are clustered and exhibit low KAM values and thus low stored energy. Figures 5.1 and 5.2 show that a limited number of grains are able to grow. These grains have a homogeneous orientation and a more equiaxed shape, compared to the deformed matrix. The growth of a limited number of grains tends to highlight the microstructure stability. This can be related to the ability of the material to recover and form substructures to reduce the system energy, during the previous hot deformation stage. This is confirmed by analyzing the evolution of LAGB specific length (LAGB length per surface area) with holding time, plotted in figure 5.3. Indeed, the LAGB specific length decreases slowly with time, especially the one of LAGB enclosing subgrains. The decrease starts to be important after approximately 25 s, when the growth of recrystallized grains is really noticeable.

Finally, figure 5.4 displays the evolution of recrystallized fraction and $\overline{ECD}_{rx}$ with holding time. Figure 5.4a confirms that recrystallization is not complete after a 200 s heat treatment performed after consequent deformation $\dot{\varepsilon} = 1.0\ s^{-1}$; $\varepsilon_f = 1.35$. The general kinetics of recrystallization is consistent with the GB mobility values identified in section 4.2.1. Indeed, at $650°C$, the GB mobility is estimated to $3.5 \times 10^{-15}\ m^4.J^{-1}.s^{-1}$ and the dislocation line energy to $1.2 \times 10^{-9} J.m^{-1}$. For a dislocation density gap of $10^{16}\ m^{-2}$, this leads to GB velocity approximately equal to 2.5 $\mu m.min^{-1}$.

Figures 5.4a and 5.4b both show that the growth of recrystallized grains is significant after 50 s of heat treatment. This observation is consistent with the ones made previously. Indeed, the tendency of the material to recover and form a large quantity of LAGB and subgrains during hot deformation reduces the driving pressures for the growth of recrystallized grains. Moreover, the numerous small grains/subgrains are initially competing to consume the deformed matrix.

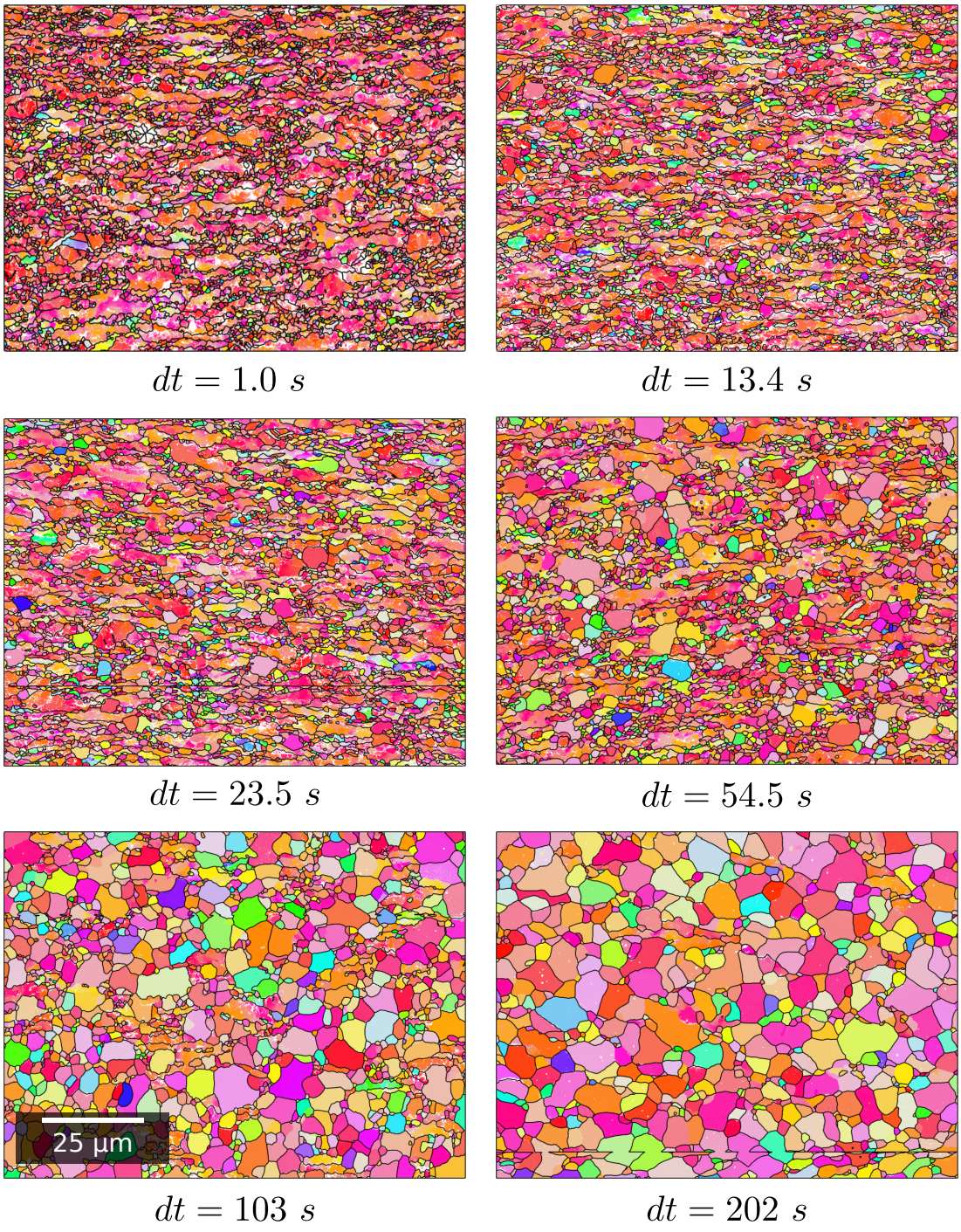


Figure 5.1: EBSD orientation maps showing microstructure evolution during holding at $T = 650°C$ after hot deformation ($T = 650°C$; $\dot{\varepsilon} = 1.0\ s^{-1}$; $\varepsilon = 1.0$). IPF Y color code.

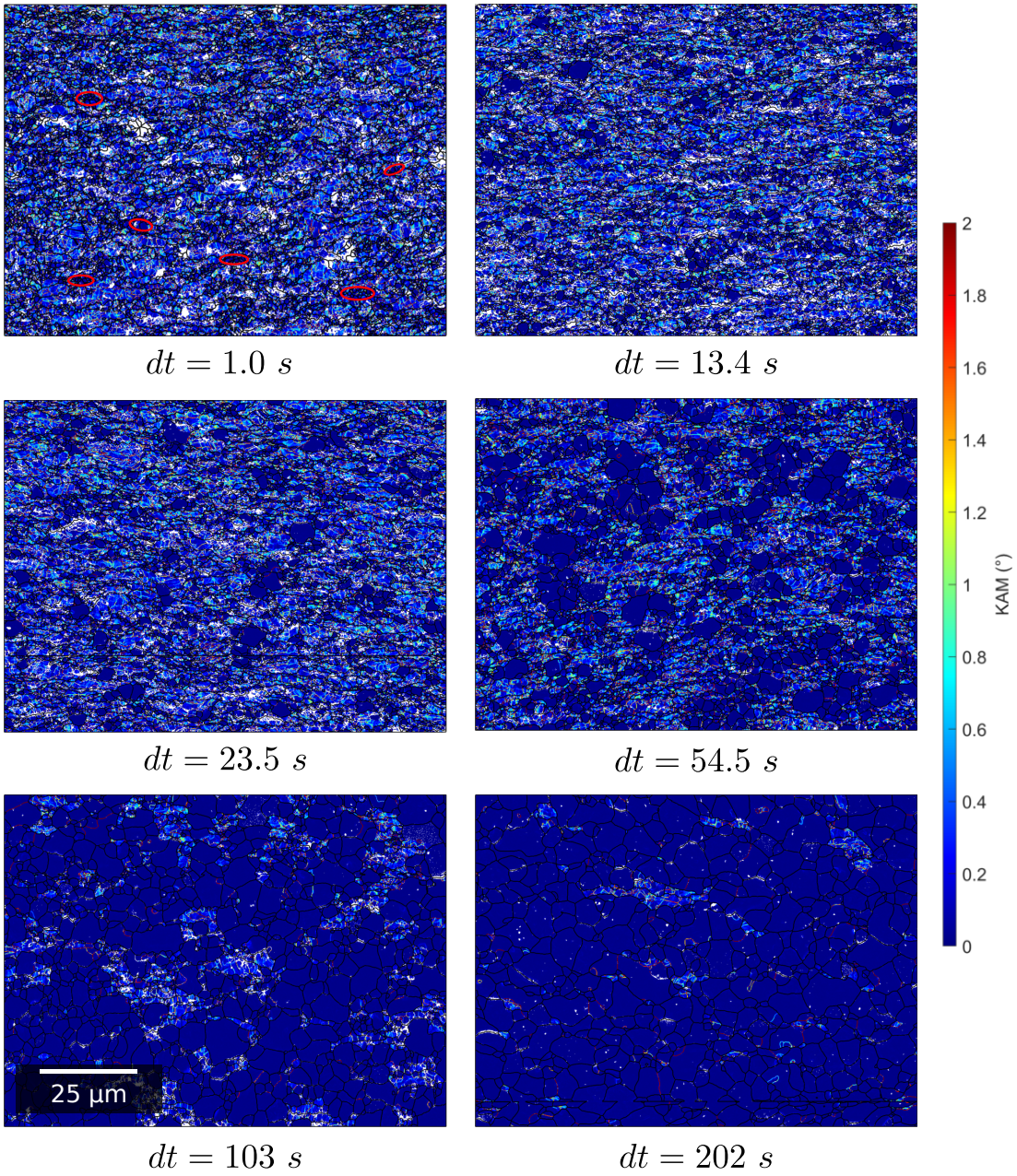


Figure 5.2: EBSD KAM maps showing microstructure evolution during holding at $T = 650°C$ after hot deformation ($T = 650°C$; $\dot{\varepsilon} = 1.0\ s^{-1}$; $\varepsilon = 1.0$).

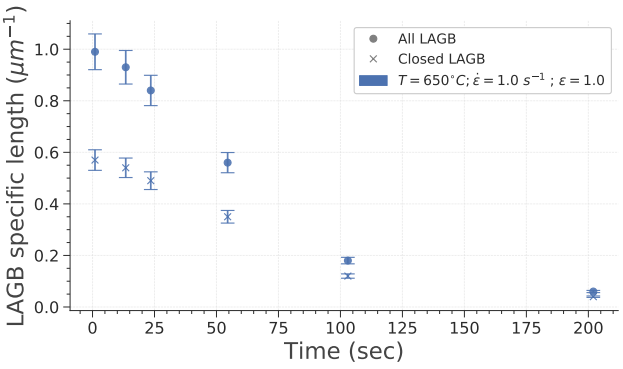
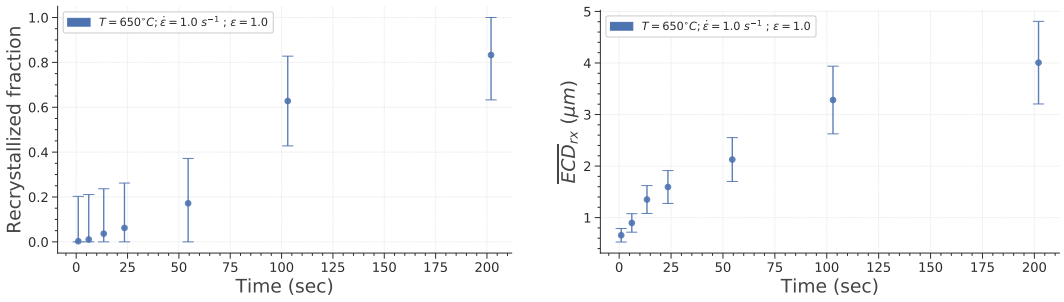


Figure 5.3: LAGB specific length evolution during holding at $T = 650°C$. **Eq** samples.

Therefore, the growth of recrystallized grains is initially slow. Then, once some of the grains with a low dislocation density have succeeded to consume some deformed area and to gain a sufficient advantage, the growth kinetics increases notably.

The average dislocation density over the whole surface is plotted in figure 5.5. The decrease seems to be really noticeable after 50 s, when recrystallized fraction exhibits an important increase and exceeds 50%.

Figure 5.6 presents the $\{0002\}$ and $\{10\bar{1}0\}$ pole figures at three instants of the heat treatment. It emphasizes the weakening of the main texture component inherited from deformation. The decrease of the texture index, from 2.6 at $dt = 1.0\ s$ to 1.7 at $dt = 202\ s$ confirms this qualitative observation. Upon PDRX, <c> axis stays tilted by a 30° angle from compression direction.



(a) Recrystallized fraction versus time.

(b) $\overline{ECD}_{rx}$ versus time.

Figure 5.4: Evolution of properties related to recrystallization during holding at $T = 650°C$. **Eq** samples.

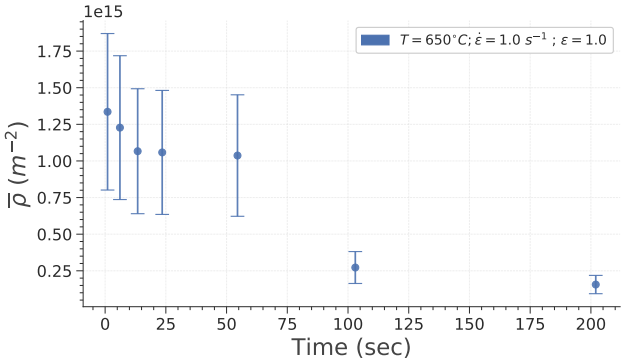
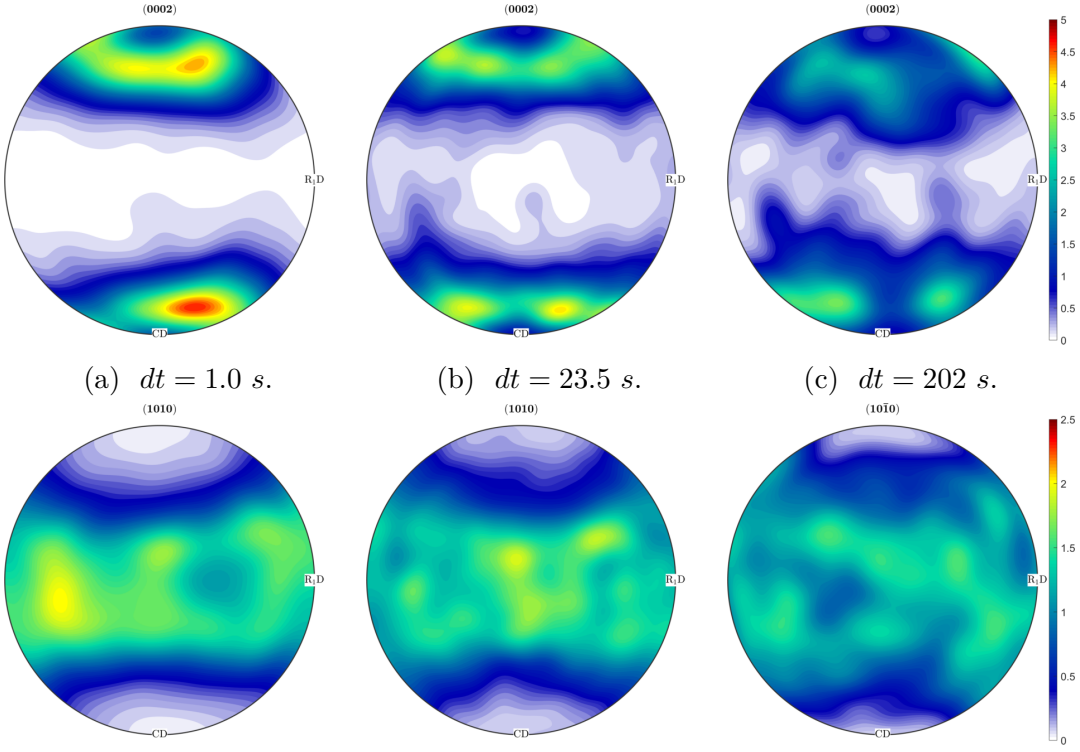


Figure 5.5: Evolution of averaged GND density during holding at $T = 650°C$. **Eq** samples.



(a) $dt = 1.0\ s.$ (b) $dt = 23.5\ s.$ (c) $dt = 202\ s.$

(d) $dt = 1.0\ s.$ (e) $dt = 23.5\ s.$ (f) $dt = 202\ s.$

Figure 5.6: $\{0002\}$ and $\{10\bar{1}0\}$ pole figures showing texture evolution during holding at $T = 650°C$ after hot deformation ($T = 650°C$; $\dot{\varepsilon} = 1.0\ s^{-1}$; $\varepsilon = 1.0$). **Eq** samples.

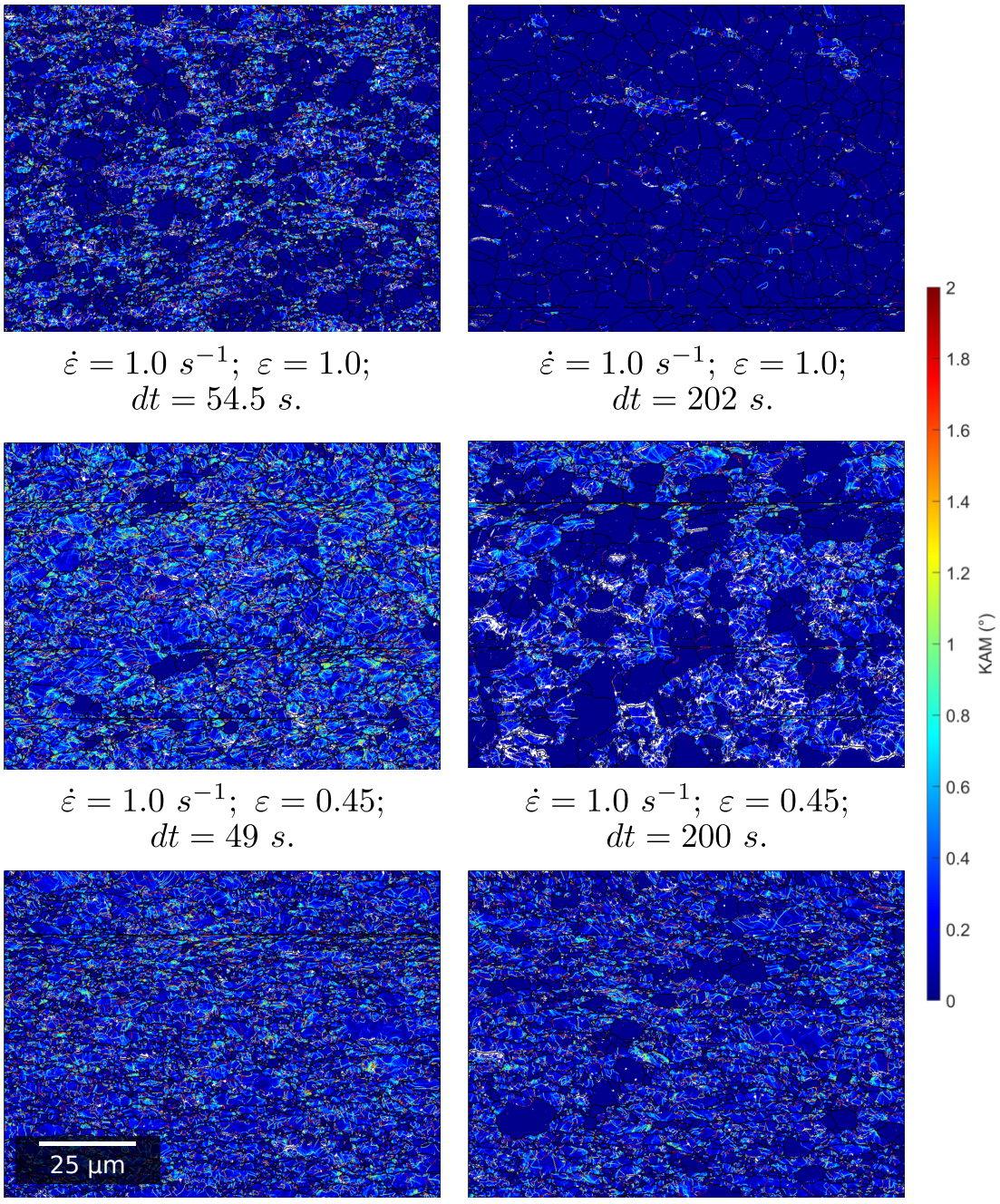
5.1.2 Influence of thermomechanical conditions

Now that consistent and reliable data are available for several thermomechanical conditions, it is possible to evaluate the influence of strain rate and final strain over post-dynamic evolutions. KAM maps corresponding to 50 and 200 s heat treatments are presented in figure 5.7. They highlight notably how the strain rate and the final strain impact strongly the recrystallization kinetics during subsequent holding at temperature. This is confirmed by figure 5.8 which describes the evolution of recrystallized fraction and $\overline{ECD}_{rx}$ with time. These plots confirm the observations that have been reported several times for other materials: increasing strain rate and/or final strain leads to faster recrystallization in post-dynamic regime [18]. The different growth kinetics of recrystallized grains depicted in figure 5.8b are remarkable. Indeed, it appears that decreasing the final strain level from 1.0 to 0.45 affects to a lower extent the average recrystallized grain size, compared to the recrystallized fraction. This points out that decreasing the final strain leads to a small decrease of driving pressure (i.e. stored energy of deformation) and to a large decrease of the number of recrystallized grains. On the contrary, decreasing the strain rate leads to an important decrease of the recrystallized grain size.

Two hypotheses could be proposed to explain the differences observed previously regarding the influence of thermomechanical conditions over recrystallization kinetics. One considers that thermomechanical conditions affect mainly the growth of small recrystallized grains. The other assumes that they impact the formation of these grains. They can be explained as follows:

- Within the ranges considered here, decreasing strain rate would contribute to lower dislocation density to a higher extent. A decrease of final strain from 1.0 to 0.45 would also lead to obtain a more heterogeneous distribution of stored energy. Therefore, the recrystallized grains would grow preferentially in clusters, as observed in figure 5.2. Then, the growth of these grains would be slowed down due to early impingement. This hypothesis is consistent with the clusters of recrystallized grains observed in figure 5.2 and with the divergence of the growth kinetics after 50 s of heat treatment, seen in figure 5.8b.

- Strain rate and final strain levels could affect the substructure. To address that question, LAGB specific length and length ratio are plotted in figure 5.9. The results indicate that strain rate impacts LAGB specific length and strain level affects the LAGB length ratio. This would prove that decreasing the strain rate induces a decrease of the length of LAGB formed during hot deformation but still leads to formation of a significant number of HAGB. On the other hand, when decreasing the final strain level, the quantity of LAGB formed stays important but a lower number of LAGB transforms to HAGB. The formation of a lower fraction of HAGB results directly in a lower number of small recrystallized grains at the beginning of PDRX.



$\dot{\varepsilon} = 1.0\ s^{-1};\ \varepsilon = 1.0;$
$dt = 54.5\ s.$

$\dot{\varepsilon} = 1.0\ s^{-1};\ \varepsilon = 1.0;$
$dt = 202\ s.$

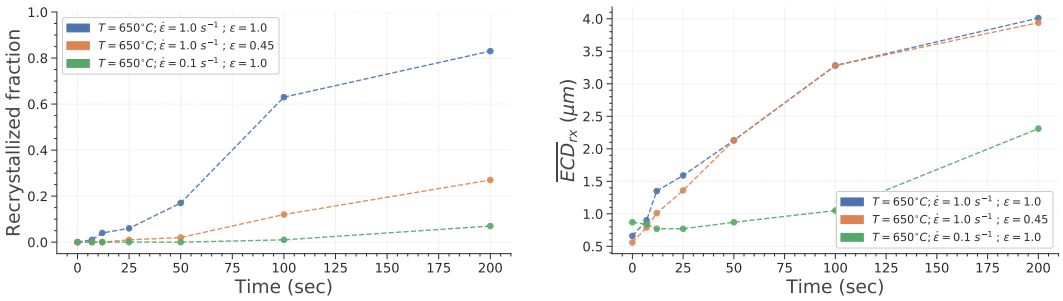
$\dot{\varepsilon} = 1.0\ s^{-1};\ \varepsilon = 0.45;$
$dt = 49\ s.$

$\dot{\varepsilon} = 1.0\ s^{-1};\ \varepsilon = 0.45;$
$dt = 200\ s.$

$\dot{\varepsilon} = 0.1\ s^{-1};\ \varepsilon = 1.0;$
$dt = 54\ s.$

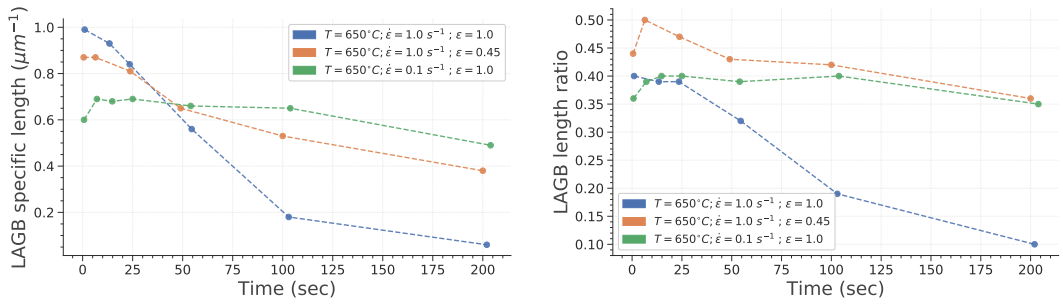
$\dot{\varepsilon} = 0.1\ s^{-1};\ \varepsilon = 1.0;$
$dt = 204\ s.$

Figure 5.7: KAM maps showing microstructural state during holding at temperature, for three different deformation conditions. **Eq** samples.



(a) Recrystallized fraction versus time. (b) $\overline{ECD}_{rx}$ versus time.

Figure 5.8: Evolution of properties related to recrystallization during holding at $T = 650°C$. **Eq** samples.



(a) LAGB specific length versus time. (b) LAGB length ratio versus time.

Figure 5.9: Evolution of GB lengths during holding at $T = 650°C$. **Eq** samples.

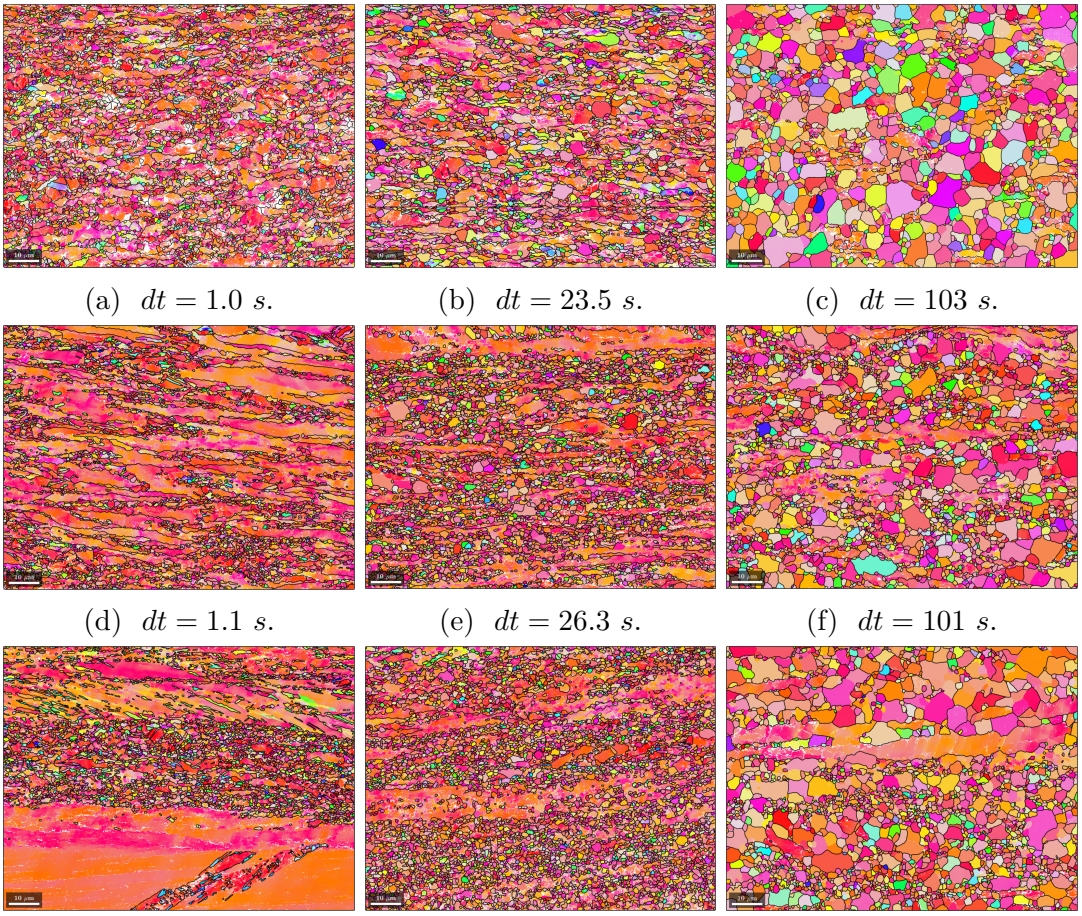
Some additional investigations and discussions are given in the following chapter (section 6.1). Indeed, the observed features are related to the previous hot deformation stage.

5.1.3 Influence of initial microstructure

EBSD orientation maps after holding at temperature at three durations, following hot deformation and for three different initial microstructures are displayed in figure 5.10. The first striking difference is the level of heterogeneity concerning initial microstructure, right after deformation. This is confirmed by GND density maps provided in figure 5.11. These maps present a 16× larger area which ensures sufficient representativity. Since the extent of heterogeneity is largely inherited from CDRX, it will be discussed in more details in section 6.1. The second difference that one can notice is the presence of a higher number of very small grains in deformed lamellar microstructures, generally clustered in horizontal bands. To evaluate quantitatively these first remarks, the evolution of recrystallized fraction and $\overline{ECD}_{rx}$ are plotted in figure 5.12.

First, it can be noticed from figure 5.12a that if initially, recrystallization kinetics for the three microstructures are comparable, lamellar microstructures (**BW** and **PP**) present a lower recrystallized fraction for longer durations. The same observation can be made looking at $\overline{ECD}$ of recrystallized grains, but to a greater extent. To assess that in more details, the recrystallized grain size distributions for a heat treatment of approximately 100 s at $T = 650°C$ are plotted in figure 5.13. This confirms quantitatively that numerous small recrystallized grains ($ECD_{rx} \leq 1\mu m$) are still present for the two lamellar microstructures, whereas very few are observable for **Eq** initial microstructure. The analysis of figure 5.14, which presents the evolution of GB specific length, reveals that initial microstructure does not seem to affect the quantity of LAGB durably. On the opposite, it impacts the HAGB specific length, both lamellar microstructures presenting a higher value. This is consistent with figures 5.10 and 5.13 showing a higher number of small recrystallized grains for **BW** and **PP**.

According to these remarks, it appears that the differences in terms of PDRX behavior caused by initial microstructure seems to be mainly related to the number and the localization of the recrystallized grains, at the beginning of the PDRX stage. Indeed, since there are more recrystallized grains in lamellar microstructures and since they are more grouped, they impinge themselves earlier and this leads to a reduction of the recrystallization kinetics. This hypothesis can be confirmed by looking at GND density maps for the three initial microstructures after ≈ 25 s and after ≈ 50 s (figure 5.15). These maps confirm that after ≈ 50 s of heat treatment, recrystallized grains start to impinge themselves only for lamellar microstructures, whereas there are distributed rather homogeneously throughout the microstructure in **Eq** sample. These observations are consistent with the discussion proposed by Hiwarkar and coworkers [203]. Additional discussions about the sources of these differences are provided in section 6.1.



(a) $dt = 1.0\ s.$ (b) $dt = 23.5\ s.$ (c) $dt = 103\ s.$

(d) $dt = 1.1\ s.$ (e) $dt = 26.3\ s.$ (f) $dt = 101\ s.$

(g) $dt = 0.7\ s.$ (h) $dt = 26.3\ s.$ (i) $dt = 100\ s.$

Figure 5.10: EBSD orientation maps showing microstructure evolution during holding at $T = 650°C$ after hot deformation ($T = 650°C$; $\dot{\varepsilon} = 1.0\ s^{-1}$; $\varepsilon_f = 1.0$). a), b) and c) figures correspond to **Eq** microstructures, d), e) and f) to **BW** microstructures and g), h) and i) to **PP** microstructures. IPF Y color code.

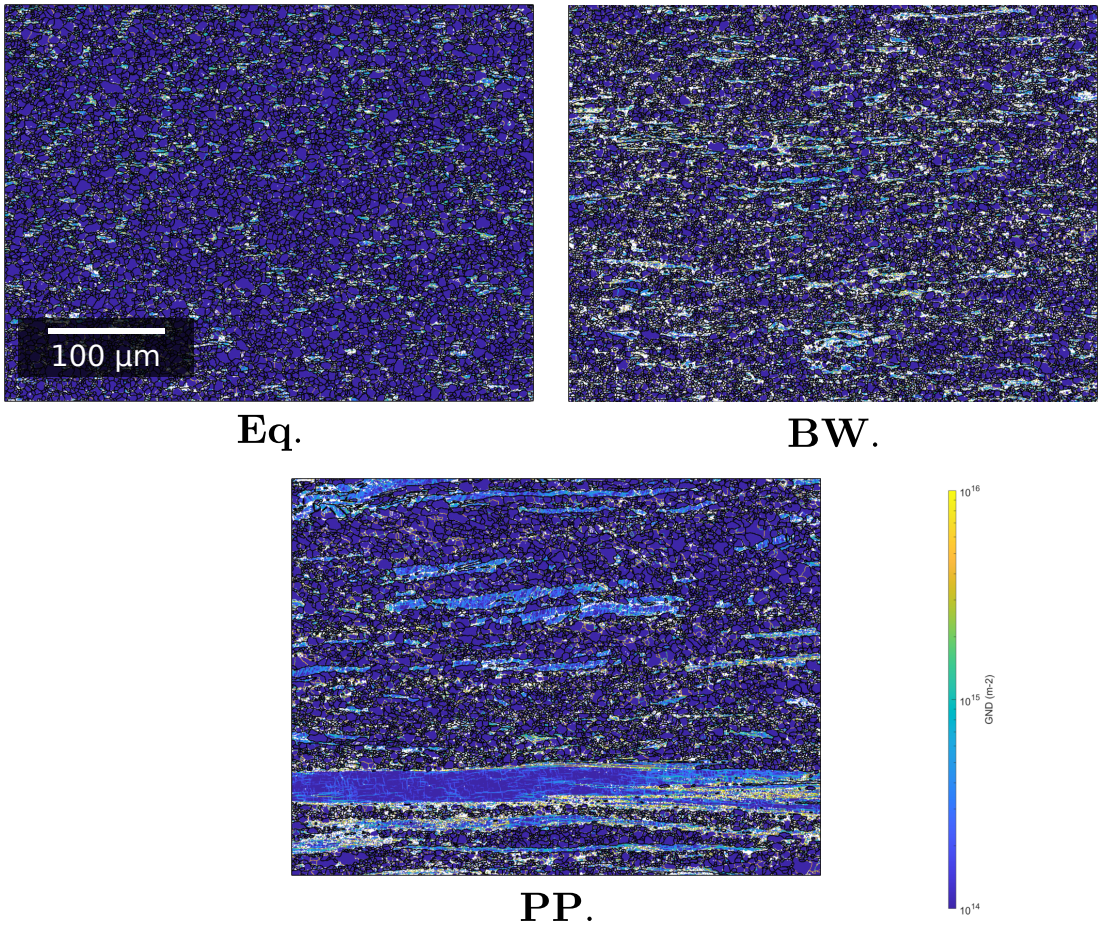
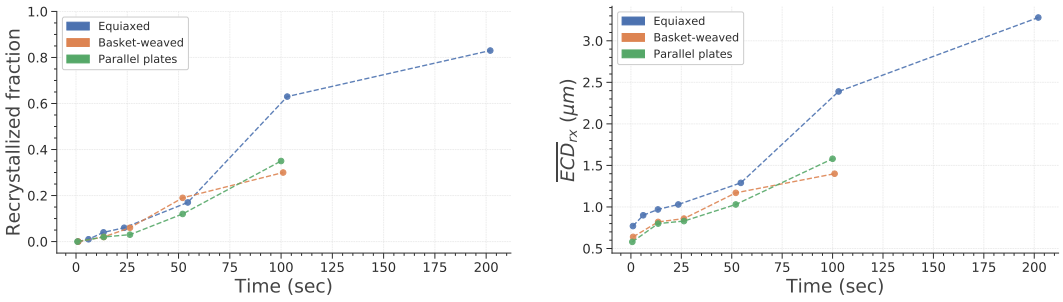


Figure 5.11: GND density maps computed from EBSD data, for the following thermomechanical conditions: $T = 650°C$; $\dot{\varepsilon} = 1.0\ s^{-1}$; $\varepsilon = 1.0 - 1.2$; $dt = 100\ s$.



(a) Recrystallized fraction versus time.

(b) $\overline{ECD}_{rx}$ versus time.

Figure 5.12: Evolution of properties related to recrystallization during holding at $T = 650°C$.

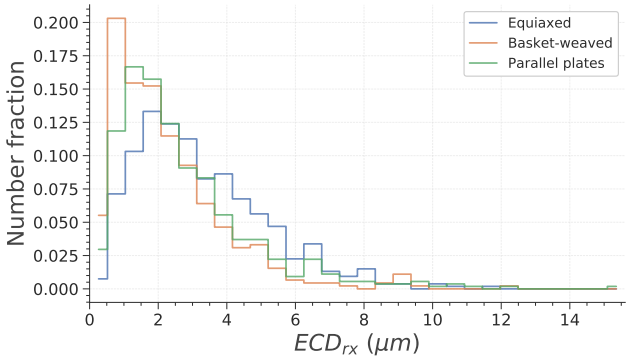
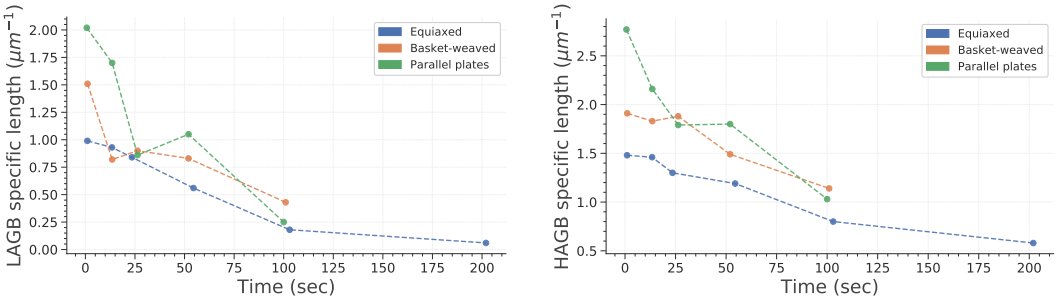
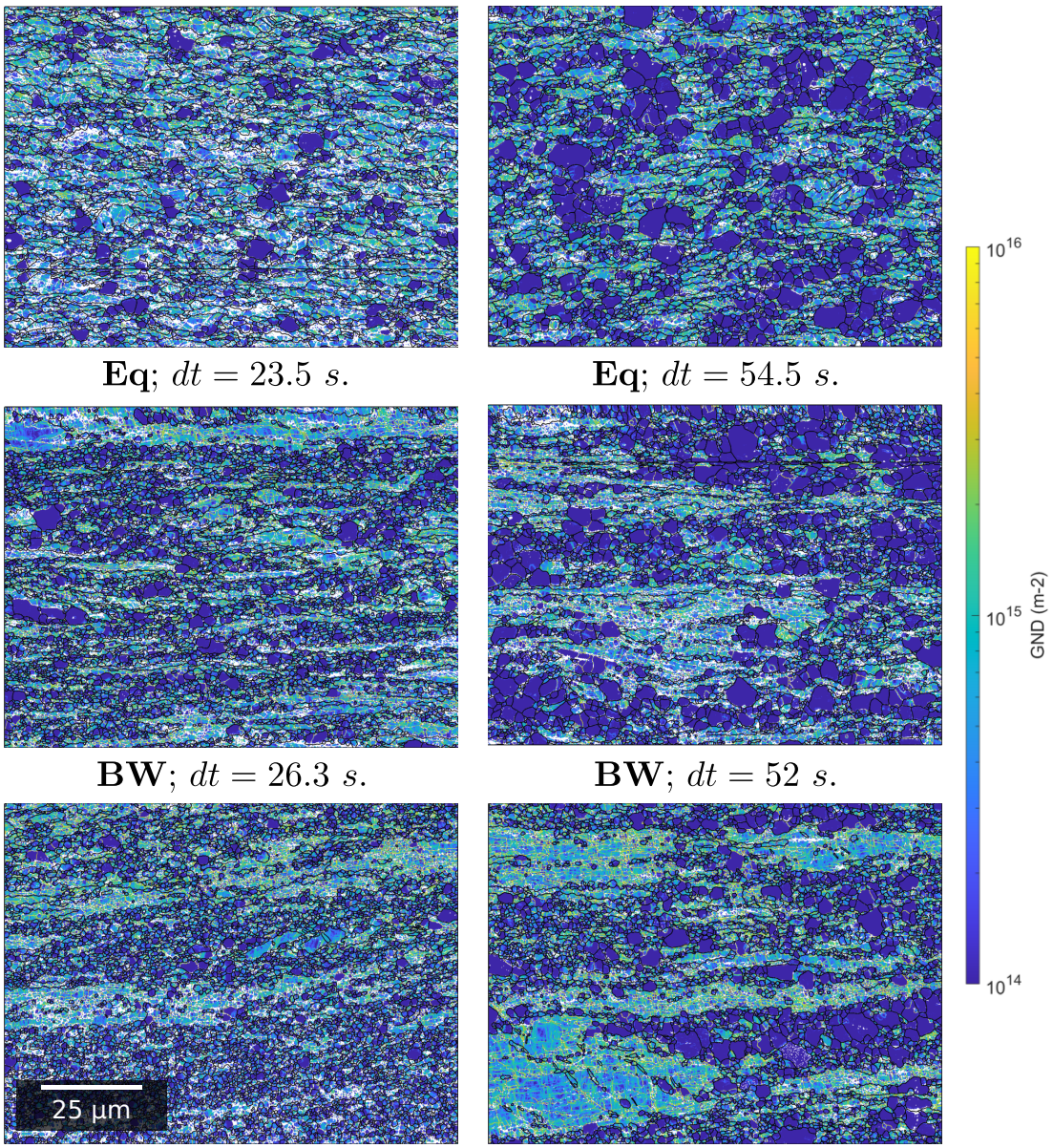


Figure 5.13: ECD_{rx} number distribution for a hold duration of 100 s at $T = 650°C$.



(a) LAGB specific length versus time. (b) HAGB specific length versus time.

Figure 5.14: Evolution of properties related to LAGB during holding at $T = 650°C$.



Eq; $dt = 23.5\ s.$ **Eq**; $dt = 54.5\ s.$

BW; $dt = 26.3\ s.$ **BW**; $dt = 52\ s.$

PP; $dt = 26.5\ s.$ **PP**; $dt = 52\ s.$

Figure 5.15: GND density maps computed from EBSD data. a) and d) figures correspond to **Eq** microstructures, b) and e) to **BW** microstructures, c) and f) to **PP** microstructures.

5.2 Simulation of PDRX

5.2.1 Principle of PDRX simulations

To model PDRX, the strategy chosen is to rely as much as possible on EBSD data. Thus, the digital microstructures are initialized by immersing experimental images (see section 3.1.4 for more details). Several experimental images are used to initialize: grain topology, grain average orientation and grain average GND (GAGND) density. Orientation is averaged per grain and subgrain. To be consistent, GND density is computed by excluding LAGB.

GB mobility is considered isotropic and GB energy taken heterogeneous, varying with disorientation according to Read-Shockley equation (equation 1.2). GB energy of HAGB is defined by the value presented in section 4.2.1 ($\gamma_{max} = 0.22\ J.m^{-2}$). GB mobility varies with temperature according to equation 4.3. Based on the experimental results presented in section 5.1, it is assumed that formation of new grains/subgrains takes place only during CDRX, i.e. MDRX is considered here. Indeed, these results do not bring any evidence of the formation of new grains/subgrains in the post-dynamic regime. Thus, it constitutes a valid working hypothesis. In the simulations where no additional details are given, GND is considered uniform within grains (by averaging the GND density estimated from EBSD data in each grain). Some supplementary simulations considering intragranular GND density gradients are provided in section 5.2.4. Considering uniform dislocation density per grain is a common simplification that provides satisfactory recrystallization kinetics in regards of experimental results and limits numerical instabilities related to high local stored energy gradients [163, 204]. In that context, the energy gradient across GB ($[\![E]\!]$) is underestimated at the first instant of recrystallization. Indeed, behind the recrystallization front, the dislocation density is equal to the average grain dislocation density. However, if dislocation density is not averaged inside the grain, the dislocation density in that area should be equal to ρ_0. This is illustrated in figure 5.16 where the GND and average GND density are displayed. In the zone surrounded by a red circle, the dislocation density gradient is much higher if heterogeneous GND density fields are considered. Obviously, at some given points of the microstructure, the averaging operation could have the opposite effect. However, on average, averaging GND density tends to reduce the energy gradient across the GB since in reality, the GND density should be almost equal to ρ_0 behind every migrating boundary. Consequently, a parameter $\delta(\dot{\varepsilon})$ has been introduced by Maire *et al.* to correct that effect [26]. This parameter is considered to vary only with strain rate since strain rate affects the extent of GND heterogeneities. In the simulations considering average GND density per grain, it has been set equal to: $\delta(0.1) = 1$ and $\delta(1.0) = 8$.

Finally, temperature varies with time and is defined by the results of the corresponding thermomechanical simulation.

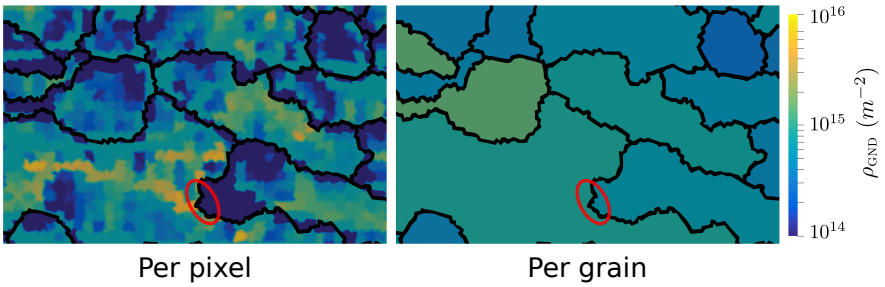
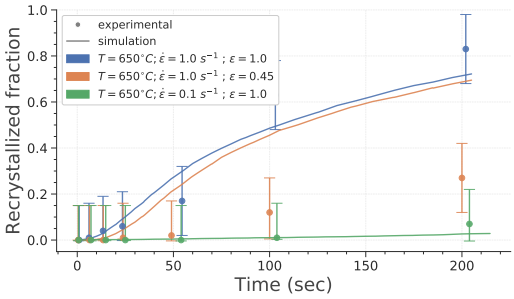


Figure 5.16: GND density, per pixel or averaged per grain, immersed into simulations. Red circles highlight a zone of interest discussed in the text.

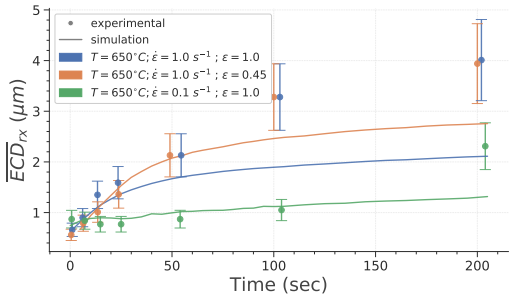
5.2.2 Influence of thermomechanical conditions

To evaluate the model predictions in PDRX regime and for different sets of thermomechanical conditions (ε and $\dot{\varepsilon}$), three microstructures are immersed. They correspond to the microstructural state obtained when the quench is performed after hot deformation. For the three cases, this delay ranges from 0.7 s to 1.1 s. The samples have been deformed in the following conditions: $T = 650°C$, $\dot{\varepsilon} = 1.0\ s^{-1}$, $\varepsilon = 1.0$; $T = 650°C$, $\dot{\varepsilon} = 1.0\ s^{-1}$, $\varepsilon = 0.45$ and $T = 650°C$, $\dot{\varepsilon} = 0.1\ s^{-1}$, $\varepsilon = 1.0$. Figure 5.17 presents the evolution of the main microstructure characteristics versus holding time: the recrystallized fraction, the average recrystallized grain size, and the LAGB specific length. Several observations can be made from these graphs. First, it appears that the model predicts correctly the recrystallized fraction for the samples with the highest strain level ($T = 650°C$; $\dot{\varepsilon} = 0.1 - 1.0\ s^{-1}$; $\varepsilon_f = 1.0$). Regarding the prediction of $\overline{ECD}_{rx}$, it should be emphasized that the model predicts correctly the growth of recrystallized grains up to 50 s. For longer durations, the model underestimates the $\overline{ECD}_{rx}$. Finally, it is noteworthy to mention that the trends for LAGB specific length evolution during PDRX are correctly predicted, for the different thermomechanical conditions considered here.

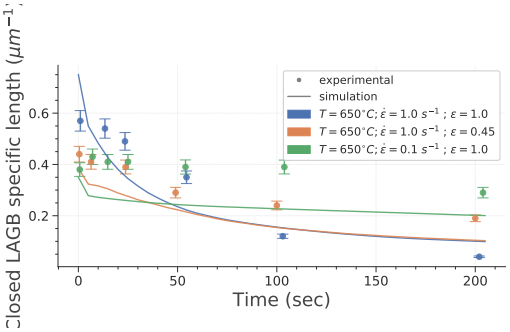
Images of the digital microstructures after 100 s heat treatment, for two different deformation levels, are compared to experimental images in figure 5.18. In addition, some ECD_{rx} distributions are plotted in figure 5.19. These two figures show that simulations predict that a large number of recrystallized grains are formed, which is not observed experimentally, especially at lower strains. Moreover, the recrystallized grains that are formed in simulation have a very narrow size distribution, on the contrary to the experimental evidences. These remarks allow to explain why both recrystallized fraction and $\overline{ECD}_{rx}$ are poorly predicted for the lower strain rate. One or more microstructural feature(s) are neglected or oversimplified into simulations. Consequently, the simulation cases presented here do not capture the heterogeneities and thus the growth of a small number of grains.



(a) Recrystallized fraction versus time.



(b) $\overline{ECD}_{rx}$ versus time.



(c) LAGB specific length versus time.

Figure 5.17: Evolution of the main microstructure descriptors with time, during PDRX simulations. **Eq** samples.

5.2.3 Influence of initial microstructure

Results from three additional simulation cases are now investigated. Initial digital microstructures correspond to samples deformed in the following conditions: $T = 650°C$; $\dot{\varepsilon} = 1.0\ s^{-1}$; $\varepsilon_f \in [1.0;\ 1.2]$ and with **Eq**, **PP** or **BW** initial microstructures. As previously, the evolution of the main microstructure variables are plotted in figure 5.20. From the first graph, one can observe that the recrystallization kinetics are correctly predicted for the three microstructures. From the two others, one can observe that the model predictions are in the right order of magnitude but exhibit some discrepancies with the experimental results. The evolution of average recrystallized grain size with time are correctly predicted for lamellar microstructures. For **Eq** microstructures, the predictions are consistent until 50 s of heat treatment, as discussed previously. Finally, the decrease of LAGB specific length with time predicted by simulations is consistent with experimental measurements, except for **PP** microstructure. This last difference between experimental and simulation results is induced by the initial microstructure. Indeed, it appears that the LAGB specific length measured for the sample immersed into simulation is rather low, in comparison to the measurements obtained for samples held longer at temperature. Consequently, this difference should not be taken into account in the latter discussion on the origin of the numerical results discrepancies.

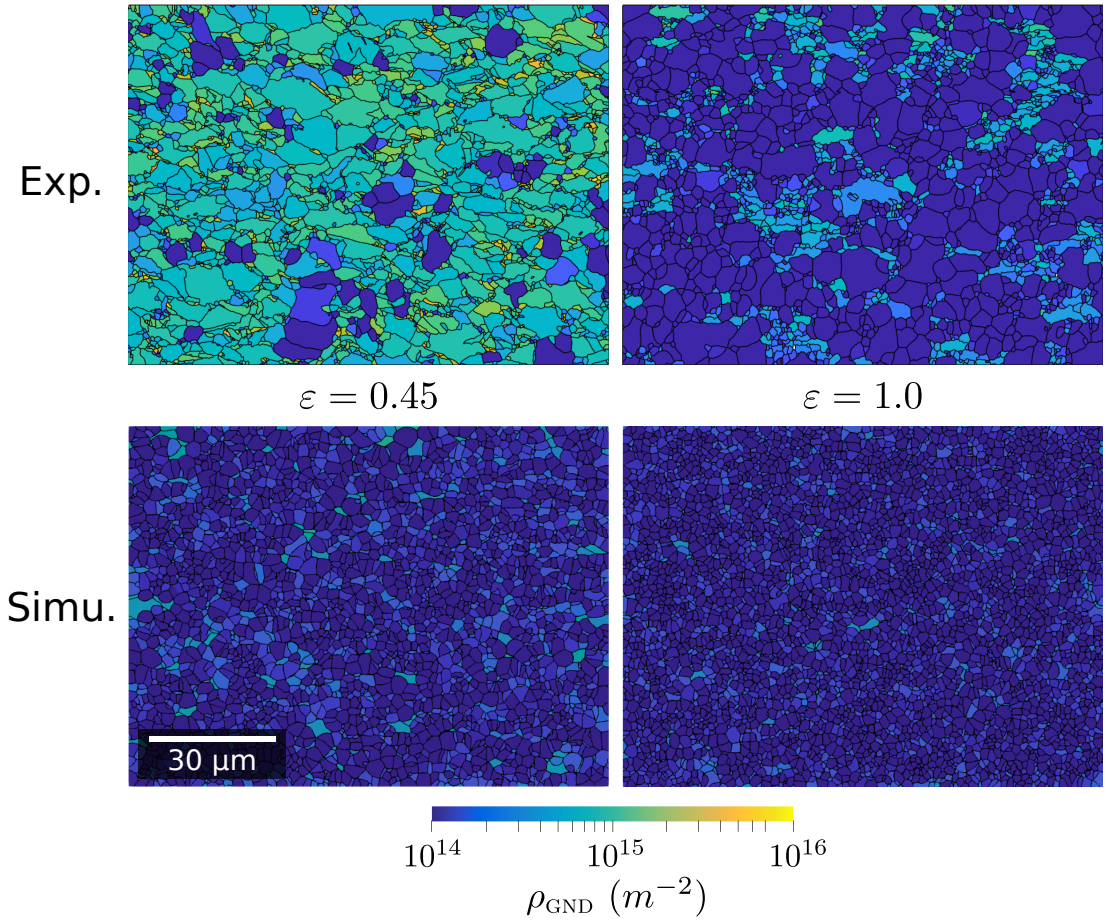
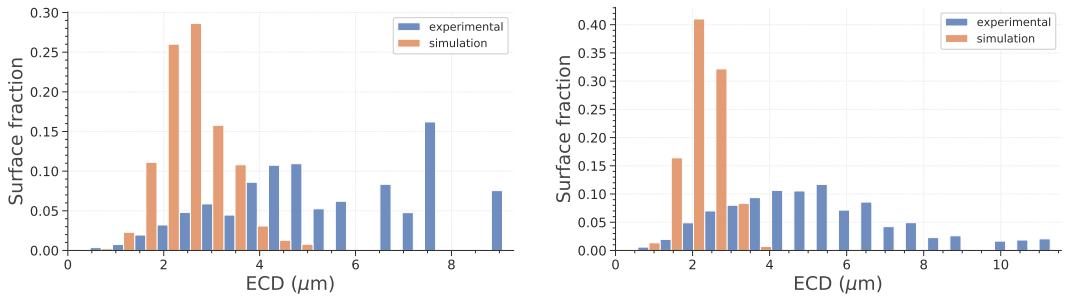
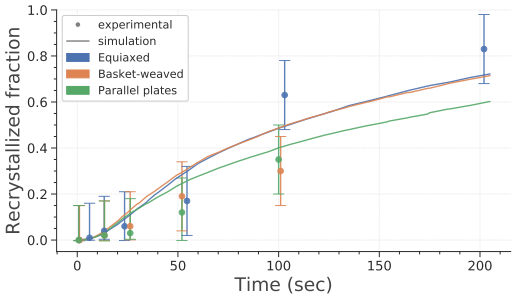


Figure 5.18: GAGND maps from EBSD and simulation data, after 100 s at $T = 650°C$. Hot deformation conditions are: $T = 650°C$; $\dot{\varepsilon} = 1.0\ s^{-1}$; $\varepsilon = 0.45 - 1.0$. **Eq** samples.

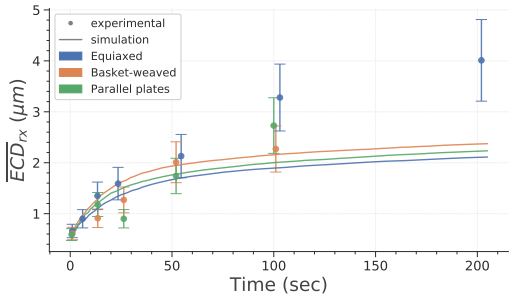


(a) $\varepsilon = 0.45$. (b) $\varepsilon = 1.0$.

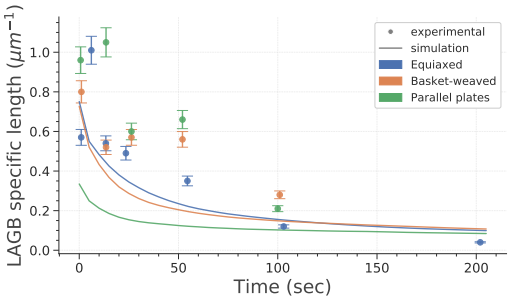
Figure 5.19: ECD_{rx} surface weighted distributions, after 100 s at $T = 650°C$, from experimental and simulation results. $T = 650°C$; $\dot{\varepsilon} = 1.0\ s^{-1}$. **Eq** samples.



(a) Recrystallized fraction versus time.



(b) $\overline{ECD}_{rx}$ versus time.

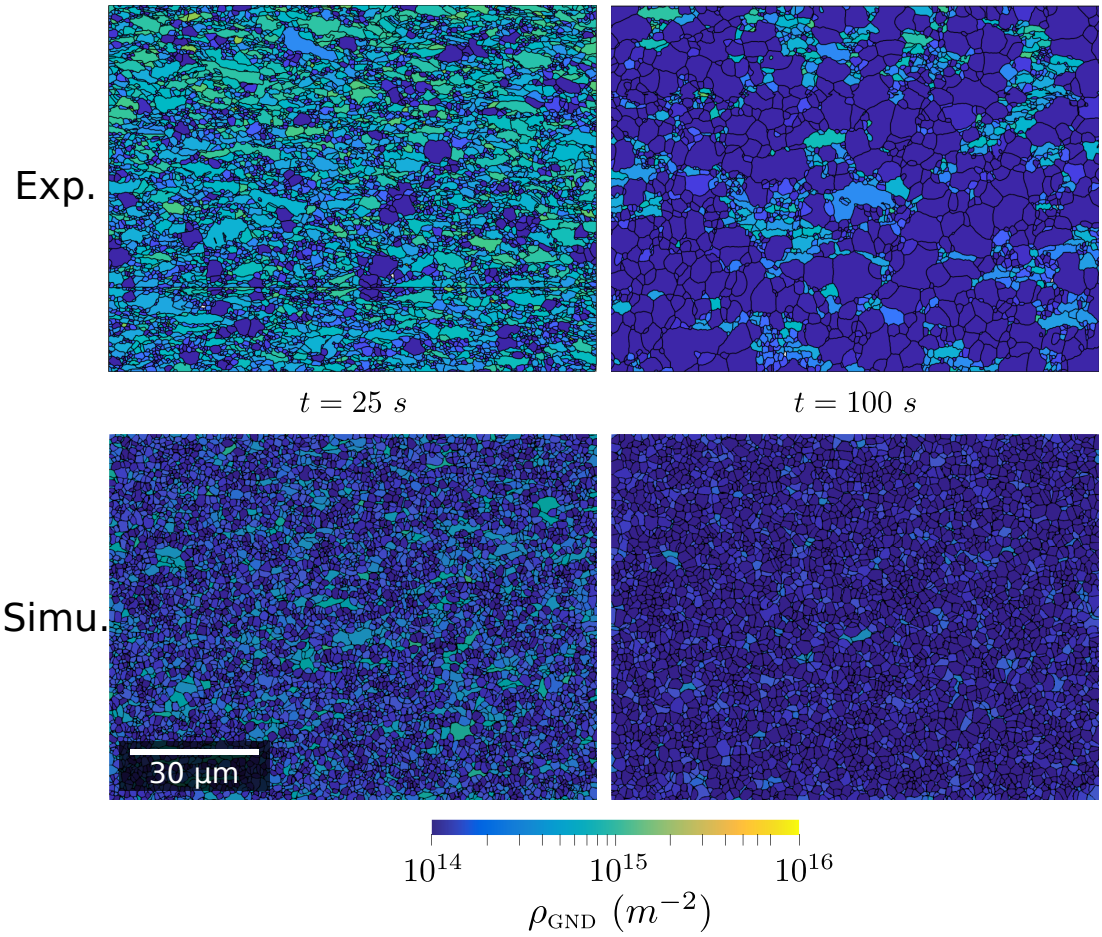


(c) LAGB specific length versus time.

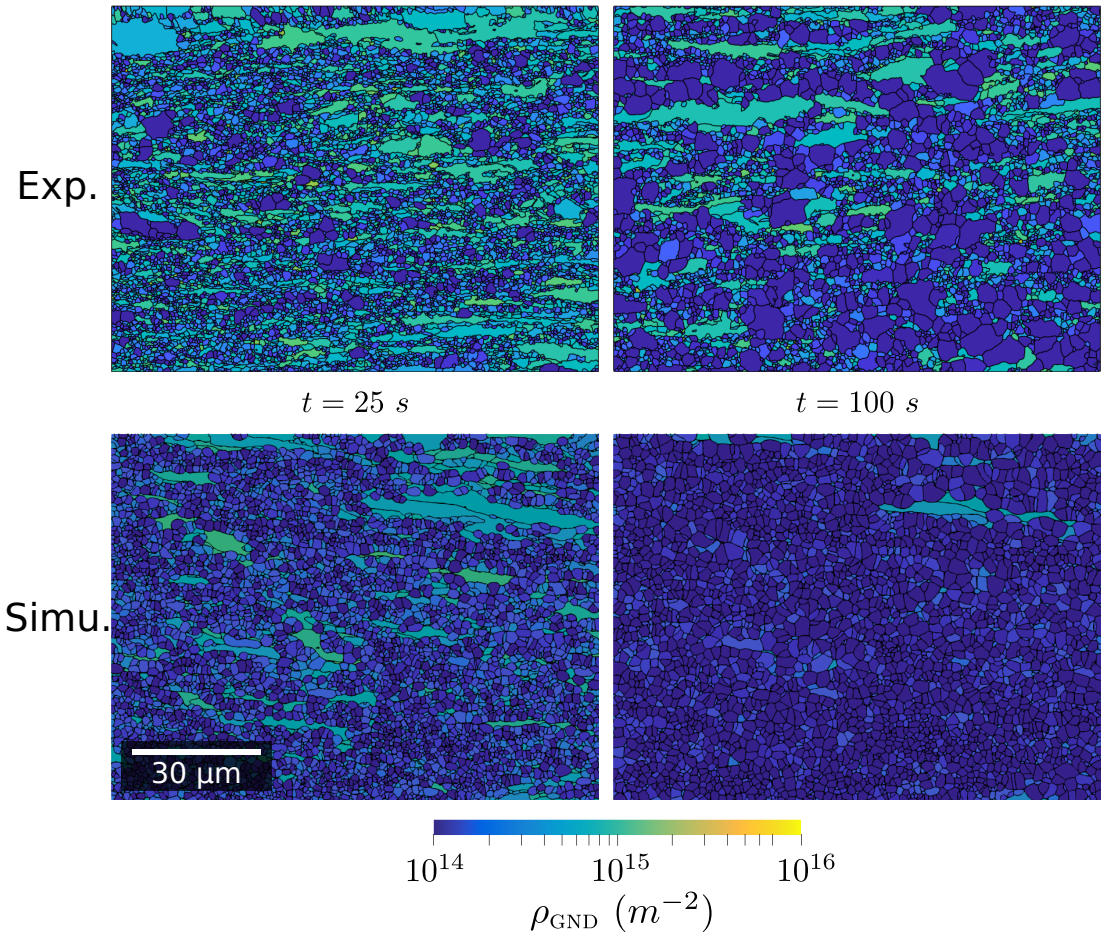
Figure 5.20: Evolution of the main microstructure descriptors with time, during PDRX simulations. **Eq**, **BW** and **PP** samples.

To discuss in more details the results presented above, a comparison between the microstructures observed experimentally and by simulation is provided in figure 5.21. Supplementary images of the microstructures obtained by simulation are available in appendix C.2 (figure C.2).

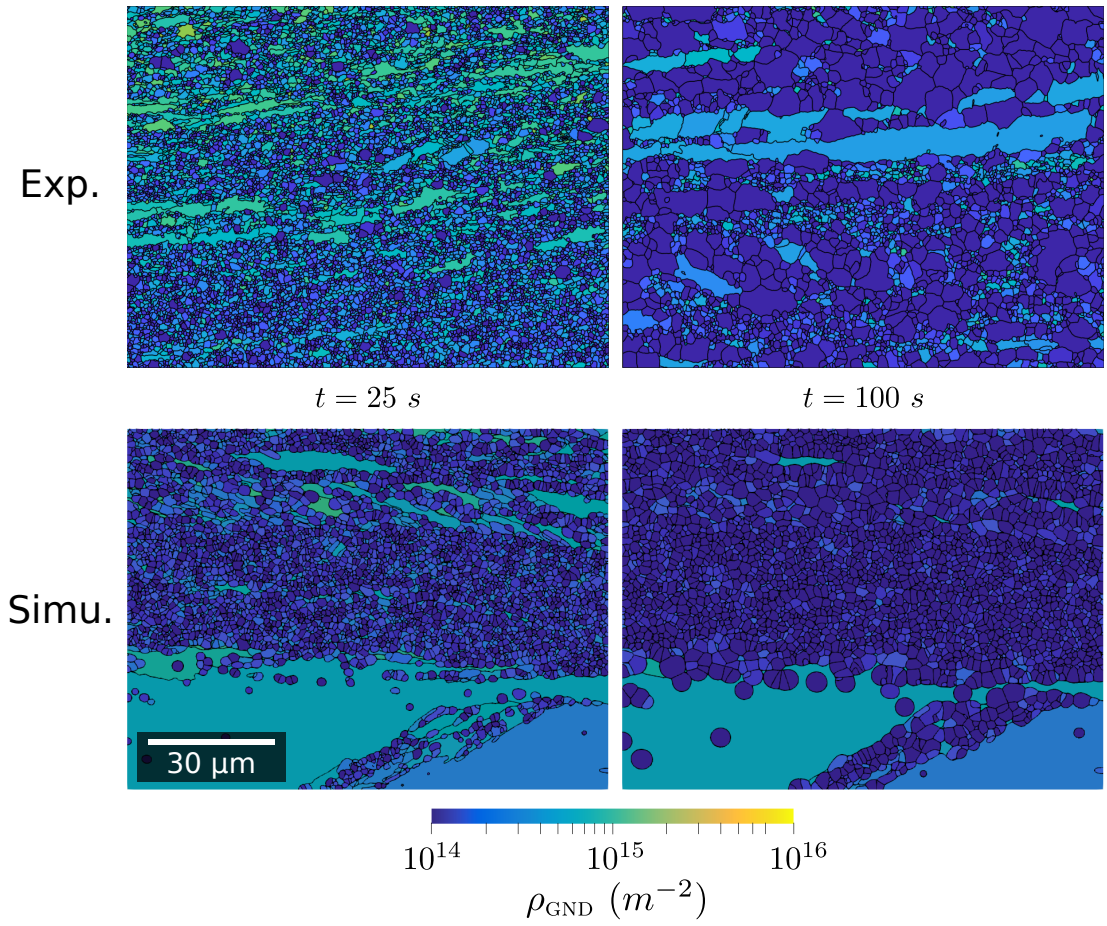
First, one can confirm that the simulations reproduce the difference of hetereogeneities observed between initial microstructures. Nevertheless, as discussed in previous section (section 5.2.2), the model does not predict the formation of a limited number of large recrystallized grains. To investigate this aspect in more details, scatter plots with marginal distributions are given in figure 5.22. These graphs complement the ECD_{rx} distributions since they allow to visualize at the same time the GAGND distribution. They highlight that the GAGND distribution predicted by simulations differs from the one measured experimentally. Indeed, in simulation, the population of large deformed grains is consumed too quickly in aid of a large number of grains with a low dislocation density. On the contrary, experimentally, a limited number of recrystallized grains grow with time. The recrystallized grain size distribution presents a wide spread. These observations allow to broaden the comments made earlier and to confirm that in simulation, a feature or a phenomenon that is greatly responsible for the selective growth of recrystallized grains is neglected/oversimplified. Various candidates could be mentioned:



(a) **Eq** microstructures.



(b) **BW** microstructures.



(c) **PP** microstructures.

Figure 5.21: GAGND maps from EBSD and simulation data, after two durations of heat treatment at $T = 650°C$. Hot deformation conditions are: $T = 650°C$; $\dot{\varepsilon} = 1.0\ s^{-1}$; $\varepsilon = 1.0 - 1.2$.

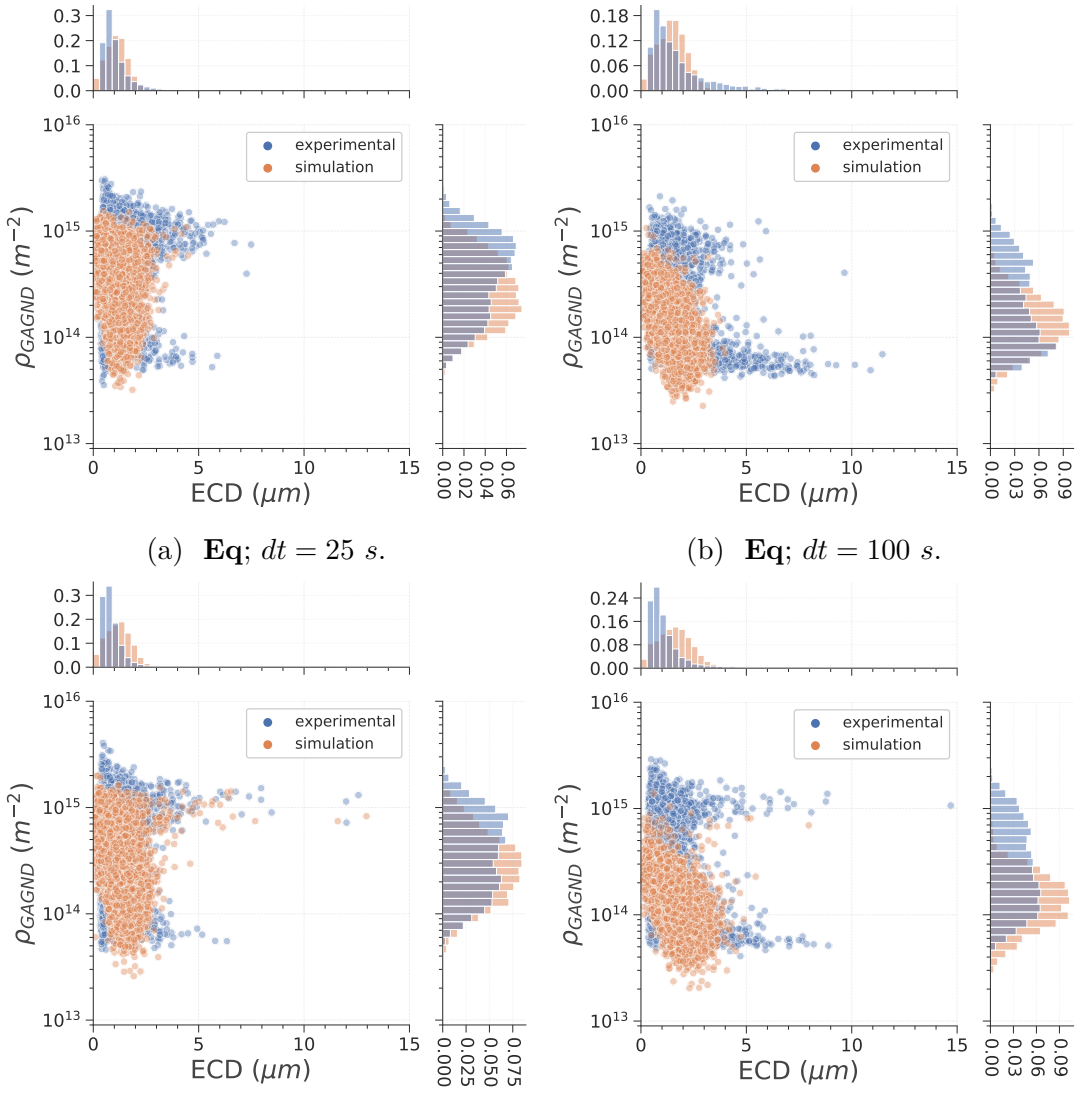
- in all the simulations presented until now, the dislocation density is averaged per subgrain/grain in a pre-processing step. However, it is clear that the dislocation density measured by EBSD is very heterogeneous within a single grain due to the anisotropic deformation behavior of Zy-4 and of the ability of dislocations to recover and form LAGB. Therefore, the averaging operation is certainly reducing the ability of simulations to reproduce the heterogeneity level observed experimentally.

- Some recovery processes could still be acting during the first instants of PDRX. Since these phenomena are acting at the dislocation scale and depend on many factors (dislocation type and density, ...), they could contribute to decrease more significantly the dislocation density in some subgrains or even to form additional subgrains that could then grow at the expense of other candidates.

- The anisotropy of GB properties could play an important role in the selective growth of a limited number of grains. Indeed, as discussed earlier, the deformation texture is consequent, meaning that most of the grains have very similar orientations. Thus, a grain could get a decisive advantage by presenting a specific disorientation with its neighbors which offers a greater boundary mobility.

The impact of static recovery is not considered as a main candidate for improving the simulation representativity. We believe that implementing the formation of new grains or subgrains in the first instants of PDRX would not be relevant to increase the degree of heterogeneities. Indeed, it would oblige us to describe using an additional law the formation of new grains/subgrains, without clear experimental evidences. Therefore, the fitting of this law would rather constitute a numerical potentiometer to fit the results which is not the aim of such models. Nevertheless, it is not excluded that recovery is playing a role to some extent and it would be interesting to get additional experimental data to assess it. Precise in-situ experiments, using EBSD and/or TEM, would certainly provide a part of the answer.

Could anisotropy of GB properties (energy and mobility) be a key factor in selective growth of recrystallized grains? A first part of the answer can be given by discussing the evolution of texture, observed experimentally and predicted by simulation. The experimental results discussed in section 5.1.1 already showed that the main texture component weakens upon PDRX and that no new texture component is observed. This fact supposes that recrystallized grains do not have a specific orientation. Figure 5.23 displays the evolution of <c> axis spatial distribution measured and predicted at three instants of the heat treatment. According to this figure, it appears that the simulation results reproduce that trend, with a slightly lower kinetics. This is consistent with the slight underestimation of recrystallization kinetics given by the model. Consequently, it appears that the low anisotropy degree considered in these simulations (isotropic GB mobility and heterogeneous GB energy) seems sufficient to reproduce the texture weakening



(a) **Eq**; $dt = 25\ s$.

(b) **Eq**; $dt = 100\ s$.

(c) **BW**; $dt = 25\ s$.

(d) **BW**; $dt = 100\ s$.

Figure 5.22: Combined scatter plots and histograms showing the distribution of grain average dislocation density (ρ_{GAGND}) and ECD. Hot deformation conditions are: $T = 650°C$; $\dot{\varepsilon} = 1.0\ s^{-1}$; $\varepsilon = 1.0 - 1.2$.

observed. Therefore, this constitutes an argument to minimize the hypothesis supposing that anisotropy of GB properties is a first order parameter for the formation of recrystallized grain size heterogeneities.

Finally, one hypothesis remains untested. Is the intragranular dislocation density heterogeneities the key feature responsible of selective growth of recrystallized grains? To discuss that question, some new simulations are presented and analyzed in the next section.

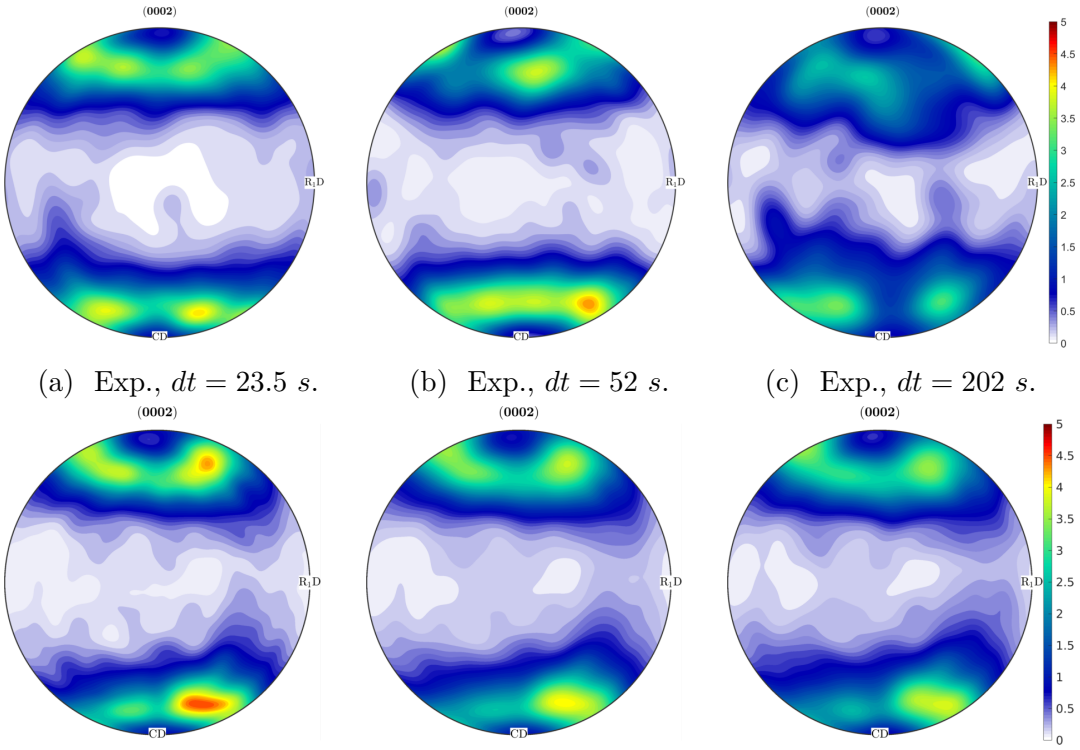
5.2.4 Effect of intragranular dislocation density heterogeneities

To evaluate the impact of intragranular dislocation density gradients, two numerical strategies are considered. In the first one, the GB velocity induced by stored energy differences is kept constant per interface [193]. To do so, dislocation density is averaged in a zone close to GB, on both sides. In the second strategy, the dislocation density field is kept heterogeneous and the energy gradient across GB is computed locally. Details about both strategies are presented in section 3.1.2. If at first glance the second approach could appear more physically-based, in fact both present advantages and drawbacks. Averaging dislocation density in zones close to interfaces reduces the magnitude of local dislocation density gradients that could cause some numerical instabilities. Moreover, the formulation computing gradients locally is dependent on the mesh and pixel sizes and supposes that only the closest dislocations contribute to exert a hold over GB. On the contrary, averaging dislocation density per interface requires to know the range of interaction between GND and GB.

To assess the impact of the hypotheses underlying these two methods, four simulation cases are run:

- dislocation density averaged per interface up to 100 nm from the GB (*Per interface;* $w_{avg} = 100\ nm$),
- dislocation density averaged per interface up to 200 nm from the GB (*Per interface;* $w_{avg} = 200\ nm$).
- Local dislocation density (*Local*),
- local dislocation density, with a pre-processing operation that consist in applying a 2D Gaussian filter to the dislocation density map. The standard deviation of the Gaussian filter is taken equal to 2 $px = 200\ nm$ (*Local, Gaussian filtered*).

In all these simulation cases, the scaling factor δ is lowered to: $\delta\,(1\ s^{-1}) = 3.0$. This decrease is discussed later on. The results obtained from these simulations are compared to the ones presented in previous section, which are referred to as *Per grain*.



(a) Exp., $dt = 23.5\ s$. (b) Exp., $dt = 52\ s$. (c) Exp., $dt = 202\ s$.

(d) Simu., $dt = 25\ s$. (e) Simu., $dt = 50\ s$. (f) Simu., $dt = 200\ s$.

Figure 5.23: {0002} pole figures showing texture evolution during holding at $T = 650°C$ after hot deformation ($T = 650°C$; $\dot{\varepsilon} = 1.0\ s^{-1}$; $\varepsilon = 1.2$). a), b) and c) are obtained from experimental data and d), e) and f) are computed from simulation results.

First, the evolution of the recrystallized fraction, of $\overline{ECD}_{rx}$ and of $\overline{ECD}$ with time are plotted in figure 5.24. The recrystallized fraction predicted by the four simulation cases considering intragranular GND density gradients are very similar. They are slightly lower compared to the per grain case and are in very good agreement with the experimental results. It is interesting to notice that using a local formulation allows to reduce the impact of the δ parameter. This confirms that averaging GND density per grain leads to reduce the stored energy gradients, on average. Nevertheless, to get predictive results, δ is not set to unity, as one could have expected. It is reduced from $\delta\,(1.0\ s^{-1}) = 8$ to $\delta\,(1.0\ s^{-1}) = 3$. Two hypotheses can be considered:

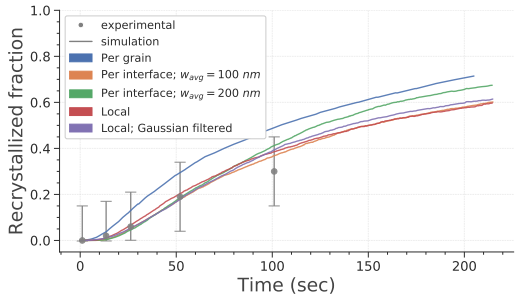
- GND density measured by EBSD could be underestimated.
- Some model parameters, governing the GB kinetics, could be inaccurate. The GB energy, for instance, has been taken from literature but the proposed value is not supported by adequate scientific evidences and/or experimental data. Therefore, if the value is in reality smaller, the mobility value identified previously (see section 4.2.1) would be higher.

From figure 5.24b, it appears that the evolution of $\overline{ECD}_{rx}$ with holding time is significantly different when intragranular GND density heterogeneities are considered. Two noticeable differences between the simulation results with GND intragranular gradients and the per grain results should be discussed. Firstly, at $t = 0\ s$, all the simulation results with GND intragranular gradients present a very low $\overline{ECD}_{rx}$. This is due to the fact that in the *Per grain* case, GND density is averaged per grain during a pre-processing operation whereas in the other cases it is done directly during the simulation. Therefore, some variations could be observed, especially since high dislocation densities are frequently observed close to GB. Since the recrystallized fraction is almost null at those times, the few grains identified as recrystallized are not the same and the differences are very important. Consequently, this feature is not relevant for the discussion but is only an artifact due to data processing. When the recrystallized fraction exceeds 40%, after approximately $t = 100\ s$, the differences of $\overline{ECD}_{rx}$ can be analyzed. The average recrystallized grain diameter predicted by the four new simulation cases is much smaller. However, looking at the evolution of the $\overline{ECD}$ taking into account all grains and subgrains, it appears that the new formulations predict to a much better extent the evolution of the average size of both grains and subgrains. In particular, the results obtained with the *per interface* formulation fit perfectly the experimental ones. The average grain size starts by decreasing for local formulations. Since the stored energy field presents very strong local variations, some GB are very serrated and can locally form new grains by pinching. It is interesting to notice that in simulation, the average size of recrystallized grains is approximately equal to the average size of all objects, grains and subgrains, no matter their dislocation density. Experimentally, the size of recrystallized grains is much higher than the size of all the objects. Two explanations can be given:

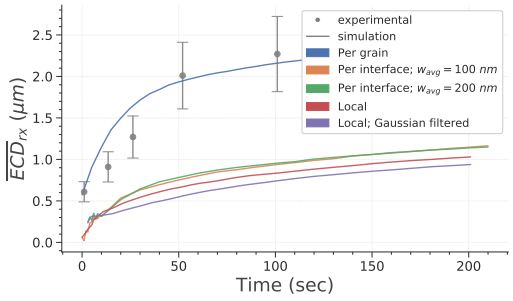
- Experimentally, the objects that are smaller than 1 μm, contain a low number of pixels. Given the number of pixels that they contain, the noise can easily affect their average dislocation density. Thus, the identification of such object using a threshold is harder.

- The dislocation density value of zones that are swept by the recrystallization front (ρ_0), is set too low in simulations. Therefore, small grains are classified as recrystallized once they have consumed a too small fraction of deformed area.

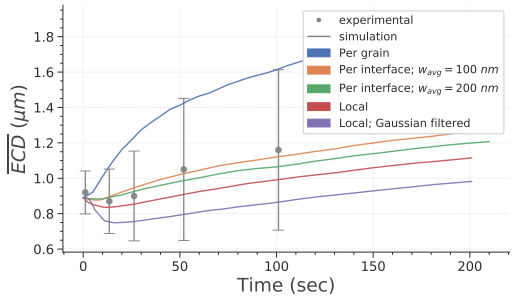
From these graphs, it appears that averaging the GND density from 100 to 200 nm gives similar results. Applying a Gaussian filter on GND density maps, before running simulations with a computation of GB kinetics that consider local GND density gradients seems to modify the results to a small extent. These two observations suggest that the results obtained with these formulations are consistent and that these formulations are rather robust. It is noteworthy and should be confirmed by an extended study.



(a) Recrystallized fraction versus time.



(b) $\overline{ECD}_{rx}$ versus time.



(c) $\overline{ECD}$ versus time.

Figure 5.24: Evolution of the main microstructure descriptors with time, during PDRX simulations. **BW** samples. Hot deformation conditions are: $T = 650°C$; $\dot{\varepsilon} = 1.0\ s^{-1}$; $\varepsilon = 1.2$.

To broaden the discussion, images of the digital microstructures are presented in figure 5.25. These figures show only a small part of the microstructure. The full maps are available in appendix C.3. Several scatter plots are provided in

figure 5.26. One can notice from these figures that the *per interface* and *local* formulations tend to better predict several features:

- the higher fraction of large grains with a high dislocation density (i.e. large deformed grains).
- The larger spread of the grain average GND density distribution.
- The shape of the grain size distribution.

Nevertheless, some characteristics are still not captured:

- The number of large grains with a low dislocation density is still underestimated. At the same time, the number of small grains with a low dislocation density is even higher than in the *per grain* formulation, leading to a degradation of the agreement with experimental data.
- The general dislocation density distribution is shifted to lower values.

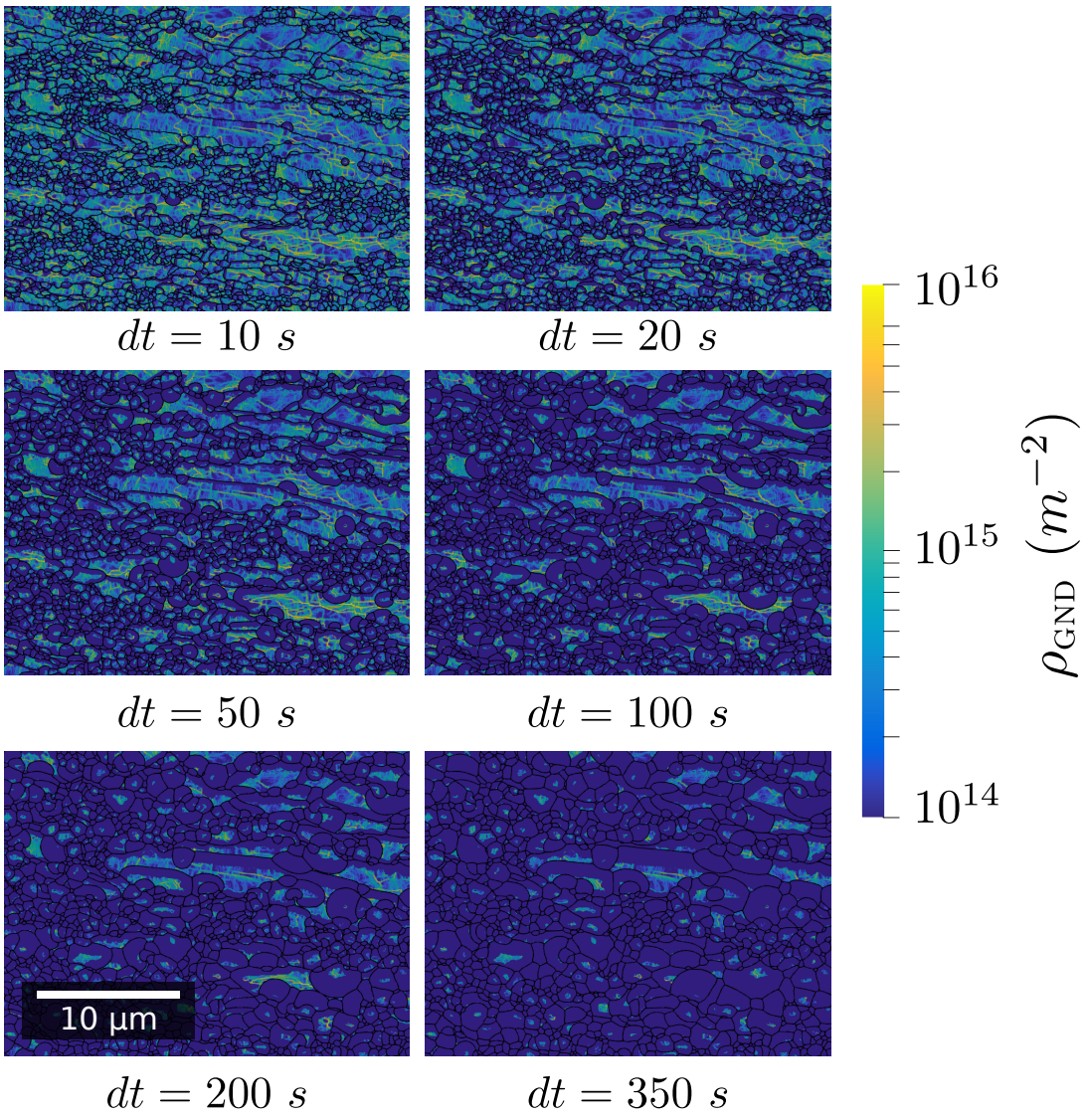
Two hypotheses could explain the discrepancies that remain with these advanced formulations. First, the results seem to point out that the ρ_0 value considered until now is too low. Indeed, figure 5.26 shows that no grain has an average GND density lower than $5.0 \times 10^{13}\ m^{-2}$. Therefore, this value would constitute a more adequate value for ρ_0. Then, until now, the impact of SPP has been neglected. This simplification is justified by the usual argument that the pinning pressure exerted by particles (so-called Smith-Zener pinning pressure P_{z}) is much lower than the driving pressure due to dislocation density gradients. To illustrate that, a rough estimation of the different pressures exerted on GB are given in table 5.1. From this table, it is clear that on average, the pinning pressure exerted by SPP is almost twenty times lower than other driving pressures.

However, when local formulations are considered, the different driving pressures could vary by several order of magnitudes during the migration of a GB within a few microns. Since the average grain size is also rather low, the capillarity effects also condition to a great extent the evolutions observed. Therefore, SPP could pin GB at specific locations where the GND density gradients are very small and be the missing phenomenon for reproducing the formation of recrystallized grains with a more dispersed size. This aspect is discussed in the following section.

Finally, to propose a complete analysis, the texture obtained by three of the simulation cases are compared to the one measured experimentally, after a heat

$P_e\ (Pa)$	$P_c\ (Pa)$	$P_{\mathrm{z}}\ (Pa)$
10^6	10^6	5×10^4

Table 5.1: Rough estimation of the driving pressure averaged over the whole domain.

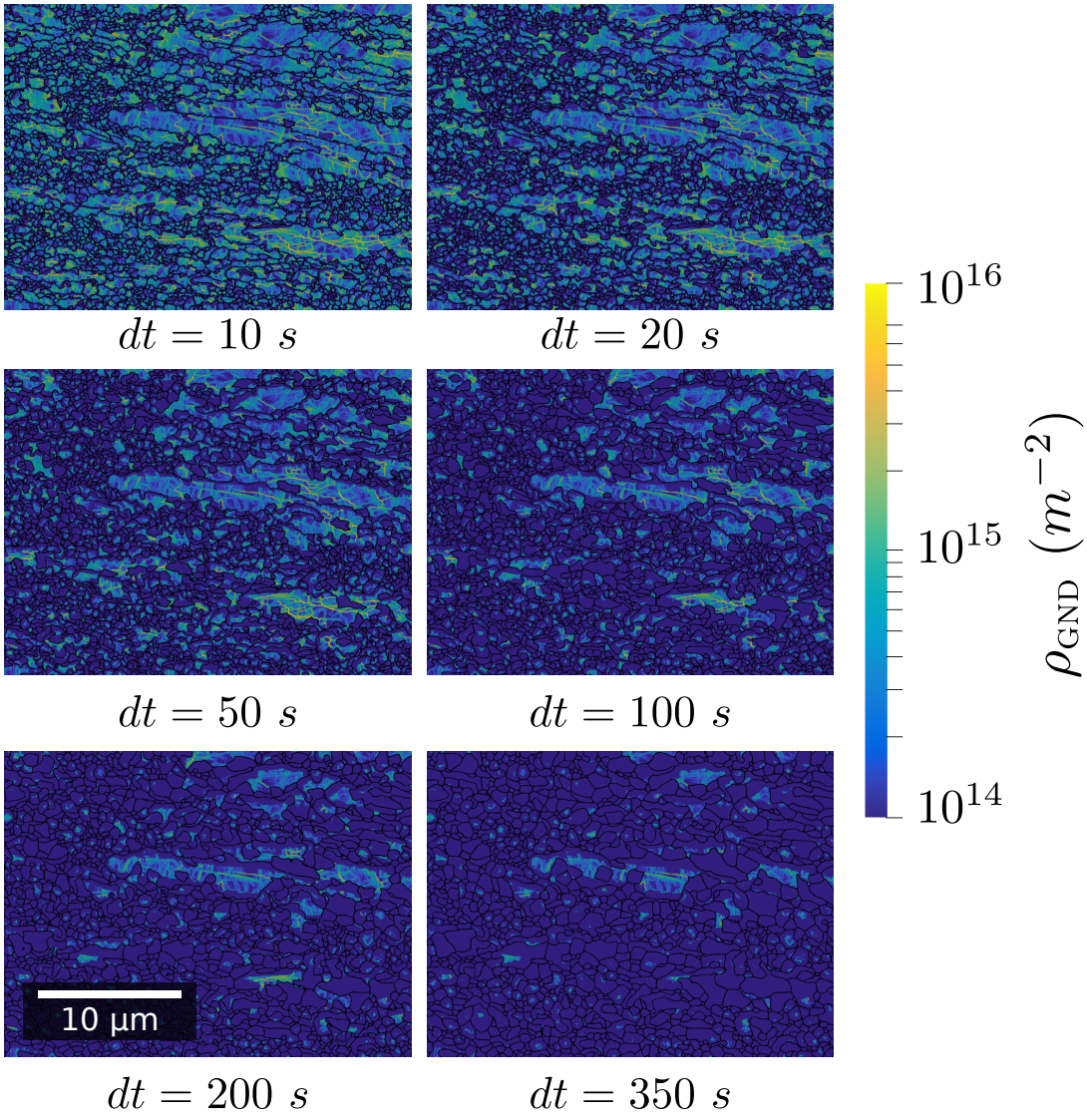


(a) Per interface.

treatment of 100 s, in figure 5.27. It appears that the main texture components are more preserved when the numerical formulation for computing the GB velocity are local. Apart from that conclusion, very few differences are observable from the different simulation results.

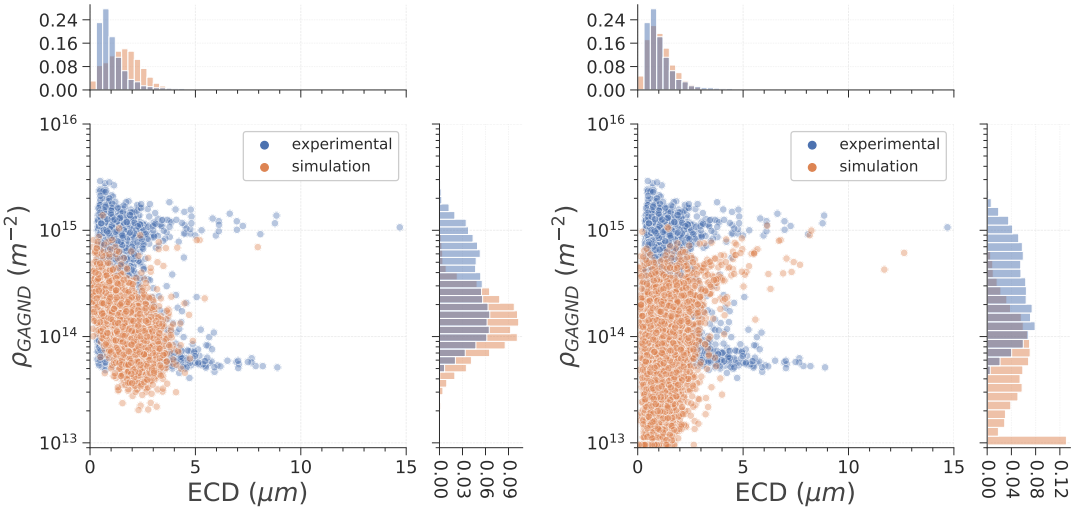
5.2.5 Impact of SPP

To evaluate the hypothesis proposed previously, two simulation cases including SPP are considered. They both rely upon the local formulation. To limit the computational costs, an equivalent SPP population is considered, as in section 4.2.2. All SPP have a diameter equal to 100 nm, and their surface fraction is scaled to conserve the same pinning pressure. In the first simulation case, SPP are distributed randomly throughout the microstructure. In the second, they



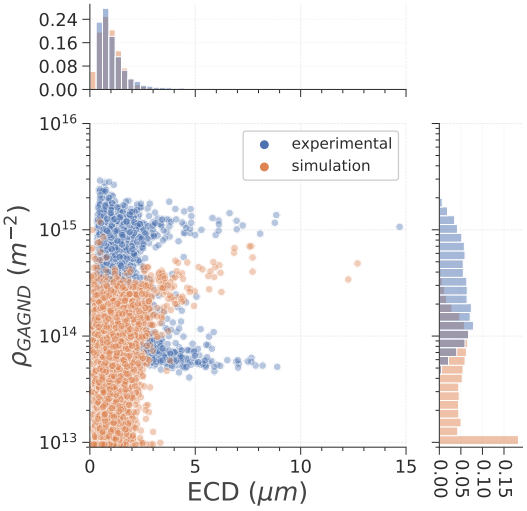
(b) Local.

Figure 5.25: Digital microstructures at different instants of the heat treatment. **BW** samples. Hot deformation conditions are: $T = 650°C$; $\dot{\varepsilon} = 1.0\ s^{-1}$; $\varepsilon = 1.2$.



(a) Per grain.

(b) Per interface; $w_{avg} = 100\ nm$.

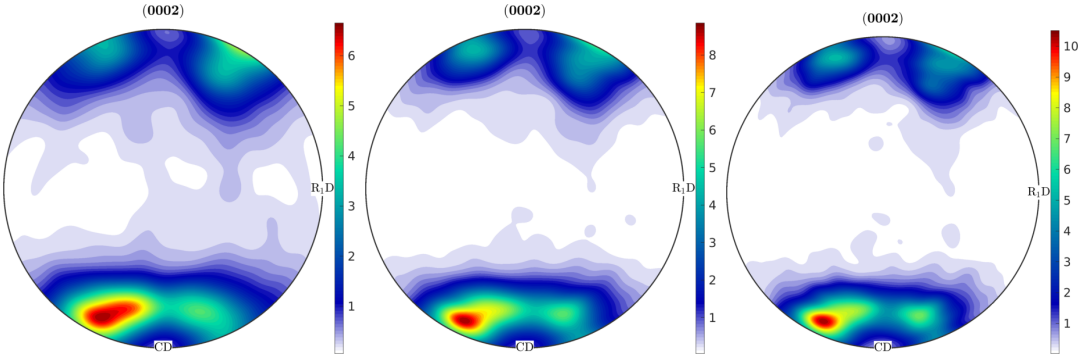


(c) Local.

Figure 5.26: Combined scatter plots and histograms showing the distribution of grain average dislocation density (ρ_{GAGND}) and ECD. Simulation and experimental results correspond to a heat treatment of 100 s. **BW** samples. Hot deformation conditions are: $T = 650°C$; $\dot{\varepsilon} = 1.0\ s^{-1}$; $\varepsilon = 1.2$.

are aligned along horizontal lines that are spaced by approximately $4\mu m$, which corresponds to the lamella width. This last case reproduces to some extent the alignment of SPP along lamellae boundaries in lamellar microstructures. Figure 5.28 presents the digital microstructures at different instants of the simulation and figure 5.29 the distribution of grain size and GND density.

From figure 5.28, it appears clear that in these simulations, SPP do not impact the microstructure evolutions to a great extent. For the longest holds, it seems that the case with aligned SPP present some larger grains that develop preferen-

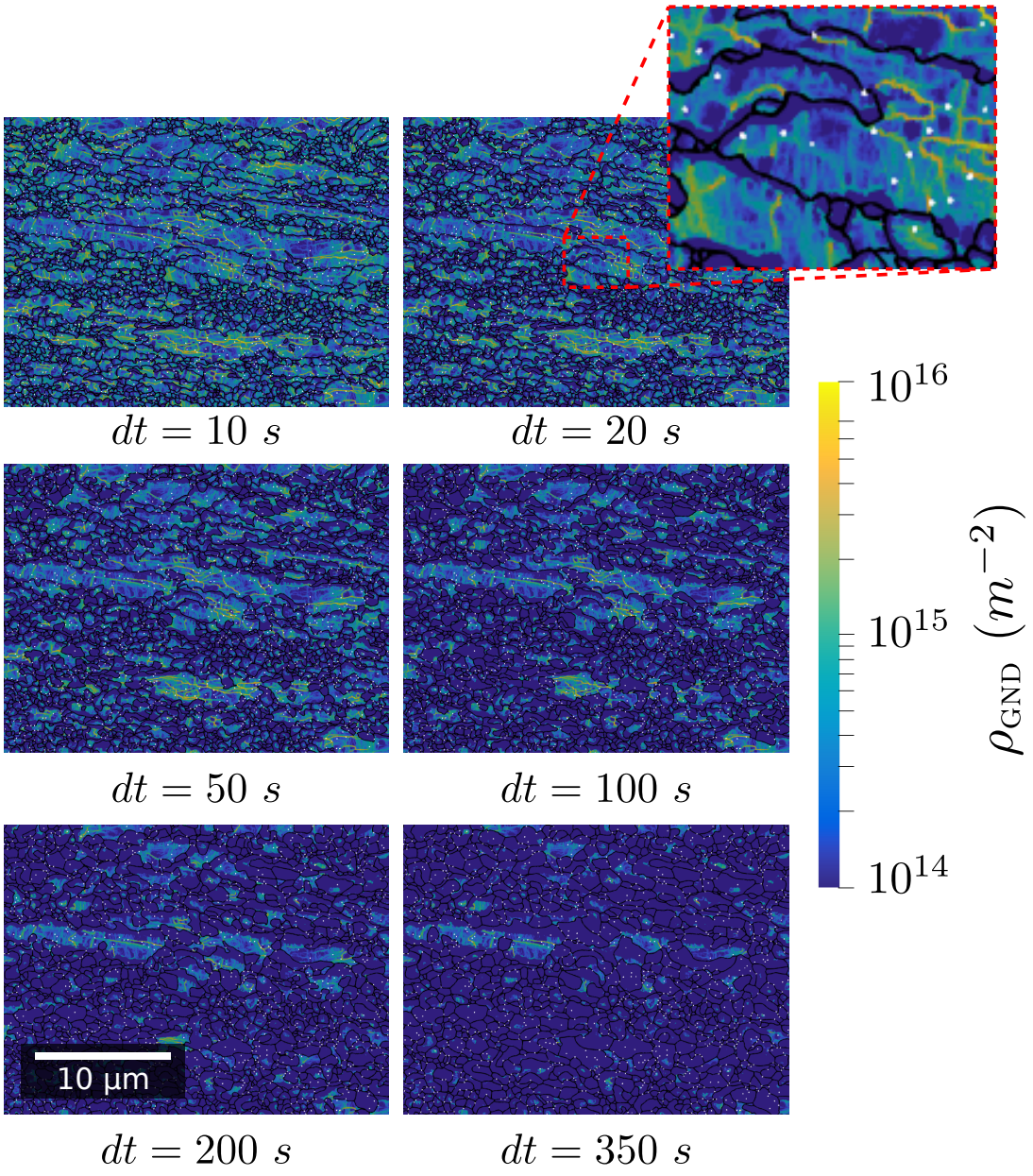


(a) Per grain. (b) Per interface; $w_{avg} = 100\ nm$. (c) Local.

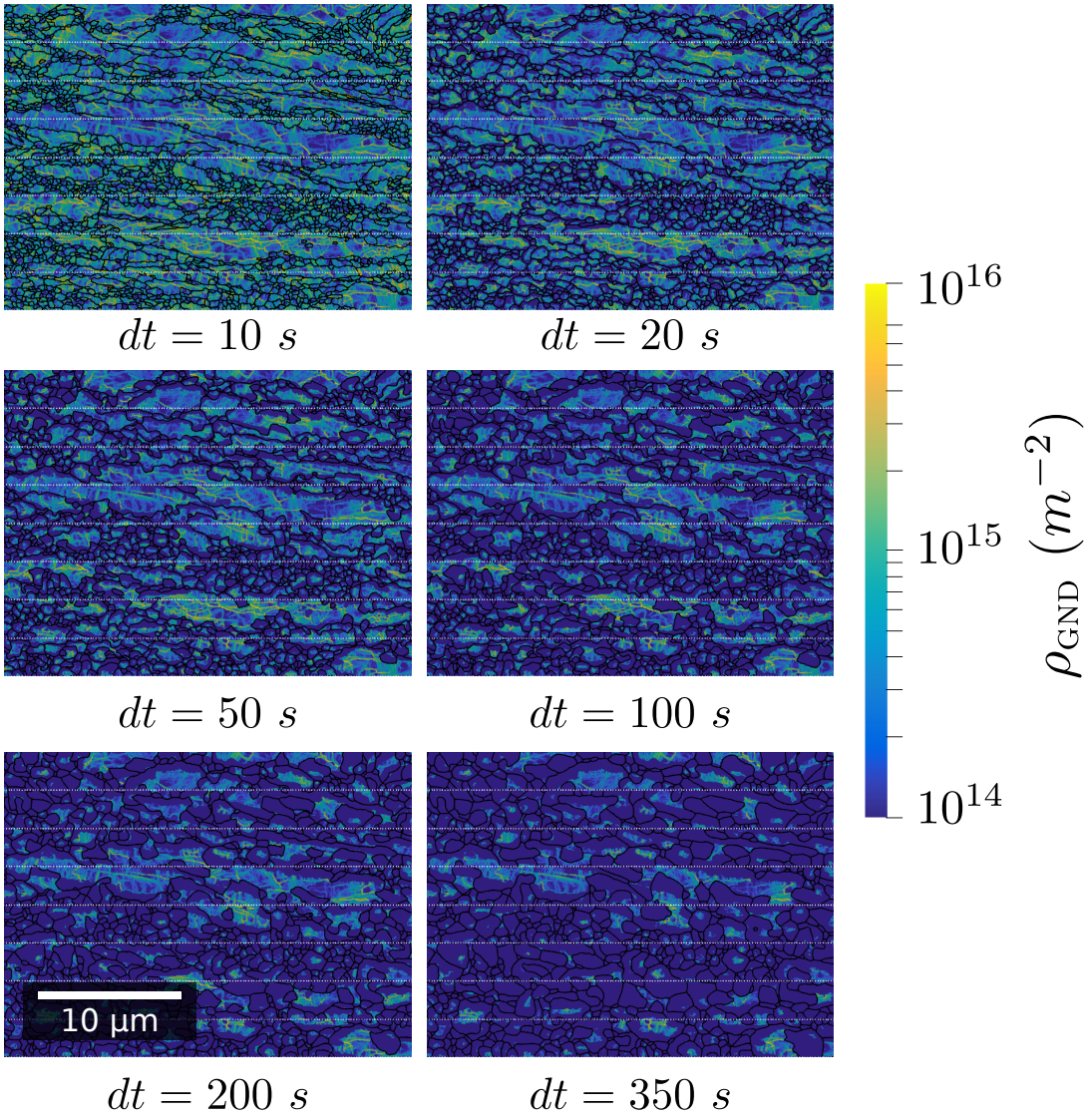
Figure 5.27: {0002} pole figures showing final texture after holding at $T = 650°C$ for 100 s, after hot deformation ($T = 650°C$; $\dot{\varepsilon} = 1.0\ s^{-1}$; $\varepsilon = 1.2$). **BW** samples.

tially in between the lines of SPP. Figure 5.29 confirms that after 350 s of hold at temperature, SPP seem to have a role in the stability of some larger grains. However, this does not help in prediction of the recrystallized grains selective growth observed experimentally.

These results seem to point out that SPP are not the microstructure feature missing in simulations to predict the selective growth of recrystallized grain. However, they also highlight that SPP with a specific spatial distribution could be one of the feature that condition these evolutions. Therefore, it would be highly valuable to run additional simulations with the exact SPP size and spatial distributions. Unfortunately, the spatial distribution of SPP cannot be determined from the EBSD data used in the present work.



(a) SPP randomly distributed.



(b) SPP aligned as horizontal bands.

Figure 5.28: Digital microstructures at different instants of the heat treatment. **BW** samples. Local formulation is considered for both simulations. Hot deformation conditions are: $T = 650°C$; $\dot{\varepsilon} = 1.0\ s^{-1}$; $\varepsilon = 1.2$.

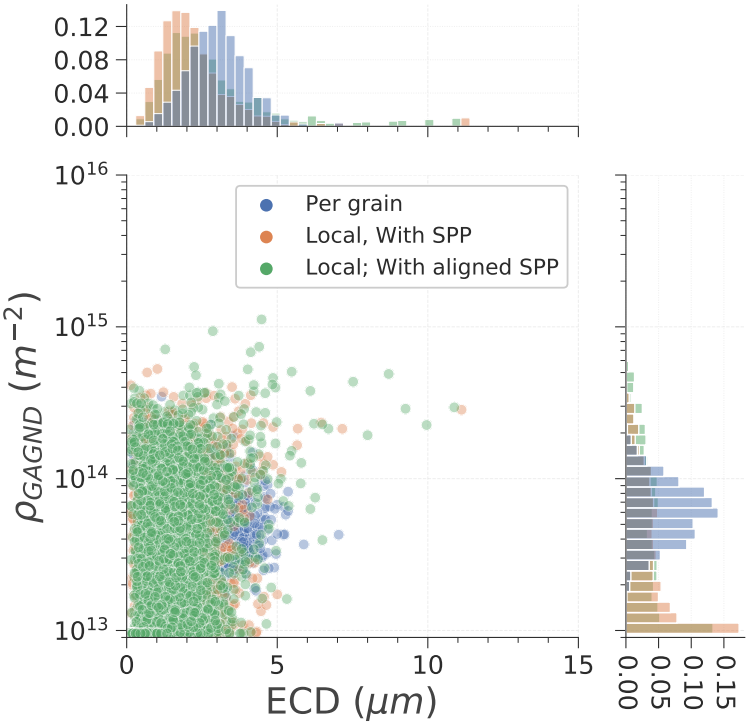


Figure 5.29: Combined scatter plots and histograms showing the distribution of grain average dislocation density (ρ_{GAGND}) and ECD. Simulation results correspond to a heat treatment of 300 s. **BW** samples. Local formulation is considered for both simulations with SPP. Hot deformation conditions are: $T = 650°C$; $\dot{\varepsilon} = 1.0\ s^{-1}$; $\varepsilon = 1.2$.

5.3 Conclusion

The evolution of microstructure during PDRX has been described and analyzed extensively, using both experimental and simulation techniques. First, experimental investigations have shown that under the conditions investigated, PDRX of Zy-4 is characterized by the growth of a limited number of recrystallized grains. Recrystallized grain size distribution is defined by a large spread, denoting a certain heterogeneity. In a second time, the EBSD data have been used to quantify the influence of thermomechanical conditions and initial microstructure. The results point out that both parameters affect the localization of small grains/subgrains and of stored energy of deformation. The extent of heterogeneity affects, in turn, the kinetics of PDRX.

The numerical tools presented in chapter 3 are applied. The results illustrate that in the standard configuration used in this study, the model is able to reproduce general trends and to capture to some extent the influence of initial microstructure. However, some assumptions of the current numerical formulation limit the model ability to predict the heterogeneities observed. Several hypotheses over the limiting assumptions were proposed. Some additional simulations with heterogeneous GND density were performed. The simulation results highlighted that this microstructural feature plays an important role in the selective growth of recrystallized grains. Indeed, the results from these simulations present a better agreement in terms of recrystallized grain size distribution. If this emphasized the role of intragranular GND gradients, it also pointed out that it is not the only missing feature playing a role in selective growth of recrystallized grains. A simple analysis of the driving pressures confirmed that if SPP can be neglected for these simulations when GND density is averaged per grain, it is certainly not the case when GND density is kept heterogeneous. The simulation results do not confirm that hypothesis but suffer from simplifying assumptions regarding SPP populations. Therefore, no definitive conclusion should be expressed from these results and this aspect constitutes a clear perspective of these works.

Résumé en français

Les évolutions microstructurales ayant lieu lors d'un traitement thermique suivant une déformation à chaud sont étudiées en détail. Dans un premier temps, les résultats expérimentaux mettent en évidence que la recristallisation post-dynamique du zircaloy-4 se caractérise par la croissance d'un nombre limité de grains recristallisés. Par conséquent, la distribution de taille de grains est relativement large. Les données EBSD sont analysés en détail afin de quantifier l'influence des conditions thermomécaniques et de la microstructure initiale. Les résultats prouvent que ces deux facteurs influencent la localisation des grains/sous-grains formés lors de la déformation. Ils mettent également en évidence leur influence sur la distribution spatiale de densité de dislocations. Le degré d'hétérogénéité spatiale de ces deux paramètres conditionne par la suite la cinétique de recristalli-

sation.

Les outils numériques présentés précédemment sont appliqués afin de modéliser la recristallisation post-dynamique. Les résultats obtenus à l'aide du formalisme standard, prenant en compte une énergie de déformation moyenne par grain, reproduisent l'évolution de certaines grandeurs. Néanmoins, ils ne sont pas capables de prédire la croissance sélective de certains grains recristallisés. Plusieurs hypothèses sont formulées. Des simulations complémentaires sont effectuées en considérant une densité de dislocation hétérogène par grain. Ces simulations mettent en évidence le rôle des gradients intragranulaires dans la croissance hétérogène des grains recristallisés. Enfin, une analyse supplémentaire relative aux effets conjoints de ces gradients d'énergie et de la présence de particules de seconde phase est réalisée. Si les premiers résultats illustrent que l'effet des précipités ne semble pas suffisant pour expliquer le degré d'hétérogénéité observé en EBSD, aucune conclusion définitive ne peut etre effectuée. En effet, ces dernières simulations souffrent d'hypothèses simplificatrices pouvant affecter les résultats. Cela constitue une perspective des simulations proposées.

Chapter 6

Characterization and modeling of continuous dynamic recrystallization

Finally, the present and last chapter takes advantage of all the observations and conclusions about microstructure evolutions during heat treatments to focus on the changes during and after hot deformation. To do so, it follows the same *modus operandi*. First, a complete experimental campaign is performed to explore large thermomechanical and initial microstructure ranges. The experimental results confirm that continuous dynamic recrystallization is the main mechanism responsible of the evolutions observed, for all conditions and initial microstructures considered. The impact of initial microstructure is quantified and discussed. The consequences of CDRX over PDRX that are approached in section 5.2 are here described in more details. Second, the implementations presented in chapter 3 are applied and compared to the experimental results. A discussion about the framework abilities and limitations is provided. Finally, some simulations representative of hot extrusion are presented to evaluate the model abilities for industrial thermomechanical paths.

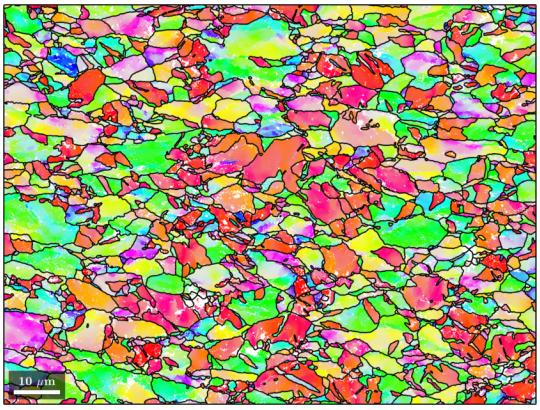
6.1 Characterization of CDRX

6.1.1 Mechanisms of CDRX

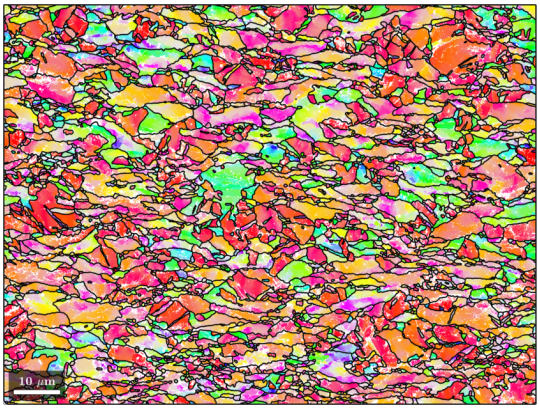
As discussed in section 1.2.4, it has been stated in a few articles [15] that Zy-4 is experiencing CDRX during hot deformation in a large range of thermomechanical conditions. However, most of these observations were made on lamellar microstructures. The first step of the part study is then to expand this discussion to equiaxed microstructures. Doing so, figures 6.1 and 6.3 present the evolution of the microstructure thanks to EBSD orientation maps and pole figures. Thermomechanical conditions selected here are at the center of the matrix (see table 2.7a). Figure 6.1 shows the topological changes happening in the microstructure due to deformation. Grains progressively elongate along horizontal plane. Some small grains are also formed. They are located rather homogeneously throughout the microstructure. They tend to group into small clusters or to be aligned along pre-existing GB. A very limited number of deformation twins are observable at all deformation levels. Their number does not seem to increase with strain, as opposed to small grains. Large intragranular orientation gradients are visible. Some well-defined subgrains are also present. These different features are highlighted in details in figure 6.2. Figure 6.3 highlights that the initial texture weakens quickly and is finally transformed to typical hot deformation texture of zirconium alloys [64]. At $\varepsilon = 1.0$, most of the grains have their <c> axis aligned at approximately 30° from the compression direction.

To complete the analysis based on EBSD orientation maps (figure 6.1), the corresponding GND density maps are plotted in figure 6.4. From these figures, it is relatively hard to draw any conclusion. Indeed, all microstructures contain a very complex deformation structure, with a high GND density. Besides, the amount of non-indexed pixels impacts the analysis since it increases with strain (see figure 6.4). Some areas with a higher concentration of GND are distinguishable.

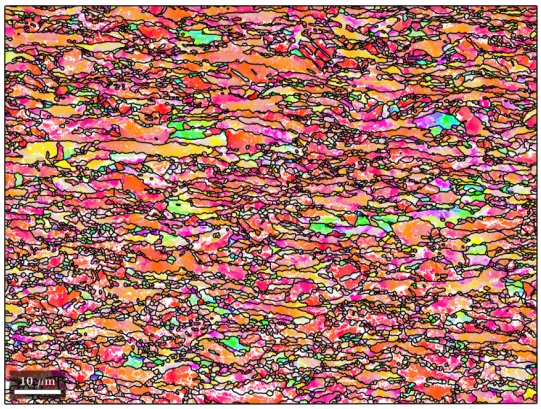
On the contrary, some more remarkable features are observable in figure 6.5, which also displays GND density maps, but for samples deformed at a higher temperature ($T = 650°C$). On all maps, it is possible to notice some small grains or subgrains, that present a very low and homogeneous dislocation density, i.e. recrystallized grains. They are designated by red circles. They seem to be more numerous at higher strains ($\varepsilon = 1.0$). They also seem to form small clusters at such strain levels. Finally, the recrystallized grains seem to be bigger at low strain rates. To complete this qualitative analysis, some scatter plots showing the distribution of GAGND and grain/sugbrain ECD are displayed in figure 6.6. From three graphs, one could conclude that the GAGND distribution shifts slightly to the high values when the strain rate increases. At the same time, the grain size distribution narrows. With increasing strain, the quantity of grains and subgrains with a lower dislocation density increases. The widening of GAGND density distribution illustrates that dynamic recovery and dynamic recrystallization mechanisms are acting. Nevertheless, no clear distinction be-



(a) $\varepsilon = 0.45$.



(b) $\varepsilon = 0.75$.



(c) $\varepsilon = 1.0$.

Figure 6.1: EBSD orientation maps showing microstructure evolution during hot deformation ($T = 550°C$; $\dot{\varepsilon} = 0.1\ s^{-1}$). **Eq** samples. IPF Y color code.

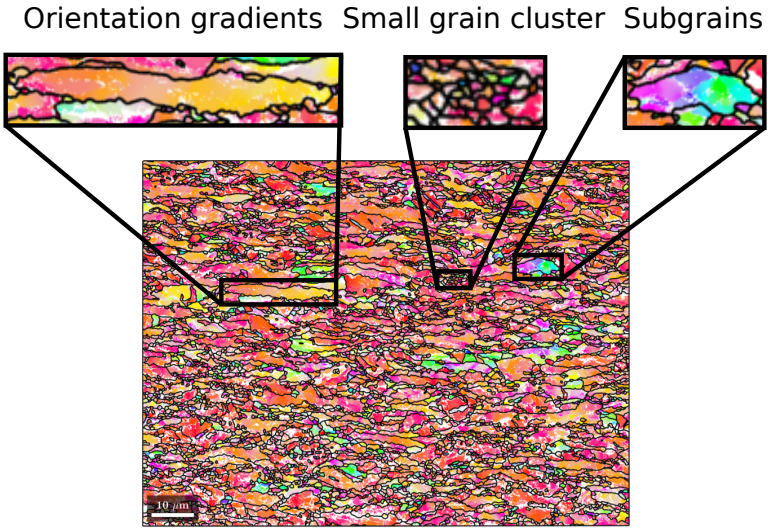
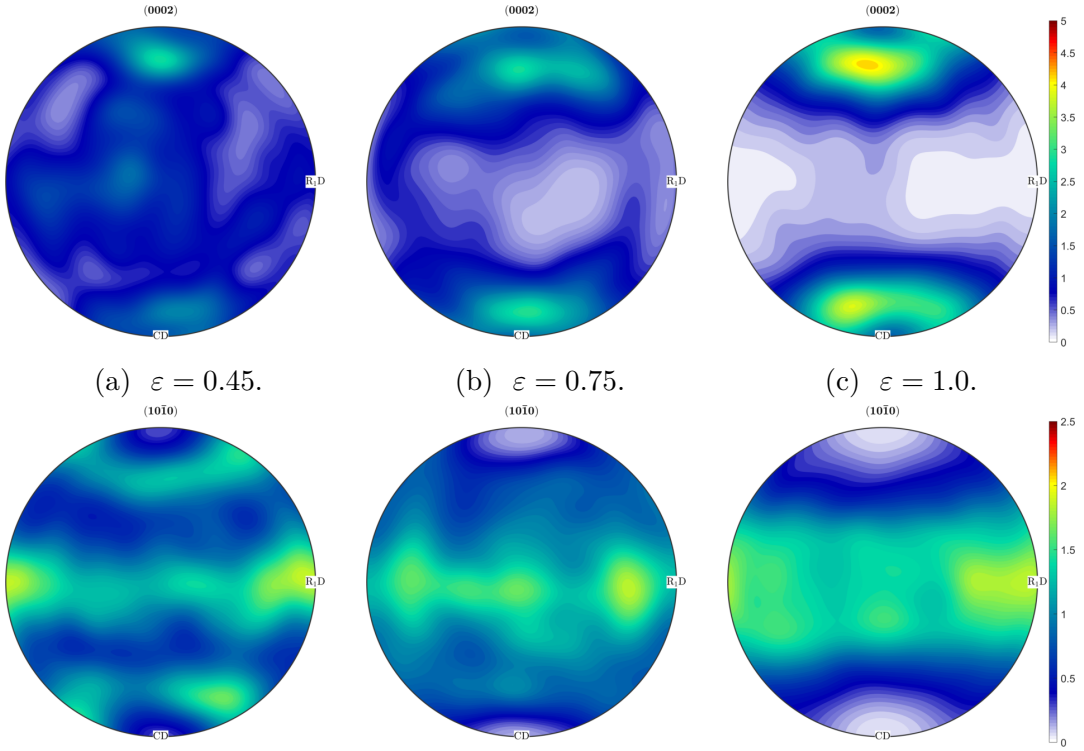


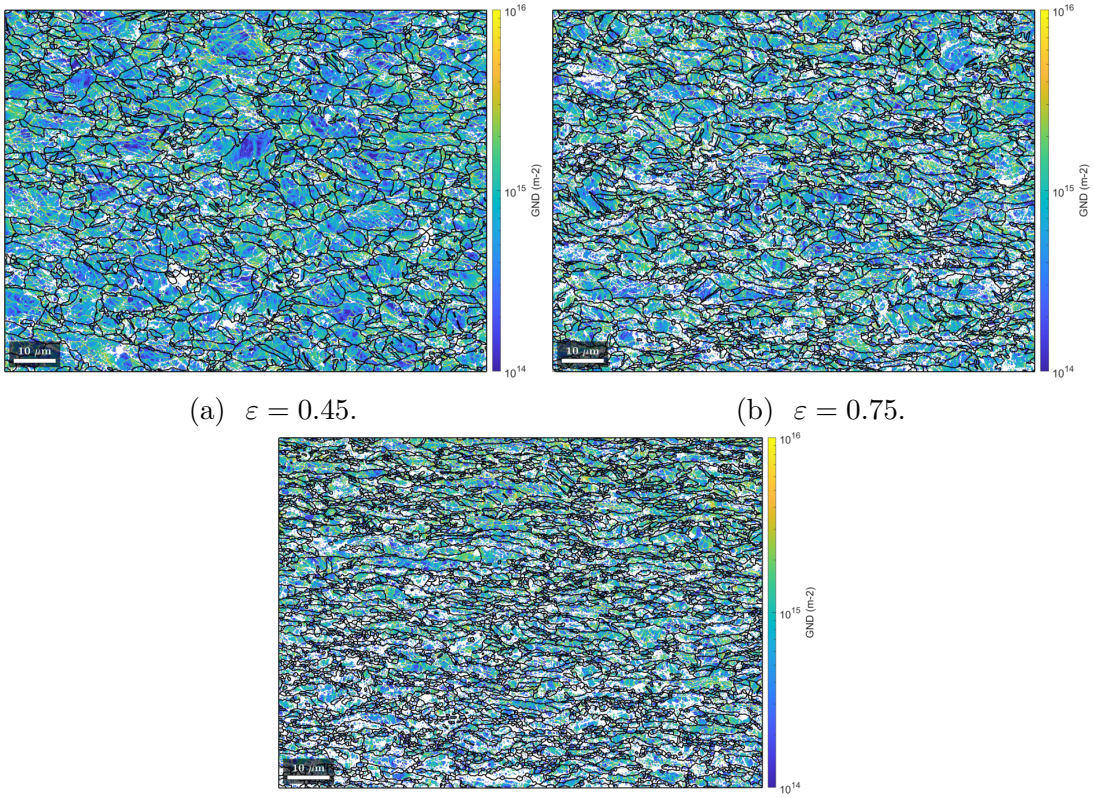
Figure 6.2: EBSD orientation map of a sample hot deformed in following conditions: $T = 550°C$; $\dot{\varepsilon} = 0.1\ s^{-1}$; $\varepsilon = 1.0$. **Eq** samples. IPF Y color code.



(a) $\varepsilon = 0.45$. (b) $\varepsilon = 0.75$. (c) $\varepsilon = 1.0$.

(d) $\varepsilon = 0.45$. (e) $\varepsilon = 0.75$. (f) $\varepsilon = 1.0$.

Figure 6.3: $\{0002\}$ and $\{10\bar{1}0\}$ pole figures showing texture evolution during hot deformation ($T = 550°C$; $\dot{\varepsilon} = 0.1\ s^{-1}$; $\varepsilon_f = 0.75$). **Eq** samples.



(a) $\varepsilon = 0.45$. (b) $\varepsilon = 0.75$.

(c) $\varepsilon = 1.0$.

Figure 6.4: EBSD GND density maps showing microstructure evolution during hot deformation ($T = 550°C$; $\dot{\varepsilon} = 0.1\ s^{-1}$). **Eq** samples.

tween a population of recrystallized grains and a population of deformed grains appear based on these distributions. This highlights the progressive character of the transformation happening here.

Finally, to complete the analysis, the evolution with strain of the mean grain size, the LAGB specific length as well as the HAGB specific length, are plotted in figure 6.7.

First, figures 6.7b and 6.7c confirm that the quantity of LAGB is significant. Then, it seems that the specific length of LAGB stabilizes when a sufficient deformation value is reached whereas the specific length of HAGB continues to increase. This is consistent with the results of Chauvy et al. [15] and confirms that at some point, an equilibrium is reached between formation and disappearance of LAGB.

From the typical features observed on EBSD maps, the distributions of GAGND-ECD and the high quantity of LAGB, one could conclude that Zy-4, with an initial equiaxed microstructure, is experiencing CDRX. One could also infer that the mechanism of progressive transformation of LAGB to HAGB is consistent with the evolution of LAGB and HAGB length ratio with strain. Indeed, once a given quantity of LAGB is formed upon hot deformation, the LAGB specific length stabilizes, whereas the microstructure topology continues evolving. This confirms that some subgrains can progressively form grains. The distributions of GAGND-ECD show that this mechanism is very gradual and contributes to the breakdown of larger deformed grains into smaller grains, with a rather wide range of dislocation density. The wide distribution of GND density, obviously, is linked with the strong anisotropy of Zy-4 mechanical behavior that leads to heterogeneous distributions of dislocation density, between grains and even within a single grain.

Finally, these observations reveal that CDRX (and then any subsequent PDRX) is very limited for temperatures lower or equal to $550°C$. Thus, the following investigations are focused on the highest temperature investigated ($T = 650°C$).

In the previous chapter, the results showed that PDRX is much faster when samples are deformed at high strain rates and deformation levels. To explain such difference, two hypotheses have been proposed: one concerns the formation of grains and subgrains, the other their growth kinetics. The previous discussion allows to get a clearer idea upon the influence of thermomechanical conditions upon CDRX and finally upon PDRX. When the final strain increases, the number of small grains and subgrains with a low dislocation density increases notably. Therefore, the number of recrystallized grains that could grow and consume the deformed microstructure is higher, leading to an increase of the PDRX kinetics. Then, increasing the strain rate contributes to increase the average stored energy difference between recrystallized and deformed grains. This, in turn, leads to significantly increase the driving pressure for PDRX. These explanations are consistent with the evolution of recrystallized fraction and $\overline{ECD}_{rx}$ displayed in figure 5.8. They confirm that both the initial number of grains and subgrains and the GND density play a role in PDRX evolutions, in the range of thermomechanical

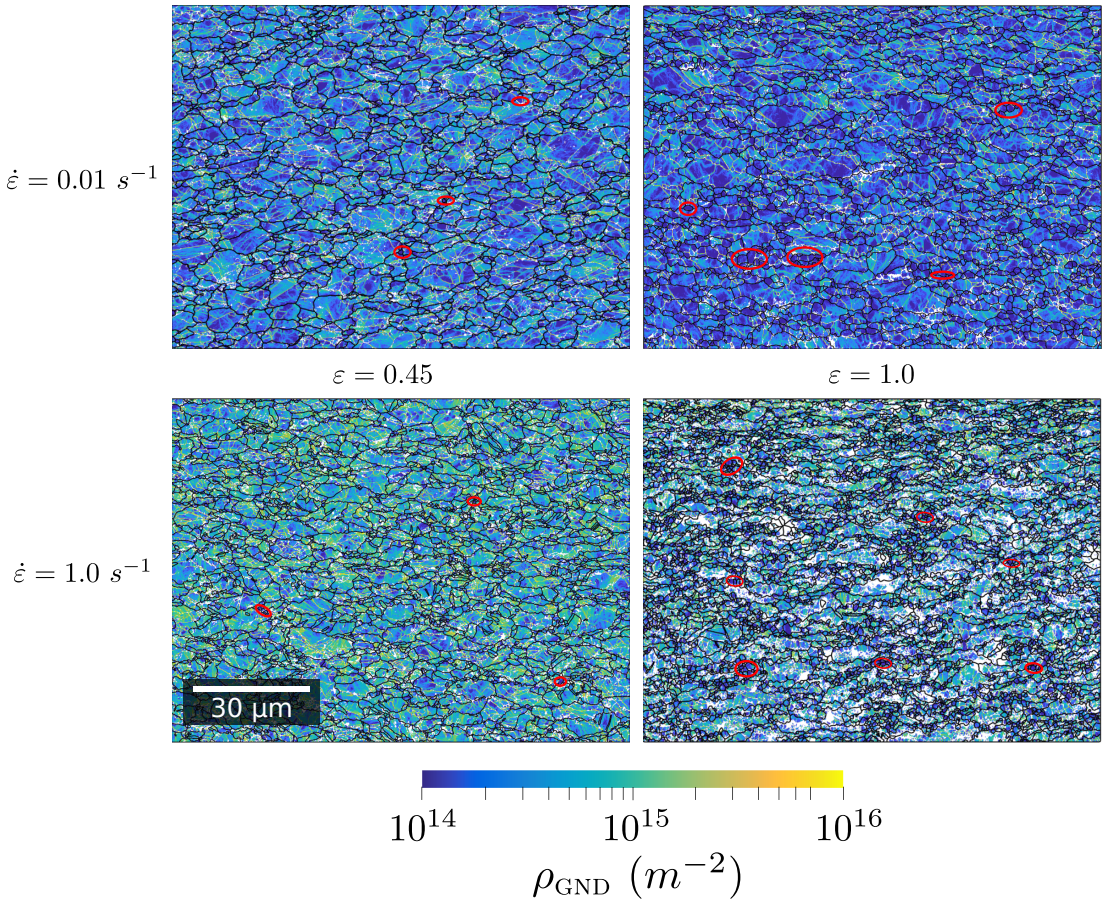
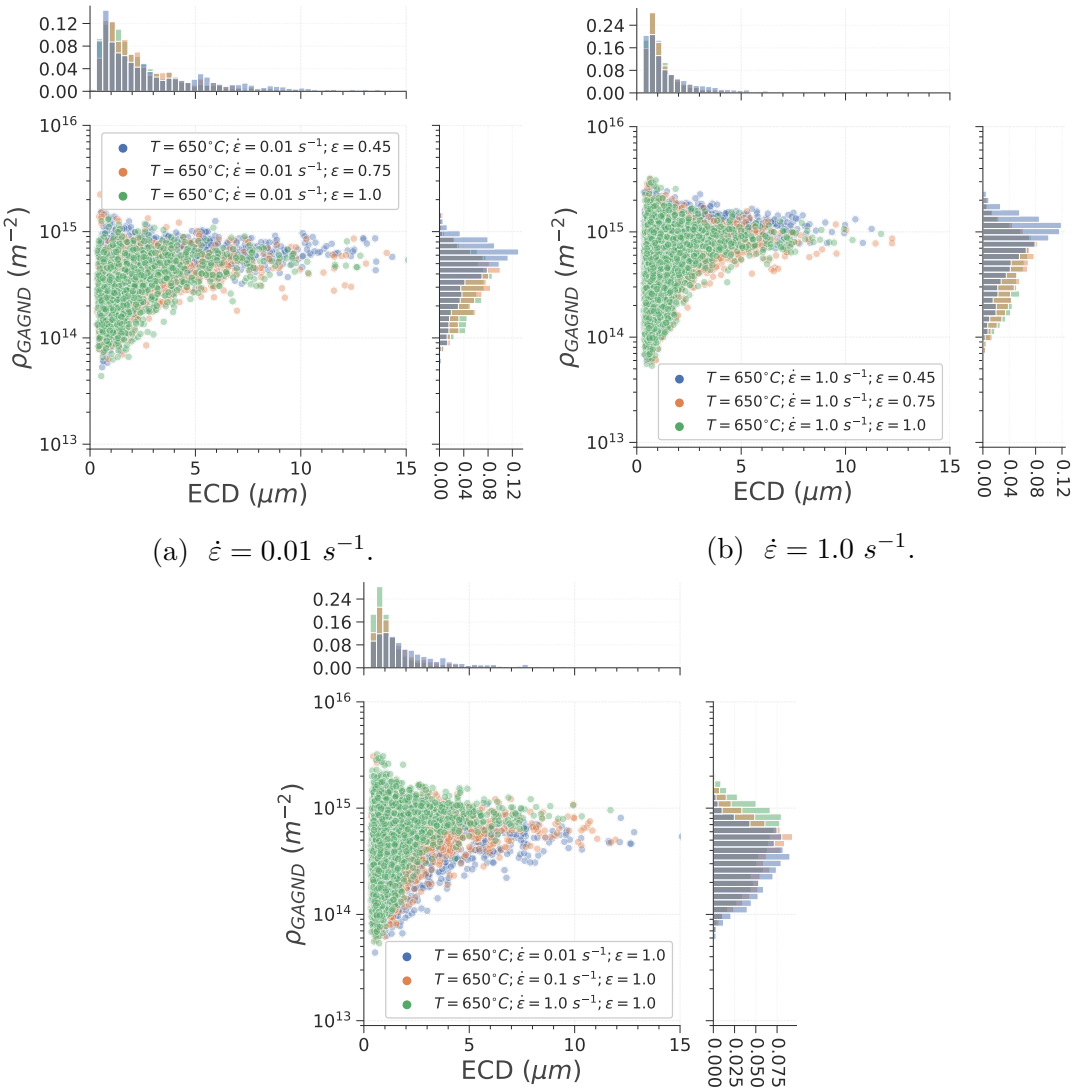


Figure 6.5: EBSD GND density maps for different hot deformation conditions ($T = 650°C$). **Eq** samples.

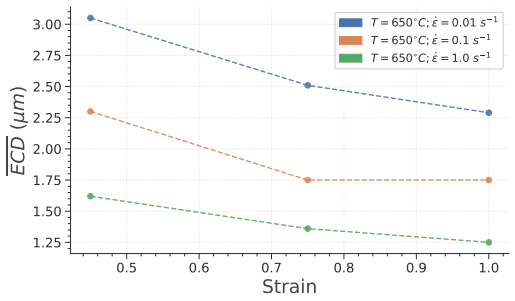


(a) $\dot{\varepsilon} = 0.01\ s^{-1}$.

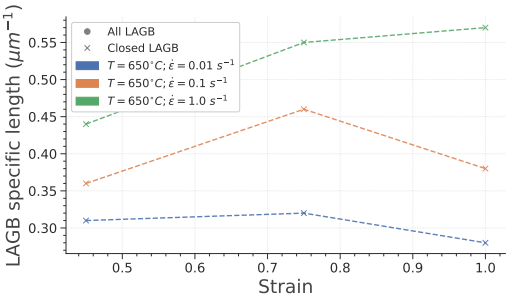
(b) $\dot{\varepsilon} = 1.0\ s^{-1}$.

(c) $\varepsilon = 1.0$.

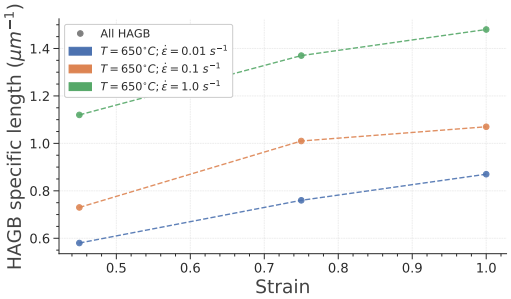
Figure 6.6: GAGND density distributions, for different strain rates and final strains. **Eq** samples.



(a) $\overline{ECD}$ versus strain.



(b) LAGB specific length versus strain.



(c) HAGB specific length versus strain.

Figure 6.7: Evolution of the microstructure topology during hot deformation at $T = 650°C$. **Eq** microstructure.

conditions of interest.

6.1.2 Influence of initial microstructure

To give an overview of the microstructure evolution observed during hot compression of lamellar microstructures, EBSD orientation maps are plotted in figure 6.8. Several remarkable features can be observed on these figures:

- a few deformation twins are observed. This is confirmed in appendix C.1 that shows several microstructure images with the twin boundaries printed in red. One can note that very few of the boundaries that were candidates for being twins based on their straight geometry verify the misorientation criterion. This confirms that the complex initial microstructure topology makes such interpretations risky, especially at high deformation levels.

- A large number of small grains is observed at all deformation levels. They form clusters or bands. Their formation seem to be largely inherited from deformation heterogeneities. Indeed, figure 6.8 clearly shows bands of small grains that are aligned and spaced rather regularly, which is consistent with heterogeneous deformation mechanisms.

- the texture seems strong, even for $\varepsilon = 0.55$.

- At largest strain, the large grains are all very elongated along horizontal direction.

- No clear progression with increasing strain can be noted. The initial quenched microstructure is quickly transformed to a deformed microstructure with subgrains and elongated grains. Besides, at small strain values, a large number of small grains are present and the texture is quite strong.

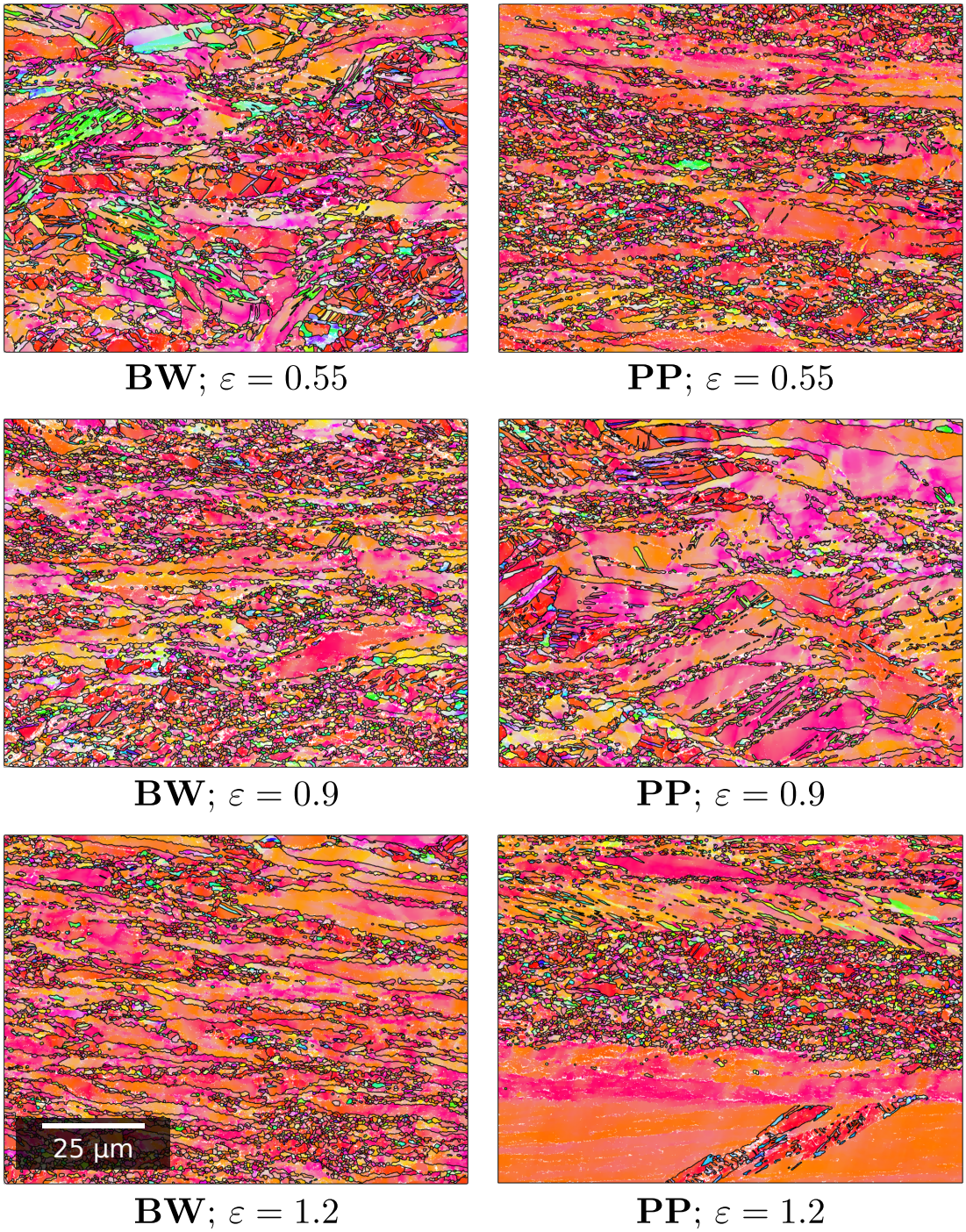
To complete the EBSD orientation maps, four GND density maps are provided in figure 6.9. Three GND distributions are displayed in figure 6.10. These maps display that GND density are very heterogeneous for **BW** and **PP** samples. Figure 6.10 confirms that the distribution presents a larger spread for lamellar samples than for **Eq** samples. In GND maps, most of the zones containing a very high dislocation density also present a large quantity of small grains and subgrains. Finally, it is noteworthy to mention than the degree of organization of GND is varying from one grain to the other, and even within a single grain.

Finally, the evolution of LAGB and HAGB specific length with strain are plotted in figure 6.11. These results confirm the comments made earlier; no clear progression is observable with increasing strain, due to the high heterogeneity in regards of the observation scale.

From the results presented above, it appears that lamellar microstructures behave very differently during hot deformation, in comparison of equiaxed ones. The results point out that these differences originate from different deformation behaviors. In zirconium alloys and in the range of temperatures considered in the present study ($T \in [450; 650]^{\circ} C$), grains mainly deform by prismatic slip [205]. Their orientation changes progressively and some dislocations are created in the material to accommodate the deformation incompatibilities.

To understand the differences between lamellar and equiaxed microstructures, one should consider the differences of initial texture. **Eq** samples present a strong texture and most of the grains initially have their <c> axis normal to the compression direction. Since the spread of initial grain orientation is low, most of the grains deform rather similarly and the deformation incompatibilities are weak. In lamellar microstructures, on the other hand, there is no initial texture. The grain initial orientations are distributed in the orientation space following the variant selection rule. Therefore, grains are more susceptible to deform differently. This generates deformation incompatibilities close to grain boundaries that present a higher GND density. These zones constitute preferential sites for formation and growth of recrystallized grains. Therefore, lamellar microstructure present a more heterogeneous recrystallization behavior.

Between **BW** and **PP** samples, the extent of heterogeneity is also rather different. In **BW** microstructures, most of the lamellae are in contact with lamellae presenting different orientations. Since the lamella thickness is low, the deformation incompatibilities affect almost all the microstructure. In **PP** microstructures, only lamellae located at ex-β GB are in contact with lamellae with different orientations. Therefore, the areas around ex-β GB are impacted by deformation

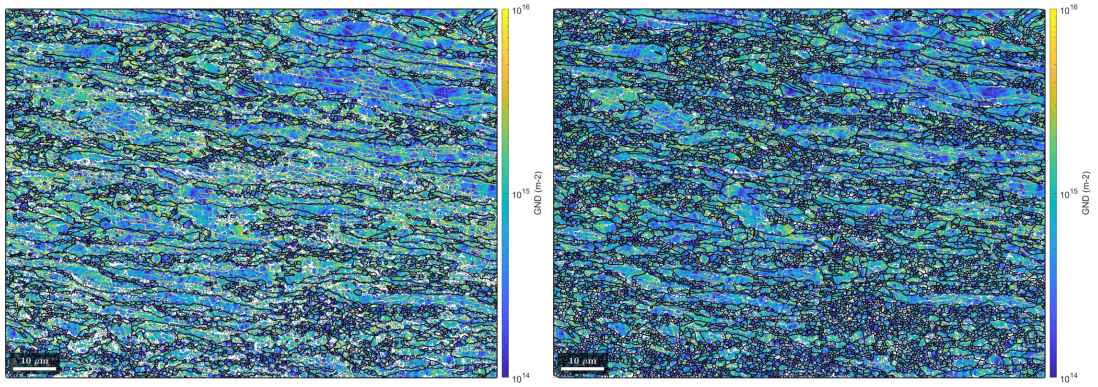


BW; $\varepsilon = 0.55$ **PP**; $\varepsilon = 0.55$

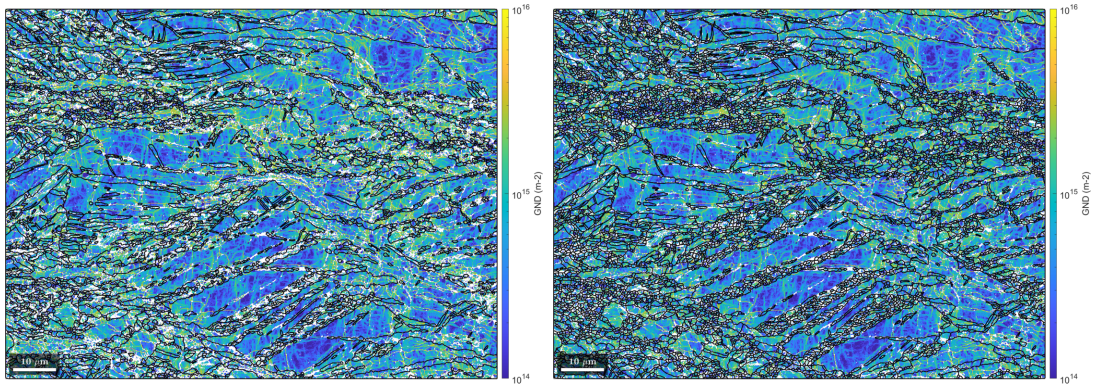
BW; $\varepsilon = 0.9$ **PP**; $\varepsilon = 0.9$

BW; $\varepsilon = 1.2$ **PP**; $\varepsilon = 1.2$

Figure 6.8: EBSD orientation maps showing microstructure evolution during hot deformation ($T = 650°C$; $\dot{\varepsilon} = 1.0\ s^{-1}$). IPF Y color code.



(a) $\varepsilon = 1.2$, **BW** sample, including LAGB. (b) $\varepsilon = 1.2$, **BW** sample, excluding LAGB.



(c) $\varepsilon = 0.9$, **PP** sample, including LAGB. (d) $\varepsilon = 0.9$, **PP** sample, excluding LAGB.

Figure 6.9: GND density maps computed from EBSD data, excluding or including the LAGB from the computation. When LAGB are excluded, they appear as boundaries and are displayed as thick black lines. $T = 650°C$; $\dot{\varepsilon} = 1.0\ s^{-1}$.

incompatibilities whereas an important part of the microstructure does not experience such effect. Therefore, there are fewer preferential zones for formation and growth of recrystallized grains and the recrystallization seems even more heterogeneous for **PP** microstructures.

Finally, it could be interesting to relate these observations to the ones made in previous chapter about evolution of these microstructures during a subsequent heat treatment. The results about PDRX are showing very heterogeneous behaviors, with some zones with a lot of small recrystallized grains and some others with very few. The grain size distribution of the recrystallized grain is wide. In addition to the maps presented in previous chapter, some additional are provided in following figure (figure 6.12). These maps highlight the role played by deformation heterogeneities in formation of recrystallized grains. They confirm that the formation of grains and subgrains is highly localized. This is consistent with the observations made by Vanderesse [56] and extends them by demonstrating their impact in the PDRX domain. The GND density maps do not show any clear correlation between the GND density localization and the large recrystallized grain location. For instance, the large band circled in red in figure 6.12d still presents

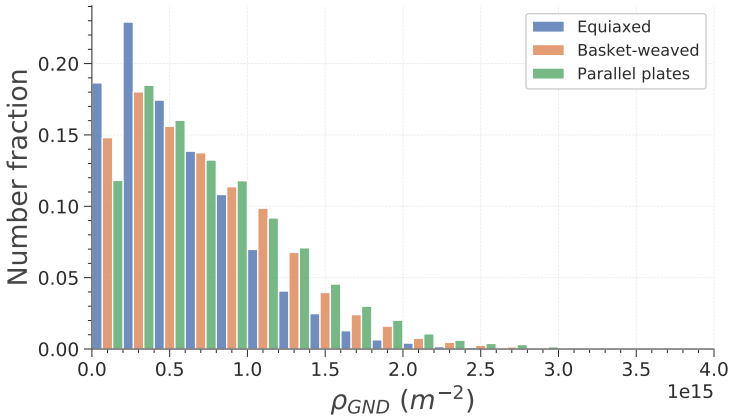
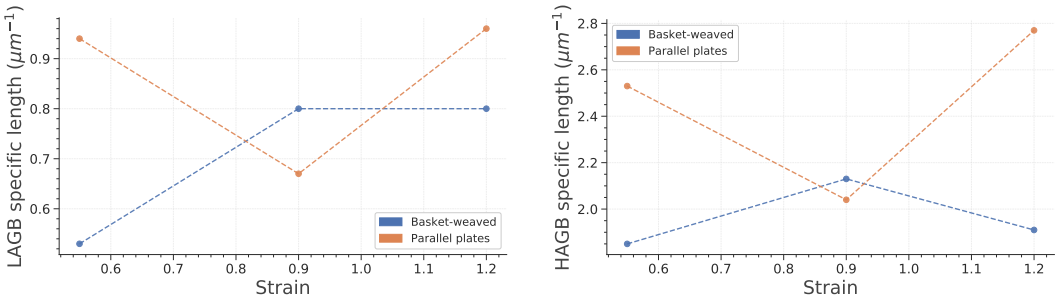


Figure 6.10: GND density distributions of samples hot deformed in following conditions: $T = 650°C$; $\dot{\varepsilon} = 1.0\ s^{-1}$; $\varepsilon = 1.0 - 1.2$.



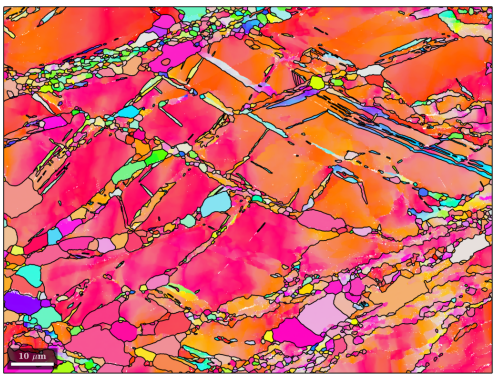
(a) LAGB specific length.

(b) HAGB specific length.

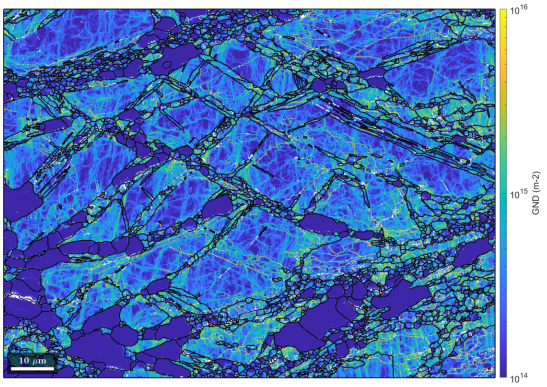
Figure 6.11: GB length versus strain, for **BW** and **PP** microstructures. $T = 650°C$; $\dot{\varepsilon} = 1.0\ s^{-1}$).

very few recrystallized grains even if the GND density is high. This is consistent with the observations made earlier from figure 6.9. Indeed, if most of the zones with a high GND density present a large number of small grains and subgrains, some remain free of such features. This points out that high GND density is a necessary but not a sufficient condition for formation of large recrystallized grains. Finally, some other grains present a well defined GND structure but do not present a large number of subgrains. A similar feature has been already mentioned in an article published by Bieler et al. about deformation mechanisms of a titanium alloy with a lamellar microstructure. Some grains with <c> axis nearly perpendicular to compression direction (i.e. grains where only prismatic slip, the softest system, is activated) were supposed to deform easily. However, these grains rather presented low defect density, implying that "single slip must have occurred with easy recovery" [54]. This incriminates the role of DRV as a concurrent mechanisms to DRX. In our case, the situation appears more complex as DRV appear as a necessary mechanism to form subgrains in some parts of the

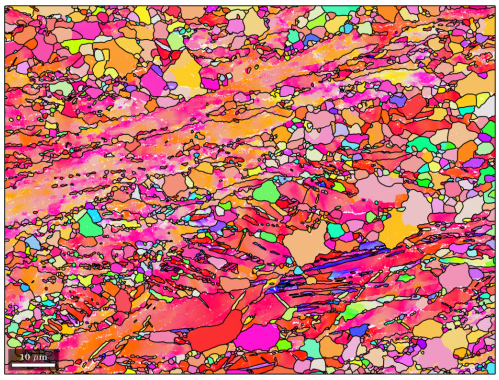
microstructure, whereas it could be a concurrent mechanism in some others.



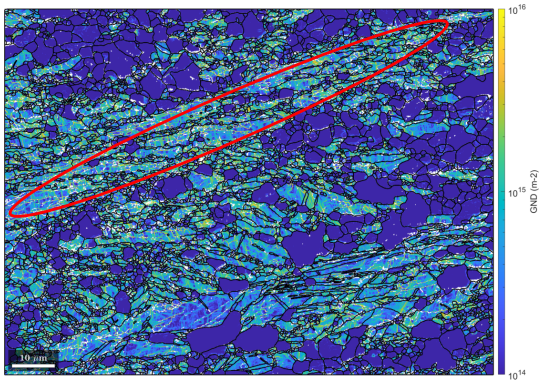
(a) $\dot{\varepsilon} = 0.1\ s^{-1}$, $\varepsilon = 1.2$, $dt = 100\ s$, **PP** sample, including LAGB.



(b) $\dot{\varepsilon} = 0.1\ s^{-1}$, $\varepsilon = 1.2$, $dt = 100\ s$, **PP** sample, excluding LAGB.



(c) $\dot{\varepsilon} = 1.0\ s^{-1}$, $\varepsilon = 0.9$, $dt = 50\ s$, **PP** sample, including LAGB.



(d) $\dot{\varepsilon} = 1.0\ s^{-1}$, $\varepsilon = 0.9$, $dt = 50\ s$, **PP** sample, excluding LAGB.

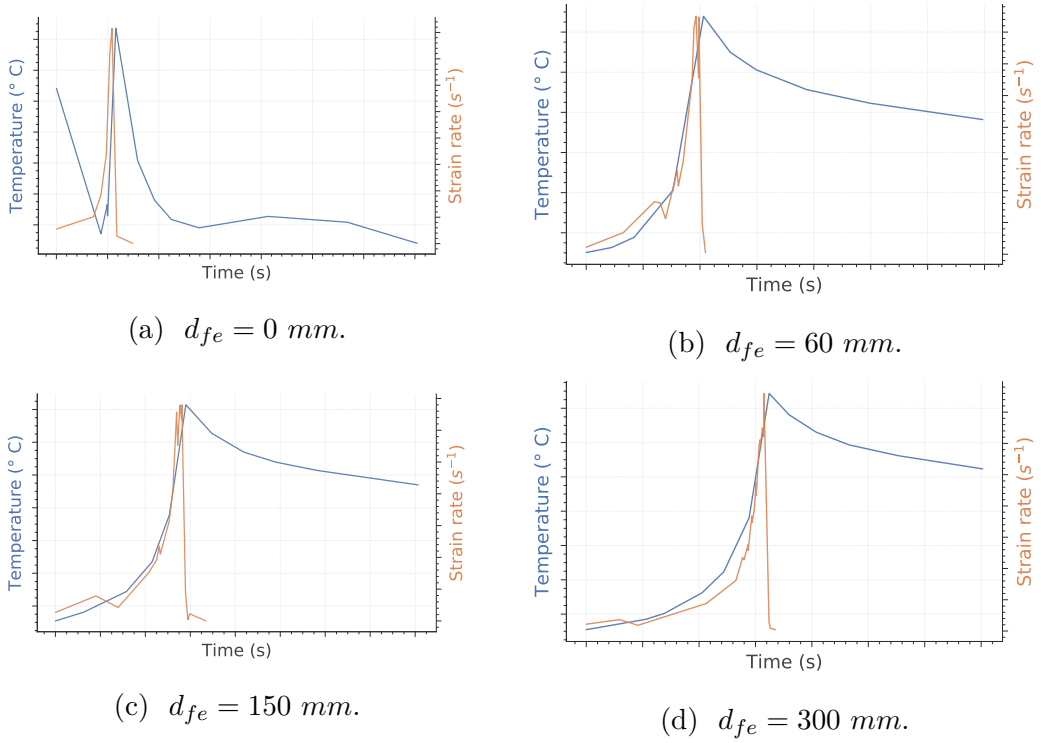
Figure 6.12: EBSD orientation and GND density maps. LAGB are excluded from GND computation and appear as boundaries and are displayed as thick black lines. $T = 650°C$.

6.1.3 Application to hot extrusion

To study the microstructure evolutions during hot extrusion, a billet used for tube manufacturing is sampled and some EBSD maps are realized at different positions. Within this study, only the characterization made at mid-thickness are considered. Four positions are observed: 0, 60, 150 and 300 mm from the front end of the tube. The corresponding thermomechanical conditions obtained from macroscopic thermomechanical simulations [66] are plotted in figure 6.13. As the exact values are confidential, they are not displayed in figure 6.13. The ranges of thermomechanical conditions experienced are:

- $500°C \leq T \leq 700°C$,
- $0\ s^{-1} \leq \dot{\varepsilon} \leq 3.0\ s^{-1}$,

- $0.5 \leq \varepsilon \leq 3.0$.



(a) $d_{fe} = 0\ mm$.

(b) $d_{fe} = 60\ mm$.

(c) $d_{fe} = 150\ mm$.

(d) $d_{fe} = 300\ mm$.

Figure 6.13: Thermomechanical conditions at mid-thickness, for four front end distances (d_{fe}). These results come from thermomechanical simulations.

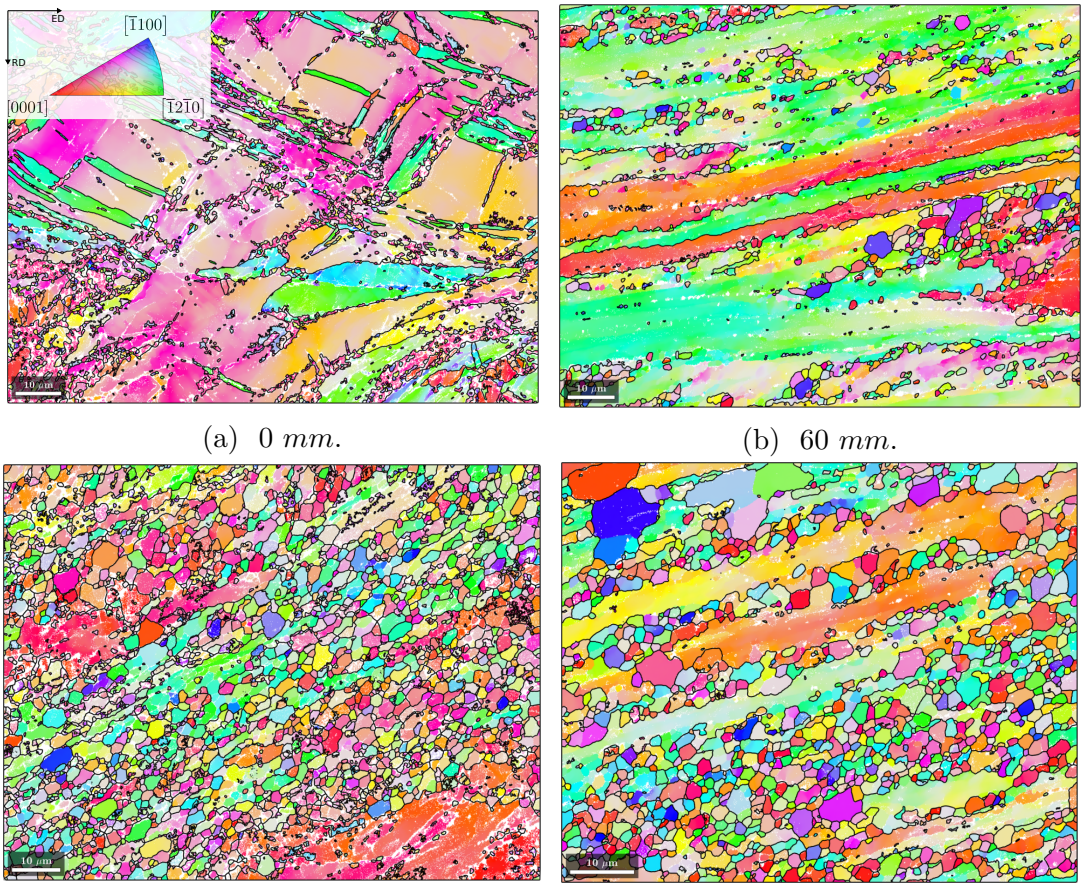
If the thermomechanical conditions displayed above and predicted by simulations are rather reliable, the evolution of temperature during the cooling stage remains unknown. As said in section 1.1.5, the billet stays in a confined environment for several minutes at the end of the process and up to now, no method for measuring the cooling kinetics is available. To tackle that problem and being able to simulate the evolutions later on, two extreme cases are considered:

- an ambient temperature equal to $100°C$, supposed to reproduce the temperature at outer of the tube.
- An ambient temperature equal to $600°C$, to replicate the higher temperature at the inner of the tube, where the environment is extremely confined.

The hot extrusion stress state is more complex than for hot compression. Nevertheless, this stress state difference remains a second order parameter in regards of recrystallization, especially since initial microstructure is lamellar without any defined texture.

EBSD orientation maps for the four distances are displayed in figure 6.14. These orientation maps confirm that the hot deformed microstructures observed after hot extrusion are very similar to the ones observed after hot compression

and holding at temperature. Since the local strain rate and final strain are higher at 150 and 300 *mm* from the front end, the microstructure seems to be more homogeneous and to contain a greater fraction of recrystallized grains. This will be discussed in more details in an upcoming section (section 6.3.3).



(a) 0 *mm*. (b) 60 *mm*.

(c) 150 *mm*. (d) 300 *mm*.

Figure 6.14: EBSD orientation maps of hot extrusion samples at mid-thickness and different front end distances. IPF Y color code. ED designates the extrusion direction and RD the radial direction. ED is not perfectly horizontal and varies from one sample to the other.

6.2 Parameters identification for modeling of CDRX

The model presented earlier in chapter 3 contains 15 parameters that define:

- the grain boundary properties: M_0, Q_m, γ_{max}, δ.
- The mechanical behavior: b, μ, ρ_0, K_1, K_2, M_T, α_T.
- The evolution of substructures, as predicted by the Gourdet-Montheillet model: θ_0, D_0, m and η.

M_0, Q_m and γ_{max} are defined in chapter 4. Values for δ are discussed in chapter 5 for $\dot{\varepsilon} = 0.1\ s^{-1}$ and $\dot{\varepsilon} = 1.0\ s^{-1}$. The following sections detail the identification procedures and justify the values taken from literature.

6.2.1 Definition of parameters related to mechanical behavior

The values of parameters related to mechanical behavior are described in table 6.1, with the exception of K_1 and K_2.

b (Å)	ρ_0 (m^{-2})	μ (GPa)	M_T	α_T
3.23 [206]	5×10^{13}	$42.52 - 0.022 \times T$ (K) [207]	2.3 [206, 208]	0.2 [209]

Table 6.1: Parameters related to mechanical behavior.

The equation proposed in table 6.1 for computing shear modulus (μ) is preferred over the ones proposed in other works [55] since it is consistent with the values provided in MATPRO documentation [210]. The value for M_T in ref. [206] is reduced from 4.0 to 2.3 since Shen et al. proved that the Taylor factor of polycrystals decreases very quickly when texture increases [208]. Since previous results show that the texture is strong for $\varepsilon \geq 0.45$, $M_\mathrm{T} = 2.3$ seems a reasonable choice. Finally, the value of α_T is set to 0.2 since Mughrabi pointed out that organization of GND into cells by recovery, leading to heterogeneous dislocation density, is susceptible to lower α_T from 0.35 to 0.2. Again, this is totally in agreement with the observations made in previous sections. Finally, the value of ρ_0 is set according to the discussion in section 5.2.4.

6.2.2 Hardening and recovery parameters identification

Most of the identification work consists in setting the Hardening and recovery parameters. The principle of the procedure is to fit the macroscopic stress-strain curves from the hot compression thanks to Yoshie-Laasraoui-Jonas and Taylor equations (equations 3.1 and 3.3). Since the Yoshie-Laasraoui-Jonas equation describes the variation of dislocation density due to strain hardening and recovery

only, the fit between the experimental and the predicted curves is realized considering only the first region of the plastic domain. In that region, recrystallization is very limited and should not affect the mechanical behavior. This strategy rests on the hypothesis that the macroscopic mechanical behavior of the sample is representative of the microstructure evolution characterized at sample center. Experimental and predicted stress-strain curves are plotted in figure 6.15 for several thermomechanical conditions. Additional figures for other temperatures are provided in appendix D.1 (figure D.1) . Since several triplets ($\sigma_0,\ K_1,\ K_2$) could be used to fit the same curve, a few rules are set to restrict the identification and ensure a reasonable evolution of these parameters with thermomechanical conditions:

- K_1 decreases with temperature and increases with strain rate,
- K_2 increases with temperature and decreases with strain rate,
- σ_0 decreases with temperature and increases with strain rate.

Once the stress-strain curves are fitted for all the thermomechanical conditions tested and for all the initial microstructure, evolution laws for ($K_1,\ K_2$) proposed by Montheillet et al. [211] and detailed in equations 6.1 and 6.2 are fitted using the least square method. The yield stress, σ_0, is described as a linear function of the Zener-Hollomon parameter logarithm (equation 6.3) [212] and is fitted using the same method. These operations are illustrated by figures 6.16 and 6.17.

$$K_1 = K_1^0 \dot{\varepsilon}^{m_h} \exp \frac{m_h Q_h}{RT}, \tag{6.1}$$

$$K_2 = K_2^0 \dot{\varepsilon}^{-m_r} \exp \frac{-m_r Q_r}{RT} \tag{6.2}$$

$$\sigma_0 = \sigma_0^s \times \ln(Z) + \sigma_0^i \tag{6.3}$$

σ_0^s and σ_0^i designate the slope and the intercept of the linear function, respectively.

The identified values are given in table 6.2.

$K_1^0\ (m^{-2})$	m_h	$Q_h\ (J \cdot mol^{-1})$	K_2^0	m_r	$Q_r\ (J \cdot mol^{-1})$	$\sigma_0^s\ (MPa)$	$\sigma_0^i\ (MPa)$
1.60×10^{14}	0.14	1.71×10^5	712	0.11	3.42×10^5	2.86	-17.8

Table 6.2: Identified values for evolution laws of K_1, K_2 and σ_0.

Finally, this gives an average value for K_1 and K_2. As discussed in section 3.1.1, one value of K_1 is set per grain to reproduce the intergranular heterogeneities discussed earlier.

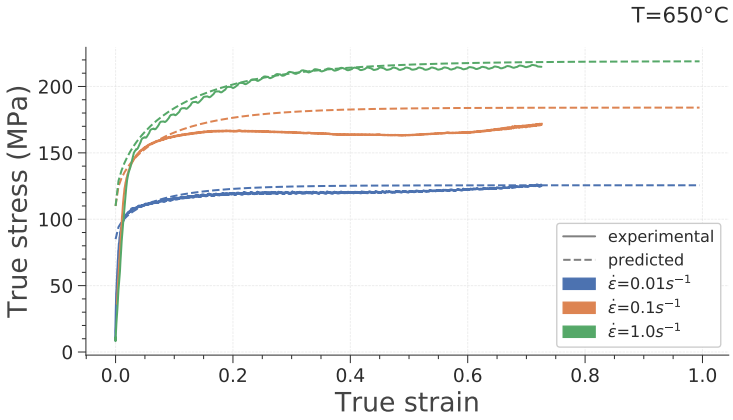
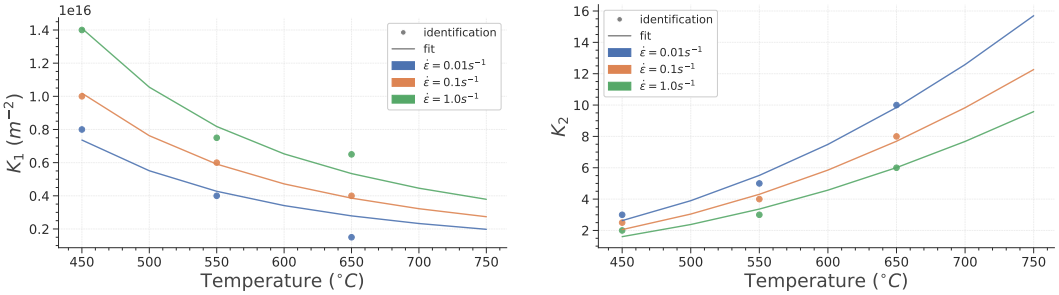


Figure 6.15: Experimental and predicted flow curves for $T = 650°C$. **Eq** samples.



(a) K_1 versus temperature. (b) K_2 versus temperature.

Figure 6.16: Hardening and recovery parameters as a function of temperature, for several strain rates. **Eq** samples.

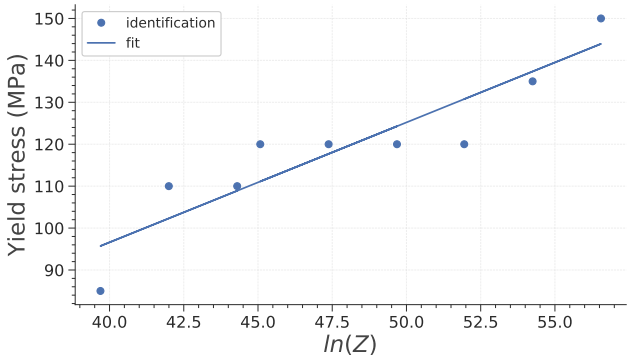


Figure 6.17: Evolution of yield stress, identified from hot compression test and predicted by equation 6.3.

6.2.3 Definition of Gourdet-Montheillet model parameters

The parameters of Gourdet-Montheillet model are given in table 6.3. They are set by following the recommendations of Gourdet [126]. No optimization of these parameters is done, since the results obtained with these parameters are satisfactory. Nevertheless, adjusting these parameters to improve the agreement with experimental results could be considered in an upcoming work.

D_0 (μm)	θ_0 ($^\circ$)	m	η
1.0	1.0	2	2

Table 6.3: Parameters of the Gourdet-Montheillet equations [125].

6.3 Modeling of CDRX and PDRX

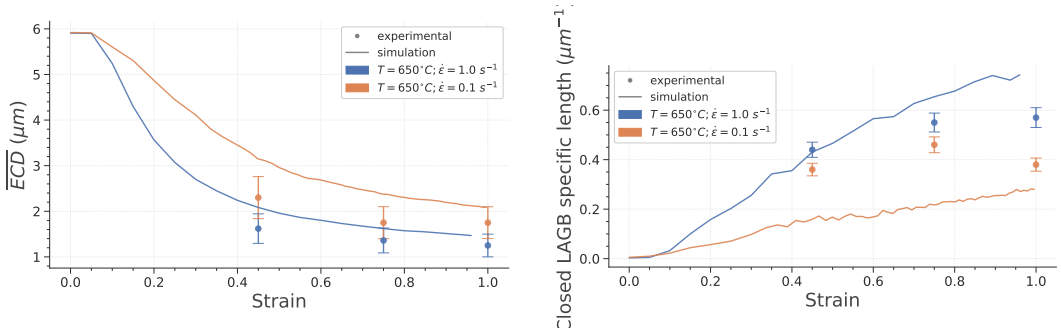
After having identified the model parameters, it is now time to simulate recrystallization during hot deformation and subsequent heat treatment. All the simulation results described in the following sections are made using the CDRX model described in chapter 3. They all include a single stage of hot deformation followed by a single heat treatment stage.

6.3.1 Influence of thermomechanical conditions

Firstly, to investigate the impact of thermomechanical conditions by simulation, the evolution of $\overline{ECD}$ and of LAGB specific length with strain are plotted in figure 6.18. From these results, it appears that the experimental trends are rather well reproduced. The model predicts the greater decrease of the average grain size and the higher LAGB formation rate at high strain rate.

To be able to analyze additional microstructural features, one should have a look at the PDRX regime. Figure 6.19 displays the digital and experimental microstructures at two instants of the hold at temperature. Figure 6.20 presents the evolution of average properties with holding time. From the comparison between experimental and digital microstructures, it is interesting to notice that the model is able to reproduce the heterogeneities. The large deformed grains with the highest dislocation density are quickly consumed by the small grains and subgrains whereas some other parts of the microstructure remain unchanged. When the final strain level is reduced, the simulation overestimates the number of large recrystallized grains. Finally, at $\dot{\varepsilon} = 0.1s^{-1}$, the digital microstructures are rather consistent with the experimental ones, even with the simplistic approach of adding spherical subgrains within the microstructure. Several observations can be made based on figure 6.20:

- the trends for recrystallized fraction are consistent with the experimental observations, even if the recrystallized fraction for $\dot{\varepsilon} = 1.0\ s^{-1};\ \varepsilon = 1.0$ is



(a) $\overline{ECD}$ versus strain. (b) LAGB specific length versus strain.

Figure 6.18: Evolution of the main microstructure descriptors with time, during CDRX-PDRX simulations. **Eq** samples.

underestimated for the longest holds.

- The evolution of the average recrystallized grain size with holding time is well predicted for the highest strain rate. It is largely overestimated for $\dot{\varepsilon} = 0.1\ s^{-1}$.
- The values of LAGB specific length converge to the correct ones, but the decrease at the beginning of the PDRX stage is too important.
- The same comments apply to the evolution of average GND density with time. However, the impact of thermomechanical conditions is well predicted. If GND density is initially lower at $\dot{\varepsilon} = 0.1\ s^{-1}$, it decreases at a much slower rate and becomes the highest after tens of seconds.

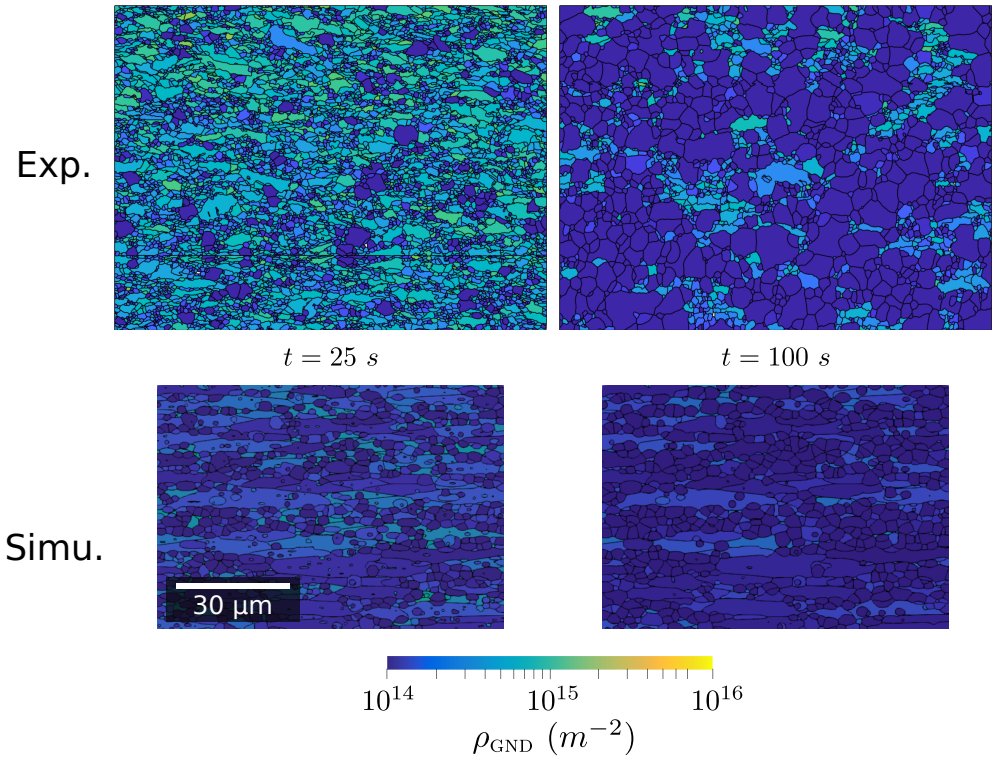
To complete these observations, a scatter plot with marginal distributions is provided in figure 6.21. The two others are only displayed in appendix D.2 since they share the same main features. Three major characteristics of the simulation results, that differ from the experimental results, should be noted:

- there are no grains with an average GND density higher than $5 \times 10^{14} m^{-2}$.
- The large deformed grains present a large scatter of average GND density.
- The quantity of very small grains is underestimated.

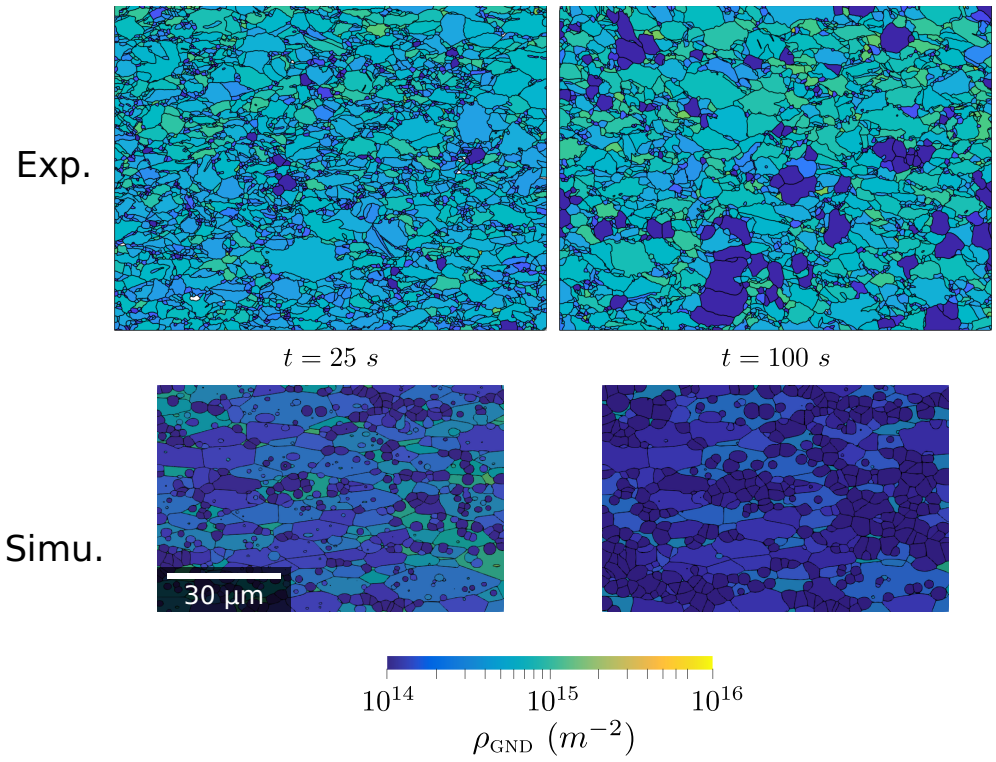
These comments seem to point out that one degree of heterogeneity is missing, as discussed in previous chapter. Indeed, if some heterogeneity appears in simulation thanks to the definition of K_1, it is still not sufficient and does not reproduce the fact that very few recrystallized grains grow at $\dot{\varepsilon} = 1.0\ s^{-1};\ \varepsilon = 0.45$. For the lowest strain rate ($\dot{\varepsilon} = 0.1\ s^{-1}$), the explanation is simpler. The values of recrystallized fraction and $\overline{ECD}_{rx}$ are affected by some large deformed grains that see their average GND density dropping below the threshold value. In simulation, this happens because there is some GB migration between deformed grains with different GND density values. Experimentally, this does not happen, certainly for two reasons. Firstly, the GND density in GB regions generally saturate and the gap between neighboring grains is lowered. Secondly, some SPP are present and contribute to pin the GB in such regions where the driving pressures are very low. Finally, as discussed earlier (see section 5.2.4), being able to consider intragranular GND density gradients would allow to improve significantly the predictions related to the stability of a large number of really small grains and subgrains.

6.3.2 Initial microstructure impact

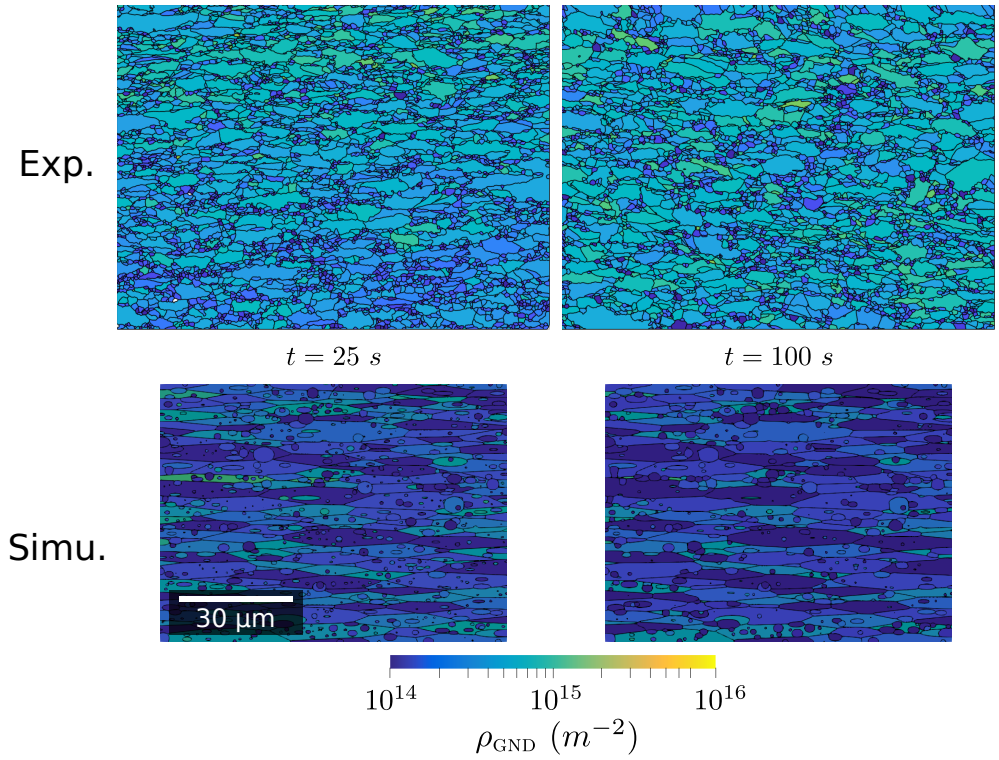
Now that the model has shown its ability to predict the impact of thermomechanical conditions over CDRX and PDRX regimes, it is time to apply the model with several initial microstructures. To do so, the evolution of the average grain size and of the LAGB specific length with strain are plotted in figure 6.22. The first



(a) $T = 650°C;\ \dot{\varepsilon} = 1.0\ s^{-1};\ \varepsilon = 1.0.$

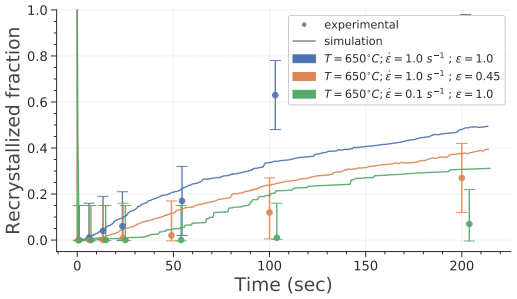


(b) $T = 650°C;\ \dot{\varepsilon} = 1.0\ s^{-1};\ \varepsilon = 0.45.$

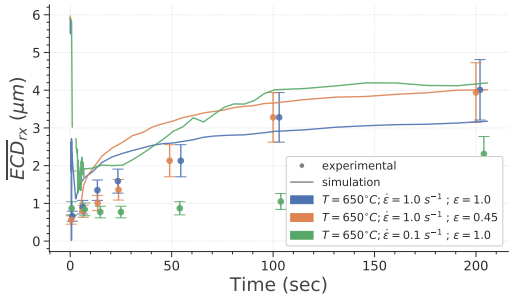


(c) $T = 650°C;\ \dot{\varepsilon} = 0.1\ s^{-1};\ \varepsilon = 1.0.$

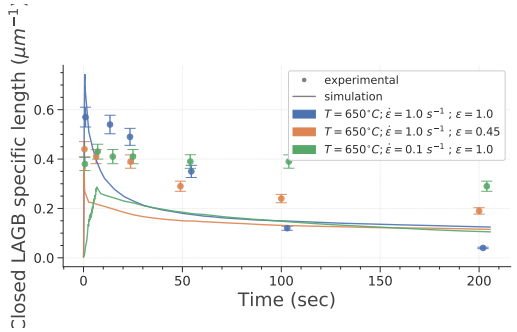
Figure 6.19: GAGND maps from EBSD and simulation data, after two durations of heat treatment at $T = 650°C$. **Eq** samples.



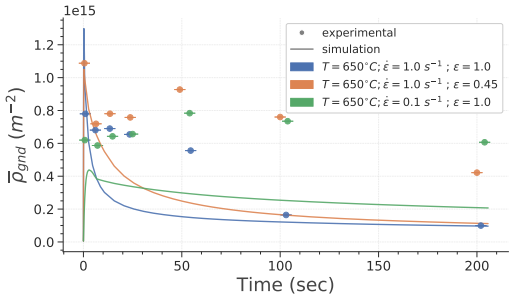
(a) Recrystallized fraction versus time.



(b) $\overline{ECD}_{rx}$ versus time.



(c) LAGB specific length versus time.



(d) Average GND density versus time.

Figure 6.20: Evolution of the main microstructure descriptors with time, during CDRX-PDRX simulations. **Eq** samples.

graph illustrates the model ability to predict the rather steady-state in terms on average grain size reached for strain greater than 0.4. The second confirms that the simulations are able to predict that lamellar microstructures form a higher fraction of LAGB.

As previously, to get a bigger picture of the problem, some images of the digital and experimental microstructures are provided along with the evolution of other microstructural features, during a subsequent heat treatment. These illustrations are respectively displayed in figure 6.23 and 6.24. One can see from figure 6.23 that the model is able to predict with great success the heterogeneities with some large zones that do not contain any new recrystallized grains. Again, the model largely underestimates the number of small grains and subgrains. Finally, the predictions in terms of recrystallized fraction, $\overline{ECD}_{rx}$ and LAGB specific length are consistent with the ones measured experimentally. Regarding the **PP** microstructure, one should keep in mind two important remarks. Firstly, at the considered scale, the results could vary significantly due to the high microstructure variability. Secondly, looking at figure 6.23c, it seems that the recrystallized fraction is much higher than 0.2. However, a large number of the objects that fulfill the criterion related to the average GND density are in fact subgrains, explaining why the recrystallized fraction stays low.

To conclude, these results show that the model is able to predict the impact of both thermomechanical conditions and initial microstructure upon the main

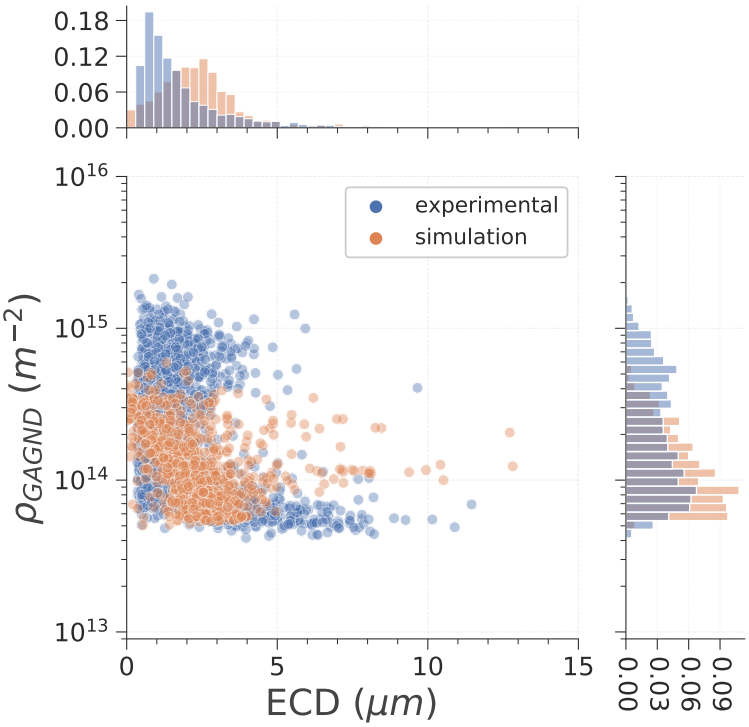
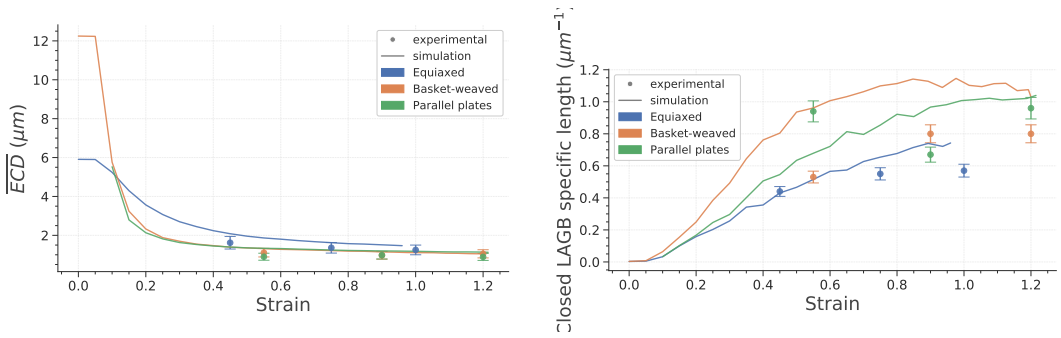
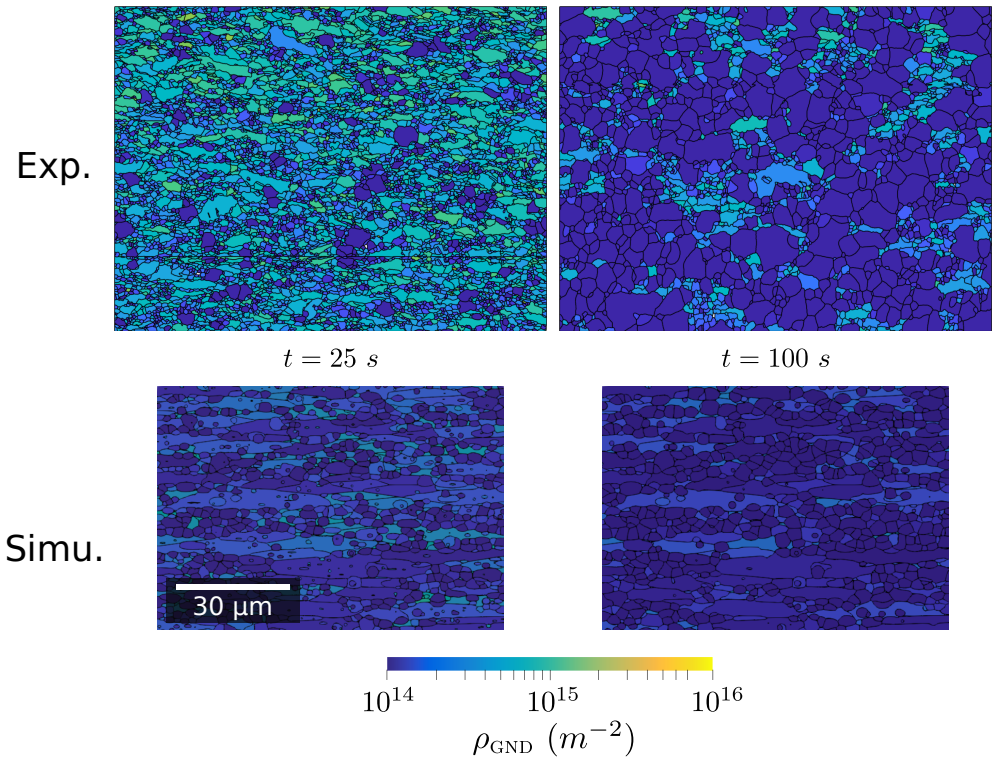


Figure 6.21: Combined scatter plots and histograms showing the distribution of grain average dislocation density (ρ_{GAGND}) and ECD. Simulation and experimental results correspond to the following thermomechanical conditions: $T = 650°C$; $\dot{\varepsilon} = 1.0\ s^{-1}$; $\varepsilon_f = 1.35$; $dt = 100\ s$.

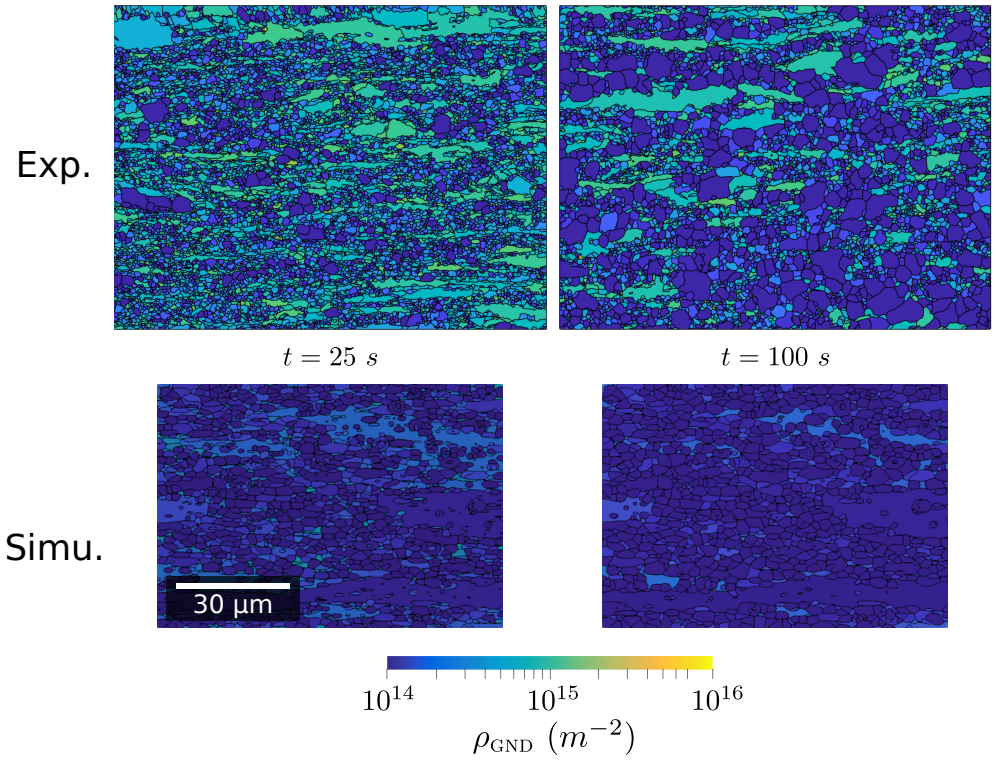


(a) $\overline{ECD}$ versus strain. (b) LAGB specific length versus strain.

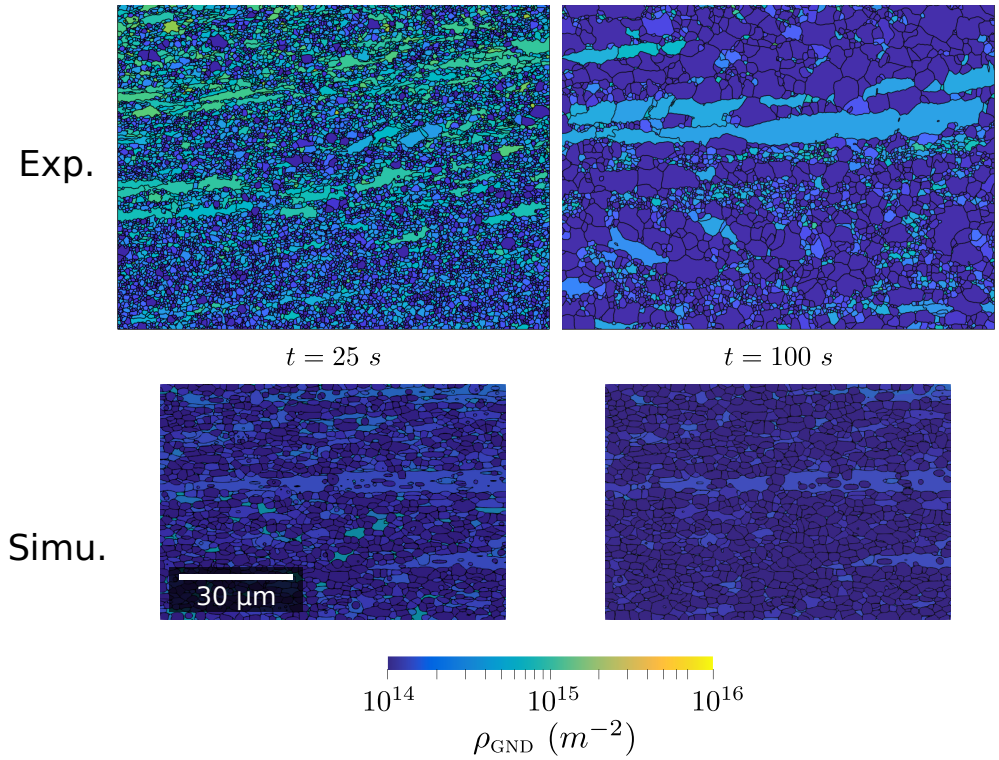
Figure 6.22: Evolution of the main microstructure descriptors with time, during CDRX-PDRX simulations. **Eq**, **BW** and **PP** samples.



(a) **Eq** microstructures.

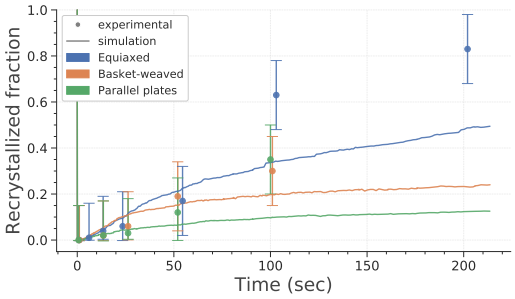


(b) **BW** microstructures.

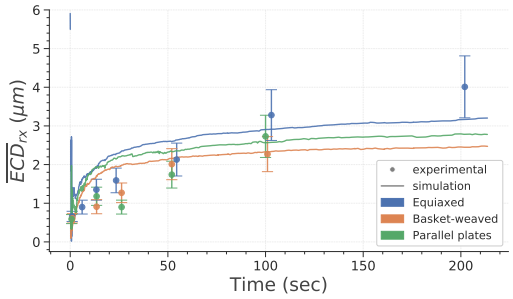


(c) **PP** microstructures.

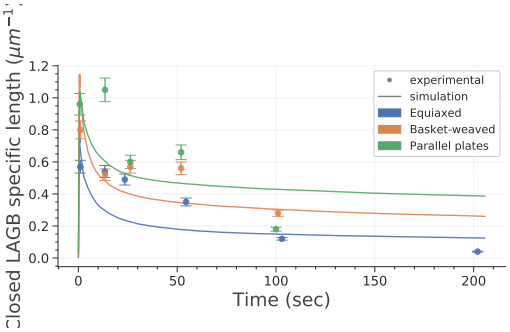
Figure 6.23: GAGND maps from EBSD and simulation data, after two durations of heat treatment at $T = 650°C$. Hot deformation conditions are: $T = 650°C$; $\dot{\varepsilon} = 1.0\ s^{-1}$; $\varepsilon = 1.0 - 1.2$.



(a) Recrystallized fraction versus time.



(b) $\overline{ECD}_{rx}$ versus time.



(c) LAGB specific length versus time.

Figure 6.24: Evolution of the main microstructure descriptors with time, during CDRX-PDRX simulations. **Eq**, **BW** and **PP** samples.

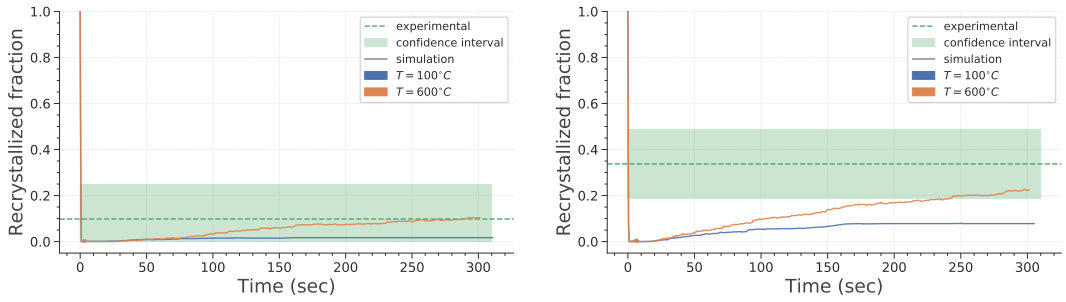
microstructure average characteristics related to recrystallization. To improve the simulation results, the hardening and recovery could be refined, in particular for the condition: $T = 650°C$; $\dot{\varepsilon} = 1.0\ s^{-1}$; $\varepsilon = 1.0$. To improve notably the results and be able to get a better prediction of the GAGND and ECD distributions, one should consider coupling the model with more advanced mechanical models (such as crystal plasticity ones). This would enable to get a precise prediction of intragranular GND gradients, a key feature impacting the growth of recrystallized grains (section 5.2.4). If this already constitutes a challenge for equiaxed microstructures, it is even more complex for lamellar microstructures. Indeed, it has been proven that for such microstructures, the lamellae orientation and organization impact greatly the deformation of a colony of lamellae [56, 55]. Therefore, to be able to predict accurately the spatial distribution of deformation and the appearance of specific features such as shear bands, the deformation model must consider the impact of both features. Due to the complex topology of lamella colonies, a 3D model would be certainly required. Finally, since it has been noted in a previous section (section 6.1.2) that DRV is playing a role in the rearrangement of dislocations and in the spatial distribution of GND density, improving the DRV model would also constitute an interesting way to improve the prediction of GND density heterogeneites that affect the PDRX regime.

6.3.3 Application to hot extrusion

Now that the model has been confronted to experimental results coming from laboratory testing, it is relevant to compare to results relatively to an industrial hot deformation process: hot extrusion. To do so, the results from thermomechanical simulations of the process are used as input data for simulation of microstructure evolutions. Two positions are considered: at mid-thickness, at $60mm$ and $300mm$ from the front end of the tube. As discussed in sections 1.1.5 and 6.1.3, the deformation stage is followed by a slow cooling at an unknown cooling rate. Therefore, simulations are run for the two extreme hypotheses considered: an ambient temperature of $100°C$ or of $600°C$. This makes a total of four simulation cases. For all these simulations cases, the initial microstructure is basket-weaved (**BW**). An additional simulation case is proposed, with the following conditions: $d_{fe} = 300\ mm$, $T_a = 100°C$, **PP** initial microstructure. The choice of running most of the simulations with a **BW** microstructure is motivated by the fact that it is most representative of the microstructures encountered industrially.

First, to compare the different results related to the **BW** microstructure, the evolution of recrystallized fraction with time is plotted in figure 6.25. These results agree with the observations made in previous sections: the model underestimates recrystallized fraction. The results for the highest ambient temperature seem to almost reach the experimental values. Nevertheless, it appears unrealistic to estimate from these results the final ambient temperature due to the high microstructure variability and to the confidence level over predicted values. These results confirm that the ambient temperature during cooling impacts significantly the microstructure after hot extrusion. They highlight the importance of controlling the cooling parameters for controlling to a greater extent microstructure evolutions.

To complement the previous observations, some images of the microstructures are provided in figure 6.26. The simulation images correspond to the microstructural state after $300s$ at an ambient temperature of $600°C$. The simulation results are very consistent with the experimental ones, the digital microstructures show-



(a) $d_{fe} = 60\ mm$. (b) $d_{fe} = 300\ mm$.

Figure 6.25: Evolution of recrystallized fraction with time, during CDRX-PDRX simulations of hot extrusion process.

ing the formation of a much larger number of recrystallized grains spread over the whole microstructure at a higher distance from the front end of the tube.

Finally, recrystallized fraction, $\overline{ECD}_{rx}$ and LAGB specific length are plotted versus the front end distance of the tube (figure 6.27). The predicted values for recrystallized fraction and $\overline{ECD}_{rx}$ present a good agreement with experimental measurements. The $\overline{ECD}_{rx}$ appears slightly overestimated but the experimental values show a large variability. Finally, figure 6.27c indicates that LAGB specific length is overestimated by simulations. However, the experimental values are very low compared to all the values presented in previous sections. Since these EBSD maps have been acquired on a different EBSD acquisition system, it is possible that the post-processing procedure used until now is not fully adapted.

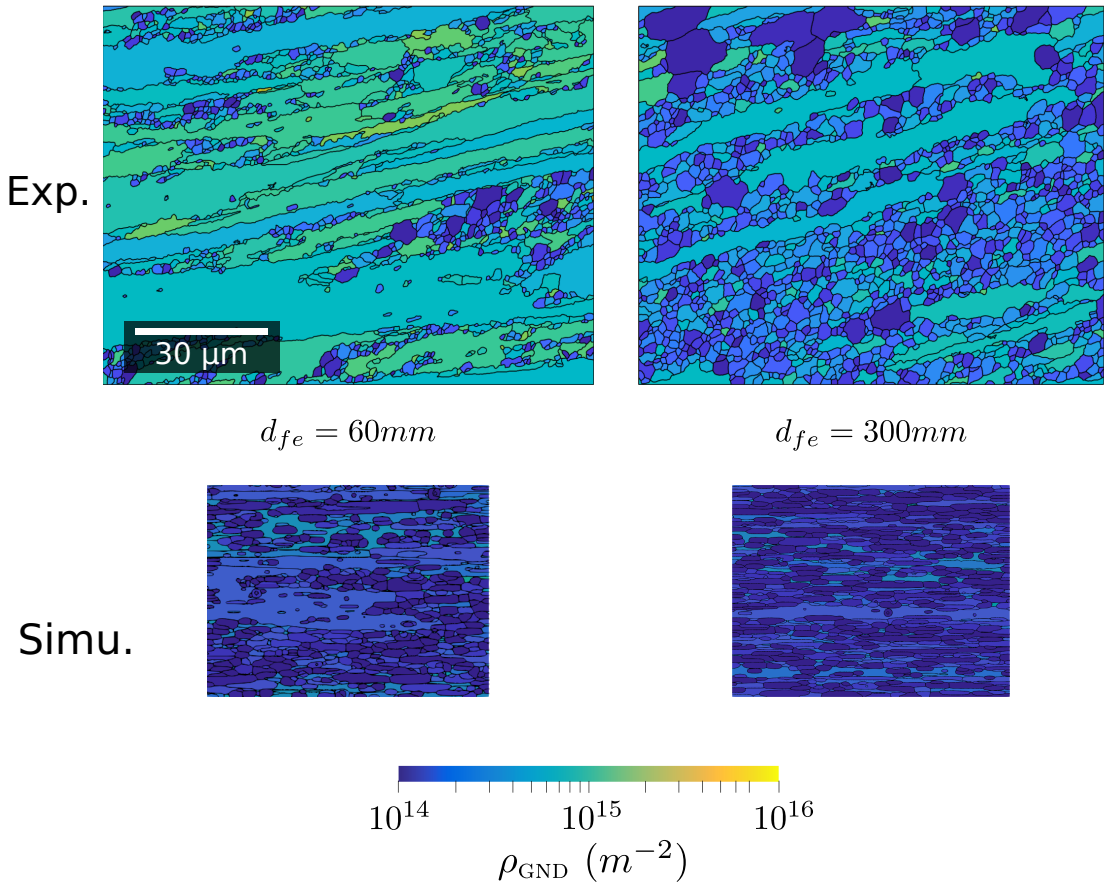
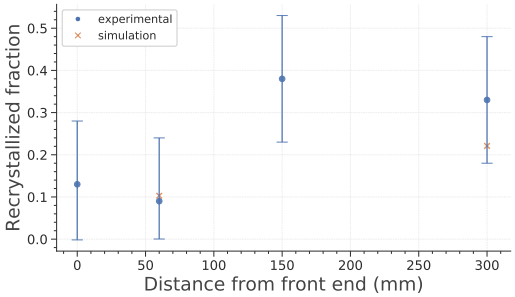
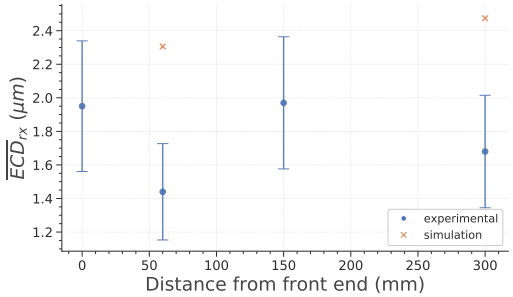


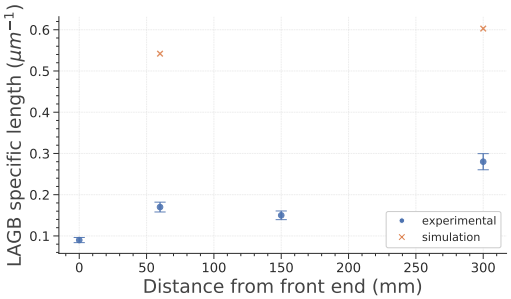
Figure 6.26: GAGND maps from EBSD and simulation data relative to hot extrusion. Simulation results correspond to the ones after $300s$ at an ambient temperature of $600°C$.



(a) Recrystallized fraction versus front end distance.



(b) $\overline{ECD}_{rx}$ versus front end distance.



(c) LAGB specific length versus front end distance.

Figure 6.27: Evolution of different microstructure characteristics at different positions of a hot extrusion billet.

6.4 Conclusion

This chapter has described in details the microstructure changes observed during hot deformation. The results confirmed that if very few recrystallized grains form during hot deformation in the range of thermomechanical conditions investigated, the changes detected affect greatly the growth of recrystallized grains during a subsequent hold. Firstly, the influence of subgrain formation (localization and number) is noticed and its relation with the strain level is demonstrated. Secondly, the decisive impact of average GND density value and of intragranular heterogeneities is highlighted. This feature seems to be directly related to the strain rate. Finally, confronting the results from different initial microstructures confirm that lamellar microstructures present a higher heterogeneity level after hot deformation. Some zones with high GND density present a large number of small grains and subgrains whereas some others do not. This confirms the importance of deformation heterogeneities in the fragmentation of the microstructure into small grains and subgrains. It also exhibits that DRV contributes to increase the heterogeneity of lamellar microstructures.

The simulation results, confronted to both laboratory and industrial experimental results, have shown that the model is able to predict the impact of both thermomechanical conditions and initial microstructure upon recrystallization. The intergranular heterogeneity is well reproduced and the agreement between experimental and digital microstructure is particularly satisfactory. Nevertheless, the model shows some limitations that are largely related to the assumptions regarding deformation. Indeed, the result discrepancies share some characteristic features with the PDRX simulation results presented in previous chapter that consider homogeneous GND density per grain.

Résumé en français

Ce chapitre détaille les évolutions microstructurales observées lors de la déformation à chaud du Zy-4. Par analogie au chapitre 5, les mécanismes de recristallisation sont tout d'abord identifiés à l'aide des résultats EBSD. Si peu de grains recristallisés sont formés lors de la déformation à chaud, les évolutions microstructurales observées conditionnent très fortement les évolutions post-dynamiques. Tout d'abord, le nombre et la localisation de sous-grains formés en fonction du taux de déformation sont quantifiés. Ensuite, le role de la densité moyenne et des hétérogénéités de densité de dislocation est évalué. Les résultats confirment que ces deux caractéristiques sont fortement affectées par la vitesse de déformation.

Les différences induites par la microstructure initiale semblent être intimement liées aux mécanismes de déformation. Les résultats expérimentaux montrent que les hétérogénéités de déformation conditionnent fortement la recristallisation. Néanmoins, il semblerait que ce ne soit pas l'unique facteur. En effet, certains grains avec une densité de dislocations élevée ne recristallisent pas ou tardivement. Par conséquent, il semblerait que les mécanismes de restauration puissent eux-

aussi contribuer à la formation d'hétérogénéités.

Les résultats de simulation montrent que le modèle est capable de prédire l'influence des conditions thermomécaniques et de la microstructure initiale. Les hétérogénéités intergranulaires sont relativement bien prédites avec ce modèle simplifié. Néanmoins, il apparait que le modèle souffre des hypothèses simplificatrices concernant la déformation. En effet, les résultats de simulation présentent des similarités avec les résultats numériques de recristallisation post-dynamique avec énergie moyennée par grain.

Chapter 7

Conclusion and perspectives

Conclusion

The main objective of this work was to improve the understanding of recrystallization mechanisms during Zy-4 hot deformation and to model it. In particular, the study was designed to quantify the impact of initial microstructure upon recrystallization. Indeed, the typical Zy-4 microstructures encountered in industrial applications are diverse. Some present grains with an equiaxed shape whereas others have grains with lamellar morphology. These lamellae can be organized as colonies of parallel plates or entangled, forming a so-called basket-weaved microstructure. In each case, some SPP are present and distributed regularly throughout the whole microstructure or at lamellae interfaces. By investigating the impact of such features, it was expected that one could discriminate the physical mechanisms and/or microstructure features that are responsible for the differences quantified.

To achieve this purpose, a twofold approach combining experimental and numerical investigations has been considered. The advantages of such strategy are numerous. On one hand, the experiments are used to build up a reliable and consistent database and to investigate the physical mechanisms responsible of the microstructure evolutions. On the other hand, thanks to simulations, one is able to target one feature or mechanism and to assess its role. From an industrial point of view, it is also of first importance since simulations allow to reduce the number of experiments that are particularly costly and time consuming.

This approach combining experimental and numerical tools was applied to different microstructure evolution mechanisms: grain growth, post-dynamic recrystallization and continuous dynamic recrystallization.

To study grain growth, two initial microstructures were considered. Both present the same equiaxed morphology, but differ by the presence of second phase particles. These two materials were characterized after heat treatments performed at different temperatures and durations. This strategy was necessary to identify the reduced mobility of grain boundaries, without any effect from precipitates. The results obtained from grain growth simulations, with or without

second phase particles showed that this strategy was successful. It also confirmed that these particles are responsible for the limitation of grain growth in equiaxed microstructures and for the stability of basket-weaved microstructures upon heat treatments.

For the study of recrystallization, three microstructures were used: an equiaxed (**Eq**) and two Widmanstatten ones. These two last were differing from the organization of the lamellae. One was mainly composed of colonies of parallel plates (**PP**) whereas the other was composed of entangled lamellae (**BW**). Samples with these three microstructures were subjected to hot compression tests with or without subsequent heat treatments.

The analysis of EBSD results after hot deformation confirmed the presence of several features of continuous dynamic recrystallization: the presence of a large number of low angle grain boundaries and the progressive and rather homogeneous fragmentation of the large grains by smaller grains and subgrains. The results also confirmed that initial microstructure impacts greatly the evolutions observed. Within the range of thermomechanical conditions investigated, increasing strain rate leads to increase the average stored energy of deformation, which in turn increases the kinetics of migration of the recrystallization front. Increasing the final strain contributes to a greater fragmentation of the recrystallization. Thus, a larger number of small grains and subgrains are formed and are susceptible to grow and consume the microstructure upon subsequent heat treatment.

The characterizations highlighted that initial microstructure determines to a great extent the recrystallization behavior. From the three initial microstructures, **PP** microstructures had the most heterogeneous behavior. On the other hand of the spectrum, **Eq** microstructures had the most homogeneous behavior. These differences of behavior were mainly attributed to differences of deformation mechanisms. Supplementary investigations on the spatial distribution of dislocation density and small grains and subgrains pointed out that dynamic recovery was also playing a role in the heterogeneities observed.

Two microstructural features were identified as determining. First, it appeared that initial texture is greatly responsible for the differences observed between equiaxed and lamellar microstructures. Because of the preceding manufacturing stage, **Eq** samples present a strong texture meaning that grain orientations have a smaller spread. Therefore, the polycrystal presents a more homogeneous deformation behavior. Lamellar samples, on the other hand, present a finite number of orientations distributed in orientation space following the variant selection rule. Neighboring grains present a greater chance of having different orientations and different deformations behavior. Thus, these samples have a very heterogeneous distribution of deformation stored energy. The grains and subgrains formed during hot deformation tend to group in clusters in zones where the dislocation density is high and the recovery efficient. Second, it was determined that the organization of lamellae was responsible for the differences observed between **BW** and **PP** samples. Indeed, in **BW** samples, the deformation incompatibilities affect

a greater fraction of the lamellae since every lamella is in contact with lamellae presenting other orientations. Therefore, the deformation incompatibilities affect almost all lamellae in **BW** samples whereas it affects only the lamellae at edges of a colony in **PP** samples. This contributes to lower the extent of heterogeneity encountered in **BW** microstructures.

To reproduce these evolutions by simulation, the equations describing subgrain formation from the Gourdet-Montheillet model were implemented within a new extended level-set framework. To reproduce to some extent the intergranular deformation heterogeneities, the Yoshie-Laasraoui-Jonas equation was modified. The hardening parameter was considered as a grain property, and initialized according to the dislocation density distribution measured from experimental results. The simulation results obtained with this framework show a good agreement with experimental results during hot deformation and subsequent heat treatment. The impact of both thermomechanical conditions and initial microstructure were both predicted correctly by the simulation framework. The intergranular heterogeneities were satisfactorily forecasted.

Nevertheless, some discrepancies between the experimental and simulation results were pointed out. By immersing some precise EBSD data into the simulation framework, the impact of intragranular dislocation heterogeneities has been identified. The simulation results highlighted that considering such feature is essential to reproduce the selective growth of a limited number of grains and subgrains during heat treatment following hot deformation. This result is of great interest in order to improve the DIGIMU software predictions where the stored energy is systematically averaged per grain.

Prospects

The results summarized previously confirmed that the present study contributed to improve the understanding of Zy-4 recrystallization. They also highlighted the interest of the simulation framework developed at CEMEF and the abilities and limitations of the current state of the model. Therefore, to continue improving the precision of the numerical framework, it is clear that coupling the model to a crystal plasticity one, such as the one developed by Ruiz *et al.* [190, 191] would present a great interest. Until now, these developments have been mainly applied to cubic materials. Recently, Brozovic applied this framework to a dual phase titanium alloy [213]. Among these two phases, the α phase adopts a hexagonal compact structure that shares many similarities with the $\alpha - Zr$ phase of zirconium alloys. Nevertheless, applying these developments to lamellar microstructures would certainly require a dedicated study. Indeed, several studies showed that the lamellar morphology was playing a significant role in the deformation structures observed at the mesoscopic scale [56, 55]. The experimental [214, 56] and simulation [55] results confirmed that the interfaces between laths were particularly subjected to localization of deformation (damage cavities, shear localization) and were impacting the general deformation behavior of a colony of

lamellae. If such simulations present a great scientific interest, their use remains limited in an industrial context, due to their computational cost. Therefore, there is probably a need for an intermediate numerical strategy that would predict the deformation at mesoscopic scale, taking into account the microstructure topology and texture while maintaining reasonable calculation times.

Applying the model developed to other industrial processes and other thermomechanical conditions would be beneficial. For instance, it could be applied to model recrystallization during the multi-stage hot rolling of Zy-4 plates. The role of the waiting time between the rolling stages remains little-known. Such simulation results could help adapting this processing parameter to improve productivity and/or adapt the process to other manufacturing routes and/or part geometries.

Since the full-field model used within the context of the present study requires consequent computational resources, there is a substantial interest in developing some mean-field models. The original mean-field formulation of the Gourdet-Montheillet model, modified by Gaudout *et al.* [16], is applied and evaluated at Framatome for several years now. The material parameters identification conducted during this study has contributed to improve the existing mean-field model parameters. Therefore, the parallel development of these two models provides now a great opportunity to improve both of them. Doing so, the mean-field model could provide a large number of results that could help for instance to refine the full-field model parameters. The full-field model results could be used to discriminate which features and/or phenomena are the most important and how they could be considered in the mean-field formulation.

Extending the investigations to 3D would also contribute to improve the knowledge about recrystallization. Indeed, in 2D investigations, the analyses always suffer from a bias. For instance, when discussing the localization of grains and subgrains, the conclusions from 2D maps neglect that these objects could in fact originate from a specific feature located below or above the observation surface. Such extension to 3D is of course not straightforward. Characterization of lamellar microstructures in 3D is a challenge since the width of lamellae is approximately 1000 times lower than the ex-β grain size. Such difference is not compatible with the abilities of the best current 3D EBSD systems.

Having additional experimental results would be valuable. First, having some characterization results from hot deformation with subsequent holding at temperatures within the range $600 - 700°C$ would be valuable. This would enable to get some insights about the impact of temperature on evolutions in the post-dynamic regime. Obtaining some additional points at longer heat treatment durations, especially for lamellar microstructures, would provide some important information upon completion of recrystallization. It would allow to confirm that the trends discussed in the present manuscript are verified for recrystallization fraction higher than 60%.

Second, in-situ EBSD characterizations during a heat treatment on a hot deformed sample would certainly provide some valuable data. The results obtained

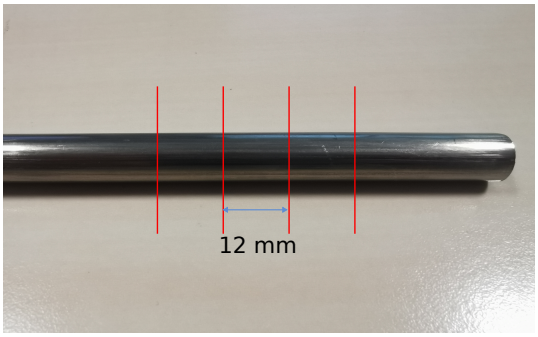
from such experiment would allow to confirm or reject the assumption made in this work that the formation of subgrains/grains during the first instants of post-dynamic recrystallization does not play a role in the microstructure changes observed.

Lastly, it would present a great industrial interest to expand the investigations related to recrystallization of other zirconium alloys. The Zr-Nb alloys represent ideal candidates. However, they have a more complex microstructure. Some additional phases are present and evolve during most of the forming processes. Thus, improving the understanding of recrystallization and phase transformation interactions is critical. Nonetheless, it raises several related questions that remain unanswered.

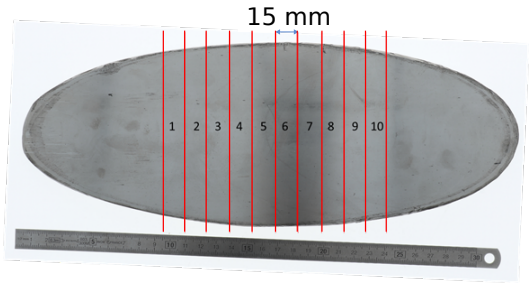
Appendix A

Materials and experimentals methods

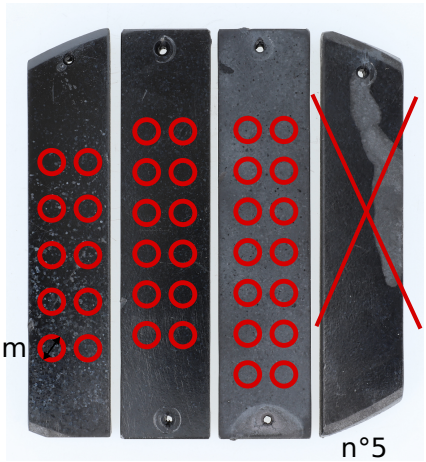
A.1 Sampling plan



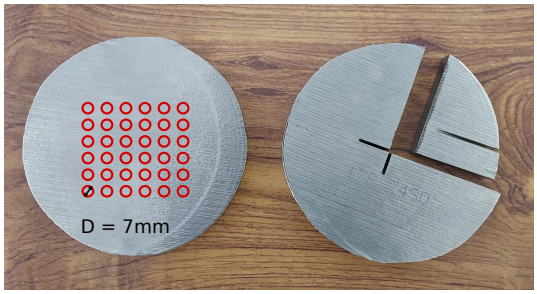
(a) Position of **Eq** samples.



(b) Position of **Wo SPP** samples.



(c) Position of **BW** samples.



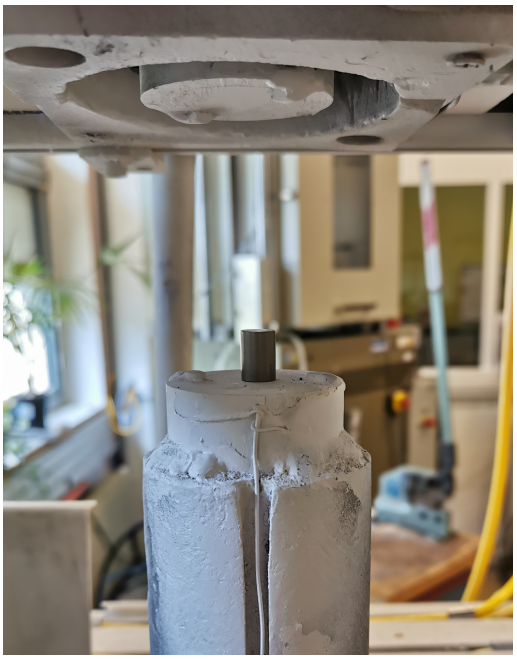
(d) Position of **PP** samples.

Figure A.1: Sampling procedure in as-received materials.

A.2 Hot compression set-up



(a) Whole hot compression set-up.



(b) Cylindrical sample positioned on the lower die. The sample height is equal to 10 mm.

Figure A.2: Photos of the hot compression set-up.

Appendix B

Numerical methods

B.1 Description of the algorithm underlying the numerical framework

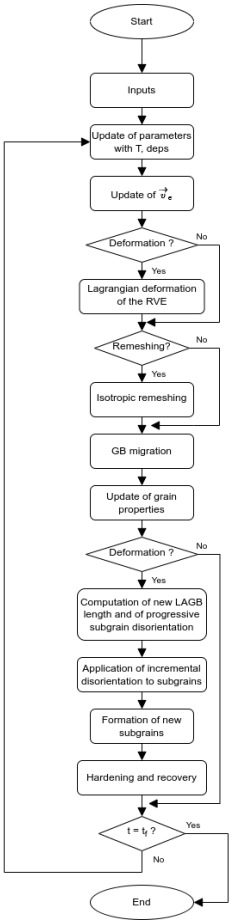
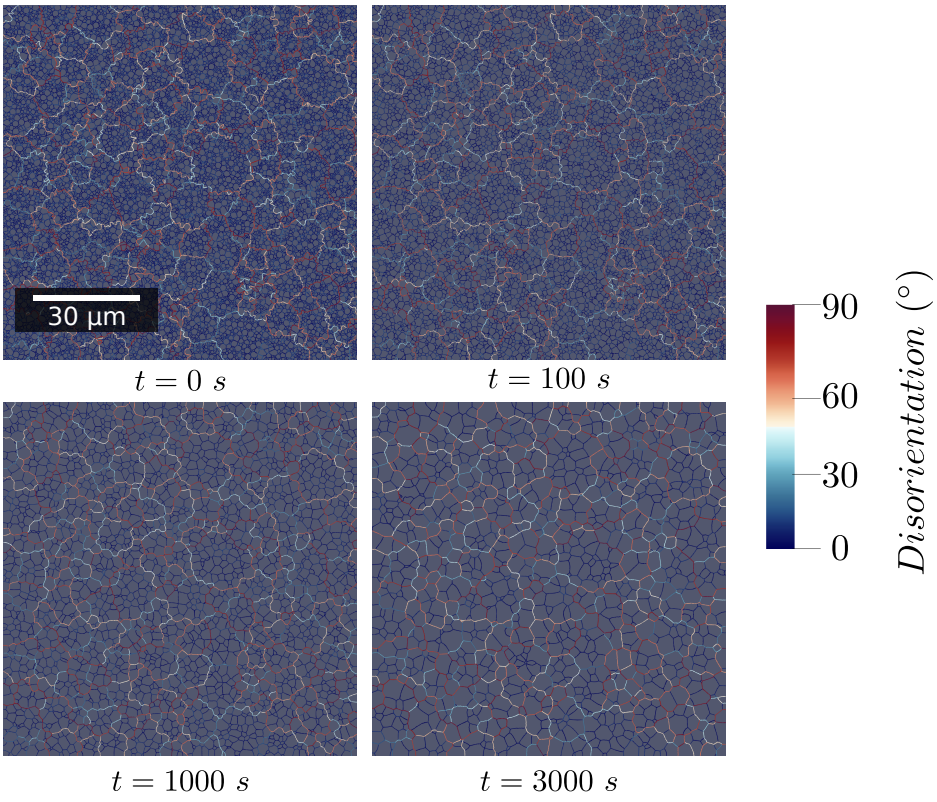
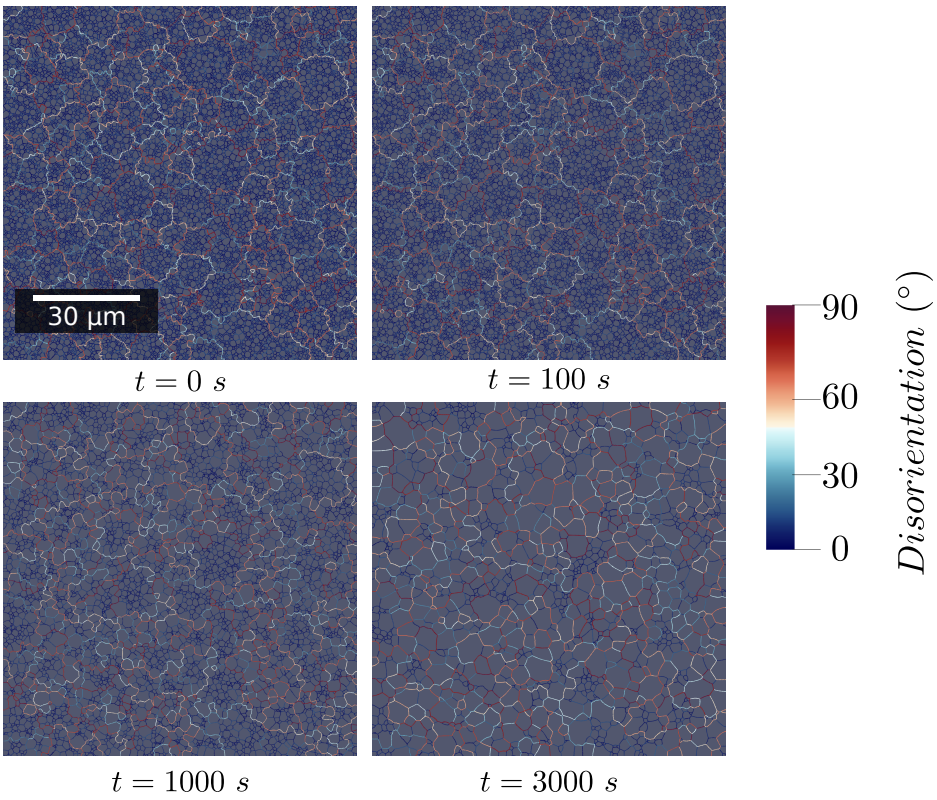


Figure B.1: Algorithm describing the numerical steps to simulate microstructure evolutions during hot deformation and holding at temperature.

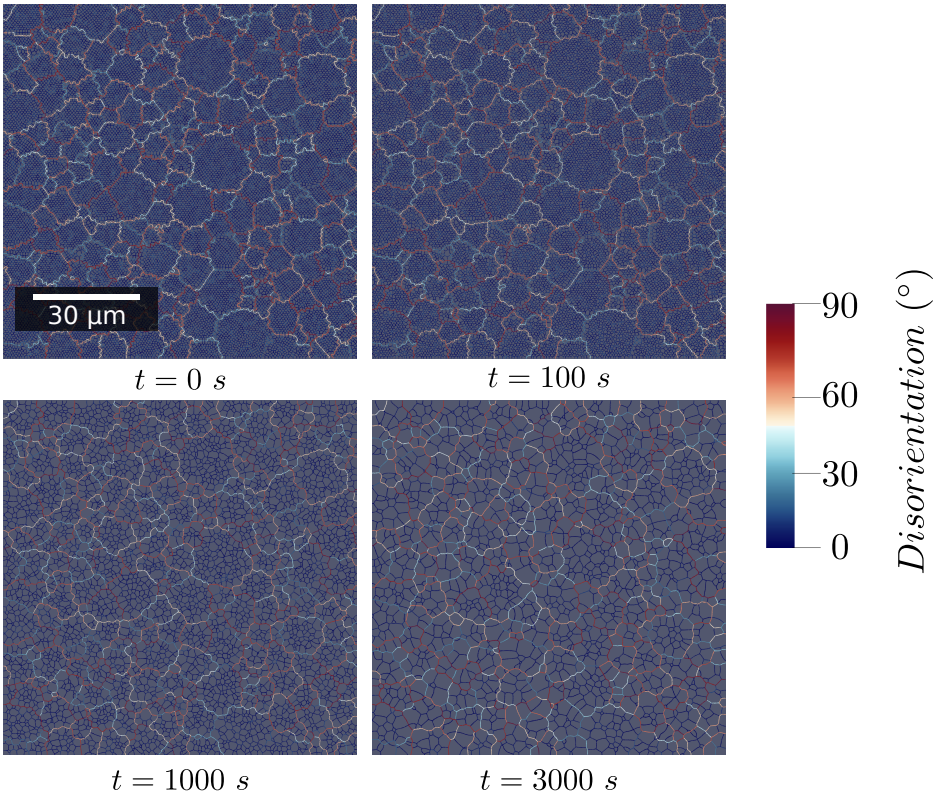
B.2 Evolution of the GB network in the whole simulated RVE



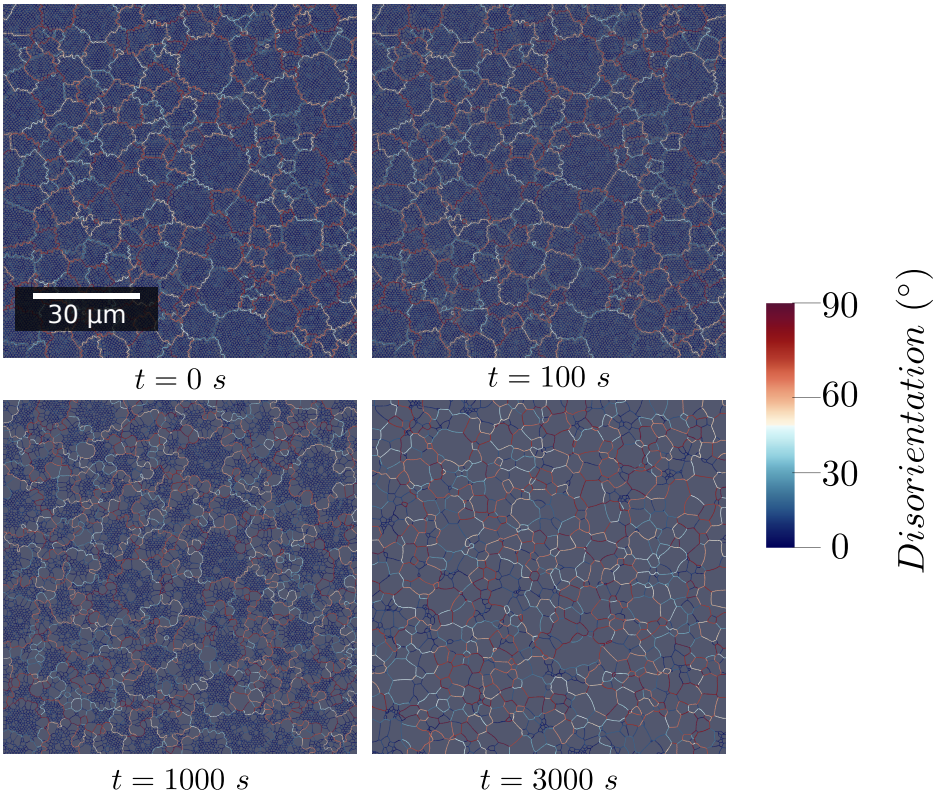
(a) Experimental subgrain size distribution - γ_h.



(b) Experimental subgrain size distribution - γ_h, M_h.



(c) Uniform subgrain size distribution - γ_h.



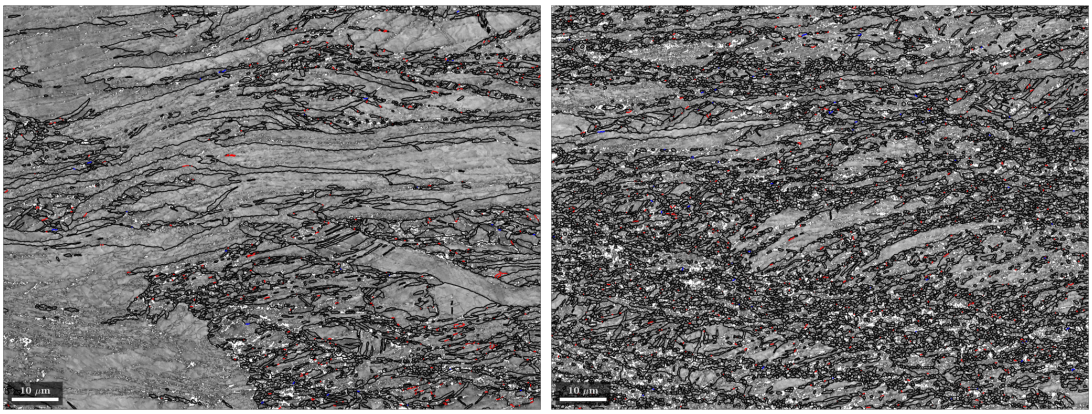
(d) Uniform subgrain size distribution - $\gamma_h,\ M_h$.

Figure B.2: Evolution of GB network with time for the four test cases.

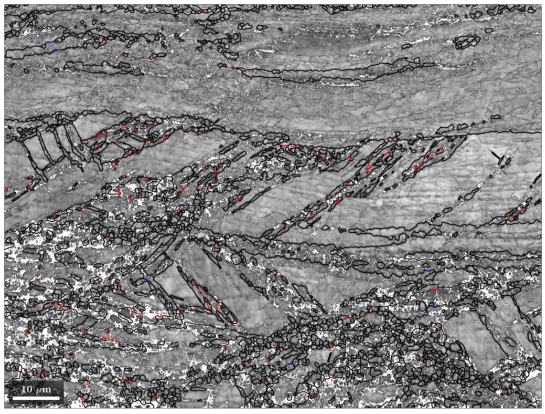
Appendix C

Characterization and modeling of post-dynamic recrystallization

C.1 Identification of deformation twin boundaries



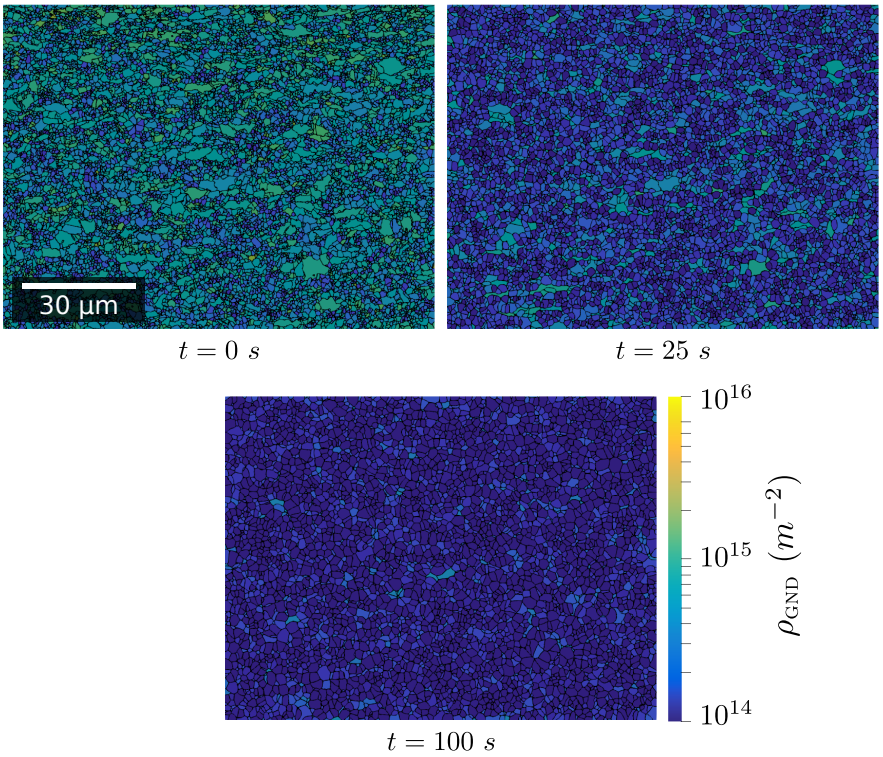
(a) $T = 550°C$, $\dot{\varepsilon} = 0.1\ s^{-1}$, $\varepsilon = 0.9$. (b) $T = 550°C$, $\dot{\varepsilon} = 0.1\ s^{-1}$, $\varepsilon = 1.2$.



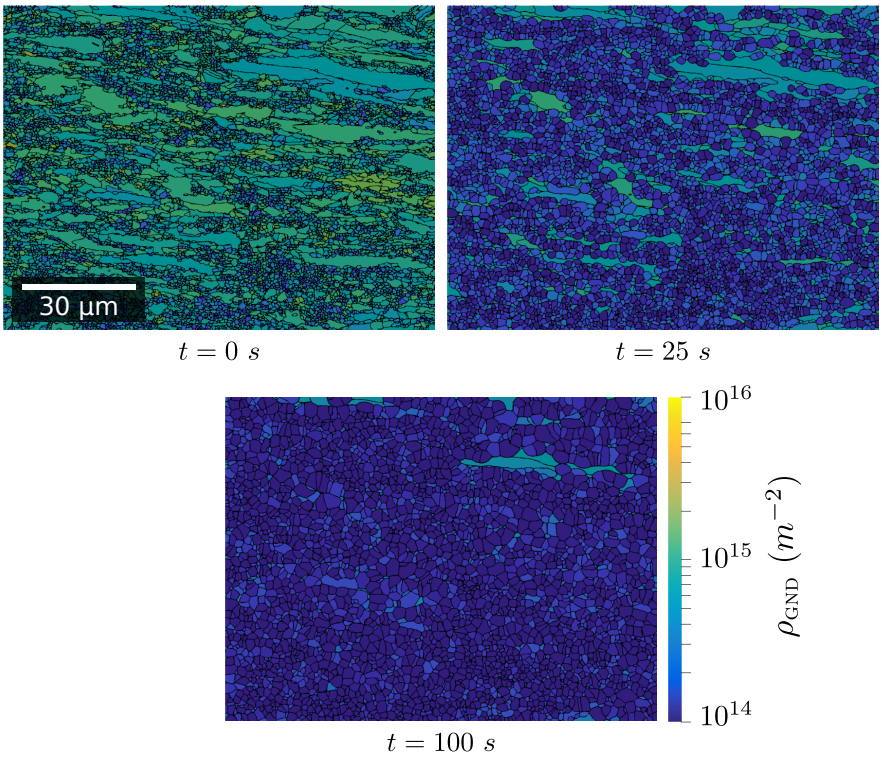
(c) $T = 650°C$, $\dot{\varepsilon} = 0.1\ s^{-1}$, $\varepsilon = 1.2$.

Figure C.1: EBSD band contrast maps of hot compressed microstructures. Traction twin boundaries are depicted as thick red lines and compression twin boundaries as thick blue lines. **PP** samples.

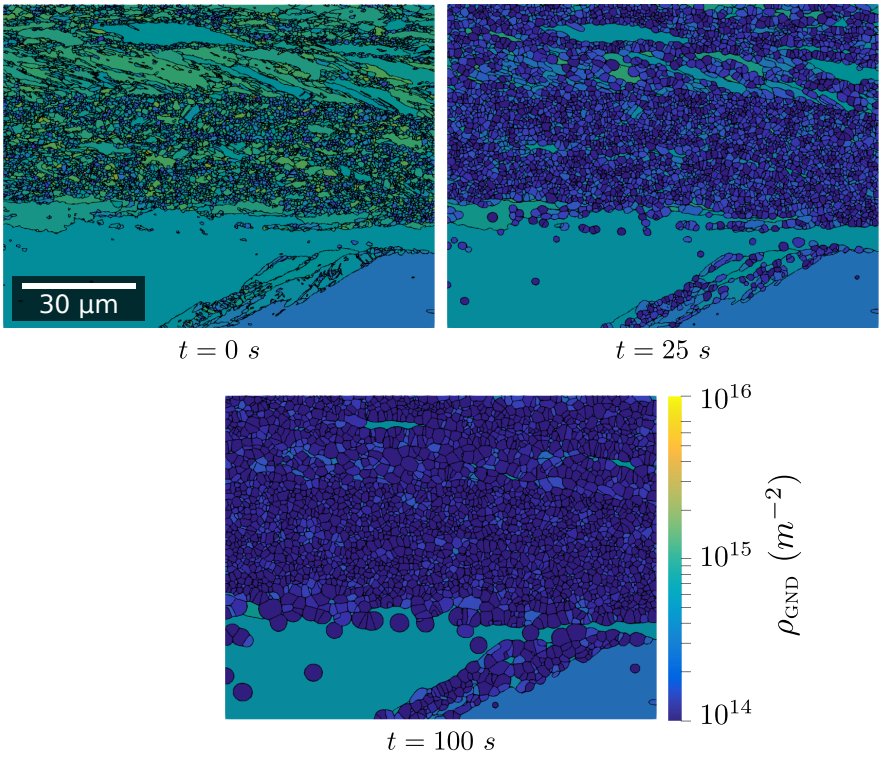
C.2 Evolution of microstructures during PDRX simulations



(a) **Eq** microstructures.



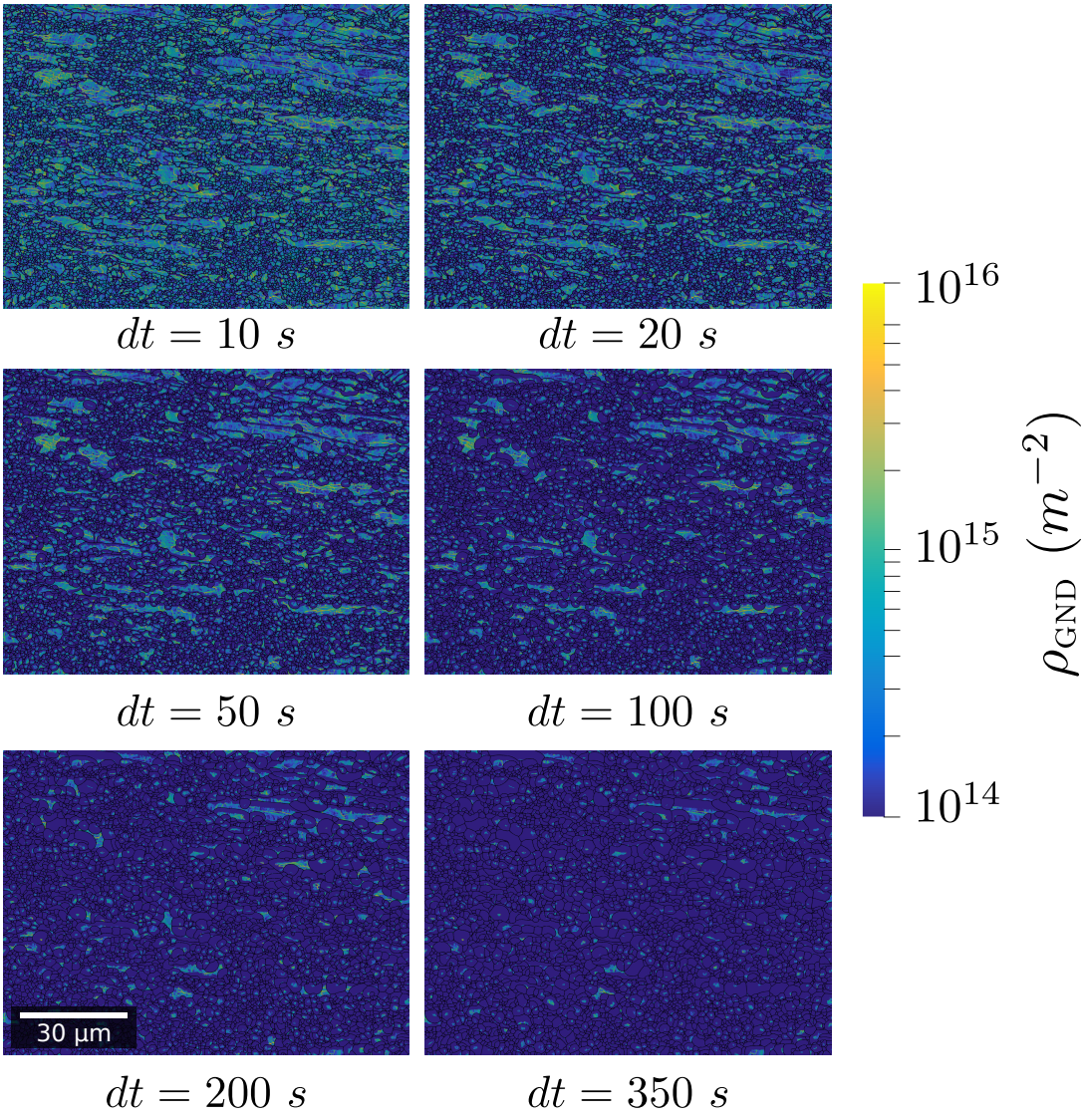
(b) **BW** microstructures.



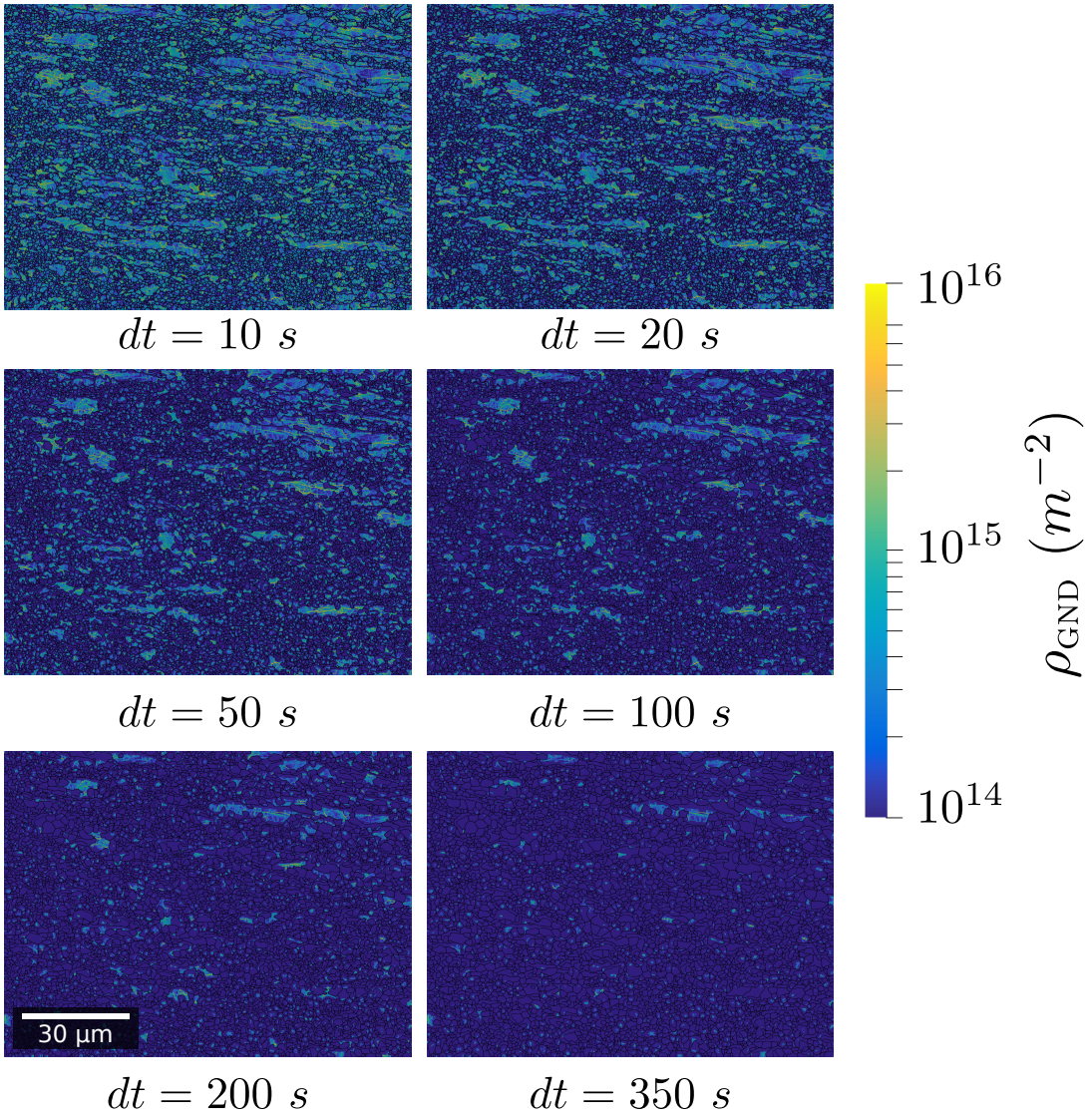
(c) **PP** microstructures.

Figure C.2: EBSD orientation maps showing microstructure evolution during holding at $T = 650°C$ after hot deformation ($T = 650°C$; $\dot{\varepsilon} = 1.0\ s^{-1}$; $\varepsilon_f = 1.0$). IPF Y color code.

C.3 Evolution of microstructures during PDRX simulations considering intragranular GND density gradients



(a) Per interface.



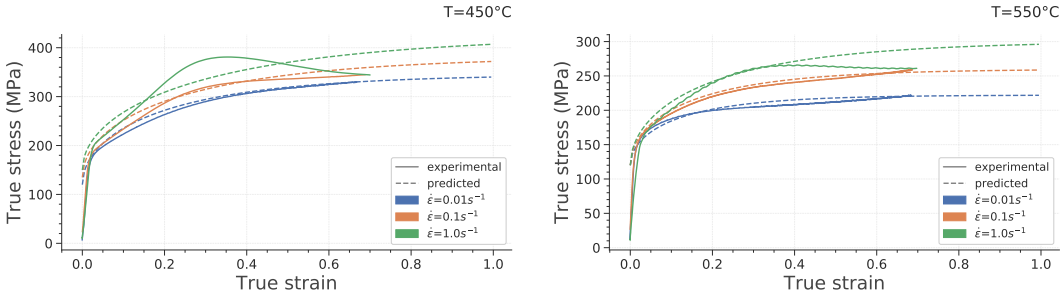
(b) Local.

Figure C.3: Digital microstructures at different instants of the heat treatment. **BW** samples. Hot deformation conditions are: $T = 650°C$; $\dot{\varepsilon} = 1.0\ s^{-1}$; $\varepsilon = 1.2$.

Appendix D

Characterization and modeling of continuous dynamic recrystallization

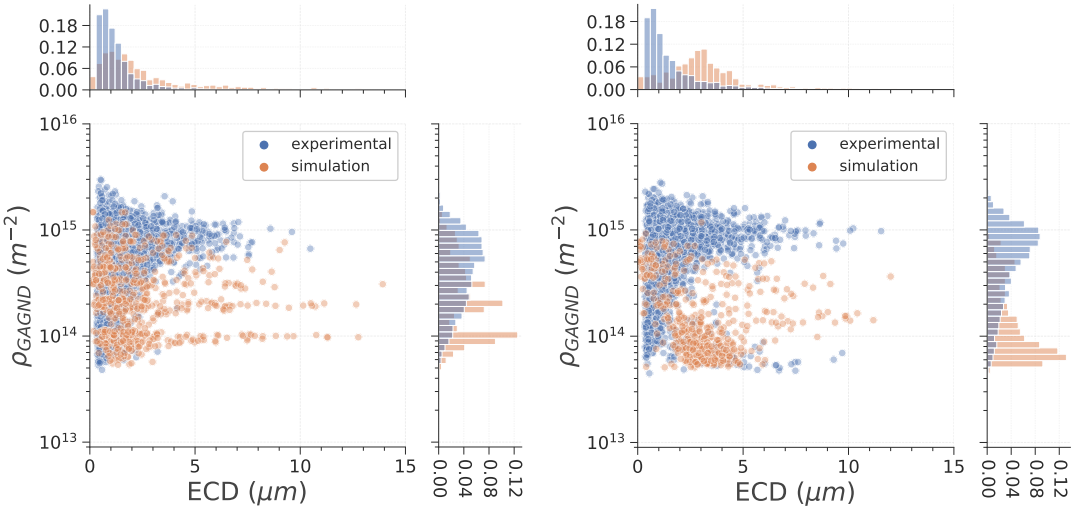
D.1 Identification of hardening parameters



(a) $T = 450°C$. (b) $T = 550°C$.

Figure D.1: Experimental and predicted flow curves for $T = 450°C$ and $T = 550°C$. **Eq** samples.

D.2 Additional scatter plots relative to recrystallization modeling during hot compression



(a) $T = 650°C$; $\dot{\varepsilon} = 0.1\ s^{-1}$; $\varepsilon_f = 1.35$; $dt = 100\ s$.

(b) $T = 650°C$; $\dot{\varepsilon} = 1.0\ s^{-1}$; $\varepsilon_f = 0.65$; $dt = 100\ s$.

Figure D.2: Combined scatter plots and histograms showing the distribution of grain average dislocation density (ρ_{GAGND}) and ECD. Simulation and experimental results correspond to hot compression tests on **Eq** samples.

Bibliography

[1] A. Brunner. Les inégalités d'espérance de vie dans le monde se réduisent. https://www.inegalites.fr/Les-inegalites-d-esperance-de-vie-dans-le-monde-se-reduisent, 2018. Accessed on September 2022.

[2] A. Brunner. L'extrême pauvreté dans le monde recule. https://www.inegalites.fr/L-extreme-pauvrete-dans-le-monde-recule?id_theme=26, 2022. Accessed on September 2022.

[3] H.-O. Pörtner, D. Roberts, M. Tignor, E. Poloczanska, K. Mintenbeck, A. Alegría, M. Craig, S. Langsdorf, S. Löschke, V. Möller, A. Okem, and B. Rama. Climate change 2022: Impacts, adaptation and vulnerability. working group II contribution to the IPCC sixth assessment report. Technical report, Cambridge University Press, 2022.

[4] Environmental Protection Agency. Sources of greenhouse gas emissions in the U.S. https://www.epa.gov/ghgemissions/sources-greenhouse-gas-emissions#t1fn3. Accessed on September 2022.

[5] J. Kearns and C. Woods. Effect of texture, grain size, and cold work on the precipitation of oriented hydrides in zircaloy tubing and plate. *Journal of Nuclear Materials*, 20(3):241–261, 1966.

[6] K. Une and S. Ishimoto. Dissolution and precipitation behavior of hydrides in zircaloy-2 and high Fe zircaloy. *Journal of Nuclear Materials*, 322(1):66–72, 2003.

[7] O. Zanellato, M. Preuss, J.-Y. Buffiere, F. Ribeiro, A. Steuwer, J. Desquines, J. Andrieux, and B. Krebs. Synchrotron diffraction study of dissolution and precipitation kinetics of hydrides in zircaloy-4. *Journal of Nuclear Materials*, 420(1):537–547, 2012.

[8] R. Kuwae, K. Sato, E. Higashinakagawa, J. Kawashima, and S. ichi Nakamura. Mechanism of zircaloy nodular corrosion. *Journal of Nuclear Materials*, 119(2):229–239, 1983.

[9] J. Bryner. The cyclic nature of corrosion of zircaloy-4 in 633 K water. *Journal of Nuclear Materials*, 82(1):84–101, 1979.

[10] D. G. Franklin and R. B. Adamson. Implications of zircaloy creep and growth to light water reactor performance. *Journal of Nuclear Materials*, 159:12–21, 1988.

[11] P. Rudling and G. Wikmark. A unified model of zircaloy BWR corrosion and hydriding mechanisms. *Journal of Nuclear Materials*, 265(1):44–59, 1999.

[12] E. Tenckhoff and P. Rittenhouse. Annealing textures in zircaloy tubing. *Journal of Nuclear Materials*, 35(1):14–23, 1970.

[13] K. M. Krishna, S. Sahoo, I. Samajdar, S. Neogy, R. Tewari, D. Srivastava, G. Dey, G. H. Das, N. Saibaba, and S. Banarjee. Microstructural and textural developments during zircaloy-4 fuel tube fabrication. *Journal of Nuclear Materials*, 383(1):78–85, 2008. Advances in Nuclear Materials: Processing, Performance and Phenomena.

[14] F. Xu, R. Holt, and M. Daymond. Modeling texture evolution during uniaxial deformation of zircaloy-2. *Journal of Nuclear Materials*, 394(1):9–19, 2009.

[15] C. Chauvy, P. Barberis, and F. Montheillet. Microstructure transformation during warm working of β-treated lamellar zircaloy-4 within the upper *a*-range. *Materials Science and Engineering: A*, 431(1):59–67, 2006.

[16] B. Gaudout. *Modeling of microstructure evolutions and study of solid film lubrication during hot extrusion of zirconium alloys*. PhD thesis, École Nationale Supérieure des Mines de Paris, 2009.

[17] F. Gerspach, N. Bozzolo, and F. Wagner. About texture stability during primary recrystallization of cold-rolled low alloyed zirconium. *Scripta Materialia*, 60(4):203–206, 2009.

[18] A. Rollett, G. S. Rohrer, and J. Humphreys. *Recrystallization and related annealing phenomena*. Elsevier, third edition, 2017.

[19] Transvalor. DIGIMU software. `https://www.transvalor.com/en/digimu`. Accessed on September 2022.

[20] M. Bernacki. Presentation of the DIGIMU consortium. `https://chaire-digimu.cemef.mines-paristech.fr/`. Accessed on September 2022.

[21] M. Bernacki, Y. Chastel, T. Coupez, and R. Logé. Level set framework for the numerical modelling of primary recrystallization in polycrystalline materials. *Scripta Materialia*, 58(12):1129–1132, 2008.

[22] M. Bernacki, H. Resk, T. Coupez, and R. Logé. Finite element model of primary recrystallization in polycrystalline aggregates using a level set framework. *Modelling and Simulation in Materials Science and Engineering*, 17(6), 2009.

[23] M. Bernacki, R. Logé, and T. Coupez. Level set framework for the finite-element modelling of recrystallization and grain growth in polycrystalline materials. *Scripta Materialia*, 64(6):525–528, 2011.

[24] B. Scholtes, M. Shakoor, A. Settefrati, P.-O. Bouchard, N. Bozzolo, and M. Bernacki. New finite element developments for the full field modeling of microstructural evolutions using the level-set method. *Computational Materials Science*, 109:388–398, 2015.

[25] B. Scholtes, R. Boulais-Sinou, A. Settefrati, D. Pino Muñoz, I. Poitrault, A. Montouchet, N. Bozzolo, and M. Bernacki. 3D level set modeling of static recrystallization considering stored energy fields. *Computational Materials Science*, 122:57–71, 2016.

[26] L. Maire, B. Scholtes, C. Moussa, N. Bozzolo, D. P. Muñoz, A. Settefrati, and M. Bernacki. Modeling of dynamic and post-dynamic recrystallization by coupling a full field approach to phenomenological laws. *Materials & Design*, 133:498–519, 2017.

[27] A. Agnoli, N. Bozzolo, R. Logé, J.-M. Franchet, J. Laigo, and M. Bernacki. Development of a level set methodology to simulate grain growth in the presence of real secondary phase particles and stored energy – application to a nickel-base superalloy. *Computational Materials Science*, 89:233–241, 2014.

[28] K. Alvarado, S. Florez, B. Flipon, N. Bozzolo, and M. Bernacki. A level set approach to simulate grain growth with an evolving population of second phase particles. *Modelling and Simulation in Materials Science and Engineering*, 29(3):035009, 2021.

[29] J. Fausty, N. Bozzolo, D. Pino Muñoz, and M. Bernacki. A novel level-set finite element formulation for grain growth with heterogeneous grain boundary energies. *Materials and Design*, 160:578–590, 2018.

[30] J. Fausty, N. Bozzolo, and M. Bernacki. A 2D level set finite element grain coarsening study with heterogeneous grain boundary energies. *Applied Mathematical Modelling*, 78:505–518, 2020.

[31] B. Murgas, S. Florez, N. Bozzolo, J. Fausty, and M. Bernacki. Comparative study and limits of different level-set formulations for the modeling of anisotropic grain growth. *Materials*, 14(14), 2021.

[32] A. E. van Arkel and J. H. de Boer. Darstellung von reinem titanium-, zirkonium-, hafnium- und thoriummetall. *Zeitschrift für anorganische und allgemeine Chemie*, 148(1):345–350, 1925.

[33] W. J. Kroll, A. W. Schlechten, and L. A. Yerkes. Ductile zirconium from zircon sand. *Transactions of The Electrochemical Society*, 89(1):263, 1946.

[34] P. Barberis. Zirconium et hafnium - métallurgie. Technical report, Techniques de l'Ingénieur, 2016.

[35] M.-T. Tran. *Caractérisation des microstructures trempées et sélection des variants dans le Zircaloy-4*. PhD thesis. École des Mines de Saint-Étienne, 2015.

[36] N. Bangaru. An investigation of the microstructures of heat-treated zircaloy-4. *Journal of Nuclear Materials*, 131(2):280–290, 1985.

[37] C. Toffolon-Masclet, T. Guilbert, and J. Brachet. Study of secondary intermetallic phase precipitation/dissolution in Zr alloys by high temperature–high sensitivity calorimetry. *Journal of Nuclear Materials*, 372(2):367–378, 2008.

[38] E. Steinberg, H. Weidinger, and A. Schaa. Analytical approaches and experimental verification to describe the influence of cold work and heat treatment on the mechanical properties of zircaloy cladding tubes. In *Zirconium in the Nuclear Industry: Sixth International Symposium, ASTM STP*, volume 824, pages 106–122, 1984.

[39] J. Gros and J. Wadier. Precipitate growth kinetics in zircaloy-4. *Journal of Nuclear Materials*, 172(1):85–96, 1990.

[40] J. Robson. Assessment of annealing parameter approximations in zirconium alloys. *Journal of Nuclear Materials*, 527:151814, 2019.

[41] C. Toffolon-Masclet, J.-C. Brachet, and G. Jago. Studies of second phase particles in different zirconium alloys using extractive carbon replica and an electrolytic anodic dissolution procedure. *Journal of Nuclear Materials*, 305(2):224–231, 2002.

[42] R. Holt. The beta to alpha phase transformation in zircaloy-4. *Journal of Nuclear Materials*, 35(3):322–334, 1970.

[43] O. Woo and K. Tangri. Transformation characteristics of rapidly heated and quenched zircaloy-4-oxygen alloys. *Journal of Nuclear Materials*, 79(1):83–94, 1979.

[44] G. Ökvist and K. Källström. The effect of zirconium carbide on the $\beta \rightarrow \alpha$ transformation structure in zircaloy. *Journal of Nuclear Materials*, 35(3):316–321, 1970.

[45] V. Quach and D. O. Northwood. Influence of the phosphorus impurity content on the microstructure of zircaloy-4 air cooled from the high temperature beta phase region. *Metallography*, 17(2):191–201, 1984.

[46] A. Massih, T. Andersson, P. Witt, M. Dahlbäck, and M. Limbäck. Effect of quenching rate on the β→α phase transformation structure in zirconium alloy. *Journal of Nuclear Materials*, 322(2):138–151, 2003.

[47] C. Smith. Introduction to grains, phases, and interfaces—an interpretation of microstructure. *Trans. Met. Soc. AIME*, 175:15–51, 1948.

[48] C. Zener. Theory of growth of spherical precipitates from solid solution. *Journal of Applied Physics*, 20(10):950–953, 1949.

[49] E. Schmid. Yield point of crystals, critical shear stress law. In *Proceedings of the First International Congress for Applied Mechanics, Delft*, volume 342, 1924.

[50] G. E. Dieter and D. J. Bacon. *Mechanical metallurgy*, volume 3. McGraw-hill New York, 1976.

[51] H. Francillette, B. Bacroix, M. Gasperini, and J. Bechade. Grain orientation effects in Zr702-α polycrystalline samples deformed in channel die compression at room temperature. *Acta Materialia*, 46(12):4131–4142, 1998.

[52] A. Akhtar. Basal slip in zirconium. *Acta Metallurgica*, 21(1):1–11, 1973.

[53] A. Akhtar. Compression of zirconium single crystals parallel to the c-axis. *Journal of Nuclear Materials*, 47(1):79–86, 1973.

[54] T. R. Bieler and S. Semiatin. The origins of heterogeneous deformation during primary hot working of Ti–6Al–4V. *International Journal of Plasticity*, 18(9):1165–1189, 2002.

[55] Y. Ben Ammar. *Traitements thermomécaniques des colonies de lamelles parallèles du Zircaloy-4 trempé-β.* PhD thesis. École des Mines de Saint-Étienne, 2012.

[56] N. Vanderesse. *Morphologie et déformation à chaud de microstructures lamellaires dans les alliages de zirconium et de titane.* PhD thesis. École des Mines de Saint-Étienne, 2008.

[57] M. H. Yoo. Slip, twinning, and fracture in hexagonal close-packed metals. *Metallurgical Transactions A*, 12(3):409–418, 1981.

[58] R. E. Reedhill, E. R. Buchanan, and F. W. Caldwell, Jr. A quantitative measurement of the fraction of tensile strain due to twinning in polycrystalline zirconium at 77 K. *Trans. Met. Soc. AIME*, 233, 1965.

[59] G. I. Taylor. Plastic strain in metals. *J. Inst. Metals*, 62:307–324, 1938.

[60] D. Hughes, N. Hansen, and D. Bammann. Geometrically necessary boundaries, incidental dislocation boundaries and geometrically necessary dislocations. *Scripta Materialia*, 48(2):147–153, 2003.

[61] J. Crépin, T. Bretheau, and D. Caldemaison. Plastic deformation mechanisms of β treated zirconium. *Acta Metallurgica et Materialia*, 43(10):3709–3719, 1995.

[62] E. Tenckhoff and P. Rittenhouse. Texture development and texture gradients in zircaloy tubing. *ASTM STP 458*, pages 50–67, 1969.

[63] W. Guo, G. Li, F. Yuan, F. Han, Y. Zhang, M. Ali, J. Ren, and G. Yuan. Texture development and mechanical behavior of zircaloy-4 alloy plates fabricated by cold rolling and annealing. *Materials Science and Engineering: A*, 807:140846, 2021.

[64] R. Logé. *Influence des conditions thermomecaniques et de la microstructure sur les evolutions de texture cristallographique du zircaloy-4 en mise en forme a chaud: application au filage de tubes*. PhD thesis. Ecole Nationale Supérieure des Mines de Paris, 1999.

[65] F. Gerspach. *Mécanismes d'évolution de texture au cours du recuit d'alliages de zirconium et de titane*. PhD thesis. Université Paul Verlaine, Metz, 2007.

[66] A. Gaillac and P. Barberis. Numerical modeling of zirconium alloys hot extrusion. *18th International Symposium on Zirconium in the Nuclear Industry, ASTM International*, 2016.

[67] J.-H. Schmitt and T. Iung. Durcissement des alliages métalliques - impact de la microstructure sur la déformation plastique. Technical report, Techniques de l'Ingénieur, 2016.

[68] D. Raabe. *Physical Metallurgy*, chapter 23 - Recovery and Recrystallization: Phenomena, Physics, Models, Simulation, pages 2291–2397. Elsevier, fifth edition, 2014.

[69] T. Sakai, A. Belyakov, R. Kaibyshev, H. Miura, and J. J. Jonas. Dynamic and post-dynamic recrystallization under hot, cold and severe plastic deformation conditions. *Progress in Materials Science*, 60:130–207, 2014.

[70] A. K. Kiss, E. F. Rauch, B. Pecz, J. Szivos, and J. L. Labar. A tool for local thickness determination and grain boundary characterization by CTEM and HRTEM techniques. *Microscopy and Microanalysis*, 21(2):422–435, 2015.

[71] A. Bhattacharya, Y.-F. Shen, C. M. Hefferan, S. F. Li, J. Lind, R. M. Suter, C. E. Krill, and G. S. Rohrer. Grain boundary velocity and curvature are not correlated in Ni polycrystals. *Science*, 374(6564):189–193, 2021.

[72] S. Florez, K. Alvarado, B. Murgas, N. Bozzolo, D. Chatain, C. E. Krill, M. Wang, G. S. Rohrer, and M. Bernacki. Statistical behaviour of interfaces subjected to curvature flow and torque effects applied to microstructural evolutions. *Acta Materialia*, 222:117459, 2022.

[73] J. Zhang, W. Ludwig, Y. Zhang, H. H. B. Sørensen, D. J. Rowenhorst, A. Yamanaka, P. W. Voorhees, and H. F. Poulsen. Grain boundary mobilities in polycrystals. *Acta Materialia*, 191:211–220, 2020.

[74] M. Winning and A. D. Rollett. Transition between low and high angle grain boundaries. *Acta Materialia*, 53(10):2901–2907, 2005.

[75] G. S. Rohrer. Grain boundary energy anisotropy: a review. *Journal of Materials Science*, 46(18):5881–5895, 2011.

[76] W. T. Read and W. Shockley. Dislocation models of crystal grain boundaries. *Phys. Rev.*, 78:275–289, 1950.

[77] Y. Huang and F. Humphreys. Subgrain growth and low angle boundary mobility in aluminium crystals of orientation 110 <001>. *Acta Materialia*, 48(8):2017–2030, 2000.

[78] Z. Trautt and Y. Mishin. Grain boundary migration and grain rotation studied by molecular dynamics. *Acta Materialia*, 60(5):2407–2424, 2012.

[79] M. Hillert. Solute drag in grain boundary migration and phase transformations. *Acta Materialia*, 52(18):5289–5293, 2004.

[80] P. A. Manohar, M. Ferry, and T. Chandra. Five decades of the zener equation. *ISIJ International*, 38(9):913–924, 1998.

[81] F. Humphreys. The nucleation of recrystallization at second phase particles in deformed aluminium. *Acta Metallurgica*, 25(11):1323–1344, 1977.

[82] D. Ponge and G. Gottstein. Necklace formation during dynamic recrystallization: mechanisms and impact on flow behavior. *Acta Materialia*, 46(1):69–80, 1998.

[83] R. Sebald and G. Gottstein. Modeling of recrystallization textures: interaction of nucleation and growth. *Acta Materialia*, 50(6):1587–1598, 2002.

[84] J. F. Humphreys. Nucleation in recrystallization. In *Recrystallization and Grain Growth*, volume 467 of *Materials Science Forum*, pages 107–116. Trans Tech Publications Ltd, 2004.

[85] I. L. Dillamore, C. J. E. Smith, and T. W. Watson. Oriented nucleation in the formation of annealing textures in iron. *Metal Science Journal*, 1(1):49–54, 1967.

[86] C. Zener and J. H. Hollomon. Effect of strain rate upon plastic flow of steel. *Journal of Applied Physics*, 15(1):22–32, 1944.

[87] K. Huang and R. Logé. A review of dynamic recrystallization phenomena in metallic materials. *Materials & Design*, 111:548–574, 2016.

[88] J. E. Bailey, P. B. Hirsch, and N. F. Mott. The recrystallization process in some polycrystalline metals. *Proceedings of the Royal Society of London. Series A. Mathematical and Physical Sciences*, 267(1328):11–30, 1962.

[89] R. Doherty, D. Hughes, F. Humphreys, J. Jonas, D. Jensen, M. Kassner, W. King, T. McNelley, H. McQueen, and A. Rollett. Current issues in recrystallization: a review. *Materials Science and Engineering: A*, 238(2):219–274, 1997.

[90] H. Hu, L. Zhen, B. Zhang, L. Yang, and J. Chen. Microstructure characterization of 7050 aluminum alloy during dynamic recrystallization and dynamic recovery. *Materials Characterization*, 59(9):1185–1189, 2008.

[91] P. M. Souza, P. D. Hodgson, B. Rolfe, R. P. Singh, and H. Beladi. Effect of initial microstructure and beta phase evolution on dynamic recrystallization behaviour of Ti6Al4V alloy - an EBSD based investigation. *Journal of Alloys and Compounds*, 793:467–479, 2019.

[92] F. Qiang, E. Bouzy, H. Kou, Y. Zhang, L. Wang, and J. Li. Grain fragmentation associated continuous dynamic recrystallization (CDRX) of hexagonal structure during uniaxial isothermal compression: High-temperature α phase in Ti-Al alloys. *Intermetallics*, 129:107028, 2021.

[93] P. A. Beck and P. R. Sperry. Strain induced grain boundary migration in high purity aluminum. *Journal of Applied Physics*, 21(2):150–152, 1950.

[94] P. Bate and B. Hutchinson. A re-evaluation of the mechanism of SIBM. *Scripta Materialia*, 36(2):195–198, 1997.

[95] P. J. Hurley and F. J. Humphreys. A study of recrystallization in single-phase aluminium using in-situ annealing in the scanning electron microscope. *Journal of Microscopy*, 213(3):225–234, 2004.

[96] M. Somerday and F. J. Humphreys. Recrystallisation behaviour of supersaturated Al–Mn alloys part 1 – Al–1.3 wt-%Mn. *Materials Science and Technology*, 19(1):20–29, 2003.

[97] M. Somerday and F. Humphreys. Recrystallisation behaviour of supersaturated Al–Mn alloys part 2 – Al–0.3 wt-%Mn. *Materials Science and Technology*, 19(1):30–35, 2003.

[98] F. J. Humphreys. Recrystallization mechanisms in two-phase alloys. *Metal Science*, 13(3-4):136–145, 1979.

[99] M. Ardakani and F. Humphreys. The annealing behaviour of deformed particle-containing aluminium single crystals. *Acta Metallurgica et Materialia*, 42(3):763–780, 1994.

[100] R. P. de Siqueira, H. R. Z. Sandim, and D. Raabe. Particle stimulated nucleation in coarse-grained ferritic stainless steel. *Metallurgical and Materials Transactions A*, 44(1):469–478, 2013.

[101] J. Konrad, S. Zaefferer, and D. Raabe. Investigation of orientation gradients around a hard laves particle in a warm-rolled Fe3Al-based alloy using a 3D EBSD-FIB technique. *Acta Materialia*, 54(5):1369–1380, 2006.

[102] J. Robson, D. Henry, and B. Davis. Particle effects on recrystallization in magnesium–manganese alloys: Particle-stimulated nucleation. *Acta Materialia*, 57(9):2739–2747, 2009.

[103] D. Kuhlmann-Wilsdorf. Overview no. 131 "regular" deformation bands (dbs) and the leds hypothesis. *Acta Materialia*, 47(6):1697–1712, 1999.

[104] I. Dillamore, P. Morris, C. Smith, and W. Hutchinson. Transition bands and recrystallization in metals. *Proceedings of the Royal Society of London. A. Mathematical and Physical Sciences*, 329(1579):405–420, 1972.

[105] A. Nicolaÿ, G. Fiorucci, J. Franchet, J. Cormier, and N. Bozzolo. Influence of strain rate on subsolvus dynamic and post-dynamic recrystallization kinetics of inconel 718. *Acta Materialia*, 174:406–417, 2019.

[106] M. Jedrychowski, B. Bacroix, O. Salman, J. Tarasiuk, and S. Wronski. Investigation of SIBM driven recrystallization in alpha zirconium based on EBSD data and Monte-Carlo modeling. Number 89, 2015.

[107] M. Jedrychowski, J. Tarasiuk, B. Bacroix, and S. Wronski. Electron backscatter diffraction investigation of local misorientations and orientation gradients in connection with evolution of grain boundary structures in deformed and annealed zirconium. A new approach in grain boundary analysis. *Journal of Applied Crystallography*, 46(2):483–492, 2013.

[108] A. Kolmogorov. Bulletin of academic science of urss. *Sci. Math. Nat.*, 3:355, 1937.

[109] W. A. Johnson and R. F. Mehl. Metallic systems proceed by the formation of nuclei and the growth of. *Transactions of the American Institute of Mining and Metallurgical Engineers*, 135:416, 1939.

[110] M. Avrami. Kinetics of phase change. i: General theory. *The Journal of Chemical Physics*, 7(12):1103–1112, 1939.

[111] M. Avrami. Kinetics of phase change. ii transformation-time relations for random distribution of nuclei. *The Journal of Chemical Physics*, 8(2):212–224, 1940.

[112] M. Avrami. Kinetics of phase change. iii: Granulation, phase change and microstructure. *Journal of chemical physics*, 9:177–184, 1941.

[113] J. Burke and D. Turnbull. Recrystallization and grain growth. *Progress in Metal Physics*, 3:220–292, 1952.

[114] M. Hillert. On the theory of normal and abnormal grain growth. *Acta Metallurgica*, 13(3):227–238, 1965.

[115] G. Abbruzzese, I. Heckelmann, and K. Lücke. Statistical theory of two-dimensional grain growth—i. the topological foundation. *Acta Metallurgica et Materialia*, 40(3):519–532, 1992.

[116] K. Lücke, I. Heckelmann, and G. Abbruzzese. Statistical theory of two-dimensional grain growth—ii. kinetics of grain growth. *Acta Metallurgica et Materialia*, 40(3):533–542, 1992.

[117] K. Lücke, R. Brandt, and G. Abbruzzese. Normal and abnormal grain growth as transient phenomena. *Interface Science*, 6(1):67–76, 1998.

[118] Y.-I. Jung, M.-H. Lee, H.-G. Kim, J.-Y. Park, and Y.-H. Jeong. Behavior of a recrystallization in HANA-4 and HANA-6 zirconium-based alloys. *Journal of Alloys and Compounds*, 479(1):423–426, 2009.

[119] H. Tian, X. Wang, W. Gong, J. Zhou, and H. Zhang. Recrystallization behavior of cold-rolled Zr–1Nb alloy. *Journal of Nuclear Materials*, 456:321–328, 2015.

[120] F. Humphreys. A unified theory of recovery, recrystallization and grain growth, based on the stability and growth of cellular microstructures—i. the basic model. *Acta Materialia*, 45(10):4231–4240, 1997.

[121] F. Humphreys. A unified theory of recovery, recrystallization and grain growth, based on the stability and growth of cellular microstructures—ii. the effect of second-phase particles. *Acta Materialia*, 45(12):5031–5039, 1997.

[122] P. Hurley and F. Humphreys. Modelling the recrystallization of single-phase aluminium. *Acta Materialia*, 51(13):3779–3793, 2003.

[123] H. Zurob, Y. Bréchet, and J. Dunlop. Quantitative criterion for recrystallization nucleation in single-phase alloys: Prediction of critical strains and incubation times. *Acta Materialia*, 54(15):3983–3990, 2006.

[124] J. Dunlop, Y. Bréchet, L. Legras, and H. Zurob. Modelling isothermal and non-isothermal recrystallisation kinetics: Application to zircaloy-4. *Journal of Nuclear Materials*, 366(1):178–186, 2007.

[125] S. Gourdet and F. Montheillet. A model of continuous dynamic recrystallization. *Acta Materialia*, 51(9):2685–2699, 2003.

[126] S. Gourdet. *Étude des mécanismes de recristallisation au cours de la déformation à chaud de l'aluminium*. PhD thesis. École des Mines de Saint-Étienne, 1997.

[127] H. McQueen and W. Blum. Dynamic recovery: sufficient mechanism in the hot deformation of al (<99.99). *Materials Science and Engineering: A*, 290(1):95–107, 2000.

[128] H. McQueen and M. Kassner. Comments on 'a model of continuous dynamic recrystallization' proposed for aluminum. *Scripta Materialia*, 51(5):461–465, 2004.

[129] R. Buzolin, D. Canelo-Yubero, F. Warchomicka, M. Lasnik, A. Krumphals, and M. Poletti. Refinement of the Ti-17 microstructure after hot deformation: Coupled mesoscale model. *Materials Science and Engineering A*, 800, 2021.

[130] Z. Sun, H. Wu, J. Cao, and Z. Yin. Modeling of continuous dynamic recrystallization of Al-Zn-Cu-Mg alloy during hot deformation based on the internal-state-variable (ISV) method. *International Journal of Plasticity*, 106:73–87, 2018.

[131] Y. Li, B. Gu, S. Jiang, Y. Liu, Z. Shi, and J. Lin. A CDRX-based material model for hot deformation of aluminium alloys. *International Journal of Plasticity*, 134:102844, 2020.

[132] T. Gan, Z. Yu, Y. Zhao, X. Fan, and X. Lai. A continuous dynamic recrystallization constitutive model combined with grain fragmentation and subgrain rotation for aluminum alloy 2219 under hot deformation. *Modelling and Simulation in Materials Science and Engineering*, 29(2), 2021.

[133] S. Chen, D. Li, S. Zhang, H. Han, H. Lee, and M. Lee. Modelling continuous dynamic recrystallization of aluminum alloys based on the polycrystal plasticity approach. *International Journal of Plasticity*, 131:102710, 2020.

[134] P. R. Dawson. Computational crystal plasticity. *International Journal of Solids and Structures*, 37(1):115–130, 2000.

[135] A. M. Habraken. Modelling the plastic anisotropy of metals. *Archives of Computational Methods in Engineering*, 11(1):3–96, 2004.

[136] M. Anderson, D. Srolovitz, G. Grest, and P. Sahni. Computer simulation of grain growth—i. kinetics. *Acta Metallurgica*, 32(5):783–791, 1984.

[137] A. Rollett, M. Luton, and D. Srolovitz. Microstructural simulation of dynamic recrystallization. *Acta Metallurgica et Materialia*, 40(1):43–55, 1992.

[138] P. Peczak and M. J. Luton. The effect of nucleation models on dynamic recrystallization i. homogeneous stored energy distribution. *Philosophical Magazine B*, 68(1):115–144, 1993.

[139] P. Peczak and M. J. Luton. The effect of nucleation models on dynamic recrystallization ii. heterogeneous stored-energy distribution. *Philosophical Magazine B*, 70(4):817–849, 1994.

[140] Y. Chun, S. Semiatin, and S. Hwang. Monte-Carlo modeling of microstructure evolution during the static recrystallization of cold-rolled, commercial-purity titanium. *Acta Materialia*, 54(14):3673–3689, 2006.

[141] M. Jedrychowski, B. Bacroix, J. Tarasiuk, and S. Wroński. Monte-Carlo modelling of recrystallization in alpha zirconium. *Computational Materials Science*, 199:110742, 2021.

[142] H. Hesselbarth and I. Göbel. Simulation of recrystallization by cellular automata. *Acta Metallurgica et Materialia*, 39(9):2135–2143, 1991.

[143] G. Kugler and R. Turk. Study of the influence of initial microstructure topology on the kinetics of static recrystallization using a cellular automata model. *Computational Materials Science*, 37(3):284–291, 2006.

[144] K. Muszka, M. Sitko, P. Lisiecka-Graca, T. Simm, E. Palmiere, M. Schmidtchen, G. Korpala, J. Wang, and L. Madej. Experimental and numerical study of the effects of the reversal hot rolling conditions on the recrystallization behavior of austenite model alloys. *Metals*, 11(1), 2021.

[145] R. Goetz. Particle stimulated nucleation during dynamic recrystallization using a cellular automata model. *Scripta Materialia*, 52(9):851–856, 2005.

[146] F. Lin, M. Sitko, L. Madej, and L. Delannay. Non-uniform grain boundary migration during static recrystallization: A cellular automaton study. *Metallurgical and Materials Transactions A*, 53(5):1630–1644, 2022.

[147] S. Liu, D. Kent, H. Zhan, N. Doan, C. Wang, S. Yu, M. Dargusch, and G. Wang. Influence of strain rate and crystallographic orientation on dynamic recrystallization of pure Zn during room-temperature compression. *Journal of Materials Science & Technology*, 86:237–250, 2021.

[148] M. Azarbarmas, S. S. Mirjavadi, A. Ghasemi, and A. M. Hamouda. A combined method to model dynamic recrystallization based on cellular automaton and a phenomenological (CAP) approach. *Metals*, 8(11), 2018.

[149] K. Kawasaki, T. Nagai, and K. Nakashima. Vertex models for two-dimensional grain growth. *Philosophical Magazine B*, 60(3):399–421, 1989.

[150] D. Weygand, Y. Bréchet, J. Lépinoux, and W. Gust. Three-dimensional grain growth: A vertex dynamics simulation. *Philosophical Magazine B*, 79(5):703–716, 1999.

[151] S. Florez, K. Alvarado, D. P. Muñoz, and M. Bernacki. A novel highly efficient lagrangian model for massively multidomain simulation applied to microstructural evolutions. *Computer Methods in Applied Mechanics and Engineering*, 367:113107, 2020.

[152] S. Florez, K. Alvarado, and M. Bernacki. A new front-tracking lagrangian model for the modeling of dynamic and post-dynamic recrystallization. *Modelling and Simulation in Materials Science and Engineering*, 29(3):035004, 2021.

[153] F. Humphreys. A network model for recovery and recrystallisation. *Scripta Metallurgica et Materialia*, 27(11):1557–1562, 1992.

[154] F. Humphreys. Modelling microstructural evolution during annealing. *Modelling and Simulation in Materials Science and Engineering*, 8(6):893–910, 2000.

[155] L.-Q. Chen. Phase-field models for microstructure evolution. *Annual review of materials research*, 32(1):113–140, 2002.

[156] H. Hallberg. Approaches to modeling of recrystallization. *Metals*, 1(1):16–48, 2011.

[157] J. W. Cahn. On spinodal decomposition. *Acta Metallurgica*, 9(9):795–801, 1961.

[158] S. M. Allen and J. W. Cahn. A microscopic theory for antiphase boundary motion and its application to antiphase domain coarsening. *Acta Metallurgica*, 27(6):1085–1095, 1979.

[159] I. Loginova, J. Ågren, and G. Amberg. On the formation of widmanstätten ferrite in binary Fe–C - phase-field approach. *Acta Materialia*, 52(13):4055–4063, 2004.

[160] L.-Q. Chen and W. Yang. Computer simulation of the domain dynamics of a quenched system with a large number of nonconserved order parameters: The grain-growth kinetics. *Phys. Rev. B*, 50:15752–15756, 1994.

[161] T. Takaki, Y. Hisakuni, T. Hirouchi, A. Yamanaka, and Y. Tomita. Multi-phase-field simulations for dynamic recrystallization. *Computational Materials Science*, 45(4):881–888, 2009.

[162] T. Takaki, C. Yoshimoto, A. Yamanaka, and Y. Tomita. Multiscale modeling of hot-working with dynamic recrystallization by coupling microstructure evolution and macroscopic mechanical behavior. *International Journal of Plasticity*, 52:105–116, 2014. In Honor of Hussein Zbib.

[163] M. Elsey, S. Esedoglu, and P. Smereka. Diffusion generated motion for grain growth in two and three dimensions. *Journal of Computational Physics*, 228(21):8015–8033, 2009.

[164] M. Elsey, S. Esedoḡlu, and P. Smereka. Large-scale simulation of normal grain growth via diffusion-generated motion. *Proceedings of the Royal Society A: Mathematical, Physical and Engineering Sciences*, 467(2126):381–401, 2011.

[165] S. Osher and J. A. Sethian. Fronts propagating with curvature-dependent speed: Algorithms based on Hamilton-Jacobi formulations. *Journal of Computational Physics*, 79(1):12–49, 1988.

[166] B. Merriman, J. K. Bence, and S. J. Osher. Motion of multiple junctions: A level set approach. *Journal of Computational Physics*, 112(2):334–363, 1994.

[167] H.-K. Zhao, T. Chan, B. Merriman, and S. Osher. A variational level set approach to multiphase motion. *Journal of Computational Physics*, 127(1):179–195, 1996.

[168] T. Coupez, H. Digonnet, and R. Ducloux. Parallel meshing and remeshing. *Applied Mathematical Modelling*, 25(2):153–175, 2000. Dynamic load balancing of mesh-based applications on parallel.

[169] H. Digonnet, L. Silva, and T. Coupez. Cimlib: A fully parallel application for numerical simulations based on components assembly. *AIP Conference Proceedings*, 908(1):269–274, 2007.

[170] M. Shakoor, B. Scholtes, P.-O. Bouchard, and M. Bernacki. An efficient and parallel level set reinitialization method – application to micromechanics and microstructural evolutions. *Applied Mathematical Modelling*, 39(23):7291–7302, 2015.

[171] ASTM E9-19, standard test methods of compression testing of metallic materials at room temperature. Technical report, ASTM International, West Conshohocken, PA, 2019.

[172] ASTM E209-18, standard practice for compression tests of metallic materials at elevated temperatures with conventional or rapid heating rates and strain rates. Technical report, ASTM International, West Conshohocken, PA, 2018.

[173] A. Nicolay. *Microstructure and properties of Inconel 718 DA screw press forged at subsolvus δ temperature*. PhD thesis. Paris Sciences et Lettres, 2019.

[174] B. Roebuck, J. Lord, M. Brooks, M. Loveday, C. Sellars, and R. Evans. Measurement of flow stress in hot axisymmetric compression tests. *Materials at High Temperatures*, 23(2):59–83, 2006.

[175] J. Schindelin, I. Arganda-Carreras, E. Frise, V. Kaynig, M. Longair, T. Pietzsch, S. Preibisch, C. Rueden, S. Saalfeld, B. Schmid, J.-Y. Tinevez, D. White, V. Hartenstein, K. Eliceiri, P. Tomancak, and A. Cardona. Fiji: an open-source platform for biological-image analysis. *Nature Methods*, 9:676–682, 2012.

[176] B. Flipon, V. Grand, B. Murgas, A. Gaillac, A. Nicolaÿ, N. Bozzolo, and M. Bernacki. Grain size characterization in metallic alloys using different microscopy and post-processing techniques. *Materials Characterization*, 174:110977, 2021.

[177] A. Buades, B. Coll, and J. Morel. Non-local means denoising. *Image Processing On Line*, 1:208–212, 2011.

[178] D. Legland, I. Arganda-Carreras, and P. Andrey. MorphoLibJ: integrated library and plugins for mathematical morphology with ImageJ. *Bioinformatics*, 32(22):3532–3534, 2016.

[179] N. Bozzolo, F. Gerspach, G. Sawina, and F. Wagner. Accuracy of orientation distribution function determination based on EBSD data - a case study of a recrystallized low alloyed Zr sheet. *Journal of microscopy*, 227(3):275–283, 2007.

[180] S. Zaefferer. A critical review of orientation microscopy in SEM and TEM. *Crystal Research and Technology*, 46(6):607–628, 2011.

[181] A. J. Schwartz, M. Kumar, B. L. Adams, and D. P. Field. *Electron backscatter diffraction in materials science*, volume 2. Springer, 2009.

[182] S. I. Wright. A parametric study of electron backscatter diffraction based grain size measurements. *Practical Metallography*, 47(1):16–33, 2010.

[183] F. Bachmann, R. Hielscher, and H. Schaeben. Grain detection from 2D and 3D EBSD data—specification of the MTEX algorithm. *Ultramicroscopy*, 111(12):1720–1733, 2011.

[184] R. Hielscher, C. B. Silbermann, E. Schmidl, and J. Ihlemann. Denoising of crystal orientation maps. *Journal of Applied Crystallography*, 52(5):984–996, 2019.

[185] J. Nye. Some geometrical relations in dislocated crystals. *Acta Metallurgica*, 1(2):153–162, 1953.

[186] M. Ashby. The deformation of plastically non-homogeneous materials. *Philosophical Magazine*, 21(170):399 – 424, 1970.

[187] A. Hadadzadeh, F. Mokdad, M. Wells, and D. Chen. A new grain orientation spread approach to analyze the dynamic recrystallization behavior of a cast-homogenized Mg-Zn-Zr alloy using electron backscattered diffraction. *Materials Science and Engineering: A*, 709:285–289, 2018.

[188] A. J. Wilkinson and D. Randman. Determination of elastic strain fields and geometrically necessary dislocation distributions near nanoindents using electron back scatter diffraction. *Philosophical Magazine*, 90(9):1159–1177, 2010.

[189] P. W. Hawkes and J. C. Spence. *Science of microscopy*, volume 1. Springer, 2007.

[190] D. Ruiz Sarrazola, D. Pino Muñoz, and M. Bernacki. A new numerical framework for the full field modeling of dynamic recrystallization in a CPFEM context. *Computational Materials Science*, 179:109645, 2020.

[191] D. Ruiz Sarrazola, L. Maire, C. Moussa, N. Bozzolo, D. Pino Muñoz, and M. Bernacki. Full field modeling of dynamic recrystallization in a CPFEM context – application to 304L steel. *Computational Materials Science*, 184:109892, 2020.

[192] A. Laasraoui and J. Jonas. Prediction of steel flow stresses at high temperatures and strain rates. *Metallurgical Transactions A*, 22(7):1545–1558, 1991.

[193] D. Ilin, N. Bozzolo, T. Toulorge, and M. Bernacki. Full field modeling of recrystallization: Effect of intragranular strain gradients on grain boundary shape and kinetics. *Computational Materials Science*, 150:149–161, 2018.

[194] K. Hitti, P. Laure, T. Coupez, L. Silva, and M. Bernacki. Precise generation of complex statistical representative volume elements (RVEs) in a finite element context. *Computational Materials Science*, 61:224–238, 2012.

[195] K. Hitti and M. Bernacki. Optimized dropping and rolling (ODR) method for packing of poly-disperse spheres. *Applied Mathematical Modelling*, 37(8):5715–5722, 2013.

[196] B. Scholtes. *Développement d'un modèle level set performant pour la modélisation de la recristallisation en 3D*. PhD thesis. Paris Sciences et Lettres, 2016.

[197] A. Després, M. Greenwood, and C. Sinclair. A mean-field model of static recrystallization considering orientation spreads and their time-evolution. *Acta Materialia*, 199:116–128, 2020.

[198] E. Holm, M. Miodownik, and A. Rollett. On abnormal subgrain growth and the origin of recrystallization nuclei. *Acta Materialia*, 51(9):2701–2716, 2003.

[199] Y. Suwa, Y. Saito, and H. Onodera. Phase-field simulation of recrystallization based on the unified subgrain growth theory. *Computational Materials Science*, 44(2):286–295, 2008.

[200] E. Roux, M. Bernacki, and P. Bouchard. A level-set and anisotropic adaptive remeshing strategy for the modeling of void growth under large plastic strain. *Computational Materials Science*, 68:32–46, 2013.

[201] I. Carneiro and S. Simões. Recent advances in EBSD characterization of metals. *Metals*, 10(8), 2020.

[202] V. S. Tong and T. B. Britton. Formation of very large 'blocky alpha' grains in zircaloy-4. *Acta Materialia*, 129:510–520, 2017.

[203] V. Hiwarkar, S. Sahoo, I. Samajdar, A. Satpathy, K. Krishna, G. Dey, D. Srivastav, R. Tewari, and S. Banarjee. Defining recrystallization in pilgered zircaloy-4: From preferred nucleation to growth inhibition. *Journal of Nuclear Materials*, 412(3):287–293, 2011.

[204] H. Hallberg. A modified level set approach to 2D modeling of dynamic recrystallization. *Modelling and Simulation in Materials Science and Engineering*, 21(8):085012, 2013.

[205] E. Tenckhoff. Deformation mechanisms, texture, and anisotropy in zirconium and zircaloy. *ASTM STP 966*, 1988.

[206] J. Dunlop, Y. Bréchet, L. Legras, and Y. Estrin. Dislocation density-based modelling of plastic deformation of zircaloy-4. *Materials Science and Engineering: A*, 443(1):77–86, 2007.

[207] J. Moon, P. Cantonwine, K. Anderson, S. Karthikeyan, and M. Mills. Characterization and modeling of creep mechanisms in zircaloy-4. *Journal of Nuclear Materials*, 353(3):177–189, 2006.

[208] J. Shen, Y. Li, and Q. Wei. Statistic derivation of Taylor factors for polycrystalline metals with application to pure magnesium. *Materials Science and Engineering: A*, 582:270–275, 2013.

[209] H. Mughrabi. The α-factor in the taylor flow-stress law in monotonic, cyclic and quasi-stationary deformations: Dependence on slip mode, dislocation

arrangement and density. *Current Opinion in Solid State and Materials Science*, 20(6):411–420, 2016.

[210] L. J. Siefken, E. W. Coryell, E. A. Harvego, and J. K. Hohorst. Matpro - a library of materials properties for light-water-reactor accident analysis. Code manual, Idaho National Engineering and Environmental Laboratory, 2001.

[211] F. Montheillet, O. Lurdos, and G. Damamme. A grain scale approach for modeling steady-state discontinuous dynamic recrystallization. *Acta Materialia*, 57(5):1602–1612, 2009.

[212] J. J. Jonas, C. M. Sellars, and W. J. M. Tegart. Strength and structure under hot-working conditions. *Metallurgical Reviews*, 14(1):1–24, 1969.

[213] M. Brozovic Gariglio. *Analyse expérimentale des microstructures et modélisation multi-échelle de la déformation à chaud d'alliages de titane*. PhD thesis, 2022. Paris Sciences et Lettres, 2022.

[214] J. Crepin, T. Bretheau, D. Caldemaison, A. Barbu, and G. Jazkierowitcz. Microstructural study of β-treated grade 702 zirconium. scanning electron microscopy and transmission electron microscopy, complementarity of two observational scales. *Journal of Materials Science*, 32(18):4841–4846, 1997.

RÉSUMÉ

Du fait de leur faible section de capture neutronique et de leurs propriétés mécaniques et de résistance à la corrosion, les alliages de zirconium sont utilisés dans l'industrie nucléaire depuis de nombreuses décennies. Les procédés de fabrication utilisés sont complexes et comprennent plusieurs étapes de déformation et de traitement thermique. Chacune des étapes de transformation doit remplir deux objectifs : converger vers la géométrie finale des produits en assurant l'absence de défauts et fournir aux produits une microstructure capable de résister aux sollicitations auxquelles l'assemblage de combustible est soumis tout au long de sa vie dans le réacteur. Par conséquent, et afin de répondre aux exigences de sûreté élevées du domaine nucléaire, il est nécessaire de connaître et maîtriser les évolutions de microstructure lors de la mise en forme et des traitements thermiques. Par ailleurs, le développement d'outils numériques fiables à l'échelle de la microstructure est donc d'un intérêt crucial.

Dans cet objectif, un grand nombre de microstructures déformées à chaud ont été caractérisées par EBSD afin de déterminer l'influence des conditions thermomécaniques et de la microstructure initiale sur les évolutions microstructurales du zircaloy-4. Ces données ont ensuite été confrontées aux résultats obtenus à l'aide de simulations en champ complet à l'échelle mésoscopique. Plus précisément, une approche de type Level-Set, intégrée dans un environnement éléments finis, et enrichie sur la base du modèle de Gourdet-Montheillet, a été validée. Cette implémentation permet de reproduire des mécanismes de recristallisation continue en régimes dynamique et post-dynamique et améliore donc la capacité de prédiction des modèles dans le cas de la recristallisation du zircaloy-4. Les résultats, expérimentaux et numériques ont permis de quantifier l'influence de la microstructure initiale mais également de discriminer les caractéristiques de la microstructure qui conditionnent les évolutions observées. Les limitations actuelles de l'approche ont également été discutées.

MOTS CLÉS

Déformation à chaud, Zircaloy-4, Recristallisation continue, Modélisation en champ complet, Level-set, Techniques de caractérisation, EBSD, essais thermomécaniques.

ABSTRACT

Due to their low neutron-capture cross-section, their good mechanical properties and their resistance to corrosion, zirconium alloys are used in nuclear industry for several decades. The manufacturing processes are complex and include several deformation and heat treatment stages. Each of these steps must fulfill two criteria: getting closer to the final product shape without any defect and provide to final product a microstructure suited to withstand the severe conditions in nuclear reactors. Consequently, and to fulfill the high security requirements of nuclear industry, it is necessary to understand and master the microstructure evolution during the forming and heat treatment processes. Moreover, the development of predictive numerical tools at the mesoscopic scale is thus of paramount importance.

To that end, many hot deformed microstructures were characterized by EBSD to determine the impact of thermomechanical conditions and of initial microstructure upon microstructure evolution of zircaloy-4. These data have been compared to full-field simulation results at the mesoscopic scale. To do so, Gourdet-Montheillet laws were introduced into a Level-Set model, embedded into a finite element framework and the results validated. This implementation enables to simulate continuous recrystallization mechanisms for dynamic and post-dynamic conditions and thus to improve the model ability to simulate recrystallization of zircaloy-4. Experiment and simulation results have enabled to quantify the influence of initial microstructure and to discriminate which microstructural features condition the observed mechanisms. The current limitations of the developed approach were also discussed.

KEYWORDS

Hot forming, Zircaloy-4, Continuous recrystallization, Full-field modeling, Level-set, Characterization, EBSD, thermomechanical testing.